Dissertation
submitted to the
Combined Faculty of Natural Sciences and Mathematics
of Heidelberg University, Germany
for the degree of
Doctor of Natural Sciences

Put forward by
Lukas Kreis
born in Frankfurt am Main.
Oral examination: 11.10.2021

Investigating the Initial State
of Heavy-Ion Collisions through
Measurements of Anisotropic Flow
using Spectator Neutrons
with ALICE at the LHC

Referees:	Prof. Dr. Silvia Masciocchi
	Prof. Dr. Norbert Herrmann
Scientific Advisor:	Dr. Ilya Selyuzhenkov

Investigating the Initial State of Heavy-Ion Collisions through Measurements of Anisotropic Flow using Spectator Neutrons with ALICE at the LHC

Above temperatures of 150 MeV, nuclear matter transitions into the quark-gluon plasma (QGP): a phase of unbound quarks and gluons. These conditions are reached in heavy-ion collisions at center-of-mass energies per nucleon-nucleon pair ($\sqrt{s_{\mathrm{NN}}}$) in the TeV scale that can generate energy densities larger than 10 GeV/fm^3. The spatial distribution of this energy originates from the fluctuating shape of the overlap of nuclei in the initial state. On a timescale of $\sim$ 10 fm/c, the QGP, a near-perfect fluid, transforms the spatial anisotropy into a momentum anisotropy of the emitted particles called anisotropic flow. The comparison of such observations to hydrodynamic model calculations allows extracting the QGP viscosity. The spectator nucleons — remnants of the colliding nuclei which rapidly decouple ($\ll$ 1 fm/c) before the anisotropic flow emerges — are sensitive to initial-state fluctuations. This thesis presents novel measurements of anisotropic flow and its fluctuations relative to the spectator deflection in lead-lead and xenon-xenon collisions at $\sqrt{s_{\mathrm{NN}}}$ of 2.76 TeV and 5.44 TeV, respectively, with ALICE at the Large Hadron Collider. These observations show an approximate universal scaling with the shape of the initial energy density. Differences between the flow measurements using spectators and those only using produced particles constrain the initial-state fluctuations. Comparisons to current initial state models without spectator dynamics indicate these dynamics are needed for improving the precision of the QGP viscosity extraction.

Untersuchungen des Anfangszustandes von Schwerionenkollisionen durch Messungen des anisotropen Flusses unter Verwendung von Zuschauerneutronen mit ALICE am LHC

Oberhalb Temperaturen von etwa 150 MeV geht Kernmaterie in ein Quark-Gluon-Plasma (QGP) über, welches aus ungebundenen Quarks und Gluonen besteht. Diese Bedingungen werden in Schwerionenkollisionen bei Schwerpunktsenergien pro Nukleonenpaar ($\sqrt{s_{\mathrm{NN}}}$) in der TeV-Skala erreicht, welche Energiedichten größer als 10 GeV/fm^3 erzeugen können. Die räumliche Verteilung dieser Energie ergibt sich aus der fluktuierenden Form der Überlappung der Kerne im Ausgangszustand. Auf einer Zeitskala von $\sim$ 10 fm/c wandelt das QGP, ein nahezu perfektes Fluid, die räumliche Anisotropie in eine Impulsanisotropie der emittierten Teilchen um, die als anisotroper Fluss bezeichnet wird. Der Vergleich solcher Beobachtungen mit hydrodynamischen Modellrechnungen ermöglicht die Extraktion der QGP-Viskosität. Die Zuschauernukleonen sind Überreste der kollidierenden Kerne, die sich bereits vor dem Auftreten des anisotropen Flusses entkoppeln ($\ll$ 1 fm/c), wodurch sie empfindlich auf Fluktuationen des Ausgangszustands reagieren. In dieser Arbeit werden neueste Messungen des anisotropen Flusses und seiner Fluktuationen relativ zur Ablenkung der Zuschauerneutronen in Blei-Blei und Xenon-Xenon Kollisionen bei $\sqrt{s_{\mathrm{NN}}}$ von 2.76 TeV bzw. 5.44 TeV mit ALICE am Large Hadron Collider vorgestellt. Diese Beobachtungen zeigen eine annähernd universelle Skalierung mit der Form der Ausgangsenergiedichte. Unterschiede zwischen der Messung des Flusses mit Zuschauern und solchen, die nur produzierte Teilchen verwenden, beschränken die Fluktuationen des Ausgangszustands. Der Vergleich mit aktuellen Ausgangszustandsmodellen ohne Zuschauerdynamik zeigt, dass die Dynamik benötigt wird, um die Genauigkeit der QGP-Viskositätsextraktion zu verbessern.

Contents

1 Introduction

1.1 Standard Model

The matter surrounding us interacts, in our current understanding, through four fundamental forces. They are, in ascending order of their coupling strength, the gravitational, weak, electromagnetic, and strong interactions. The interactions between elementary particles of matter (fermions) through the exchange of force carriers (gauge bosons) is described within the so-called Standard Model of particle physics. Figure 1.1 shows an overview of all particles in the Standard Model. To each fermion there exists an antiparticle of opposite charge. In the following, the four fundamental interactions and their relation to the elementary particles of the Standard Model are described.

Natural units $c = \hbar = k_B = 1$ are being used throughout this thesis, unless specified otherwise.

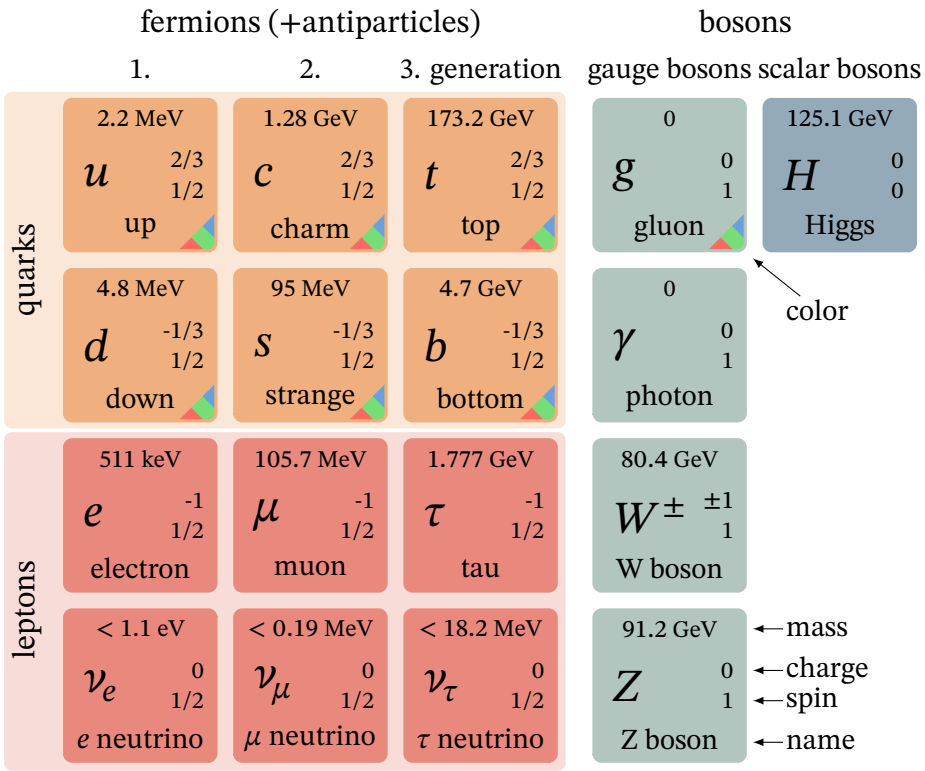

Figure 1.1: The particles of the Standard Model of particle physics. Adapted from the particle listing in ref.[3].

Gravity describes the attraction between objects which carry mass or energy. On the scale of elementary particles, it only has a negligible impact due to its small coupling strength. Since gravity is always attractive, it becomes one of the dominant effects on macroscopic scales. It is responsible for many of the astronomical phenomena, such as the formation of stars and the trajectories of astronomical bodies. Gravity is described best by the theory of general relativity, in which it is realized as a geometric property of a four-dimensional spacetime. Because general relativity is a classical theory, it is not yet integrated into the Standard Model of particle physics.

The electromagnetic interaction describes the force between electrically charged objects, such as the binding of electrons to the nucleus. The force is mediated by the photon and acts on the quarks (up, down, strange, charm, bottom, and top) and the electrically-charged leptons (electron, muon, and tau). Because the photon has no mass, the range of the interaction is infinite. At low energy scales the coupling strength is characterized by the coupling strength of approximately 1/137. At higher energy scales, however, its coupling strength increases. For example, at the energy scale of the Z^0 boson[3] it reaches $\approx 1/127$. This dependence of the coupling constant on the energy scale is known as a running coupling. The electromagnetic force is described by quantum electrodynamics.

The weak interaction describes the underlying mechanism behind the decay of some unstable particles, such as the β decay of radioactive nuclei. Fundamentally, the weak force affects all (left-handed) fermions, as well as the Higgs boson. The force is mediated by its three force carriers, the massive W^+, W^-, Z^0 bosons. Because the force carriers are massive, the weak interaction has a very short effective range. Decays of particles caused by it have a much larger lifetime compared to electromagnetic decays. At higher energies or short distances, the weak interaction is of the same strength as the electromagnetic interaction. The weak and electromagnetic force can be described within the same framework of the electroweak theory.

Closely related to the electroweak theory is the all-pervasive Higgs field, which is responsible through the Higgs mechanism[4,5] for the mass of the W^+, W^-, Z^0 bosons as well as the masses of the charged leptons and quarks through the Yukawa interaction[6]. The Higgs mechanism predicts the existence of a scalar boson referred to as the Higgs boson, which was discovered[7,8] in 2012.

The strong interaction is what binds quarks and gluons into nucleons and nucleons into nuclei. The force, which is mediated by the gluons, acts on the color charge carried by quarks and gluons. There are three different colors[9]: red, green, blue. Quarks carry color, antiquarks carry anticolor, and gluons carry a combination of color and anticolor. In the typical length scale of hadrons (a few femtometers) the coupling constant of the strong interaction is on the order of 1. At these scales, it is 10^2 times stronger than the electromagnetic force, 10^6 times stronger than the weak force, and an estimated 10^{38} times stronger than the gravitational force. The strong interaction is described by the theory of quantum chromodynamics.

1.2 Quantum Chromodynamics

The strong interaction between quarks and gluons is formulated as a non-abelian gauge theory called QCD. The dynamical behavior of the strongly interacting particles is encoded in the Lagrangian of QCD[3]

$$\mathcal{L}_{QCD} = \sum_{q=u,d,s,\ldots} \overline{\psi}_{q,a}(i(\gamma^\mu D_\mu)_{ab} - m_q\delta_{ab})\psi_{q,b} - \frac{1}{4}F^A_{\mu\nu}F^{A\mu\nu}\,. \tag{1.1}$$

The Einstein summation convention is used to abbreviate the notation. $\psi_{q,a}$ is the quark field spinor of a quark with flavor q and a color index a that runs from 1 to $N_c = 3$. The color indices correspond to the three colors. The term $-m\overline{\psi}\psi$ explicitly includes the mass of the

quarks, which are generated by the Yukawa interaction. The gauge covariant derivate D_μ is defined as

$$D_\mu = \partial_\mu \delta_{ab} - g_s \gamma^\mu t^C_{ab} \mathcal{A}^C_\mu \,. \tag{1.2}$$

γ^μ are the Dirac γ-matrices. $\mathcal{A}^C_\mu$ corresponds to the gluon fields, where C runs from 1 to $(N_c^2 - 1) = 8$. The gluon fields do not distinguish between the quark flavors. The t^C_{ab} are 3×3 matrices which encode the color-changing aspect of the interaction of a quark with a gluon. A color singlet gluon does not exist. The t^C_{ab} matrices are related to the Gell-Mann matrices[10] $\lambda^C_{ab} = 2t^C_{ab}$. The coupling constant of QCD is give by $g_s = \alpha_s/4\pi$. Besides the quark masses it is the only free parameter of the model.

The gluon field strength tensor $F^A_{\mu\nu}$ encodes the interaction of the gluons with the quarks and the gluon self-interaction. It is given by

$$\begin{aligned} F^A_{\mu\nu} &= \partial_\mu \mathcal{A}^A_\nu - \partial_\nu \mathcal{A}^C_\mu - g_s f_{ABC} \mathcal{A}^B_\mu \mathcal{A}^C_\nu \\ [t^A, t^B] &= i f_{ABC} t^C \,. \end{aligned} \tag{1.3}$$

QCD exhibits three important properties.

First is the property of *color confinement*[11]; It postulates that (anti)quarks and gluons, which carry color charge, cannot be observed directly. They always form composite systems known as hadrons. There are two types of hadrons: mesons consist of a quark and antiquark pair; baryons are composed of three quarks or antiquarks. The resulting hadrons are always color neutral. Because gluons also carry color, they are affected by color confinement as well. The confinement of the gluons restricts the range of the strong interaction to a few femtometers.

The second property is *asymptotic freedom*[12,13]; It describes how the strength of the interaction between quarks and gluons changes when the energy scale increases, or equivalently the length scale decreases. The running coupling strength of QCD behaves contrary to the running coupling in QED. At very high energy scales, the quarks and gluon become *asymptotically free*. Figure 1.2 shows the coupling constant of the strong interaction as a function of the energy scale Q. In the measurement, the energy scale is given by the momentum transfer in the given process. The coupling constant is extracted from the measurement using perturbative calculations. These calculations are only possible for interactions between particles at high energy scales due to the small coupling constant. The low energy scales where the coupling is strong is only accessible by other means, such as lattice QCD, or effective theories.

The third property of QCD is *chiral symmetry breaking*[14]. The Lagrangian of QCD of massless quarks and gluons exhibits chiral symmetry; This means the fundamental left- and right-handed parts of the quark fields transform independently. This symmetry of QCD is broken in two ways: explicit breaking meaning the theory itself is not invariant under transformations and spontaneous breaking meaning the chiral symmetry of the Lagrangian is not realized by the ground state. The spontaneous breaking of the chiral symmetry in QCD with massless quarks of two flavors (up and down) gives rise to three massless Nambu-Goldstone bosons. In reality, pions are much lighter than the other hadrons, but they are not massless. Their small, but finite mass, is explained by the mass term for quarks $-m\bar{\psi}\psi$ in the Lagrangian of

QCD (eq. (1.1)). This mass term explicitly mixes the left- and right-handed components of the quarks. At low energy scales, the spontaneous breaking of chiral symmetry is responsible for most of the mass of the hadrons; The explicit breaking of the chiral symmetry due to the mass of the quarks only contributes a small amount[15].

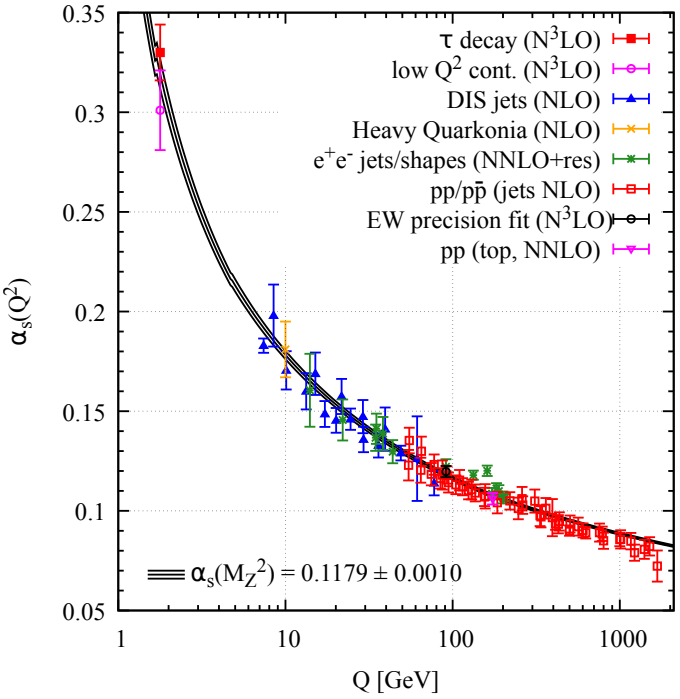

Figure 1.2: Summary of the measurements of α_s as a function of the energy scale Q. The QCD perturbation theory used to extract the value is listed inside the parenthesis. Figure taken from ref.[3].

1.3 Strongly-interacting Matter under Extreme Conditions

As established in the previous section, under normal conditions color confinement of the strong interaction binds quarks and gluons into hadrons. If such matter, consisting of a gas of hadrons, is heated to very high temperatures, numerous additional hadrons are created. However, for such a matter, an upper limit of the temperature exists, at which point instead of a further increase of the temperature more and more hadrons start to appear. This limiting temperature is called Hagedorn temperature; For a gas of hadrons it limits[16] the temperature to approximately 150 MeV. Matter interacting through the strong interaction (strongly interacting matter) can surpass this limiting temperature by undergoing a phase transition from a gas of hadrons to a phase of quarks and gluons, called QGP[17]. In the QGP, the quarks and gluons are no longer confined to hadrons; they are deconfined. Besides the transition to deconfined matter, a transition to a chiral symmetric phase is also expected[18]. In a chiral symmetric phase, the quarks are approximately massless.

In the early history of the universe, about 10 microseconds after the big bang such a transition from a QGP to a hadron gas takes place. A slight imbalance between matter and antimatter causes the annihilation of all antimatter, which ultimately leads to the matter-dominated universe seen today. The observations and theoretical predictions give strong indications for a rich structure of different phases of strongly interacting matter exists. Studying the behavior

of strongly interacting matter at extreme conditions can give insights into the early time of the universe which is inaccessible using astronomy[19].

The phases of matter are usually studied relative to the external conditions. On the boundary between the different phases, the phase transitions describe how one phase transitions to another under the change of the external conditions. These transitions can be categorized into different orders according to the Ehrenfest classification[20].

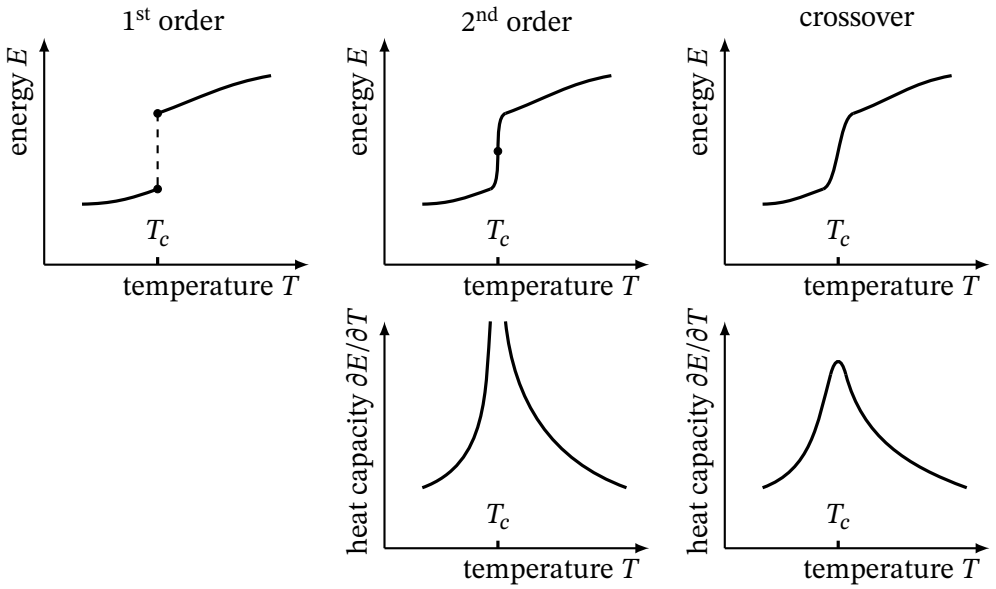

Figure 1.3: Temperature dependence of the thermodynamic energy for first-, second-order, and crossover phase transitions.

Figure 1.3 sketches the different orders of phase transitions. The temperature dependence of the thermodynamic energy E and its first derivate with respect to the temperature T the heat capacity is shown for a canonical ensemble of particles.

A first-order phase transition (left panel) is one in which the thermodynamic energy as a function of a thermodynamic variable is discontinuous. Such a phase transition is associated with the absorption or release of latent heat. The ice-water and water-gas transitions are an example of first-order phase transitions.

A second-order phase transition (center panel) is one in which the energy is continuous, but the first derivative is discontinuous. At the critical endpoint of the first-order liquid-gas phase transition of water a divergence of the heat capacity is observed, which corresponds to a second-order transition.

A crossover (right panel) is a transition that does not exhibit any discontinuities. Such a phase transition is observed for water beyond the critical endpoint of the liquid-gas transition (supercritical water) between liquid-like and gas-like states[21].

The phases and their phase boundaries are depicted in a graph called the phase diagram. Analogous to the phase diagram of water which depicts the ice, water, and gas phases as a function of pressure and temperature, the phases of strongly interacting matter and their

transitions are shown as a function of the temperature and the baryon-chemical potential μ_B. The baryon-chemical potential describes how the energy of the system changes, when another baryon is added to the system. Figure 1.4 and fig. 1.5 show the phase diagrams of water and strongly interacting matter, respectively. In the phase diagrams (fig. 1.5 and fig. 1.4) the first-order phase transitions are shown by solid black lines.

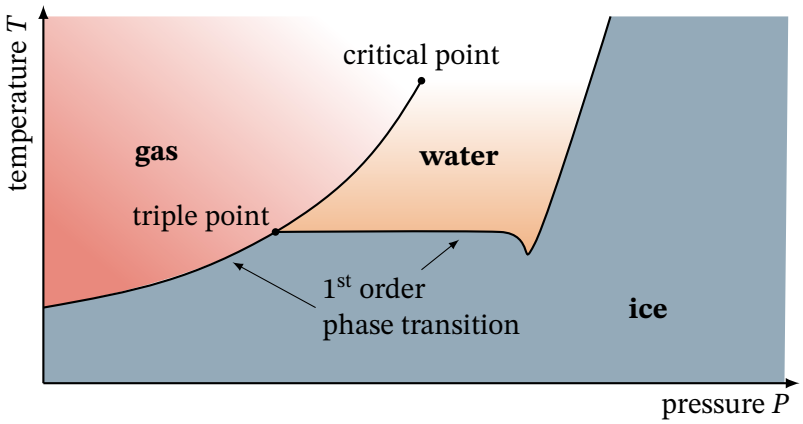

Figure 1.4: A simplified phase diagram of water.

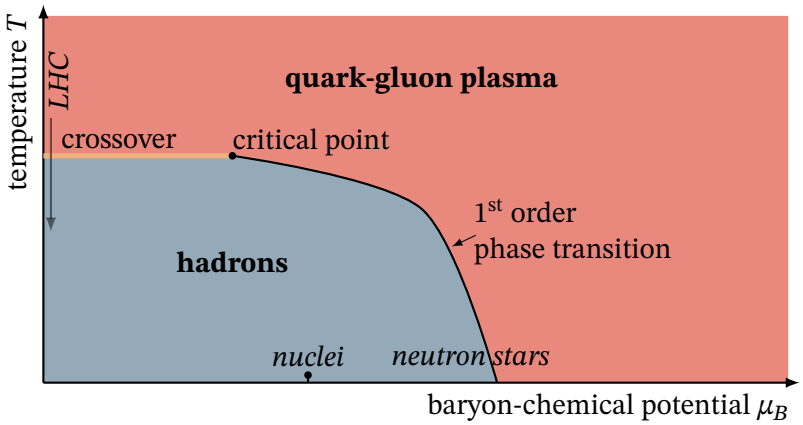

Figure 1.5: The phase diagram of strongly interacting matter. The bold labels show the phases. The solid lines show first-order phase transitions. The italic labels show regions of the phase diagram realized in nature and in the laboratory. The crossover transition is shown by the yellow line. The down-facing arrow on the left shows the region of the phase diagram probed at high-energy heavy-ion collisions.

Strongly interacting matter also exhibits a rich phase structure. The QGP of the early universe is located at very high temperatures and vanishing $\mu_B \approx 0$. As the universe cooled it went through the crossover region as the quarks and gluons formed a gas of hadrons[22]. Calculations indicate that the chiral transition and the deconfinement transition coincide[23] at vanishing μ_B. The crossover extends until the critical endpoint of the first-order phase

transition between the QGP and the hadronized matter. The exact location of this critical endpoint is matter of current research. The first-order phase transition continues towards higher μ_B and $T = 0$. Normal nuclear matter is localized at vanishing temperatures and high $\mu_B \approx 1\,\text{GeV}$.

At even higher μ_B the matter composing neutron stars is expected. Weather this matter is purely hadronic, or is composed in part of quarks and gluons is still being studied[24].

The phase diagram of strongly interacting matter is explored using theory calculations, for example, lattice QCD or effective models, and experimental measurements such as collisions of relativistic heavy ions.

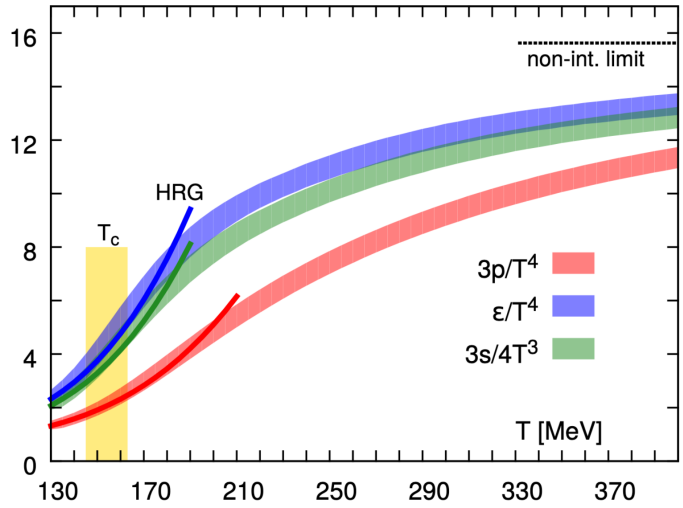

Figure 1.6: Temperature dependence of the energy density, entropy density and pressure of (2+1 flavor) QCD. All quantities have been scaled to the non-interacting limit. The yellow band shows the crossover region. The colored lines show the calculations from a hadron resonance gas. Figure taken from ref.[25].

Figure 1.6 shows the evolution of the energy density, pressure, and entropy density as a function of the temperature for a system of light quarks (2+1 flavors) and gluons at $\mu_B = 0$ calculated using lattice QCD. In the limit of very high temperatures, the interactions between quarks and gluons are expected to weaken due to the asymptotic freedom of QCD. The upper limit of a non-interacting gas of quarks and gluons is shown in the figure. The calculations show that this limit is not reached even for temperatures larger than two times the crossover temperature T_c. The calculations are compared to a hadron resonance gas model. It describes the lattice calculations for temperatures in the hadronic regime. However, above the crossover temperature the model, which does not include quarks and gluons as degrees of freedom, fails to describe the lattice calculations. Below the crossover, the energy density is comparable to that of normal nuclear matter[25] ($150\,\text{MeV/fm}^3$).

1.4 Heavy-Ion Collisions

[†] Whether QGP is found in smaller collision systems (pp, p-A) is debated[26].

The formation of a QGP requires very high energy densities and temperatures. In the laboratory such conditions can only be realized in collisions of relativistic heavy ions (A-A collisions)[†]. In such collisions, energy densities of more than 12 GeV/fm^3 are reached[27] approximately 3×10^{-23} s or 1 fmc^{-1} after the collision at a center-of-mass energy per nucleon-nucleon pair of $\sqrt{s_{\mathrm{NN}}} = 2.76$ TeV. This corresponds to more than 20 times the energy density in a proton[25] (450 MeV/fm^3). These energy densities are comparable to those from lattice QCD calculations at temperatures of over 300 MeV. In addition to the high energy density, the number of particles and therefore the entropy produced in these collisions is also huge. Before the collision, the entropy of the initial incoming nuclei is essentially zero. In the final state of the collision more than 10 000 particles can be present.

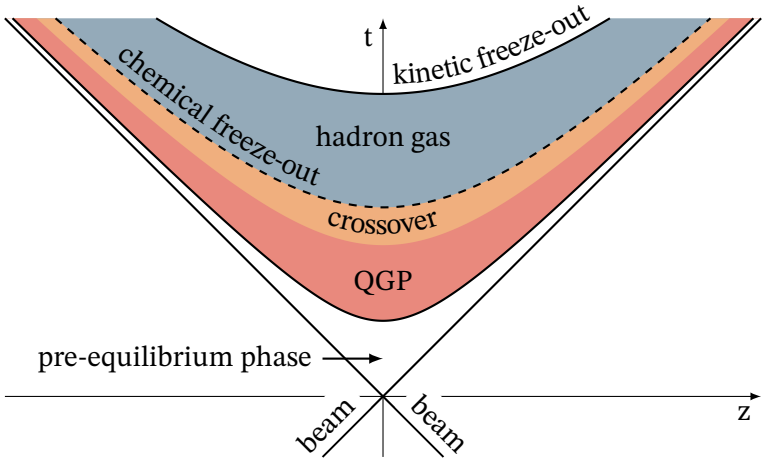

Figure 1.7: Sketch of the space-time evolution of a heavy-ion collision in the laboratory frame. The hyperbolic curves show the regions of constant proper-time τ. The light axes correspond to a good degree to the LHC beams. The consecutive phases of the heavy-ion collision are explained in the text.

Figure 1.7 depicts the space-time evolution of a relativistic heavy-ion collision at a particle collider. The abscissa corresponds to the spatial direction of the beams; the ordinate shows the time. The diagonal lines correspond to the propagating ion beams. To reach the high energy densities in the collision which are needed for a transition to the QGP, the heavy ions are accelerated to relativistic speeds of more than 0.99 % the speed of light. At these high velocities, the nuclei inside the beams are highly Lorentz-contracted into thin disks when observed from the laboratory frame of reference.

At time of the collision, $\tau = 0$, the transverse structure of the nuclei is described by the instantaneous positions of the nucleons. In this instant, the energy density reaches its maximum value, due to the high contraction of the nuclei. The majority of the quarks and gluons participating in the collision only experience a collision of low momentum transfer (soft). These are dominated by collisions between gluons which only carry a small fraction of the total momentum of the nuclei[28]. Only very few of the constituents experience a hard collision, which corresponds to a high momentum transfer and resulting large *transverse*

momentum component. Most of the entropy production of the collision happens in this initial moment[29]. The initial state of the collisions can be described using different effective models (see section 1.5).

Transverse momentum p_T component of momentum $\vec{p}$ perpendicular to the beam direction z.

Longitudinal momentum component of momentum $\vec{p}$ parallel to the beam direction z.

As the remnants of the nuclei continue to recede from the point of the collision, numerous new particles are produced in the "fireball" initiated by the strong gluon fields. These particles rapidly equilibrate and the "fireball" continues to expand in the direction of the beams. In addition, a transverse expansion develops. At the point where it reaches thermal equilibrium it can be described as a QGP. Immense transverse and longitudinal pressure gradients are present in the matter, which drive its expansion. These pressure gradients develop from the density difference of the matter to the vacuum and inhomogenities of the matter in the initial state. The expansion of the QGP can be described using relativistic fluid dynamics (see section 1.6). As the "fireball" further expands, the energy density and temperature continue to decrease.

When the energy density drops through the crossover region, the QGP transitions to a hadron gas. As Interactions between the particles becomes weaker, the fluid dynamic description breaks down. The composition of hadrons becomes fixed, as soon as the inelastic collisions between the particles cease. This point in time is called the chemical freeze-out. The comparison between lattice QCD and measurements shows an agreement between the chemical freeze-out temperature and the crossover temperature at high collision energies[30]. The particles continue to elastically scatter, until the medium becomes so dilute that the momentum distribution of the particles is fixed. This point in time is called the kinetic freeze-out. Afterwards, the particles continue to free-stream towards the detector. Long-lived unstable particles continue to decay and a mix of particles from the primary interaction and decay particles is measured in the detector. From these measured particles the whole timeline of the collision needs to be inferred.

1.5 Initial State

The initial state of the collision is very important for understanding the fast thermalization and the generation of entropy. Gaining this knowledge purely from QCD is difficult, because the non-perturbative real-time dynamics of the system which cannot be studied directly with lattice QCD[31]. Experimental studies alone also cannot answer these questions, since the full initial state is not directly accessible, as only the final state of the collision is measured. To resolve these problems effective theories are being used to characterize the initial state. They can be broadly divided into two categories. Dynamical models, which try to simulate the dynamical behavior of the initial state and the pre-equilibrium phase using effective field theories[32], as well as static models, which do not simulate the dynamics behavior and only provide a snapshot at the time of thermalization by asserting an ansatz for the deposition of entropy.

The picture of the initial state at the thermalization time obtained from the different models can be divided into a geometric and a fluctuating component. The geometric component is illustrated by the example of a symmetric collision of smooth-density nuclei. Figure 1.8 shows a sketch of the initial state of two identical nuclei modeled by a constant density distribution. The impact parameter b gives the separation of the nuclei along the abscissa. The initial

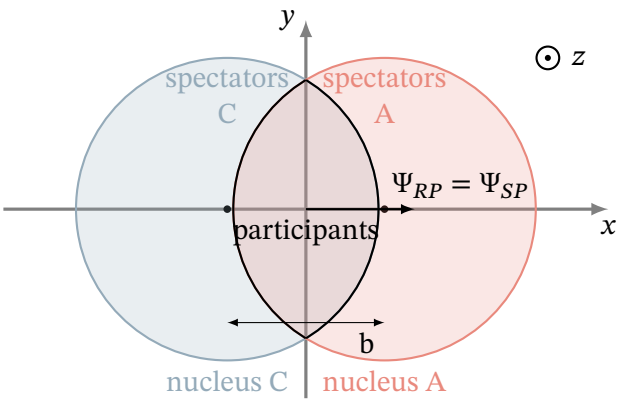

Figure 1.8: Transverse view of the initial state assuming a constant density distribution for both nuclei. The impact parameter b is indicated by the black horizontal arrow.

transverse energy density $\rho(r, \phi)$ is shown by the overlap of the two nuclei, which is called participants in the sketch. The remnants of the nuclei that do not experience a collision are called spectators. The shape, or anisotropy, of the initial energy density in the overlap region is determined only by the impact parameter. The shape is commonly parametrized using the eccentricities[33] ε_n with the harmonic numbers n

$$\varepsilon_n e^{in\Psi_n} = -\frac{\int r^n e^{in\phi} \rho(r,\phi) r dr d\phi}{\int r^n \rho(r,\phi) r dr d\phi} = \varepsilon_{n,x} + i\varepsilon_{n,y} \,. \tag{1.4}$$

r and ϕ are the polar coordinates in the coordinate system centered on the collision and aligned with the reaction plane and Ψ_n is a chosen symmetry plane. In the case of the smooth picture, the symmetry planes Ψ_n are equal to the reaction plane Ψ_{RP}, which is spanned by the impact parameter b and the direction of the beams z. This statement is equivalent to a vanishing $\varepsilon_{n,y}$ and therefore the eccentricity relative to the reaction plane (reaction plane eccentricity) is given by $\varepsilon_{RP} = \varepsilon_{n,x}$. In this model all eccentricity of odd-harmonic vanish.

The fluctuating component can be shown by a more realistic model of a heavy-ion collision where the initial energy density is not smooth. In this case, the initial energy density is determined by the internal structure of the nuclei in addition to the impact parameter. Figure 1.9 sketches the transverse and longitudinal view of a heavy-ion collision, which includes the internal structure by assuming a momentary position of the nucleons shown by the full and open circles. The initial energy density in the overlap region is depicted by the gray area. The black arrow on the left sketch indicates symmetry plane angles of the participants Ψ_n, They are in general not aligned with the reaction plane with angle Ψ_{RP}, which is given by the abscissa in the sketch. The symmetry plane angles are determined by

atan2(y, x) gives the phase of the complex number $x + iy$.

$$\Psi_n = \text{atan2}(\varepsilon_{n,y}, \varepsilon_{n,x}) \tag{1.5}$$

The right sketch illustrates the deflection of the spectators. The symmetry planes of the spectators, with angle Ψ_{SP}, are spanned by the deflection of the spectators and the beam direction. This deflection depends on the position of the nuclear matter in the nuclei and the momentum transfer between the participants and the spectators during the passing of the nuclei. If fluctuations are present, the symmetry planes of the spectators are also not aligned with the reaction plane.

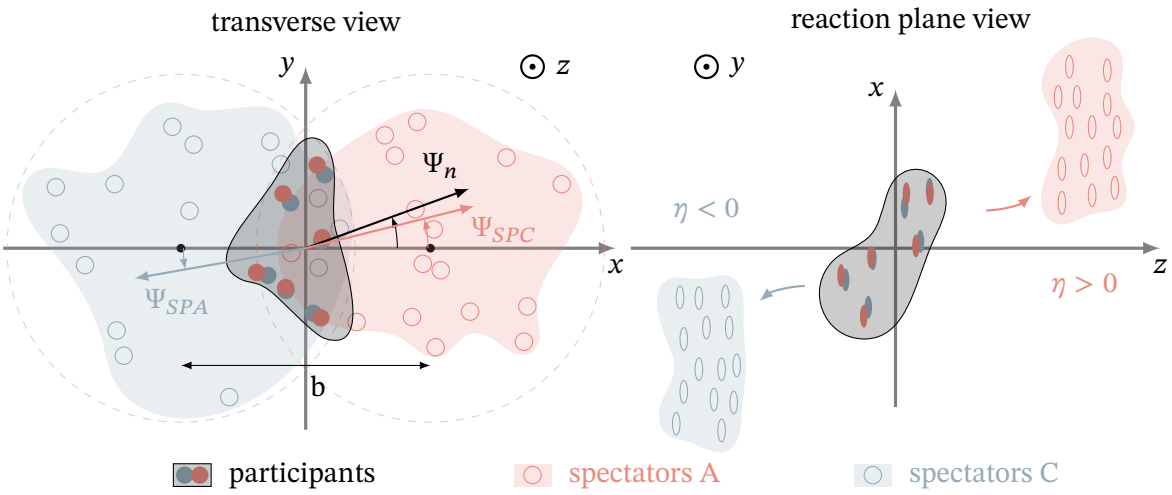

Figure 1.9: Transverse and longitudinal view of the initial state. The closed (open) circles represent the participants (spectators). The arrows on the right sketch indicate the deflection of the spectators.

The fluctuating component will vary in each collision due to the variations of the position of the constituents and their momentum fraction of the total momentum of the nucleus. This variation of the initial energy density introduces collision-by-collision fluctuations of the eccentricities. This means even for a fixed impact parameter the eccentricities are not fixed. Therefore, in an ensemble of collisions the eccentricities fluctuate according to a generally unknown distribution function. In addition, the variations of the initial energy density give rise to non-zero odd-harmonic eccentricities. The nature of the eccentricity fluctuations give insight into the initial state of the system. The fluctuations can be studied using the cumulants of the eccentricity distribution of many collisions. The first to even cumulants $\varepsilon_n\{2\}$ and $\varepsilon_n\{4\}$ and the average reaction plane eccentricity $\varepsilon_n\{\Psi_{RP}\}$ are given by

$$\begin{aligned} \varepsilon_n\{\Psi_{RP}\} &= \langle \varepsilon_{n,x} \rangle \\ \varepsilon_n\{2\} &= \langle \varepsilon_n^2 \rangle^{\frac{1}{2}} \\ \varepsilon_n\{4\} &= \left(2\langle \varepsilon_n^2 \rangle^2 - \langle \varepsilon_n^4 \rangle\right)^{\frac{1}{4}} , \end{aligned} \tag{1.6}$$

where the angular brackets correspond to the expected value[34,35].

The mechanism of the generation of the energy density and the modeling of the colliding nuclei depend on the implementation of the initial state models. For more information on dynamical models, the reader is referred to the refs[32,36–38]. In the following, only the static models are discussed in more detail.

1.5.1 Static Models

In the static picture, the initial state of the collisions is treated as a superposition of binary nucleon-nucleon collisions. This approach, called Glauber model[39], is based on the following

assumptions. The positions of the nucleons inside the nuclei are frozen, due to their large longitudinal momentum. At the time of the collision, the nucleons undergo binary nucleon-nucleon scattering. The probability for such a nucleon-nucleon collision to occur is given by the measured inelastic nucleon-nucleon cross section σ_{NN}^{inel}. The transverse momentum p_T acquired in these collisions is small relative to their original longitudinal momentum. Therefore, to a good approximation they are assumed to be traveling in straight line trajectories. The distribution of quarks and gluons in the nucleon, which is given by the parton distribution function, changes only slightly when the nucleons are embedded into a nucleus (nuclear parton distribution function)[40,41]. The nucleons, which undergo at least one scattering are called participants; Those that do not are called spectators. In each of these collisions, entropy is deposited. The way how the entropy is deposited depends on the model. The models only provide a snapshot of the energy density at the thermalization time. They do not provide any explanation for the thermalization, but they are able to provide the input for fluid dynamics of the QGP. These models focus on providing an input for the transverse dynamics of the participant region. The longitudinal dynamics of the collision and therefore the dynamics of the spectators are not modeled. In practice, these models are often calculated using a Monte Carlo approach.

As most of the entropy in a heavy-ion collision is created in the initial state, the number of particles of the final state is proportional to the initial entropy. This property is used to classify collisions into so-called centrality classes. The procedure which evaluates these centrality classes in explained in section 2.5.

1.5.1.1 MC Glauber

The MC Glauber approach[42] describes the position of the nucleons using a well-defined three-dimensional distribution function. The Woods-Saxon distribution describes such a three-dimensional distribution

$$\rho(r) = \frac{\rho_0}{1 + \exp\left(\frac{r-R}{a}\right)}, \tag{1.7}$$

where R is the radius parameter of the nucleus and a is the surface thickness of the nucleus, which determines how quickly the nuclear density falls off at the borders of the nucleus[43]. The parameters are extracted from low energy electron-ion scattering experiments. To treat the repulsive force of the strong nuclear force a minimum separation between the nucleons is implemented. The same nuclear profile is assumed for protons and neutrons. In some implementations, the neutron-skin effect is implemented using the average of proton and neutrons distributions with different parameters R and a. The nucleons in each nucleus are then sampled according to eq. (1.7).

In the next step, the inelastic collisions between the nucleons are implemented using the measured inelastic cross section from pp collisions at equal interaction energies σ_{NN}^{inel}. The two nuclei are shifted relative to each other by a random impact parameter b. Two nucleons are assumed to collide, if their distance d fulfills the relation

$$d < \sqrt{\sigma_{NN}^{inel}/\pi}\,. \tag{1.8}$$

Subsequent collisions are all treated equally. In each of the nucleon-nucleon collisions, a "blob" of initial energy density is deposited for the participating nucleons.

In addition to the eccentricities, a collision in the MC Glauber model is characterized by the number of nucleon-nucleon collisions N_{coll}, the total number of participants N_{part}, and the impact parameter b.

1.5.1.2 TRENTo

T$_{\mathrm{R}}$ENTo[44] is an alternative approach to the MC Glauber model. It is an effective model which intends to generate realistic initial conditions without an assumption of a specific physical mechanism for the entropy generation, pre-equilibrium dynamics, or thermalization. It is based on the thickness functions $T_{A,B}(x,y)$ along the transverse directions x and y, which integrate the density of nuclear matter $\rho_{A,B}^{part}$, that participates in the inelastic collision of the corresponding projectile A, B, along the direction of the beam z:

$$T_{A,B}(x,y) = \int dz \rho_{A,B}^{part}(x,y,z)\,. \tag{1.9}$$

In the model, a scalar field T_R generates the entropy from the thickness function

$$T_R(p;T_A,T_B) = \left(\frac{T_A^p + T_B^p}{2}\right)^{\frac{1}{p}}\,. \tag{1.10}$$

This field is known as the reduced thickness function. The parameter p encodes the physical mechanism of the entropy production and can take any real value. For $p = 1$, the model is equivalent to the MC Glauber model. For $p = 0$, a single roughly symmetry blob of entropy is deposited in the center of the collision. For $p = -1$, entropy production is suppressed along the impact parameter. The entropy density at thermalization time is proportional to the reduced thickness function

$$\left.\frac{dS}{dy}\right|_t \propto T_R(p;T_A,T_B)\,. \tag{1.11}$$

The nuclear density of two colliding nucleons A, B is given by

$$\rho_{A,B} = \rho_{nucleon}(x \pm b/2, y)\,, \tag{1.12}$$

assuming the impact parameter b is along the x direction. The nucleon thickness function $\int dz \rho_{nucleon}$ is assumed to be calculable. The probability for the nucleons to collide is given by the overlap integral of the two nucleon thickness functions

$$P_{coll} = 1 - \exp\left[-\sigma_{gg}\int dxdy \int dz \rho_A \int dz' \rho_B\right]\,. \tag{1.13}$$

The effective parton-parton cross section σ_{gg} is tuned so that the total cross section reproduces the measured inelastic nucleon-nucleon cross section σ_{NN}^{inel}. To reproduce the multiplicity

fluctuations observed in proton-proton collisions an additional weight w is introduced. The weights are sampled from a gamma distribution with the probability

$$P_k(w) = \frac{k^k}{\Gamma(k)} w^{k-1} e^{-kw} \,. \tag{1.14}$$

k is a parameter of the model and may be used to enhance, or suppress multiplicity fluctuations. $0 < k < 1$ corresponds to large fluctuations, whereas $k > 1$ suppresses the fluctuations. Similar to the MC Glauber model the positions of the nucleons in the nuclei are sampled from a Woods-Saxon distribution (eq. (1.7)). When simulating many collisions a random impact parameter b is chosen. For each pair of nucleons the probability in eq. (1.13) is sampled. Those that do collide are marked as participants. The participants i are added to the thickness function of their respective nucleus

$$T_A = \sum_i = 1^{N_{part}} w_i \int dz \rho_{nucleon}(x - x_i, y - y_i, z - z_i) \tag{1.15}$$

with their weights w_i and position (x_i, y_i, z_i). The obtained thickness functions are inserted into eq. (1.10) from which the transverse energy density of the collisions is obtained.

1.5.2 Parametrizations of the Eccentricity Fluctuations

The different static and dynamic models may predict different magnitudes of the initial anisotropy[45]. The uncertainty associated with the initial state anisotropy resulting from these disagreements limits the precision to which the hydrodynamic behavior can be extracted from measurements[46]. An alternative prescription to the Monte Carlo based approaches is the parametrization of the underlying probability density distribution of the initial eccentricities.

1.5.2.1 Bessel-Gaussian Model

The simplest approach is the assumption that the distributions of $\varepsilon_{n,x}$ and $\varepsilon_{n,y}$ can be described using a Gaussian distribution with a width that is approximately equal in both directions[47]. This approach is called Bessel-Gaussian model of eccentricity fluctuations. Integration over the azimuthal plane gives the probability distribution for ε_n

$$P(\varepsilon_n) = \frac{\varepsilon_n}{\sigma^2} I_0\left(\frac{\varepsilon_n \varepsilon_0}{\sigma^2}\right) \exp\left(-\frac{\varepsilon_0^2 + \varepsilon_n^2}{2\sigma^2}\right) , \tag{1.16}$$

where I_0 is the modified Bessel function of the first kind. ε_0 and σ give the mean anisotropy relative to the reaction plane and the magnitude of the eccentricity fluctuations around the anisotropy, respectively. In the Bessel-Gaussian model of eccentricity fluctuations only the second order cumulant of the $\varepsilon_n\{2\}$ is different from the average reaction plane eccentricity ε_{RP}. All the higher order cumulants $\varepsilon_n\{2m, m \geq 1\}$ are degenerate with the reaction plane eccentricity ε_{RP}. These results are analoguous to a standard Gaussian distribution where only the first two cumulants (mean and variance) are non-zero.

1.5.2.2 Elliptic Power Model

The elliptic power model[48] (EPM) addresses the shortcomings of the previous Bessel-Gaussian parametrizations. It includes new observations from MC simulation in the parametrization. It was observed that the width of the distribution in larger in the y than in the x direction. In addition, the distribution is also skewed to the left side in the x direction, whereas the Bessel-Gaussian model assumed an isotropic distribution.

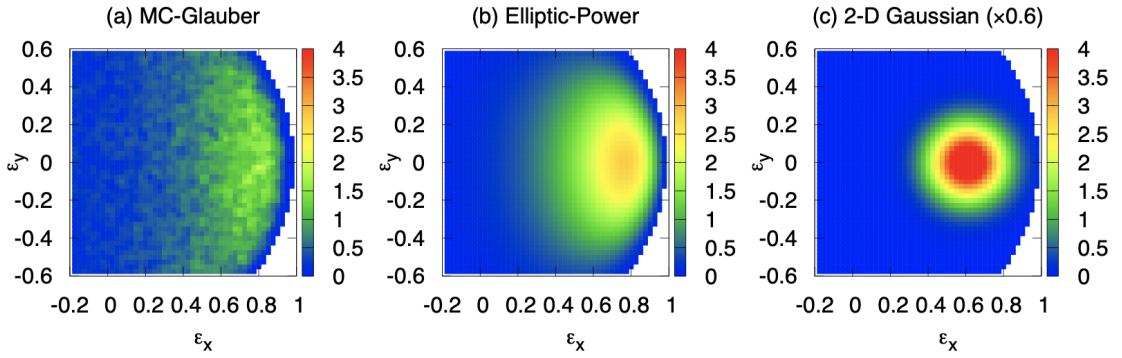

Figure 1.10: Distribution of the eccentricities $\varepsilon_{x,2}$ and $\varepsilon_{y,2}$ for an MC Glauber model in Pb-Pb collisions at $\sqrt{s_{\mathrm{NN}}} = 2.76\,\mathrm{TeV}$ in 75 % to 80 % centrality. The elliptic power model, and the Bessel-Gaussian model (called 2-D Gaussian in the figure) are fit to the generated collisions. The right figure is rescaled to the same z-axis. Figure taken from ref.[48].

Figure 1.10 shows the distributions in the ε_x and ε_y plane, where ε_x is the eccentricity of the participants in the reaction plane. The left figure shows the distribution from a MC Glauber simulation. The asymmetries described earlier are visible. The Bessel-Gaussian model does not capture these features; the elliptic power model provides a better description. The following assumption were made to derive the model. The energy density profile is given by a number of point-like identical sources. Their individual positions are independent. To guarantee a physical result the eccentricity parameter of the model is constrained to the unit disk $\varepsilon_0 < 1$. It corresponds to the eccentricity of the source distribution in the reaction plane. The second parameter of the model is α. The eccentricity distribution in the elliptic power model is given by the analytic equation

$$P(\varepsilon_n) = 2\varepsilon_n\alpha(1-\varepsilon_n^2)^{\alpha-1}(1-\varepsilon_n\varepsilon_0)^{-1-2\alpha}(1-\varepsilon_0^2)^{\alpha+\frac{1}{2}}{}_2F_1\left(\frac{1}{2}, 1+2\alpha; 1; \frac{2\varepsilon_n\varepsilon_0}{\varepsilon_n\varepsilon_0-1}\right). \quad (1.17)$$

${}_2F_1$ is the hypergeometric function. In the limit of $\varepsilon_0 \ll 1$ and $\alpha \gg 1$ the Bessel-Gaussian model is recovered with $\sigma = 1/2\sqrt{\alpha}$ as shown in eq. (1.16). Additionally, as for the Bessel-Gaussian model also all cumulants can be calculated with this approach. In contrast to the simpler approach, all cumulants are non-zero. An ordering is observed[48] $\varepsilon_n\{2\} > \varepsilon_n\{4\} > \varepsilon_n\{6\} > \varepsilon_{RP}$. The average reaction plane eccentricity is the smallest by construction. Therefore, the ratio of $\varepsilon_{RP}/\varepsilon_n\{4\}$ is always expected to be smaller than 1. Higher harmonic eccentricities can also be described with this parametrization. For example, the triangular eccentricity $\varepsilon_3\{4\}$ reduces the model essentially to a one parameter model as ε_0 goes to zero because in symmetric collisions the third harmonic originates only from the fluctuations. Figure 1.11 shows the fit of the

Bessel-Gaussian and the elliptic power model to the distribution of the eccentricity ε_2 in Pb-Pb collisions at $\sqrt{s_{\mathrm{NN}}} = 2.76\,\mathrm{TeV}$ simulated using the T$_\mathrm{R}$ENTo model. For central collisions, both models provide a good agreement with the simulation over the whole distribution. For more peripheral collisions, the Bessel-Gaussian model fails to capture the features of the T$_\mathrm{R}$ENTo model accurately. The residuals of the fit increase.

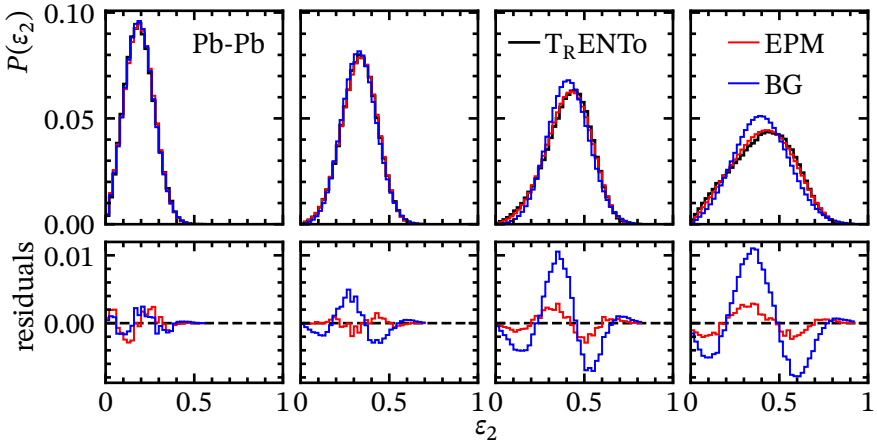

Figure 1.11: Comparison of the EPM and Bessel Gaussian (BG) model fits to the distribution of ε_2 from T$_\mathrm{R}$ENTo simulations of Pb-Pb collisions at $\sqrt{s_{\mathrm{NN}}} = 2.76\,\mathrm{TeV}$ in different centrality intervals. The top panels show the simulated data in black and the respective model fit blue and red lines. The bottom panels show the fit residuals.

1.6 Hydrodynamic Evolution of QGP

As introduced in the section 1.4, the matter created in heavy-ion collisions undergoes a phase of rapid thermalization, after which it can be described using a number of intensive properties in the formalism of fluid dynamics. In this section, the fluid dynamical description of the QGP is explained.

Fluid dynamics or hydrodynamics give a macroscopic description of liquids in motion. It can be used without explicitly referencing the microscopic degrees of freedom of the liquid. In this description, the information about the state of matter is encoded in the transport coefficients and the equation of state. One of the prerequisites to apply a fluid dynamical description in a given system is the presence of local thermal equilibrium. This means the intensive properties describing the system may vary in space and time, but only so slowly that a thermal equilibrium can be assumed in the neighborhood around any point. In the description of the fluid a continuous distribution of the properties are assumed, even if the particles composing the fluid are discrete objects.

The state variables for a relativistic fluid are the energy-momentum tensor $T^{\mu\nu}$ and the net baryon number current N^μ. In the rest frame of the fluid the energy-momentum tensor

is

$$T^{\mu\nu}_{RF} = \begin{pmatrix} \varepsilon & 0 & 0 & 0 \\ 0 & P & 0 & 0 \\ 0 & 0 & P & 0 \\ 0 & 0 & 0 & P \end{pmatrix} \tag{1.18}$$

where ε is the energy density and P the pressure. In the laboratory frame the fluid is moving with the fluid velocity u^μ, so the energy-momentum tensor becomes

$$T^{\mu\nu}_{eq} = \epsilon u^\mu u^\nu + P(g^{\mu\nu} + u^\mu u^\nu)\,, \tag{1.19}$$

where $g^{\mu\nu}$ is the metric tensor diag$(-,+,+,+)$. The fluid velocity has the components

$$u^0 = \frac{1}{\sqrt{1-\vec{v}^2}} \text{ and } \vec{u} = \frac{\vec{v}}{\sqrt{1-\vec{v}^2}}\,, \tag{1.20}$$

where $\vec{v}$ is the velocity of the fluid in the laboratory frame. For u^μ the relation $g_{\mu\nu}u^\mu u^\nu = -1$ holds. In the local thermal equilibrium the energy momentum tensor is of the form above, except that the energy density ε and velocity u^μ vary smoothly with the position x

$$\varepsilon = \varepsilon(x) \quad u^\mu = u^\mu(x)\,. \tag{1.21}$$

The net baryon number current is $N^\mu = nu^\nu$, where n is the baryon number.

For a fluid the conservation laws allow to determine the equations of motion. For a relativistic ideal fluid the energy, momentum, and net baryon number are conserved

$$\begin{aligned} \partial_\mu T^{\mu\nu} &= 0 \\ \partial_\mu N^\mu &= 0\,. \end{aligned} \tag{1.22}$$

There are 5 different equation of motions for six different variables $(u^\mu, P, \varepsilon, n)$. For the system to be closed an equation of state is needed, which relates the thermodynamic properties ε, P and n.

When viscous effects of the medium need to be taken into account, the energy momentum tensor can be written more generally as

$$T^{\mu\nu} = T^{\mu\nu}_{eq} + \Pi^{\mu\nu}\,, \tag{1.23}$$

where the viscous stress tensor $\Pi^{\mu\nu}$ can be decomposed into two parts: the shear stress tensor $\pi^{\mu\nu}$ and the bulk viscous pressure Π

$$\Pi^{\mu\nu} = \pi^{\mu\nu} + \Pi\Delta^{\mu\nu}\,. \tag{1.24}$$

The operator $\Delta^{\mu\nu} = g^{\mu\nu} - u^\mu u^\nu$ projects on the space orthogonal to the fluid velocity u^μ. In first-order hydrodynamics, or Navier-Stokes hydrodynamics, the shear stress tensor and the bulk viscous pressure are given by the gradients relative to u^μ

$$\Pi = \zeta\partial_\mu u^\mu \tag{1.25}$$

$$\pi^{\mu\nu} = 2\eta_s\sigma^{\mu\nu}\,. \tag{1.26}$$

$\sigma^{\mu\nu}$ is the rate-of-shear tensor

$$\sigma^{\mu\nu} = (\nabla^{\mu} u^{\nu} + \nabla^{\nu} u^{\mu}) - \frac{1}{3}\partial_{\mu} u^{\mu} \Delta^{\mu\nu} \,, \tag{1.27}$$

with the space-like derivative

$$\nabla^{\alpha} = \Delta^{\mu\alpha} \partial_{\mu} \,. \tag{1.28}$$

It describes the change of shape of at constant volume. $\partial_{\mu} u^{\mu}$ describes the volume expansion ζ, and η_s are the bulk and shear viscosity[49].

The application to heavy-ion collisions is not directly possible, because the Navier-Stokes equations are only applicable to non-relativistic speeds. If they were to be applied, an acausal signal propagation leads to instabilities[46]. This problem can be solved by taking second-order terms in the gradient expansion of hydrodynamics into account. With these terms, $\pi^{\mu\nu}$ and Π are dynamical variables[50]. The super-luminal signal propagation is solved by implementing a time delay between the appearance of gradients, which drive the system out of equilibrium and the response of the dissipative effects.

Calculations of the transport coefficients and their temperature dependence from first principles are under study with different methods[51,52]. From the AdS/CFT theory a lower bound for η_s/s has been conjectured[53]

$$\frac{\eta_s}{s} \geq \frac{\hbar}{4\pi k_b} \,, \tag{1.29}$$

with the entropy s and the boltzmann constant k_b. So far, no measurement of any fluid violates this lower bound. Measurements in ultra-relativistic collision of heavy ions show that the QGP is very close to this ideal lower limit. Therefore, it is often referred to as a perfect fluid.

For the calculation of fluid dynamics in heavy-ion collisions further simplifications are often made. In the so-called Bjorken picture[54], a fluid velocity in the longitudinal direction is assumed $u_z(t, x, y, z) = z/t$. Using the coordinates of proper time $\tau = \sqrt{t^2 - z^2}$, x, y, and the pseudorapidity $\eta = \arctan(z/t)$ the problem can be simplified. With the initial conditions $\epsilon = \epsilon(\tau_0)$ and $u^{\mu} = (1, 0, 0, 0)$ The equation of ideal fluid dynamics simplifies to

$$\frac{d\epsilon}{d\tau} = -\frac{\epsilon + p}{\tau} \,. \tag{1.30}$$

If one assumes the densities only depend on the proper time τ, the expansion will evolve such that the densities are independent on η. The system is then referred to as being boost-invariant. This approximation of boost-invariance holds well in mid-rapidity[54,55] ($|\eta| \approx 0$).

Figure 1.12 shows a Bayesian estimation of the shear and bulk viscosities of the QGP from Pb-Pb collisions at $\sqrt{s_{\mathrm{NN}}} = 2.76\,\mathrm{TeV}$ and $\sqrt{s_{\mathrm{NN}}} = 5.02\,\mathrm{TeV}$ using such a boost-invariant hydrodynamic model[56]. The uncertainties shown take the experimental uncertainties, the statistical uncertainties of the model, uncertainties related to the fit procedure and systematic biases coming from the models, such as the T$_{\mathrm{R}}$ENTo initial state model, into account. Alternative analyses, such as the FLUIDuM approach in ref.[57] which uses a different approach to the implementation of the hydrodynamic evolution and a different T$_{\mathrm{R}}$ENTo initial state parameters,

give different viscosity over entropy density ratios. Whereas, the Bayesian estimation[56] yields $(\eta_s/s)_{min} = 0.085^{+0.026}_{-0.025}$, the FLUIDuM approach[57] gives $\eta_s/s = 0.164^{+0.07}_{-0.079} \pm 0.007$. Improvement to the models, including the initial state, could result in reduction of the uncertainties of the extracted viscosities of the QGP.

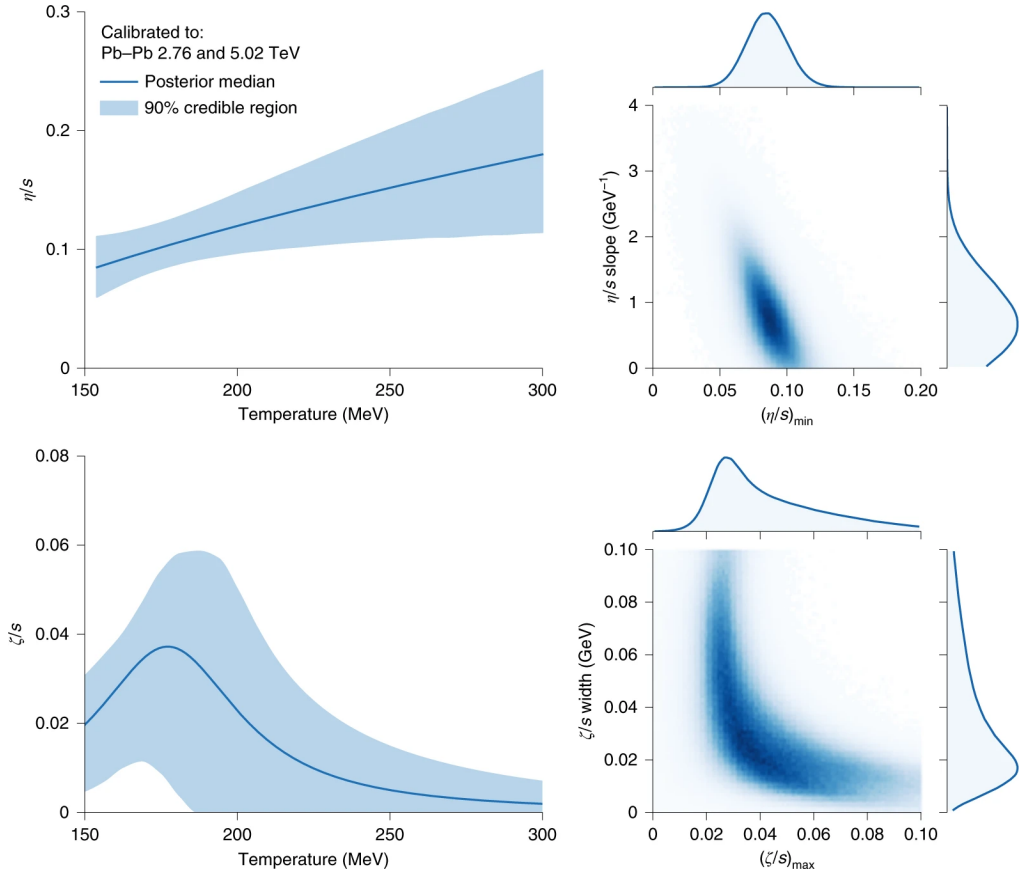

Figure 1.12: Shear η_s/s and bulk viscosity ζ/s extracted from fits of hydrodynamic simulation to Pb-Pb collisions at $\sqrt{s_{\mathrm{NN}}} = 2.76$ TeV and $\sqrt{s_{\mathrm{NN}}} = 5.02$ TeV The left panels show the temperature dependence. The uncertainties are shown as 90 % credible regions. The right panels show the joint distribution of the parameters of the temperature dependence of the viscosities. Figure taken from ref.[56].

1.7 Hadronization

Hadronization describes the formation of hadrons from quarks and gluons. It occurs when the medium locally cools down below the crossover temperature. The physical mechanism behind hadronization is not yet fully understood. Due to the energy scales involved it cannot be calculated with perturbative QCD.

Measurements at particle colliders have demonstrated that hadrons seem to be formed in chemical equilibrium over a large range of collision systems, collision energies and hadron masses. The phenomenological description of hadronization by the so-called statistical hadronization model incorporates these ideas[30,58]. In heavy-ion collisions, the state of the hadronized

medium is modeled in a grand canonical ensemble by a partition function which includes all known baryonic and mesonic states. The free parameters of the model are the temperature, the baryon-chemical potential, and the volume of the medium.

Figure 1.13 shows a comparison of the model to the hadron yields measured in heavy-ion collisions. The parameters obtained from the fit to the data are: $T_{ch} = 156.6 \pm 1.5$ MeV, $\mu_B = 0.7 \pm 3.8$ MeV and $V = 5280 \pm 410\,\mathrm{fm}^3$. Even very lightly bound systems with binding energies lower than the extracted temperature are accurately described by the model. One such example shown on the right-side of the figure, is the hypertriton ${}^{3}_{\Lambda}\mathrm{H}$ which has a Λ-separation energy[59] of only 0.13 ± 0.05 MeV. The extracted temperature from the statistical hadronization model is on good agreement with the values extracted from lattice QCD. This indicates that the collisions of heavy ions at sufficiently high energies directly probe the QCD transition between QGP and hadron matter[30].

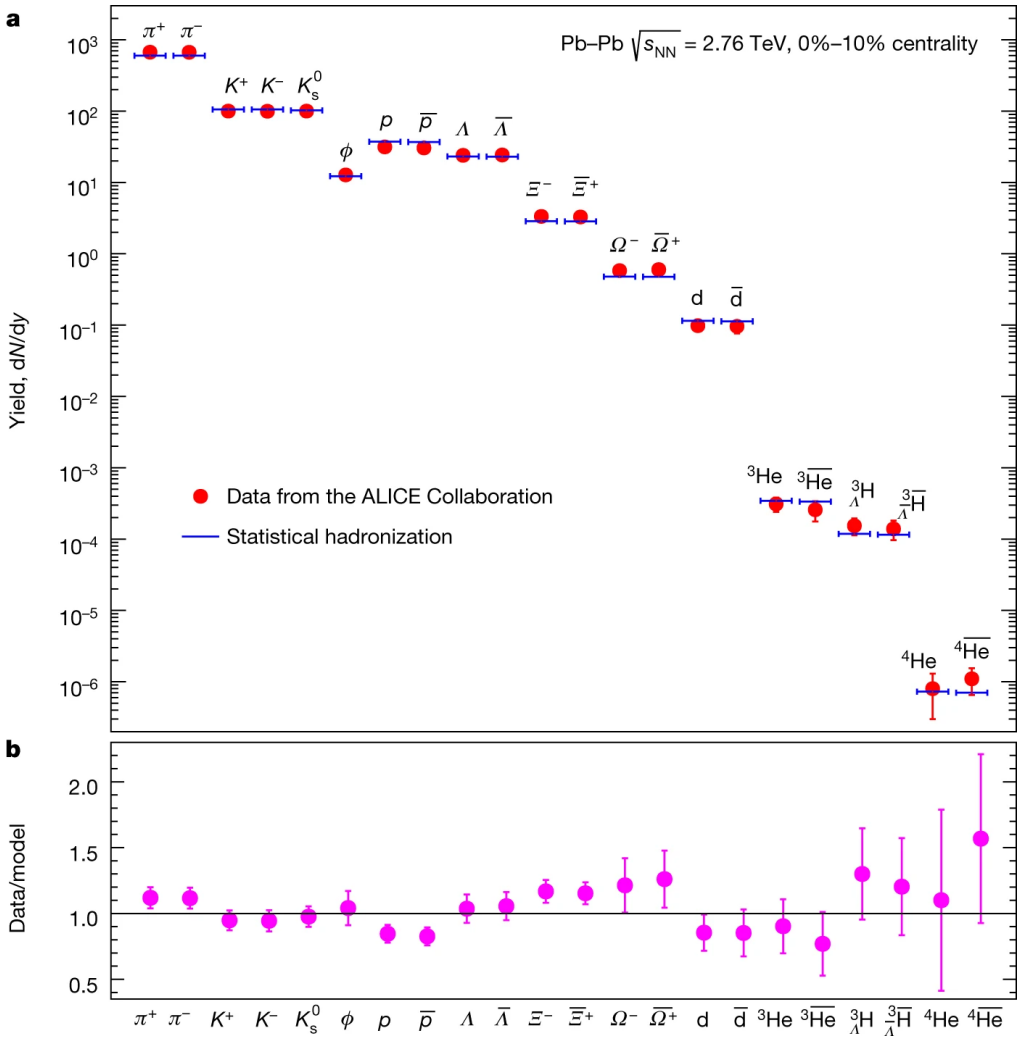

Figure 1.13: Fit of the statistical hadronization model to different hadron species measured by ALICE at LHC energies. Panel a shows the hadron yields in red. The model fits are shown in blue. Panel b shows the ratio of the data to the model fit. Figure taken from ref.[30].

1.8 Collective Flow

After thermalization strong transverse and anisotropic pressure gradients are present in the medium. During the hydrodynamic evolution these pressure gradients are transformed into the radial expansion and into momentum anisotropies in the medium. Figure 1.14 shows the transformation of the spatial anisotropy of the initial state into the momentum anisotropy inside the hydrodynamic medium. The subsequent hadronization of the medium preserves this collective signature. This collective expansion is called collective flow. It can be divided into the isotropic component of the radial expansion, or radial flow, and the anisotropic expansion, or anisotropic flow. In the following section, these final state observables and their connection to the initial state via the hydrodynamic expansion are explained.

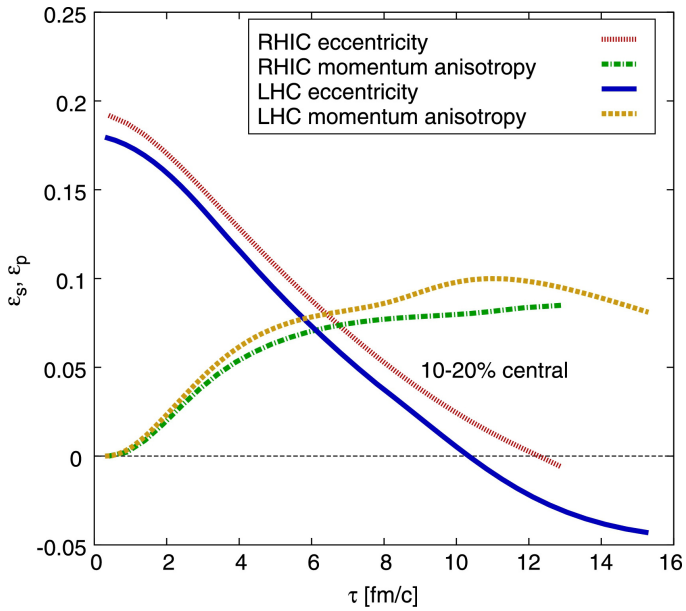

Figure 1.14: Time evolution of the spatial eccentricity and momentum anisotropy for two collision systems, Pb-Pb at $\sqrt{s_{\mathrm{NN}}} = 2.76\,\mathrm{TeV}$ labeled as (LHC) and Au-Au at $\sqrt{s_{\mathrm{NN}}} = 200\,\mathrm{GeV}$ labeled as (RHIC). Figure taken from ref.[60].

1.8.1 Radial Flow

The steep transverse pressure gradients between the dense QGP and the vacuum cause a radial expansion of the medium. Low transverse momentum and high mass particles in the medium are pushed by this collective expansion of the medium towards higher transverse momenta[61]. This effect is observed in transverse momentum dependence of the invariant yield $d^2N/(N_{ev}2\pi p_{\mathrm{T}} dy d p_{\mathrm{T}})$ for the different hadron species. Figure 1.15 shows the measured invariant yields for pions, kaons, and protons for two different center-of-mass energies. The transverse momentum dependence of the yields of kaons and protons are flatter than the pion yield. This is an indication that the protons and kaons experience a larger push towards higher transverse momentum than the less massive pions. A significantly larger radial flow is observed in collisions at higher center-of-mass energies. The measurement is described by the hydrodynamic models which include a collective radial flow. Using hydrodynamics the average velocity of the transverse expansion can be extracted. In Pb-Pb collisions[62] at $\sqrt{s_{\mathrm{NN}}} = 2.76\,\mathrm{TeV}$ it is $\langle\beta\rangle = 0.65 \pm 0.02$. This is approximately 10 % larger than $\langle\beta\rangle = 0.59 \pm 0.05$ measured in

Au–Au collisions[63] at $\sqrt{s_{\mathrm{NN}}} = 200\,\mathrm{GeV}$. The measurement of the invariant yields alone is not sufficient to constrain the hydrodynamic transport coefficients, since bulk (suppresses) and shear (enhances) viscosities have opposite effect on the radial flow[46].

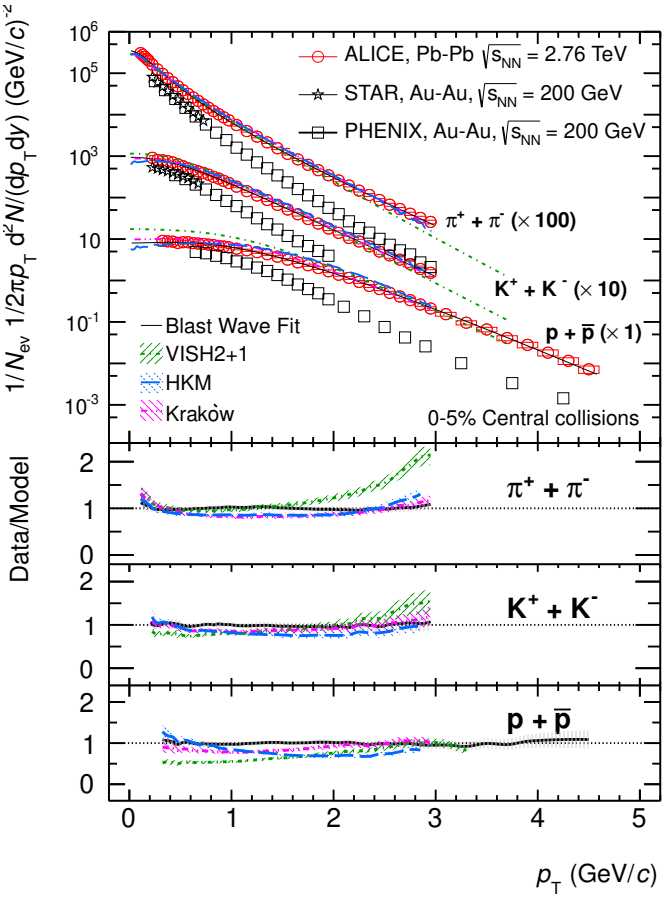

Figure 1.15: Transverse momentum dependence of the invariant yield of pions, kaons, protons measured in Pb-Pb collisions at $\sqrt{s_{\mathrm{NN}}} = 2.76\,\mathrm{TeV}$ and Au–Au collisions at $\sqrt{s_{\mathrm{NN}}} = 200\,\mathrm{GeV}$. The data points are compared to hydrodynamic models. The average transverse velocity of the medium is extracted from the blast-wave model fit[61]. Figure taken from ref.[62].

1.8.2 Anisotropic Flow

A differential measurement of the yields along the azimuth of a collision is sensitive to the anisotropic expansion of the medium. It is particularly sensitive to the transport coefficients.

Mathematically, the anisotropies of final state particles can be expressed by a Fourier expansion of the triple differential invariant yield of the particles in a single collision

$$\frac{dN}{p_{\mathrm{T}} dp_{\mathrm{T}} d\eta d\phi} = \frac{1}{2\pi} \frac{dN}{p_{\mathrm{T}} dp_{\mathrm{T}} d\eta} \left(1 + 2 \sum_{n=1}^{\infty} v_n(p_{\mathrm{T}}, \eta) \cos(n(\phi - \Psi_{RP})) \right) . \tag{1.31}$$

The angle ϕ is the azimuthal angle of the particle in the lab frame. The coefficients v_n are called flow coefficients of the n$^{\mathrm{th}}$ harmonic. They describe the azimuthal shape modulations of the

particle yield. The v_n coefficient in a single collision is determined by

$$v_n = \langle \cos(n(\phi - \Psi_{RP})) \rangle = \frac{\int_0^{2\pi} \cos(n(\phi - \Psi_{RP})) \frac{dN}{p_T dp_T d\eta d\phi} d\phi}{\int_0^{2\pi} \frac{dN}{p_T dp_T d\eta d\phi} d\phi} . \tag{1.32}$$

Singular angular brackets $\langle ... \rangle$ correspond to the average over the particles in a single collision. In general, the v_n depend on the impact parameter of the collision and the type, and kinematic quantities of the particles. By averaging over all collisions the average flow is determined

$$\langle v_n \rangle = \langle \langle \cos(n(\phi - \Psi_{RP})) \rangle \rangle . \tag{1.33}$$

The double angular brackets corresponds to the average over the particles in many collisions. The first anisotropic flow coefficients v_n are called directed flow v_1, elliptic flow v_2 and triangular flow v_3. For symmetric collisions without fluctuations the triangular flow and all other flow coefficients with odd-numbered harmonics are zero. This is analogue to the initial state anisotropy (section 1.5). In experimental measurements, the $\langle v_n \rangle$ is often written without the average $\langle ... \rangle$. Figure 1.16 visualizes the first three v_n coefficients.

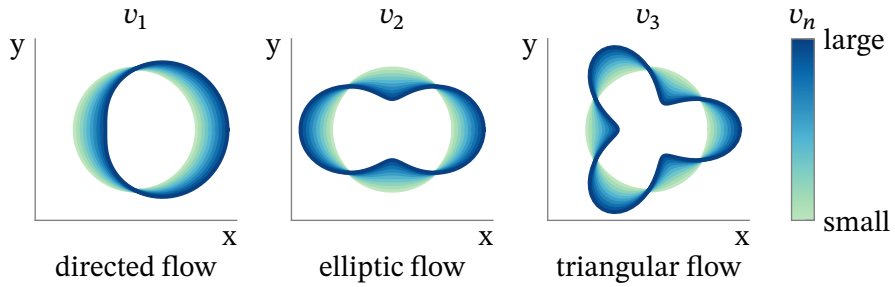

Figure 1.16: Visualization of the first three anisotropic flow coefficients v_n for different sizes of the flow coefficients.

1.8.2.1 Energy Dependence of Elliptic Flow

Figure 1.17 shows the measurement of the integrated collision-averaged flow v_2 as a function of the center-of-mass energy of the collision. Collisions in the 20 % to 30 % centrality range are studied. A negative sign of the elliptic flow is indicative of an increased particle production perpendicular to the reaction plane (out-of-plane). A positive sign of the elliptic flow is observed for increased in-plane particle production. At lowest energies the v_2 is positive. It is dominated by the deflection of the spectator matter, also called the bounce-off effect. Going to higher $\sqrt{s_{NN}}$, a sign change of the elliptic flow coefficient is observed. The negative sign of the elliptic flow coefficient is related to the so-called squeeze-out effect. Due to the long passing time of the nuclei the particle production in the in-plane direction is shadowed by the spectator neutrons. At increasing $\sqrt{s_{NN}}$, the longitudinal size of the passing nucleons becomes small compared to the transverse size and the passing time of the two nuclei becomes negligible compared to the characteristic time with which the collective flow develops. Therefore, a second sign change is observed. At approximately 4 GeV, the v_2 energy-dependence starts to flatten. A difference of less than 5 % is observed between the two highest measured energies

$\sqrt{s_{\mathrm{NN}}} = 2.76\,\mathrm{TeV}$ and $\sqrt{s_{\mathrm{NN}}} = 5.02\,\mathrm{TeV}$. As shown in fig. 1.14, most of the momentum anisotropy is already developed in the first 5 fm/c to 6 fm/c.

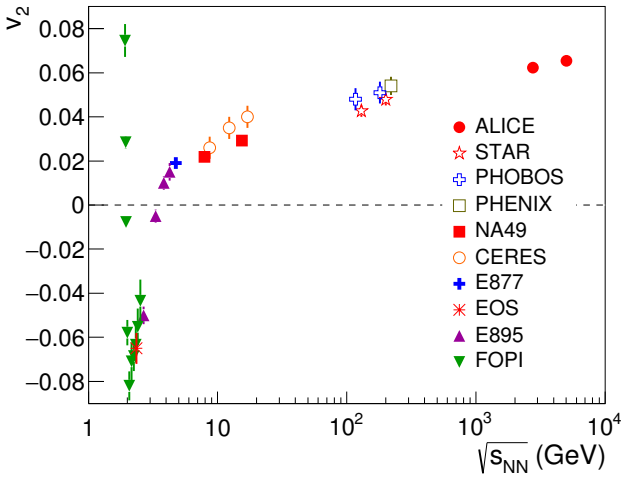

Figure 1.17: Energy dependence of integrated elliptic flow. Figure taken from ref.[64].

A scaling of the elliptic flow v_2 divided by the initial eccentricity ε_2 with the final multiplicity dN_{ch}/dy per unit overlap area S is suggested by ideal hydrodynamics[65]

$$\frac{v_2}{\varepsilon_2} \propto \frac{1}{S}\frac{dN_{ch}}{dy}\,. \tag{1.34}$$

In ideal fluids the initial entropy density is directly measured by the right side of the equation. This means that for ideal fluids all differences between two collision systems, such as impact parameter, the center-of-mass energy, or the size of the collision system can be described by changes of the final hadron multiplicity. In this sense, the hydrodynamic evolution between different systems is universal. This observation is therefore also called "multiplicity scaling of the elliptic flow"[66]. For ideal hydrodynamics such a proportionality is expected, as the fluid is scale independent and only depends on the stiffness of the equation of state. This scale invariance is broken by the freeze-out of the matter. The freeze-out introduces another scale into the system, which does not directly depend on the size of the system, but rather on the hadronic cross sections. Therefore, even in the case of an ideal hydrodynamic evolution of the QGP a breaking of the scaling is expected. Viscous hydrodynamics predict violations of the scaling, which is dependent on the value of the specific shear viscosity[66]—the ratio of the shear viscosity over entropy density η_s/s.

Figure 1.18 shows the difference of the multiplicity scaling for ideal and viscous hydrodynamics obtained from simulations. Approximate scaling is observed for all points. Subtle scaling violations for viscous hydrodynamics at large multiplicities are larger than for ideal hydrodynamics. No significant differences are observed for small multiplicities. A linear rise is seen for all simulations for large multiplicities.

Figure 1.19 shows measurements of the multiplicity scaling of elliptic and triangular flow in Pb-Pb and Xe-Xe collisions from ALICE at $\sqrt{s_{\mathrm{NN}}} = 5.02\,\mathrm{TeV}$ and $\sqrt{s_{\mathrm{NN}}} = 5.44\,\mathrm{TeV}$, respectively. The scaling behavior is compared to six different initial state models. For most models a drop of

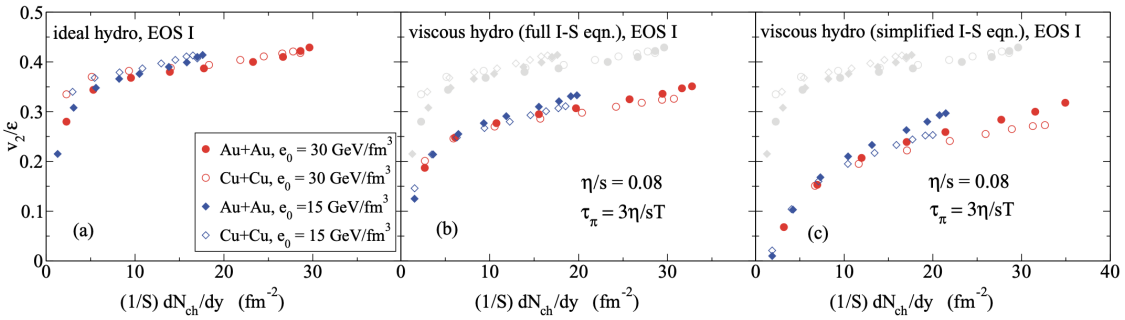

Figure 1.18: Comparison of multiplicity scaling of the elliptic flow in hydrodynamic simulations. The left panel shows results from ideal hydrodynamics. The center and right panels show results from viscous hydrodynamics using the full and simplified Israel-Stewart equations, respectively. Figure taken from ref.[66].

the elliptic flow scaled with eccentricity is observed for central collisions (large $1/S\, dN_{ch}/d\eta$). This drop is not predicted by hydrodynamics[66,67]. Approximate scaling is observed for all but the most central collisions. The Scaling behavior also depends on the initial state models. MC Glauber model implementing quark degrees of freedom observe a better scaling than those only implementing nucleon degrees of freedom.

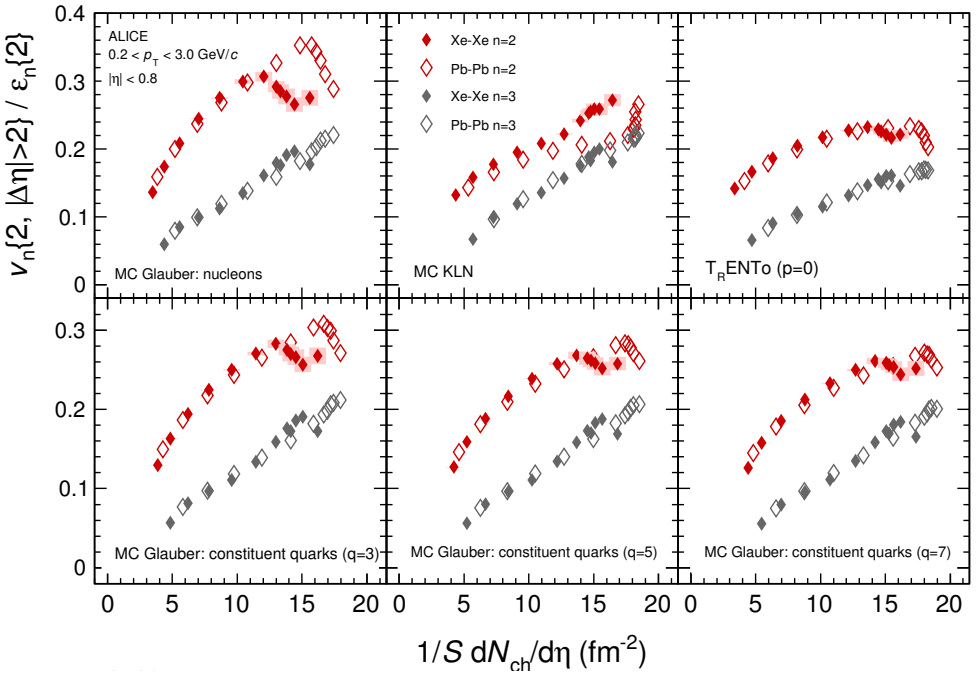

Figure 1.19: Multiplicity scaling of the elliptic and triangular flow in Pb-Pb and Xe-Xe collisions measured by ALICE. Six different initial state models are used for scaling. Figure taken from ref.[67].

1.8.2.2 Flow Fluctuations

The fluctuations of the initial state anisotropy are propagated to the final state anisotropies. In the presence of these fluctuations, the symmetry planes of the different harmonics are not aligned with the reaction plane of the collision (compare to fig. 1.9). The triple differential yield is generalized using these symmetry planes Ψ_m. The azimuthal probability density distribution of produced particles is obtained by normalizing the differential yield

$$\rho(\phi - \Psi_m) = \frac{1}{2\pi}\left(1 + 2\sum_{n=1}^{\infty} v_n \cos(n(\phi - \Psi_m))\right). \tag{1.35}$$

Equivalently, the flow coefficients are

$$v_n = \langle \cos(n(\phi - \Psi_m)) \rangle . \tag{1.36}$$

The flow fluctuations give rise to triangular flow and other odd-harmonic flow coefficients in symmetric collision systems. In addition to the appearance of odd-harmonic flow coefficients, the fluctuations are also encoded in the moments of the underlying probability density distribution of the flow coefficients. Flow measured with the cumulants method is sensitive to these moments.f The cumulant method is explained in detail in chapter 3. Depending on the underlying shape of the fluctuations differences of the flow coefficients calculated with various cumulants are expected. Whereas the Bessel-Gaussian model of flow fluctuations predicts the following hierarchy

$$v_2\{2\} > v_2\{4\} = v_2\{6\} = v_2\{8\} = v_2\{\Psi_{RP}\}, \tag{1.37}$$

the EPM predicts

$$v_2\{2\} > v_2\{4\} > v_2\{6\} > v_2\{8\} > v_2\{\Psi_{RP}\}. \tag{1.38}$$

Where $v_2\{X\}$ is the X-order cumulant and $v_2\{\Psi_{RP}\}$ is the flow shown in eq. (1.33). Figure 1.20 shows ratios between flow coefficients from sixth- and eighth-order cumulant to fourth-order cumulant in Pb-Pb collisions at $\sqrt{s_{\mathrm{NN}}} = 2.76\,\mathrm{TeV}$. A fine-splitting is observed between the cumulants which increases in size for more peripheral collisions. Flow coefficients calculated with higher-order cumulants are smaller than the fourth-order cumulant. A combined model of MC Glauber initial conditions and a hydrodynamic simulation is in agreement with the measurement.

The relation between the initial anisotropies and the final state anisotropies measured in the experiment can be expressed as a relationship between the eccentricities ε_n and the measured flow coefficients v_n. In the simplest approach a linear scaling, with a response coefficient κ, between ε_n and v_n is assumed

$$v_n \approx \kappa \varepsilon_n . \tag{1.39}$$

κ encodes the hydrodynamics response of the medium. In contrast to the initial eccentricity it does not fluctuate. Deviations from such a linear scaling of the initial eccentricities are also being investigated using collision by collision hydrodynamics or the EPM model[69,70]. Non-linear contributions are found to be small and not strongly dependent on the centrality of the collision, such that eq. (1.39) holds approximately.

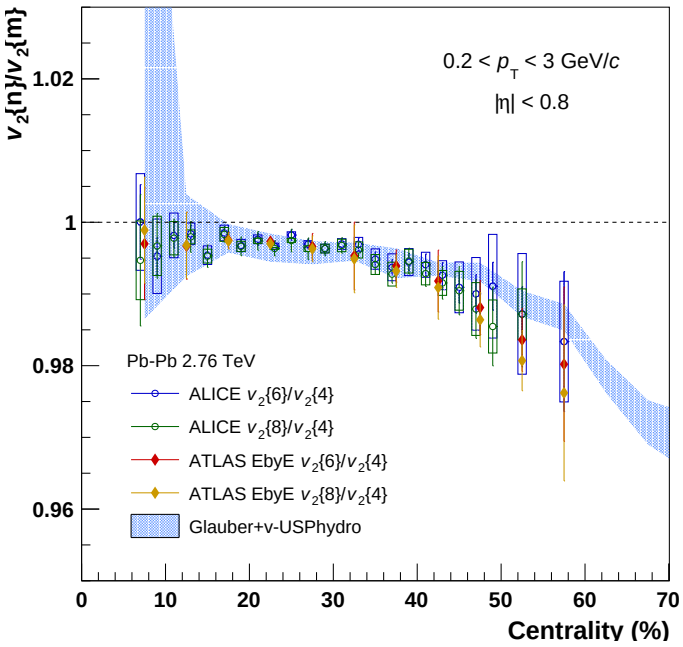

Figure 1.20: Ratios of flow from higher order cumulants as a function of centrality in Pb-Pb collisions at $\sqrt{s_{\mathrm{NN}}} = 2.76\,\mathrm{TeV}$. The data points show measurements from the ALICE and ATLAS experiments. The band shows a hydrodynamic simulation. Figure taken from ref.[68].

Using these linear dependence the initial state fluctuations can be mapped to the flow fluctuations. Figure 1.21 shows a comparison between the distribution of v_2 measured in Pb-Pb collisions at $\sqrt{s_{\mathrm{NN}}} = 2.76\,\mathrm{TeV}$ (red and green data points) and a fit of the elliptic power model (black band). The elliptic power model describes the shape of the flow fluctuations over a wide range of collision centralities. The flow fluctuations are sensitive to the initial state model as shown by the comparison to the simulations of the initial state plus the hydrodynamic phase. The characterization of the flow fluctuations is insensitive of the transverse momentum of the selected particles.

The flow fluctuations can be measured differentially in transverse momentum to investigate this common origin. Figure 1.22 shows the transverse momentum dependence of the elliptic flow fluctuations in different centrality classes estimated with

$$\sqrt{\frac{v_2\{EP\}^2 - v_2\{4\}^2}{v_2\{EP\}^2 + v_2\{4\}^2}}\,. \tag{1.40}$$

It is proportional to the elliptic flow fluctuations $\sigma_{v_2}/\langle v_2\rangle$ when contributions from non-flow correlations are small[71]. Within errors the flow fluctuations are independent of the transverse momentum up approximately to 8 GeV/c for centrality classes 5 % to 30 %. This is well beyond the region where the flow magnitude is well described by Hydrodynamic simulations (2 GeV/c to 3 GeV/c). This indicates that the flow fluctuations seem to have a common origin up to the region where hard scatterings and jets dominate. In peripheral collisions and central collisions a p_{T} dependence is observed for transverse momenta larger than 1.5 GeV/c.

Non-flow is explained in chapter 3

The flow fluctuations also depend on the collision system. Figure 1.23 shows a comparison of elliptic and triangular flow for central Pb-Pb and Xe-Xe collisions at similar center-of-mass energies $\sqrt{s_{\mathrm{NN}}}$. For elliptic flow an excess of Xe-Xe over Pb-Pb is observed for the most

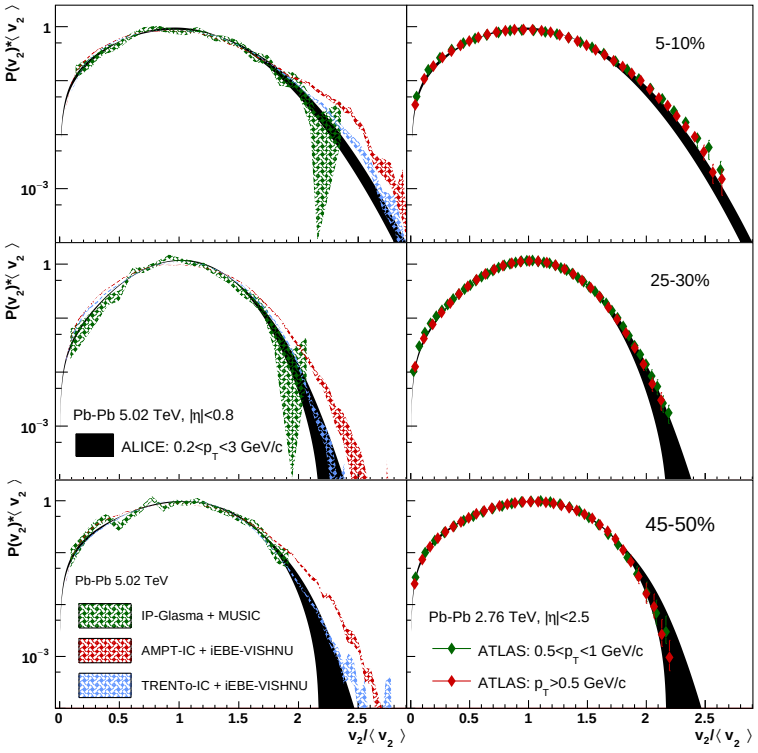

Figure 1.21: Distribution of the elliptic flow coefficients v_2 for three different centrality classes determined in Pb-Pb collisions. The data points show measurements from ATLAS experiments. The black bands show the elliptic power model fit to ALICE data. The colored shaded bands indicate hydrodynamic simulations. Figure taken from ref.[70].

central collisions. In contrast, for triangular flow such an enhancement in central collisions is not observed as triangular flow primarily originates from flow fluctuations. The ratio between Pb-Pb and Xe-Xe collisions indicate that the fluctuations are increased in Xe-Xe collisions, because the number of sources contributing to the eccentricity is smaller at the same centrality. Simulations show that the size of the fluctuations depends inversely on the number of sources or nucleons in the initial state in spherical symmetric systems[73]. A second observation is that the shape of the nuclei contribute to the initial eccentricity. Whereas Pb is spherically symmetric, Xe is deformed. This deformation gives additional contributions to the eccentricities in central collisions, where the geometric component in collisions of spherically-symmetric nuclei vanishes[67].

So far the measurements at the high collision energies have focussed on measuring flow fluctuations relative to the produced particles. The full three-dimensional picture of the collision has not fully been explored. By using the spectators the reaction plane can be estimated independently of the produced particles. With this the flow fluctuations could be measured relative to the geometrical plane of the collision. The elliptic power model predicts a hierarchy of initial eccentricities and flow cumulants (see eq. (1.38)). The hierarchy could be tested by measuring the elliptic flow relative to the spectator plane and assuming that the spectator plane approximates the reaction plane $\Psi_{SP} \approx \Psi_{RP}$:

$$v_2\{2\} > v_2\{4\} > v_2\{\Psi_{SP}\} \approx v_2\{\Psi_{RP}\}\,. \tag{1.41}$$

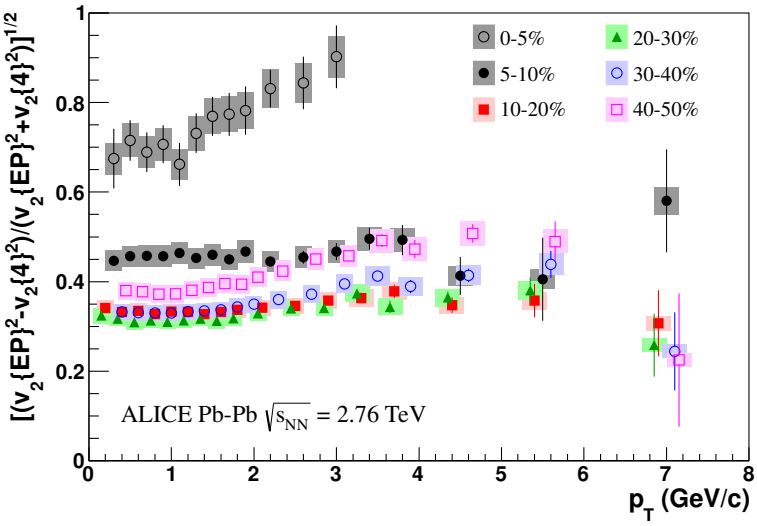

Figure 1.22: Transverse momentum dependence of the flow fluctuations for different centrality classes measured in Pb-Pb collisions at $\sqrt{s_{\mathrm{NN}}} = 2.76\,\mathrm{TeV}$ by ALICE. Boxes show the systematic uncertainties. Lines show the statistical uncertainties. The central values of centrality classes larger than 10 % are slightly shifted along the horizontal axis for clarity. Figure taken from ref.[72].

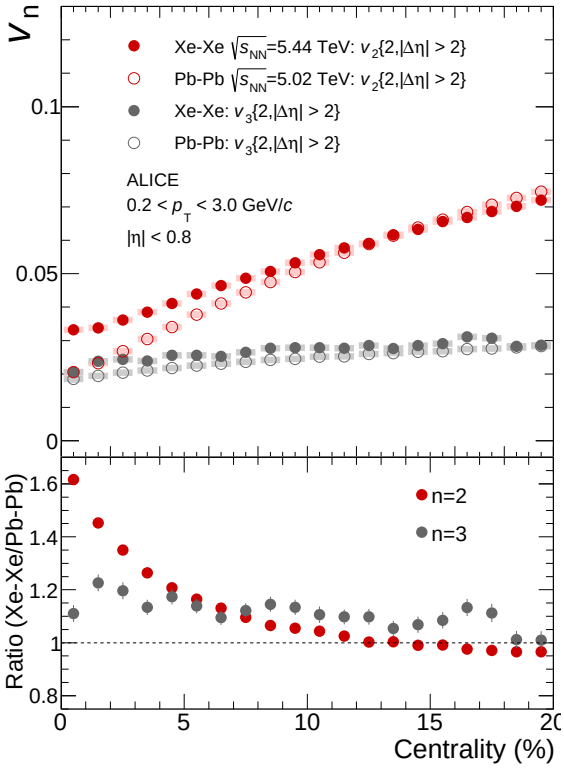

Figure 1.23: Elliptic and triangular flow measured in central Pb-Pb and Xe-Xe collisions at $\sqrt{s_{\mathrm{NN}}} = 5.02\,\mathrm{TeV}$ and $\sqrt{s_{\mathrm{NN}}} = 5.44\,\mathrm{TeV}$, respectively. The top panel shows the flow harmonics and the bottom panel shows the ratio of the different collision systems. Figure taken from ref.[67].

1.8.2.3 Three-dimensional Picture of the Collision

The longitudinal dynamics are also sensitive to the transport coefficients of the QGP. The viscosities of the QGP generally are temperature dependent. At larger pseudorapidities (forward) the temperatures drop. A lower temperature means less time of the medium is spent in the QGP phase. This means the measurement is sensitive to the temperature dependence and hadronic viscosities[74,75]. In the previously introduced measurements, the simplified Bjorken picture allows to accurately describe the collective flow measured at mid-rapidity. By extending the measurements to the larger pseudorapidities the validity of the Bjorken picture can be tested.

Figure 1.24 shows the pseudorapidity dependence of the elliptic flow. At mid-rapidity $|\eta| < 1$, the Bjorken picture is a good approximation. The measured flow only changes mildly with pseudorapidity in this interval. For larger pseudorapidities the measured flow falls of steeply and therefore the Bjorken picture is not valid anymore. The measurement is compared to a hydrodynamic simulation. The steep fall-off seen in the data is not accurately reproduced by the hydrodynamic model. This demonstrates the high sensitivity of the measurements exploiting the three-dimensional dynamics of the collision to the hydrodynamic evolution of the QGP.

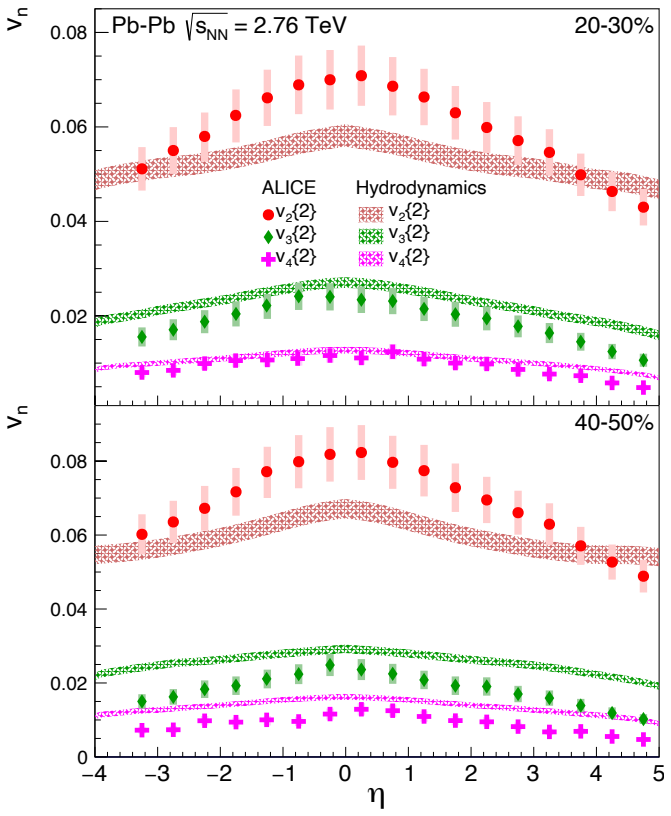

Figure 1.24: Pseudorapidity dependence of elliptic flow in Pb-Pb collisions at $\sqrt{s_{NN}} = 2.76\,\text{TeV}$. The measured data points are compared to a hydrodynamic simulation shown as colored bands. Figure taken from ref.[74].

The directed flow measured relative to the spectator deflection is also highly dependent on the longitudinal and early time dynamics of the collision. As illustrated in fig. 1.9, the directed flow in the medium develops along the reaction plane. This reaction plane is estimated by the

deflection of the spectators from the participant region. It is depends on the distribution of nuclear matter in the colliding nuclei and the momentum transfer between the participants and the spectators. Since the interaction of the spectators and the participant region happens very early in the initial state the spectator deflection probes the dynamics of the initial state of the collisions. An exact description requires a detailed modeling of the early time dynamics, which includes the spectators. By including the spectators, the measurement is sensitive to the orientation of the participant region relative to the direction of the spectators. Without the spectators, the orientation or tilt of the medium cannot be determined.

For a non-fluctuating smooth nuclear matter distribution, an anti-symmetric structure of the directed flow relative to the pseudorapidity is expected. If fluctuations of the initial state are included, a symmetric component also appears due to the difference of the spectator and reaction planes.

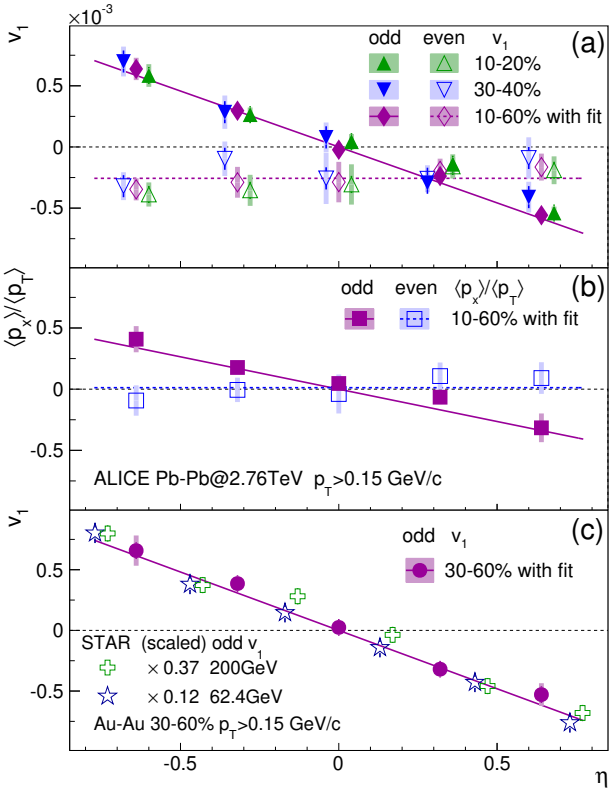

Figure 1.25: Directed flow and relative momentum shift as a function of pseudorapidity for 3 different centrality intervals measured in Pb-Pb collisions at $\sqrt{s_{\mathrm{NN}}} = 2.76\,\mathrm{TeV}$. Compared to measurements at lower center-of-mass energies. The data labelled even and odd correspond to the symmetric and anti-symmetric components of the directed flow. Figure taken from ref.[76].

Figure 1.25 shows the directed flow and the relative momentum shift as a function of the pseudorapidity. For the 30 % to 40 % most central Pb-Pb collisions at $\sqrt{s_{\mathrm{NN}}} = 2.76\,\mathrm{TeV}$, the spectators receive an estimated transverse-momentum kick of

$$p_{\mathrm{T,sp}} = \sqrt{s_{\mathrm{NN}}}\frac{d}{z} = 16\,\mathrm{MeV/c}\,, \tag{1.42}$$

where d is the mean deflection of the spectators measured by the detector and z is the distance of the detector to the interaction point[76]. Non-zero signals for both symmetric and antisymmetric components of the directed flow are measured. Both components also show no strong dependence on the collision centrality. Compared to the directed flow measured at smaller

collision energies a factor 3 smaller antisymmetric component is measured. This suggests the medium is less tilted in collisions at $\sqrt{s_{\mathrm{NN}}} = 2.76\,\mathrm{TeV}$ than in collisions at $\sqrt{s_{\mathrm{NN}}} = 200\,\mathrm{GeV}$. The small magnitude of the symmetric v_1 relative to measurements which do not rely on spectator measurements indicate a weak correlation between the fluctuating spectator and participant symmetry planes[76,77].

Fluctuations of the spectator deflection indicate a difference between the spectator plane and the reaction plane of the collision. A measurement of the flow fluctuations using the spectator plane as described previously could be sensitive to differences between the spectator plane and the reaction plane. The correlation between the magnitude of initial eccentricity of the collision and collective flow and other properties of the collision can be studied using ESE. Utilizing the flow fluctuations, collisions are classified into classes with small and large flow magnitude. MC studies have revealed a sensitivity to the initial state eccentricities.

Figure 1.26 shows ratios of the invariant yields in classes of collisions with low and high magnitude of elliptic flow as a function of transverse momentum. In collisions with large elliptic flow (large ellipticity), the ratios strongly rise with transverse momentum. This indicates a larger radial flow in collisions with larger ellipticity.

The results on radial flow demonstrate that event shape engineering is sensitive to the correlation between different aspects of the expansion of the collisions when fluctuations of flow are present. The method could be used to study the correlation between the deflection of the spectators and the anisotropic expansion of the medium at mid-rapidity using elliptic flow. Such a measurement would be sensitive to the momentum transfer between the spectators and the participant region in the initial state of the collision.

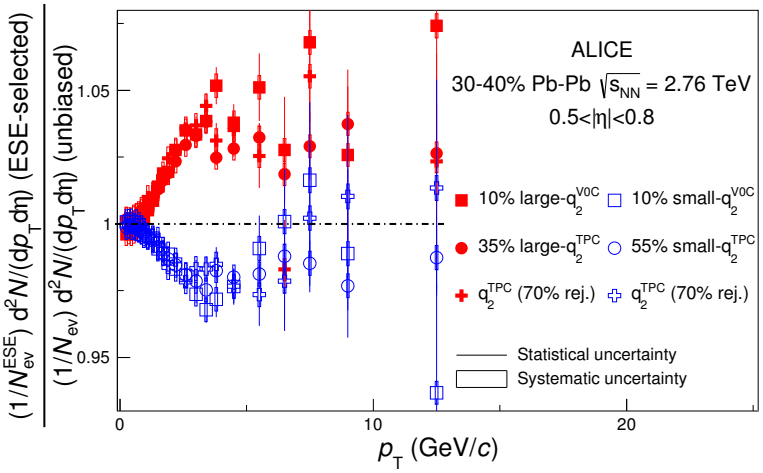

Figure 1.26: Ratio of ESE-selected invariant yields of charged particles to the unselected invariant yields as a function of the transverse momentum. Red (blue) points show collisions with large (small) q_2. Figure taken from ref.[78].

2 The Experimental Setup

The European Organization for Nuclear Research, also known as CERN, is the largest physics laboratory in the world. It is hosting many particle accelerators, which allows studying nuclear and particle physics at the highest available collision energies. In this section, the experimental setup is introduced.

2.1 The Large Hadron Collider

The Large Hadron Collider (LHC)[79–82] is currently the largest accelerator ring at CERN with a circumference of 26.7 km. It is the final accelerator of a system of the CERN particle accelerators. Figure 2.1 shows the accelerator complex of CERN.

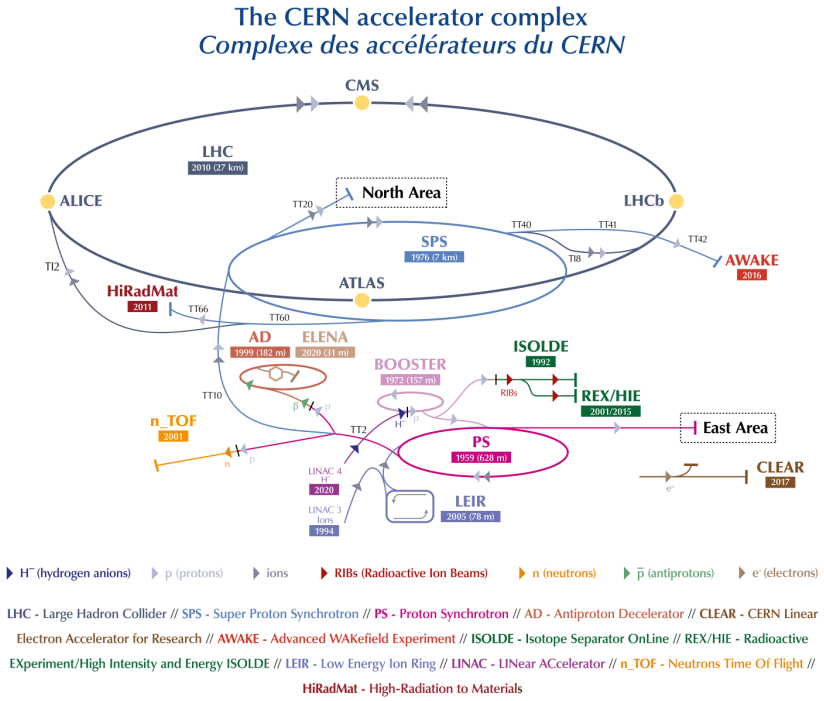

Figure 2.1: Overview of the CERN accelerator complex[83]. The heavy-ion injector chain is explained in the text.

The heavy-ion acceleration scheme is explained using the example of Pb ions. In the beginning, the Pb ions are extracted by electrostatic fields from the ion source. The partially stripped Pb ions are sequentially stripped of all their electrons during the further acceleration steps. The continuous beam of ions is split into pulses by a radio frequency quadrupole. Afterward, the pulses are transferred to a linear accelerator LINAC3, where their energy is increased to 4.2 MeV/nucleon. Several pulses are accumulated into bunches which are accelerated in the Low Energy Ion Ring (LEIR) to 72.2 MeV/nucleon. The bunches occupy a single so-called

RF bucket of radio-frequency cavities. Stable motion of the ions in a bunch is possible inside these RF buckets. They are then transferred to the Proton Synchrotron Booster (PSB) where they gain another 21.8 MeV/nucleon. In the Proton Synchroton (PS) they are accelerated 5.9 GeV/nucleon. During the transfer to the next acceleration step, the Pb ions are fully stripped of the electrons. Next, the Pb ions are accelerated to the injection energy of the LHC (177 GeV/nucleon) in the Super Proton Synchroton (SPS). Finally, the ions are filled into the LHC, where they are accelerated up to the maximum energy of 5.02 TeV/nucleon. The bunches in the final configuration of the LHC contain 1.22×10^8 ions[84].

The LHC is a synchrotron type accelerator, which features two different counter-rotating beams. At the highest energy, the superconducting dipoles, responsible for bending the particle beams, operate magnetic field strength[79] B of 8.33 T. The acceleration of particles to the maximum energy in the LHC of both beams takes about 20 minutes. After the maximum energy is achieved and the beams are in stable conditions, the experiments can begin with data-taking. There are four interaction points in the LHC where the beams are focussed and brought into collision.

The four major experiments are located at these interaction points. ALICE[85] (A Large Ion Collider Experiment) is a dedicated high-energy nuclear physics experiment and specializes in the study of strongly-interacting matter at very high energy densities. The ALICE experimental setup is explained in detail in section 2.2.

ATLAS[86] (A Toroidal LHC ApparatuS) and CMS[87] (Compact Muon Solenoid) are general-purpose experiments exploring similar physics topics. The main physics motivations for these experiments include the search for the Higgs boson, precision tests of QCD and electroweak theory, and searches for beyond standard model physics.

LHC-b[88] (LHC-beauty) is a forward spectrometer, which specializes in the detection of bottom quarks decays, and CP-violation.

There are also four smaller experiments, which share the interaction points with the larger experiments. The experiments are dedicated to different physics topics: the search for new particles and study of high energy neutrinos with FASER[89] (ForwArd Search ExpeRiment); the study of forward physics to better understand high energy cosmic rays with LHCf[90] (LHC-forward); the search for magnetic monopoles with MOEDAL[91] (Monopole and Exotics Detector At the LHC); the study of diffractive processes with TOTEM[92] (Total Cross Section, Elastic Scattering and Diffraction Dissociation).

2.1.1 Beam Parameters

The properties of the particle beams are important for understanding the measurements performed by the experiments at the LHC. In this section, the relevant beam parameters for the experiments are summarized. A complete overview of accelerator physics is available in, for example, ref.[93].

The center-of-mass energy $\sqrt{s}$ for relativistic particles with energies E_1 and E_2, and a charge to mass ratio of one in a collider is given by

$$\sqrt{s} = E_1 + E_2 \,. \tag{2.1}$$

The center-of-mass energy per nucleon-nucleon pair of a heavy-ion collision is given by

$$\sqrt{s_{\mathrm{NN}}} = Z/A\sqrt{s} \tag{2.2}$$

where Z/A is the charge to mass ratio, and $\sqrt{s}$ is the collision energy of an equivalent proton-proton collision. For a 3.5 ZTeV beam this gives a $\sqrt{s_{\mathrm{NN}}}$ for a Pb-Pb collision of $\sqrt{s_{\mathrm{NN}}} =$ 2.76 TeV.

The trajectory of the beam inside a collider ring can to linear approximation be described by the solution of a second-order differential equation, the so-called Hill's equation[93]. This solution features a position-dependent $\beta(s)$, which is related to the transverse size of the beam by

$$\sigma(z) = \sqrt{\epsilon\beta(z)}\,. \tag{2.3}$$

z is the nominal position along the nominal beam trajectory. The beam emittance ϵ gives the average spread in position and momentum phase space. It is constant for the whole collider ring. At an interaction point, the β-function is called β^* and is minimized to increase the interaction rate between the two beams. In close vicinity of the interaction point the beta function can be approximated as

$$\beta(s) = \beta^* + z^2/\beta^*\,. \tag{2.4}$$

eq. (2.4) shows that the smaller β^* at the interaction point the faster the β-function rises for $|z| > 0$. In other words, β^* gives an indication of how strong the beam is focussed at the interaction point. This can also be expressed as the beam divergence at the interaction point D, which is calculated by

$$D = \sqrt{\epsilon/\beta^*} \tag{2.5}$$

The beams at an interaction point can arrive at an angle to minimize reactions away from the interaction point, which may reduce the lifetime of the beam. This angle is called the crossing angle.

The ability of a collider to produce a certain number of interactions in a given time is quantified by its luminosity. The luminosity is given by the interaction rate dN/dt divided by the cross section of the reaction σ_r

$$\mathcal{L} = \frac{1}{\sigma_r}\frac{dN}{dt}\,. \tag{2.6}$$

It depends on many parameters, such as the beam properties and the considered target and projectile nuclei. At LHC collision energies, electromagnetic processes have much larger cross sections (180 b) than the hadronic processes[94] 7 b. The high cross section of electromagnetic interactions leads to a quick burn-off of the initial peak luminosity[95]. The luminosity continues to decay during a single fill of ions in the collider ring.

If needed, the peak luminosity can be controlled in different ways, such as introducing a separation between the beams, adjustment of the β^*, or reducing the number of colliding bunches. The number of colliding bunches counts those which have a nominal bunch crossing at one of the interaction points. Reducing the luminosity can be necessary for experiments, which are not designed for the high luminosity provided by the collider. When a lower

luminosity than the peak luminosity of the collider is used, through a procedure known as luminosity leveling the luminosity can be kept constant at its (lower) maximum value over a long period. This is achieved through the continuous adjustment of either the separation of the beams, or the β^*. As soon as either adjustment is at its maximum value, the luminosity will decay as normal. Such a procedure was employed during the LHC Run 2 heavy-ion operation in 2018 at the ALICE interaction point[96].

In the delivery of the Pb ions to the accelerator, ions can fill up RF buckets adjacent to the designated bucket. At the LHC[79], the RF buckets have a spacing of 2.5 ns. The ion bunches in the RF buckets adjacent to the main bunch are referred to as satellite bunches. Collisions of the type main-satellite and satellite-satellite may contribute to the background in the experiment and need to be rejected.

The beam parameters of the LHC heavy-ion data taking periods are shown in section 4.1.

2.2 ALICE Setup

ALICE is the dedicated heavy-ion experiment at the LHC. The main purpose is the study of the strongly interacting matter at extreme energy densities, where the quark-gluon plasma forms. In this section, the ALICE coordinate system and the detector subsystems are explained.

In the coordinate-system of ALICE the z axis points towards the tunnel that leads to the ATLAS experiment. The y axis points upwards and the x axis points into the LHC ring[97]. By convention the polar angle of a particle is usually measured using the pseudorapidity $\eta = -\ln(\tan(\theta/2))$, where the polar angle θ is the angle to the axis of the beam z. For high momentum particle the pseudorapidity is approximately equal to the rapidity.

$$\eta = \frac{1}{2}\ln\left(\frac{p + p_L}{p - p_L}\right) \approx \frac{1}{2}\ln\left(\frac{E + p_L}{E - p_L}\right), \tag{2.7}$$

because the rest mass of the particle is negligible compared to its total energy. The coordinate system is divided into two sides. The A-side (positive η) points towards the tunnel leading to ATLAS. The C-side (negative η) points towards the tunnel leading to CMS.

The acceptance of the ALICE subsystems is characterized by the pseudorapidity and azimuthal angles. In the context of detectors “forward” and “backward” refers to an acceptance close to the beam axis and therefore large $|\eta|$. A “mid-rapidity” acceptance is sensitive to regions of small $|\eta|$, which are pointing away from the beam-axis. In ALICE, mid-rapidity usually corresponds to $|\eta| < 0.9$, or an angle of $\approx \pm 45°$ around the $x - y$ plane.

The ALICE setup can be broadly divided into the central barrel and the muon arm. The central barrel is located inside the large solenoid magnet. It contains detectors for tracking particle identification, calorimetry, and multiplicity measurement. The muon arm is composed of the forward muon spectrometer and the dipole magnet. The names of the detectors, which are divided into two separate subsystems on either side, are appended with the respective letter (A or C) to identify them.

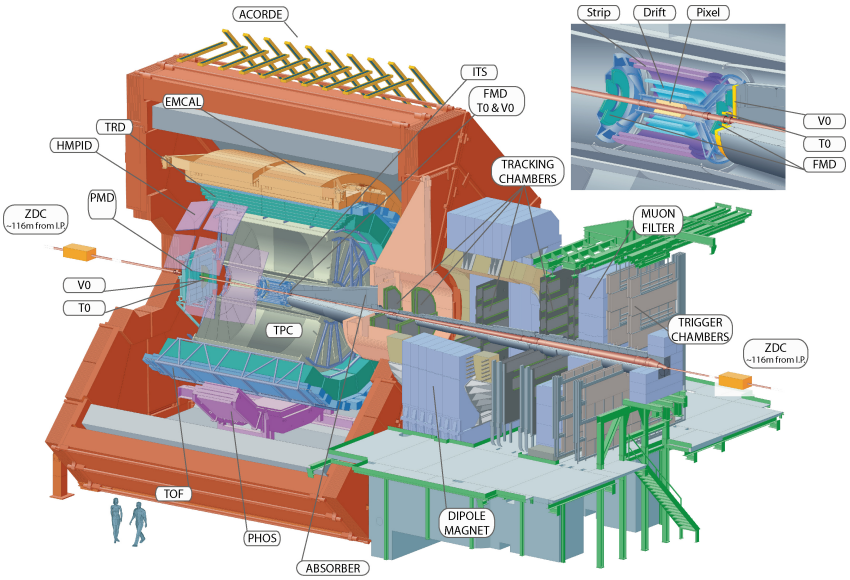

Figure 2.2: Schematic of the ALICE setup with labels showing the different subsystems.

Figure 2.2 shows a schematic overview of the ALICE setup[98]. The large solenoid magnet (shown in the sketch in red) has a nominal magnetic field strength of $B = 0.5\,\mathrm{T}$. The magnet bends the trajectories of the particles, which allows determining their momentum. The particle trajectories in the central barrel are reconstructed using the Inner Tracking System (ITS) and the Time Projection Chamber (TPC). The identification of the particle type can be performed by the ITS, the TPC, the Time Of Flight (TOF) detector, the Transition Radiation Detector (TRD), or the High Momentum Particle Identification Detector (HMPID). The V0 is a forward scintillator providing triggering and measuring bulk properties of the interaction. It is used to estimate the centrality of the heavy-ion collisions (see section 2.5).

The PHOton Spectrometer (PHOS) is a calorimeter dedicated to the measurement of electromagnetic radiation. It works in combination with the Charged-Particle Veto (CPV) detector, which vetos charged particles to measure photons from the strongly-interacting matter, or radiative decays. The ElectroMagnetic Calorimeter (EMCal) is dedicated to the measurement of highly energetic photons, electrons, pions, or jets. The ACORDE (A Cosmic Ray DEtector for ALICE) on top of the solenoid magnet is a detector acting as a trigger for cosmic rays. The ALICE Diffractive (AD) detector system is dedicated to the measurement of diffractive proton-proton processes. The Forward Multiplicity Detector (FMD) is a forward detector for extending the particle multiplicity measurement to high $|\eta|$ to measure bulk properties of the interactions. The TO is a fast trigger detector, which also gives the starting time for the time of flight measurements with the TOF. The muon spectrometer allows the reconstruction of heavy quarkonia states using pairs of muons. The muon-spectrometer dipole, located on the C-side next to the solenoid, bends the muon trajectories. The muons are isolated with an absorber, and their trajectory and transverse momentum is determined using a tracking system in conjunction with the magnetic field. The Zero Degree Calorimeter (ZDC) measures spectator nucleons escaping from the collisions.

Because neutrons are not bent by the magnetic fields, they travel on straight-line trajectories,

which originate from the interaction point. To ensure a good acceptance of the ZDC, the crossing angle of the beams needs to be within a threshold set by the geometric acceptance of the detector. Otherwise, the neutron spectators originating from the interaction point could be intercepted by the aperture of other instruments installed in between the interaction point and the calorimeters. In addition to the external crossing angle from the LHC beam settings, the muon dipole causes an intrinsic vertical crossing angle of the beam to be present in the ALICE interaction point

$$\alpha_{int} = \frac{Z}{A}\frac{E_0}{E}\alpha_0 \,, \tag{2.8}$$

where $\alpha_0 = 280\,\mu$rad and $E_0 = 3.5$ TeV/nucleon. The internal crossing angle is dependent on the Energy E, charge Z and mass A of the colliding heavy ions[98]. This crossing angle needs to be compensated by the external crossing angle such that the total half crossing angle is smaller than $\alpha_{tot} < 60\,\mu$rad which allows the neutron spectators to reach the ZDC detectors[99,100].

In the following sections, the detectors used in this analysis is explained in more detail.

2.2.1 Inner Tracking System

The ITS[101] consists of six concentric layers of silicon detectors. It is the innermost detector system, with a nominally complete azimuthal coverage and a pseudorapidity reach of $|\eta| < 0.9$. Its basic functions are the determination of the primary vertex of the collision and secondary vertices from weak decays of particles, the standalone tracking and particle identification of low-momentum particles, as well as the combined tracking of particles together with the TPC. For this purpose, the detector requires a high granularity to cope with the high particle density in nucleus-nucleus collisions.

The innermost two layers, the SPD, are silicon pixel detectors which consist of high granularity pixel detectors. They are located at a radius of 3.9 cm and 7.6 cm, respectively. The layers are very close to the beam pipe, which as a radius at the ALICE interaction point of 3 cm. A short distance between the innermost layer of the SPD to the interaction point is important for the tracking of charged particles. The third and fourth layers are silicon drift detectors (SDD) and are located at 15 cm and 23.9 cm. The fifth and sixth layers, the SSD, are silicon strip detectors. They are located at a radius of 38 cm and 43 cm, where the charge particle density is below one particle per cm^2. The four outer layers of the ITS, provide the particle identification via the specific energy-loss of particles in the detector. Due to cooling problems, a significant portion of the SPD was offline during the first data-taking period in the years 2009-2011, which reduced the azimuthal acceptance.

2.2.2 Time Projection Chamber

The TPC[102] is the main tracking and particle identification device in ALICE. It has the shape of a cylinder mantle with a inner radius of 0.85 m and a outer radius of 2.47 m for its active volume, which is filled with a specific gas-mixture. In the azimuth it covers $|\eta| < 0.9$ for particles, which traverse the whole radial expanse of the detector. The detector is divided along the beam axis into two equally large drift regions by a central cathode. Each drift region

has a length of 2.5 m. On the opposite sides of the central electrodes is the readout based on multi-wire proportional chambers. Each of the 18 readout chambers covers an azimuth of 20 deg. As the charged particle density in the detector decreases with increasing radial distance to the interaction point, the readout chambers are divided into two regions with differing readout pad sizes.

Charged particles travel on curved trajectories through the active volume of the TPC. During the interactions with the gas, they lose part of their energy by ionizing the gas atoms. The positively charged ion drift towards the central cathode. The liberated electrons drift towards the positively charged amplification region of the readout chambers. On their way to the readout chamber, the electrons can liberate secondary electrons. However, the number of electrons is not large enough to be directly detected. Therefore, the readout of the TPC uses multi-wire proportional chambers to amplify the signal. Inside the readout chambers, electron avalanche creation provides the necessary amplification for the signal detection on the readout pads. A gating grid, located in front of the amplification region, prevents the electrons and ions created in the amplification region from drifting back into the active volume. After a trigger has fired, within a window of 100 μs, the gating grid is transparent to the incoming electrons.

The three-dimensional trajectories of the original particles are reconstructed from the position of the signal on the readout chamber and the time of arrival of the electrons. With the curvature due to the surrounding solenoid field, the momentum of the particle can be determined. In each of the interactions of the particles with the gas atoms, they lost part of their kinetic energy. The mean rate of this energy loss at the intermediate velocities present in the experiment ($0.1 < \beta\gamma < 1000$) can be described by the Bethe equation[3,103]. The energy loss only depends on the velocity β of the particle. Together with the momentum measurement, this is used to determine the identity of the particle.

In the course of an upgrade project, the multi-wire proportional chambers of the TPC are being replaced by newly designed readout chambers based on the GEM technology[104]. The new electron amplification scheme allows the TPC to operate without the need for a gating grid. The new readout chambers allow a trigger-less operation of the detector. As a service work to the ALICE collaboration, I have contributed to the testing of the GEM foils and the construction of the outer readout chambers at the detector lab in GSI[105].

2.2.3 V0 Scintillators

The V0[106] detector system consists of two separate scintillators on the A and C-side of ALICE. The V0 is the main minimum bias trigger detector in ALICE. It measures the multiplicity of particles using an array of plastic scintillators connected to photomultipliers. This measurement is used to estimate the centrality of the collisions. Both detectors have complete coverage of the azimuthal acceptance. It is segmented into eight sectors in the azimuth and fo sectors in the radial direction. Their pseudorapidity acceptance varies due to different geometries between the two detectors. The V0-A has an acceptance of $2.8 < \eta < 5.1$ and the V0-C has an acceptance of $-1.7 < \eta < -3.7$.

2.2.4 Zero Degree Calorimeters

The ZDC[99] consists of three calorimeters systems. It can be used to trigger certain classes of collisions, to determine the centrality, or measure the properties of the spectators. Two different types of spectators can be measured. The neutrons are measured in the neutron calorimeters and the proton in the proton calorimeters. The spectators bound in nuclear fragments cannot be measured. They are deflected by different amounts due to their varying charge to mass ratios and do not impinge on the detectors. Based on the centrality of the collisions a different composition of these different type of spectators are present. For central collisions, there are only low amounts of spectators created in the collision. In mid-central collisions, the number of neutron spectators is large. For peripheral collisions, the number of neutron spectators diminishes as most of the neutrons remain bound in the nuclear fragments[99].

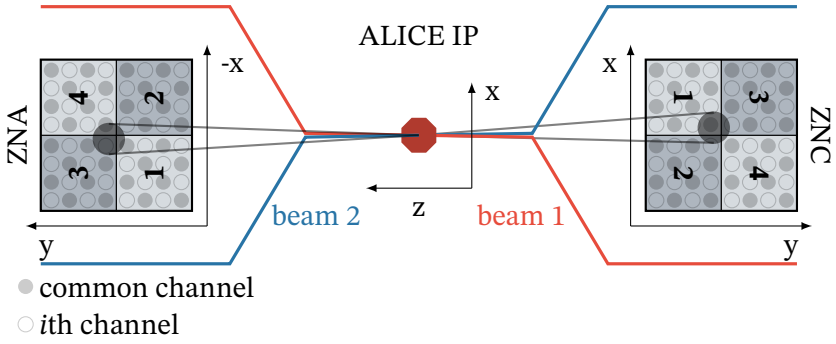

Figure 2.3: Schematic overview of the neutron ZDC detectors relative to the ALICE interaction point. The flight path of the neutrons is sketched by the transparent gray cones.

Figure 2.3 shows the position of the calorimeters relative to the ALICE interaction point. The calorimeters are located on either side of ALICE inside the LHC tunnel approximately 114 m distance from the interaction point. They measure the spectators in $|\eta| > 8.8$ using quartz fiber spaghetti calorimetry[107]. In LHC run 2, the ZDC detectors were moved closer to the interaction point to a distance of 112.5 m.

The neutron calorimeters are called ZNA and ZNC. They are located between the two beamlines on a raisable platform. The proton calorimeters are called ZPA and ZPC. They are located next to the inner (outgoing) beamline.

The high energy spectators impinging on the detectors cause a shower in the absorber material. The neutron ZDC use a tungsten absorber to contain the shower inside the detector. For the proton ZDC a brass absorber is used. Quartz fibers are embedded into the absorber matrix. A shower particle traversing such an optical fiber causes the release of light due to the Cherenkov radiation[108]. The optical fibers guide the light to the readout based on photomultipliers. The fibers are oriented at 0 deg relative to the direction of the beam. This orientation does not maximize the light yield. However, the energy resolution is not significantly affected by this choice. At LHC energies, the light yield is so large that fluctuations of the resulting number of photoelectrons do not influence the resolution[109,110]. The intrinsic speed of the emission of Cherenkov light gives the ZDC a very fast response time.

Each of the detectors is segmented into four zones. In each zone, half of the fibers are read out by a dedicated photomultiplier tube. The other half are routed to a common photomultiplier, which is shared among all segments. This segmentation is illustrated for the neutron calorimeters in fig. 2.3. This common channel can be used for the calibration of the device.

The proton ZDC is 20.8 cm wide,12 cm high and 150 cm long. It is located 19 cm next to the beam axis of the outgoing beam pipe. Due to the deflection of the protons in the magnetic field of the separator dipole between interaction point and ZDC, a large horizontal dispersion of the protons is observed. Therefore, it is only segmented in the x-direction. Simulations have also shown that a fraction of protons also interact with the beam pipe at the exit of the separator dipole and do not reach the detectors[99].

The neutron ZDC has a 7 cm by 7 cm transverse size and is 100 cm long. The detector has a two by two segmentation in the transverse plane. The segmentation into four quadrants allows the determination of the centroid position of the spectator neutrons. The detector is able to contain 80 % of the shower created by an impinging neutron. This allows achieving an energy resolution of 10 %. The contamination from particles produced at the interaction point and along the beamline has been shown in simulations to be on the order of 10 % for the worst case of central collisions.

For the determination of the centrality using neutron ZDC additional measurements are needed to remove ambiguity between central and peripheral collisions. These measurements are provided by the third system of the ZDC called the ZEM. The ZEM measures the energy carried by photon at forward rapidity $4.8 < \eta < 5.7$. It is located 7.35 m from the interaction point on the A-side[97].

2.3 Data-Taking

The LHC data taking can be organized into the different operational runs. The LHC Run 1 took place from 2009 to 2013. In the time from 2013 to 2015, known as the LHC long shutdown 1, upgrades were applied to the detectors and LHC. The LHC Run 2 took place from 2015 to 2018. From 2019-2022 the LHC is in another long shutdown, where major upgrades to the detectors are being installed. The LHC Run 3 is scheduled to begin data taking of proton-proton collision in 2022[100] at the nominal energy of $\sqrt{s_{\mathrm{NN}}} = 5.5\,\mathrm{TeV}$.

In ALICE the operational runs are further divided into different periods. A period consists of many fills of the LHC. A typical fill lasts around six hours[111]. During this time, data may be taken in several data runs. A data runs specifies a time frame in which the data-taking conditions were constant. Between data runs, the data-taking conditions can change, such as the trigger configuration or the active detector subsystems. There can also be variations of the conditions in time during a data run, such as the leveling of the luminosity. These effects may introduce a time dependence on the detector performance. The data samples which were used in the analysis of the data are introduced in section 4.1.

2.3.1 Trigger

Not all collisions can be recorded to the disk. This is limited by the rate by which collisions can be read out from the experiment. To down-sample the number of collisions, a trigger is required. The fraction of collisions that are selected is controlled by a trigger. Most of the measurements performed with ALICE look at physics phenomena of low transverse momentum phenomena. These collisions do not have a clear signal on which a trigger can select. The solution is to record the data with a minimum bias trigger, which fires if a minimal activity is seen by the detector. The V0 detector and in some cases the SPD is used for minimum bias triggering. The trigger threshold per V0 segment is chosen to be equal to the energy deposition of one minimum-ionizing particle[112].

The implementation of the triggers varies slightly between the Pb-Pb and Xe-Xe data-taking periods. In the 2010 Pb-Pb data-taking period collisions were triggered on combinations of hits in the SPD, V0-A, and V0-C detectors[98]. Two different minimum bias triggers were used in combination with a bunch crossing. The MBand trigger requires a coincident signal in the V0-A and V0-C. The MBor trigger requires a signal in the V0 and SPD.

For the Xe-Xe data-taking period, the definition of this trigger was different due to the lower magnetic field of the ALICE solenoid[113]. At a magnetic field of $B = 0.2\,T$, the probability for particles from electromagnetic interactions reaching the V0 detector is higher than in the standard configuration. To suppress these background collisions, a coincidence of signals in the V0-A, V0-C, ZNA, and ZNC is required. This trigger has full efficiency for hadronic interactions within 0 % to 90 % centrality. It was confirmed by comparing to a control trigger based on the coincidence of V0-A and V0-C.

These online triggers are supplemented by further offline triggers or selections to reduce contamination from non-hadronic processes and machine-induced background, which are introduced in section 4.3.

2.4 Collision and Particle Reconstruction

During data-taking, the raw data is recorded to disk. After the data-taking, the raw data is "reconstructed". This procedure includes the calibration of detectors, the rejection of background, the reconstruction of tracks of particles, and the reduction of the data volume to make it available for the various physics analyses performed by the collaboration.

From the raw data, the individual particles are identified, and their kinematic properties are reconstructed. This procedure takes signals from multiple detectors into account. The first step is the calibration of every individual detector. The calibration data is derived during the data-taking from the data itself and possibly from calibration data. The exact calibration procedure depends on the specific detector. These include alignment, mapping of bad or noisy elements, or the calibration of timing and amplitude of a detector.

Using the calibrated detectors, the position of the primary vertex of a collision and the trajectories of the particles can be found using vertex finding, and track reconstruction algorithms, respectively. The centrality of a collision can be determined using the calibrated signal amplitudes from a detector subsystem, for example, the V0. The algorithms for vertex

finding, track reconstruction, and centrality determination are explained in the following sections.

2.4.1 Vertex Finding

Before the track reconstruction in the central barrel, a preliminary vertex is determined using the two SPD layers[98]. First, segments are constructed from the clusters in the two layers. Next, the point in space where the most tracklets intersect is defined as the preliminary vertex. It is used for the track reconstruction algorithm. After the track reconstruction, the interaction vertex is determined for ITS-TPC and TPC-only tracks, separately. The procedure makes a first approximation of vertex position by propagating the tracks to the closest approach to the nominal beam axis. After far outliers are removed, the approximate position is determined. This first approximation is improved by a precise vertex fit, which includes the suppression of outliers based on their residuals. These final vertex positions have higher resolutions than the preliminary vertex. The estimate based on ITS-TPC tracks is the most precise.

2.4.2 Track Reconstruction

Tracks of charged particles are reconstructed within the central barrel of ALICE[98]. The track reconstruction algorithm operates on clusters. These clusters are obtained in each detector separately by assigning the measured data such as position, amplitudes, times, and their errors to a cluster.

After all the raw data is transformed into clusters, tracking is performed using a Kalman filter technique[114]. Up to three track-fitting iterations in moving in different radial directions, according to the inward-outward-inward scheme presented here. In the beginning, the tracks are seeded in the TPC using TPC clusters at large radii or a combination of TPC clusters and the preliminary vertex. The track is then propagated inwards and updated based on the encounters TPC clusters. Multiple reconstructions of the same physical particle are suppressed by a specialized algorithm searching for tracks with shared clusters. The tracks, which meet minimum quality requirements, are then propagated into the inner radius of the TPC. The TPC-only parametrization of the track is stored in the event with and without a constraint to the preliminary primary vertex.

A preliminary particle identification allows ionization energy loss corrections in the subsequent tracking iterations. The track is then seeded into the outermost layer of the ITS. Afterward, the track is propagated to the next layer and updated. This procedure is repeated for all layers. To account for the efficiency of particle detection in the ITS also tracks without hits in the previous layers are propagated further. However, a penalty factor, which accounts for the missing hits, is added to the track quality parameter. One track in the TPC creates multiple possible tracks in the ITS. The ITS track with the overall best performing fit is used.

Due to energy-loss effects and multiple scattering, a sharp fall-off is observed for the track reconstruction efficiency at 200 MeV/c for pions. Tracks with lower transverse momentum can be reconstructed using only the ITS. These ITS-only tracks are seeded from clusters in

proximity, which do not belong to a previously found ITS-TPC track. The tracks with the best fit are found using a Kalman-Filter approach. Their corresponding clusters are then removed from further searches. The efficiency of the procedure is increased by repeating it several times after all tracks have been found. With each iteration, the proximity search windows are progressively wider. This allows the tracking of particles with transverse momentum as low as 80 MeV/c for pions.

This ends the first inward propagation of the tracks. In the second iteration, the tracks are propagated outwards from their extrapolated point of closest approach to the preliminary vertex. The tracks are again updated with the clusters encountered in the ITS and TPC. In Addition, the track length and expected flight time for the different particle species are updated for the particle identification with TOF. The tracks are matched with hits in the TOF and TRD and to the EMCal, PHOS, and HMPID calorimeters. The track matching to the detectors outside the TPC is not used to update the track kinematics. In the final iteration, an inward propagating track fit to the clusters is performed one more time. It starts at the outer radius of the TPC. This step is also referred to as refitting. As a next step, the track parameters of the global ITS-TPC fit with refit are stored in the event, with and without a constraint to the primary vertex. After this iteration is completed and the final primary vertex is determined from the tracks using the procedure outlined in section 2.4.1. In the last step, the secondary vertices originating from particle decays and photon conversions are identified by their decay topology.

The tracking parametrizations from the different steps of the track reconstruction, have different acceptance, efficiency, and transverse momentum resolution. The global ITS-TPC tracks give the best estimate of the tracking parameters. The drawback, however, is the limited acceptance in the azimuthal angle. During the 2010 data-taking up to 20 % of the two innermost layers of the ITS, the SPD, was offline. For Run 2 operation, this issue was largely resolved by improvements to the cooling system. In contrast, TPC-only tracks offer a very uniform track acceptance, modulated only by the readout chamber borders.

Figure 2.4 shows a comparison of the transverse momentum resolution of the different track parametrizations. The transverse momentum resolution of TPC-only is far worse than for global tracks. This is due to the larger distance and more material, which is in between the TPC and the interaction point. The transverse momentum resolution is, however, far worse than the one obtained with the global tracks. This can partly be mitigated by a constraint of the TPC-only track to the primary vertex during the track fit step. For low transverse momentum particles ($p_{\mathrm{T}} < 10\,\mathrm{GeV}/c$) the resolution is of similar magnitude as the ITS-TPC global track estimates. Additionally, the contamination from secondary particles is higher for TPC-only tracks In the case of global tracks, an additional vertex constraint does not yield further improvements to the transverse momentum resolution.

During the data analysis, additional criteria based on the tracking parameters further refine these selections. They are being used to reject tracks from erroneous reconstruction, which do not belong to a real physical particle, tracks originating from secondary vertices, and tracks with low momentum resolution.

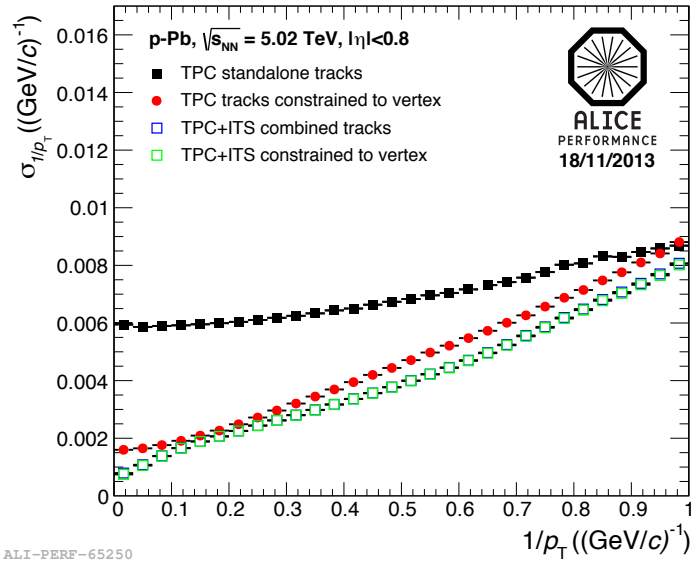

Figure 2.4: Comparison of the transverse momentum resolution as a function of $1/p_{\mathrm{T}}$ for the different track parametrizations (shown with different symbols and colors). The results were obtained in p-Pb collisions at $\sqrt{s_{\mathrm{NN}}} = 2.76$ TeV. Figure from ref.[98]

2.5 Centrality Determination

Because the impact parameter of a collision is not directly measurable, it has to be estimated from the measured quantities. The collisions are classified according to the centrality c, which is defined as a percentile of the hadronic cross section σ_{AA} corresponding to the number of particles (multiplicity) N above a given threshold N_{THR} measured in the experiment[115]

$$c \approx \frac{1}{\sigma_{AA}} \int_{N_{THR}}^{\infty} \frac{d\sigma}{dN} dN \,. \tag{2.9}$$

By comparing the multiplicity distributions measured in the experiment with models, the mean geometrical parameters $((N_{part}, N_{coll}, N_{spec}, b))$ can be determined in each centrality class. The models introduced in section 1.5.1, give the correlation between the impact parameter b and the number of collisions N_{coll} and participant (spectator) nucleons N_{part} (N_{spec}) in each collision.

The model and data can be compared by coupling the initial state model to an ansatz of particle production. In ALICE, a MC Glauber model (see section 1.5.1.1) is coupled to a two-component model of particle production[115]. A monotonic relation is assumed between the number of participants and the number of produced particles. This relation can be implemented using a negative binomial distribution for the particle multiplicity. The number of ancestors $N_{ancestor}$, so the number of sources which produce the particles, are given by a two-component model. For each collision, the number of binary collisions N_{coll} and the number of nucleons which experience at least one collision N_{part} are counted. In the two-component model, particle produced through soft processes are assumed to scale with N_{part}. Particle production through hard processes is assumed to scale with N_{coll}. With this assumption the $N_{ancestor}$ is calculated by

$$N_{ancestor} = f N_{part} + (1 - f) N_{coll}, \tag{2.10}$$

where f is controlling the relative importance of soft and hard processes in the particle production.

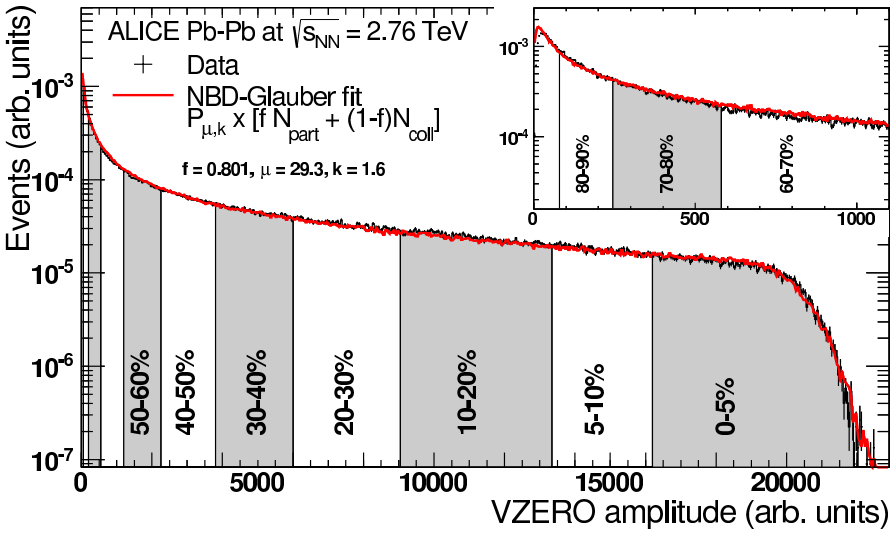

Figure 2.5: Sum of the signal amplitudes of both V0detectors. The distribution is fitted with the NBD-Glauber model. The centrality intervals are indicated in percent in the figure. Figure taken from ref.[116].

The probability for the number of particles n produced per ancestor is assumed to follow the negative binomial distribution

$$P_{\mu,k}(n) = \frac{\Gamma(n+k)}{\Gamma(n+1)\,\Gamma(k)} \frac{(\mu/k)^n}{(\mu/k+1)^{n+k}}. \tag{2.11}$$

The parameters μ and k control the mean and the width of the negative binomial distribution, respectively. The distribution is sampled $N_{ancestor}$ times per collision. The result resembles the particle multiplicity measured in the collision.

A minimization procedure on the χ^2 needs to be applied to find the best fit of the model, with the parameters μ, k, and f, to the measured particle multiplicity. The particle multiplicity is measured using the V0 detector. The fit is performed for all collisions with a large enough V0 signal so that the efficiency of the event selection and purity of the collisions are 100 %. This has the consequence that the very peripheral collisions in the 90 % to 100 % centrality class are excluded from the fit, as they do not satisfy these requirements. The definition of centrality based on the signal measured by the V0 may bias the selection of collisions compared to a selection based on the impact parameter. The two definitions differ due to the fluctuations of the V0 multiplicity. However, the bias is small for both Xe-Xe and Pb-Pb collisions in the centrality range 0 % to 80 % percent[116].

Figure 2.5 shows the resulting fit of the Glauber model (red line) to the sum of the signal amplitudes of the V0 detector (black line). The borders of the centrality intervals, which are indicated in the figure, are used to classify the collision.

3 Observables

As introduced in section 1.8, the measurement of the anisotropic flow coefficients gives insights into the properties of the QGP. However, the flow coefficients cannot be directly measured using eq. (1.32), because the symmetry planes Ψ_m are not directly experimentally accessible. The flow coefficients need to be estimated from correlations of particles measured with the detector. When only anisotropic flow is present and flow fluctuations vanish, the particles created in a collision are only correlated to the symmetry planes. Using this independence, the azimuthal probability density function (PDF) of m-particles $f(\phi_1, \dots, \phi_m)$ can be factorized into m individual PDFs $f(\phi_i)$ $i \in [1, m]$

$$f(\phi_1, \dots, \phi_m) = f(\phi_1) \dots f(\phi_m)\,, \tag{3.1}$$

where ϕ_i is the azimuthal angle of the i$^{\text{th}}$ particle. This generic factorization property of the PDF can be used to study moments of the anisotropic flow coefficients using azimuthal correlations of any number of particles.

This ideal picture is complicated by the fact that the flow coefficients fluctuate from collision to collision due to the fluctuations of the initial state. These fluctuations lead to different underlying PDF in eq. (3.1) for each collision. The moment of the flow coefficient $E(v_n)$ no longer fulfills the relation $E(v_n^k) = E(v_n)^k$, where the $E(v_n)$ is defined as

$$E(v_n^k) = \int v_n^k f(v_n) dv_n\,. \tag{3.2}$$

Further complications due to correlations through other processes, such as momentum conservation, particle decays, or Bose-Einstein correlations need to be taken into account in reality. These so called non-flow sources bias the measured flow coefficients. The observables introduced in this chapter suppress these non-flow biases.

Besides biases from non-flow also a non-uniform acceptance of the detector can influence the measured flow coefficients. Its influence on the observable and the correction procedure, which includes the implementation of a new software library, is explained after the observables are introduced.

3.1 Flow Vector

The directly inaccessible symmetry planes can be estimated from the measured particles using flow vectors, also referred to as Q-vectors. For the n$^{\text{th}}$ harmonic of the Fourier expansion the flow vector is given by

$$\begin{aligned} u_n &= x_n + i y_n = e^{in\phi_i} \\ Q_{n,p} &= X_{n,p} + i Y_{n,p} = \sum_{j=1}^{M} w_j^p u_{n,j}, \end{aligned} \tag{3.3}$$

where u_n is the unit flow vector of a single particle and M is the multiplicity of the measured particles. ϕ and w^p are the azimuthal angle and weight assigned to a given particle to the power

p, respectively. The power of the weight p of the flow vector is needed for the correct subtraction of autocorrelations when using multi-particle cumulants introduced in this chapter, see section 3.2.5. The flow vector can be viewed as a two-dimensional vector in the transverse plane with the components $X_{n,p}$ and $Y_{n,p}$. The weights are used to correct for inefficiencies of the detector. The correction procedure is introduced in section 3.5. For unit weights a simplified notation is used, $Q_{n,1} = Q_n$. To simplify the notation, it is useful to note that a negative harmonic corresponds to the complex conjugated flow vector

$$Q_{-n,p} = Q^*_{n,p}. \tag{3.4}$$

The relation of the flow vector to the anisotropic flow coefficients can be shown by performing an average over collisions with a fixed symmetry plane Ψ_k. This average is denoted by $\langle \ldots \rangle_{\Psi_k}$. To have parity with the measurement in a real experiment a further average over all possible symmetry plane orientations needs to be performed. The average over all possible symmetry plane orientations is zero for any given flow vector, as long as the distribution of the symmetry planes are uniform. A non-zero signal is only observed by performing correlations between different flow vectors. The average over all collisions with a fixed reaction plane is equivalent to the integral of the particle production PDF weighted with u_n. The particle production PDF is given by rewriting eq. (1.31) as

$$\rho(\phi - \Psi_k) = \frac{1}{2\pi}\left(1 + 2\sum_{n=1}^{\infty} v_n \cos(n(\phi - \Psi_k))\right). \tag{3.5}$$

A perfect detector acceptance is assumed to simplify the equations involving the unit flow vector ($w_i^p = 1$). The following relation for a unit flow vector average over fixed symmetry planes is obtained

$$\begin{aligned}
\langle u_n \rangle_{\Psi_k} &= \langle e^{in\phi} \rangle_{\Psi_k} && (3.6)\\
&= \frac{\int_0^{2\pi} d\phi e^{in\phi} \rho(\phi - \Psi_k)}{\underbrace{\int_0^{2\pi} d\phi \rho(\phi - \Psi_k)}_{1}} \\
&= \int_0^{2\pi} d\phi \; e^{in\phi} \; \rho(\phi - \Psi_k) \\
&= \int_0^{2\pi} \frac{d\phi}{2\pi} e^{in\phi} \left(1 + 2\sum_{m=1}^{\infty} v_m \cos(m(\phi - \Psi_k))\right) && \Big| \text{ insert eq. (3.5)} \\
&= \sum_{m=1}^{\infty} \int_0^{2\pi} d\phi \frac{1}{\pi} e^{in\phi} v_m \cos(m(\phi - \Psi_k)) \\
&= \int_0^{2\pi} d\phi \frac{1}{\pi} [\cos(n\phi) + i\sin(n\phi)] v_m \cos(n(\phi - \Psi_k)) && \Big| \; m \neq n \rightarrow \int \cdots = 0 \\
&= \frac{1}{2\pi} v_n \left(\phi e^{in\Psi_k} - \frac{i e^{-in(\Psi_k - 2\phi)}}{4n} \right)\Bigg|_0^{2\pi} \\
&= v_n \left(\cos(\Psi_k) + i\sin(\Psi_k)\right). && \Big| \; n \in \mathbb{Z}_{\neq 0} && (3.7)
\end{aligned}$$

The periodicity of the trigonometric functions eliminates all terms with $m \neq n$. The second term of the integral vanishes because n is always a nonzero integer number.

If one generalizes the flow vector to have an arbitrary number of particles one equivalently obtains

$$\begin{aligned} \langle Q_n \rangle_{\Psi_k} &= \langle \sum_{j=1}^{M} e^{in\phi_j} \rangle_{\Psi_k} \\ &= \langle M v_n \rangle_{Q_n} (\cos(\Psi_k) + i \sin(\Psi_k)) \\ &= V_n (\cos(\Psi_k) + i \sin(\Psi_k)) . \end{aligned} \tag{3.8}$$

$\langle M v_n \rangle_{Q_n}$ corresponds to the average of M and v_n using only the particles that were used for the construction of the flow vector Q_n. The flow vector corresponds to a vector in the transverse plane, that has on average the same direction as the symmetry plane. Detectors are not required to measure individual particles to be able to reconstruct the symmetry plane. As long as the detector is sensitive to the shape of the particle distribution in the transverse plane, the flow vector can be determined. For the case of a segmented detector, such as a calorimeter, the mean position of the individual channels correspond to u_n. The channel amplitudes correspond to the weights w_j^p assigned to the u_n in eq. (3.3). A segmented detector needs a segmentation which is larger than $2n$ to be able to measure the flow vector of harmonic n. In section 3.3 segmented detectors are used to estimate the coefficients of the elliptic flow relative to the spectator plane.

The average flow in eq. (3.8) is recovered by dividing the flow vector by the multiplicity M, as long as the multiplicity fluctuations in the sample of collisions are small. The flow vector normalized by the sum of the weights $\sum_{i=1}^{M} w_i^p$ is denoted by a lower case letter

$$q_{n,p} = \frac{Q_{n,p}}{\sum_{i=1}^{M} w_i^p}. \tag{3.9}$$

The angle of the flow vector and, therefore, the angle of the corresponding symmetry plane can be determined using

$$\Psi_n\{Q_{n,p}\} = \frac{1}{n} \text{atan2}(Y_{n,p}, X_{n,p}) . \tag{3.10}$$

3.2 Cumulant Method

Due to the factorization of the PDF azimuthal multi-particle correlation techniques can be used to construct observables which are sensitive to various combinations of the moments of the flow harmonic coefficients and their symmetry planes. As mentioned before the factorization can be broken by non-flow correlations and flow fluctuations. Non-flow contributions can be, to a large extent, removed by using multi-particle cumulants, which will be explained in this section. The breaking due to flow fluctuations is unavoidable. However, the different multi-particle cumulants are affected by flow fluctuations[73]. This allows to study the properties of the underlying distribution of the fluctuations by comparison of the different cumulants. In the following, the observables will be constructed using the multi-particle correlations without explicitly treating the effects of non-flow and flow fluctuations.

3.2.1 Azimuthal Multi-Particle Correlations

In this section the azimuthal multi-particle correlation is introduced, which is the basic building block of the cumulant methods. They are being used to define the multi-particle cumulants and estimate the flow harmonic coefficients. In a single collision the generic correlation of m-particles each with an azimuthal angle ϕ and an associated harmonic index n is given by

$$\begin{aligned}\langle m\rangle_{n_1,\ldots,n_m} &= \langle e^{in_1\phi_1}\ldots e^{in_m\phi_m}\rangle = \langle e^{i(n_1\phi_1+\cdots+n_m\phi_m)}\rangle \\ &= \sum_{\substack{l_1,\ldots,l_m \\ l_1\neq\cdots\neq l_m}}^{M} w_{l_1}\cdots w_{l_m} e^{i(n_1\phi_{l_1}+\cdots+n_m\phi_{l_m})} \Bigg/ \sum_{\substack{l_1,\ldots,l_m \\ l_1\neq\ldots\neq l_m}}^{M} w_{l_1}\cdots w_{l_m}\,,\end{aligned} \tag{3.11}$$

where M is the total number of particles. The particle weights $w_i,\ i\in[1,m]$ can be used to correct biases due to inefficiencies of the detectors. For a fully-efficient detector the weights are equal to one. Acceptance corrections using particle weights are explained in section 3.5. The uniqueness of the indices in the sum ($l_1 \neq \ldots \neq l_m$) needs to be enforced to exclude autocorrelations.

The denominator of eq. (3.11) is equal to the sum of particle weights. For a perfect detector ($w_{l_i}=1$) it is equivalent to the number of ordered arrangements of m particles of a set of M particles (called m-permutations of M[117])

$$\sum_{\substack{l_1,\ldots,l_m \\ l_1\neq\cdots\neq l_m}}^{M} w_{l_1}\cdots w_{l_m} \overset{w_{l_i}=1}{=} \frac{M!}{(M-m)!}\,, \tag{3.12}$$

The relation of the multi-particle correlations to the moments of the flow harmonics v_n and the symmetry planes Ψ_n can be shown by inserting eq. (3.5) into eq. (3.11) and using the factorization of the correlations and orthogonality of the trigonometric functions

$$\langle m\rangle_{n_1,\ldots,n_m} = v_{n_1}\ldots v_{n_m} e^{n_1\Psi_{n_1}+\cdots+n_m\Psi_{n_m}}\,. \tag{3.13}$$

The average over all particles in all collisions is denoted by $\langle\langle\ldots\rangle\rangle$. The azimuthal correlation function of m-particles averaged over L collisions is

$$\begin{aligned}\langle\langle m\rangle\rangle_{n_1,\ldots,n_m} &= \sum_{k=1}^{L}\langle\langle m\rangle\rangle_{n_1,\ldots,n_m k}\sum_{\substack{l_1,\ldots,l_m \\ l_1\neq\cdots\neq l_m}}^{M_k} w_{l_1}\cdots w_{l_m} \Bigg/ \sum_{k=1}^{L}\sum_{\substack{l_1,\ldots,l_m \\ l_1\neq\cdots\neq l_m}}^{M_k} w_{l_1}\cdots w_{l_m} \\ &= \sum_{k=1}^{L}\sum_{\substack{l_1,\ldots,l_m \\ l_1\neq\cdots\neq l_m}}^{M_k} w_{l_1}\cdots w_{l_m} e^{i(n_1\phi_{l_1}+\cdots+n_m\phi_{l_m})} \Bigg/ \sum_{\substack{l_1,\ldots,l_m \\ l_1\neq\ldots\neq l_m}}^{M_k} w_{l_1}\cdots w_{l_m}\,.\end{aligned} \tag{3.14}$$

The weight of a collision is determined by the sum of the product particle weights $w_{l_1}\cdots w_{l_m}$, which is equivalent to the denominator of the correlation function shown in eq. (3.11). These averaged multi-particle correlations are used to extract the underlying flow coefficients.

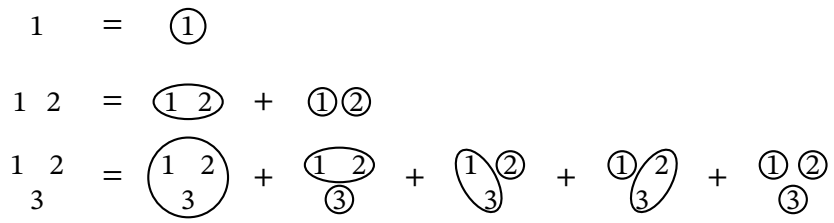

Figure 3.1: All possible partitions of sets with 1, 2, 3 elements into non-empty blocks. Each term corresponds to a partition and each ellipse to a block.

3.2.2 Cumulant Expansion

In addition to collective flow, correlations of multiple particles, introduced in the previous section, may have contributions from non-flow sources. Since these non-flow sources only correlate a subset of all particles in a collision, they can be removed using a cumulant expansion which isolates the genuine multi-particle correlation. All contributions of correlations of fewer particles are therefore removed. The dependence of such a non-flow bias on the number of correlated particles is explained in section 3.2.4.

First, the general properties of cumulants and their relation to the moments of the distribution will be explored. Afterwards the method will be applied to show how the multi-particle cumulants are constructed.

The cumulants are a set of quantities of a probability density, which give an alternative description of a distribution to the moments. If the moments of two probability density distributions are identical, it is guaranteed that their cumulants are also identical. Formally the cumulants can be defined by the cumulant generating function, which is related to the moment generating function[118]. Below the relation between moments and cumulants is used to define them. The relations between the first three moments $E(X^n)$ (first moment is the mean of a distribution) and cumulants κ_n of the random variable X are

$$\begin{aligned} E(X^1) &= \kappa_1 \\ E(X^2) &= \kappa_2 + \kappa_1^2 \\ E(X^3) &= \kappa_3 + 3\kappa_2\kappa_1 + \kappa_3^3 \,. \end{aligned} \tag{3.15}$$

The first cumulant is equivalent to the mean, the second moment corresponds to the variance and the third cumulant to the third central moment.

To apply this idea to the azimuthal correlation function of many particles eq. (3.11) cumulants of more than one random variable are needed. These cumulants are known as joint cumulants, or multi-variate cumulants with the random variables $X_1 \cdots X_n$. Similarly to the moments of one random variable, the joint moments of more than one random variable can also be expressed by joint cumulants. The joint cumulant expansion of the joint moments need to account for every possible way of how to partition the set of random variables into different non-empty subsets called blocks. Figure 3.1 gives an example of how sets of one, two, and three elements can be partitioned. Each partition corresponds to a term in the sketch and each block to an outline.

In the following, the properties of the joint cumulants and their meaning are explained using the examples of joint moments of one, two and three random variables. In the examples the partitions are indicated in the equations by π_i and braces{...}, and the blocks are shown by $B_{i,j}$ and brackets [...].

For one random variable ($m = 1$) there is only one partition π_1 with only one block $B_{1,1}$ with size 1

$$\pi_1 = \{B_{1,1}\} = \{[X_1]\} .$$

The complete expansion is therefore

$$c(X_1) = E(X_1) . \tag{3.16}$$

The joint cumulant of one random variable is identical to its mean.

For $m = 2$ there are two different partitions

$$\begin{aligned} \pi_1 &= \{B_{1,1}\} &&= \{[X_1, X_2]\} \\ \pi_2 &= \{B_{2,1}, B_{2,2}\} &&= \{[X_1], [X_2]\} \end{aligned}$$

Therefore, partition π_1 only has one block with size $|B_{1,1}| = 2$ and partition π_2 has two blocks of size $|B_{2,1}| = |B_{2,2}| = 1$. The complete expansion is

$$E(X_1, X_2) = c(X_1, X_2) + c(X_1)c(X_2) , \tag{3.17}$$

Or equivalently expressed using $E(X_i) = c_1(X_i)$ from eq. (3.15) as

$$c(X_1, X_2) = E(X_1 X_2) - E(X_1)E(X_2) . \tag{3.18}$$

This means the cumulant of two random variables is identical to their covariance. For two identical random variables this reduces to the variance.

For $m = 3$ there are five different partitions

$$\begin{aligned} \pi_1 &= \{B_{1,1}\} &&= \{[X_1, X_2, X_3]\} \\ \pi_4 &= \{B_{2,1}, B_{2,2}\} &&= \{[X_1, X_2], [X_3]\} \\ \pi_3 &= \{B_{3,1}, B_{3,2}\} &&= \{[X_1, X_3], [X_2]\} \\ \pi_2 &= \{B_{4,1}, B_{4,2}\} &&= \{[X_2, X_3], [X_1]\} \\ \pi_5 &= \{B_{5,1}, B_{5,2}, B_{5,3}\} &&= \{[X_1], [X_2], [X_3]\} . \end{aligned}$$

Using the relation from eq. (3.17) all terms with cumulants of two random variable can be rewritten as a covariance. Thus, the cumulant expansion of three random variables can be expressed as

$$\begin{aligned} E(X_1X_2X_3) &= c(X_1, X_2, X_3) + c(X_1, X_2)c(X_3) + c(X_1, X_3)c(X_2) + c(X_2, X_3)c(X_1) \\ &\quad + c(X_1)c(X_2)c(X_3) \\ c(X_1, X_2, X_3) &= E(X_1X_2X_3) - E(X_1X_2)E(X_3) - E(X_1X_3)E(X_2) - E(X_2X_3)E(X_1) \\ &\quad + 2E(X_1)E(X_2)E(X_3) \end{aligned} \tag{3.19}$$

For more than two random variables the relation of joint cumulants and joint moments takes a more complicated form.

For independent random variables X_1 and X_2 the moment $E(X_1X_2)$ factorizes $E(X_1X_2) = E(X_1)E(X_2)$. That means if a cumulant includes at least two independent random variables the whole cumulant vanishes. Therefore, the cumulants can be interpreted as a measure, which shows how far the random variables are from independence. As shown in eq. (3.19) after isolating the cumulant of m-random variables all n-body interactions for $n < m$ are subtracted. Therefore, the joint cumulant of m-random variables $c(X_1, \dots, X_m)$ measures the strength of the m-body type interaction.

For higher order moments a generic relation between moments $E(X_1 \cdots X_n)$ and the joint cumulants c is can be formulated

$$E(X_1 \cdots X_m) = \sum_{\pi} \prod_{B \in \pi} c(X_i : i \in B) \,. \tag{3.20}$$

π runs over the list of all possible ways to partition the random variables. As illustrated in the examples given above, the number of possible partitions of a set follows the Bell numbers[119] Bell_m. The first terms, starting with $\text{Bell}_0 = \text{Bell}_1 = 1$, are

$$1, 1, 2, 5, 15, 52, 203, 877, 4140, \dots \tag{3.21}$$

The 6 element set already has 877 unique partitions. Each partition is divided into multiple blocks. The number of blocks in a partition is given by $|\pi|$. B runs over all blocks of a given partition π. The index i runs over all random variable X_i included in a given block B.

Equivalently, the cumulant can also be expressed by the moments

$$c(X_1, \dots, X_m) = \sum_{\pi} (|\pi| - 1)!(-1)^{|\pi|-1} \prod_{B \in \pi} E\left(\prod_{i \in B} X_i \right) , \tag{3.22}$$

where the prefactor of a partition depends on its number of blocks.

3.2.3 Application to Azimuthal Multi-particle Correlations

The methods of joint cumulants can now be applied to the measurement of the azimuthal multi-particle correlations to isolate the genuine multi-particle interactions. The average of the multi-particle correlation function over all collisions is used as an unbiased estimator of the expected values $E(X_1, \dots, X_m) = \langle\langle m \rangle\rangle_{n_1,\dots,n_m}$ and the azimuthal angle is identified as the random variable $X_i = e^{in\phi_i}$. With these substitutions the one, two, and three-particle cumulants of the azimuthal multi-particle correlations can be expressed by

For clarity the particle weights not shown for $c_{n_1,n_2}\{2\}$ and $c_{n_1,n_2,n_3}\{3\}$.

$$c_{n_1}\{1\} = \langle\langle w_1 e^{in_1\phi_1} \rangle\rangle \tag{3.23}$$

$$c_{n_1,n_2}\{2\} = \langle\langle e^{i(n_1\phi_1 + n_2\phi_2)} \rangle\rangle - \langle\langle e^{in_1\phi_1} \rangle\rangle \langle\langle e^{in_2\phi_2} \rangle\rangle \tag{3.24}$$

$$\begin{aligned} c_{n_1,n_2,n_3}\{3\} = {} & \langle\langle e^{i(n_1\phi_1 + n_2\phi_2 + n_3\phi_3)} \rangle\rangle - 2\langle\langle e^{in_1\phi_1} \rangle\rangle \langle\langle e^{in_2\phi_2} \rangle\rangle \langle\langle e^{in_3\phi_3} \rangle\rangle \\ & - \langle\langle e^{in_1\phi_1 + in_2\phi_2} \rangle\rangle \langle\langle e^{in_3\phi_3} \rangle\rangle \\ & - \langle\langle e^{in_1\phi_1 + in_3\phi_3} \rangle\rangle \langle\langle e^{in_2\phi_2} \rangle\rangle \\ & - \langle\langle e^{in_2\phi_2 + in_3\phi_3} \rangle\rangle \langle\langle e^{in_1\phi_1} \rangle\rangle \,. \end{aligned} \tag{3.25}$$

The relation can be simplified by using properties of the azimuthal multi-particle correlation functions. Averaging over all collisions in the laboratory frame forces all non-isotropic correlations to average out to zero, since the symmetry plane of the collision does not have a preferred direction. Correlations are non-isotropic, or not invariant under transformations of the angles ϕ, if they do not fulfill the relation[120] $\sum_{j=1}^{k} n_j = 0$. This requirement is fulfilled for an even number of particles when all the harmonic indices of the multi-particle correlation function $n_1, \ldots, n_m$ for $m = 2k$ satisfy

$$n_1 = \cdots = n_k = -n_{k+1} = \cdots = -n_m \,. \tag{3.26}$$

In this case, the notation can be simplified to $c_{n_1,\ldots,n_m}\{m\} = c_n\{m\}$. $c_n\{m\}$ is known as the m-particle cumulant of harmonics n. For an odd-number of particles the relation can only be satisfied using mixed harmonic indices. They will be explored in section 3.3.3.

An additional feature of the azimuthal multi-particle correlation function is that the indices can be relabeled e.g. $\langle\langle e^{in(\phi_1-\phi_2)}\rangle\rangle = \langle\langle e^{in(\phi_2-\phi_1)}\rangle\rangle$, since the particle averages are performed over all possible arrangements. With the aforementioned simplifications, the two and four-particle cumulants are obtained

$$c_n\{2\} = \langle\langle 2\rangle\rangle_{n,-n} \tag{3.27}$$

$$c_n\{4\} = \langle\langle 4\rangle\rangle_{n,n,-n,-n} - 2\langle\langle 2\rangle\rangle_{n,-n}{}^2 \,. \tag{3.28}$$

Now relation between the flow coefficients and the multi-particle cumulants is demonstrated starting from eq. (3.27) and eq. (3.28) and using the cumulant expansion and the factorization of the PDF of flow. The azimuthal multi-particle correlations have contributions from flow as shown in eq. (3.13) and from non-flow sources.

Below, the contributions from non-flow sources are denoted by $\delta_{m,n}$ where m is the number of correlated particles and n is the harmonic index. Inserting all possible combinations of the flow and non-flow sources into the multi-particle correlations in eq. (3.27) and eq. (3.28) gives

$$\begin{aligned} c_n\{2\} &= \langle\langle 2\rangle\rangle_{n,-n} \\ &= \langle\langle e^{in(\phi_1-\Psi)} e^{in(\phi_2-\Psi)} + \delta_{2,n}\rangle\rangle \\ &= \langle v_n^2 + \delta_{2,n}\rangle \\ &= \langle v_n^2\rangle + \langle\delta_{2,n}\rangle \\ &\approx \langle v_n^2\rangle \qquad\qquad \big| \, \langle v_n^2\rangle \gg \langle\delta_{2,n}\rangle \end{aligned} \tag{3.29}$$

$$\tag{3.30}$$

$$
\begin{aligned}
c_n\{4\} &= \langle\langle 4\rangle\rangle_{n,n,-n,-n} - 2\langle\langle 2\rangle\rangle_{n,-n}{}^2 \\
&= \langle\langle e^{in(\phi_1-\Psi)}e^{in(\phi_2-\Psi)}e^{in(\phi_3-\Psi)}e^{in(\phi_4-\Psi)} + \delta_{4,n} + \\
&\quad + e^{in(\phi_1-\Psi)}e^{in(\phi_3-\Psi)}\delta_{2,n} + e^{in(\phi_1-\Psi)}e^{in(\phi_4-\Psi)}\delta_{2,n} \\
&\quad + e^{in(\phi_2-\Psi)}e^{in(\phi_4-\Psi)}\delta_{2,n} + e^{in(\phi_2-\Psi)}e^{in(\phi_3-\Psi)}\delta_{2,n} \\
&\quad + 2\delta_{2,n}^2\rangle\rangle - 2\langle\langle e^{in(\phi_1-\Psi)}e^{in(\phi_2-\Psi)} + \delta_{2,n}\rangle\rangle^2 \\
&= \langle v_n^4 + \delta_{4,n} + 4v_n^2\delta_{2,n} + 2\delta_{2,n}^2\rangle - 2\langle v_n^2 + \delta_{2,n}\rangle^2 \\
&= \langle v_n^4\rangle + \langle\delta_{4,n}\rangle + 4\langle v_n^2\delta_{2,n}\rangle + 2\langle\delta_{2,n}^2\rangle - 2\langle v_n^2\rangle^2 - 4\langle v_n^2\rangle\langle\delta_{2,n}\rangle - 2\langle\delta_{2,n}\rangle^2 \\
&\approx -\langle v_n^4\rangle + \langle\delta_{4,n}\rangle \qquad \big| \ \langle v_n^2\rangle^2 \approx \langle v_n^4\rangle \\
&\approx -\langle v_n^4\rangle\,. \qquad \big| \ \langle v_n^4\rangle \gg \langle\delta_{4,n}\rangle
\end{aligned}
\tag{3.31}
$$

The terms have been separated using the linearity of the expected values $\langle\langle X\rangle + \langle Y\rangle\rangle = \langle\langle X\rangle\rangle + \langle\langle Y\rangle\rangle$. To arrive at the final relation two assumptions have been made. First, the flow fluctuations have been assumed to be small $\langle v_n\rangle^k = \langle v_n^k\rangle$. Second, the non-flow correlations are assumed to be negligible $\delta_{m,n} \approx 0 \to \langle v_n^2\rangle \gg \langle\delta_{2,n}\rangle$. The validity of this approximation is explored in section 3.2.4.

With these approximations the v_n coefficients are given by

$$v_n\{2\} = \sqrt{c_n\{2\}} \tag{3.32}$$

$$v_n\{4\} = \sqrt[4]{-c_n\{4\}}\,. \tag{3.33}$$

Differences between $v_n\{2\}$ and $v_n\{4\}$ indicate contributions from flow fluctuations and non-flow. The relation between flow coefficients and cumulants can be generalized, which allows the calculation of flow by using any number of particles[121]

$$v_n\{2k\} = \sqrt[2k]{(-1)^{k-1}\frac{1}{M_k}c_n\{2k\}}, \text{ where } k \in \mathbb{N}_1\,, \tag{3.34}$$

where the coefficient M_k is related to the Bessel function[122] and can be calculated by

$$
\begin{aligned}
M_k &= \sum_{i=1}^{k-1}\binom{k}{i}\binom{k}{k-i}M_i M_{k-i} \\
M_1 &= 1\,.
\end{aligned}
$$

3.2.4 Contamination from Non-flow

As shown in eq. (3.29) and eq. (3.31) different non-flow sources can contribute to the different cumulants. In practice, the large number of involved processes makes an exact calculation and subtraction of all non-flow terms unfeasible. Therefore, it is important to study the robustness of the cumulants against non-flow biases. Correlations from non-flow can only bias the cumulant $c_n\{m\}$, if they cause a genuine m-particle correlation. By definition all

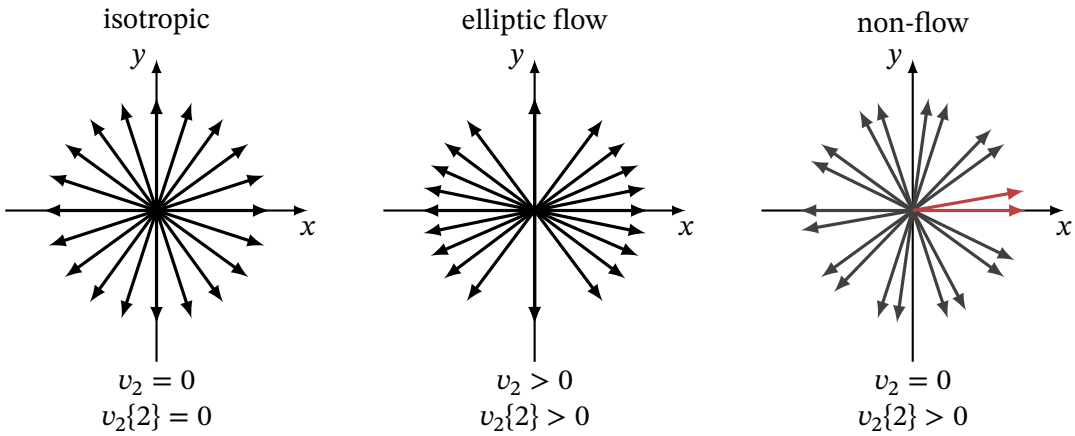

Figure 3.2: Sketch of unit flow vectors of 20 particles in a collision distributed according to an isotropic distribution on the left, a distribution including only elliptic flow in the middle, and a distribution including only non-flow correlations through 10 two-pronged decays.

contributions of fewer particles are removed. In this section the non-flow bias on $c_n\{2\}$ and $c_n\{4\}$ are compared. The scaling of this bias with the number of particles is estimated using combinatorics.

A correlation caused by a two-pronged decay can bias the two-particle cumulant. The right sketch in Figure 3.2 shows an example of zero elliptic flow v_2, but non-zero $v_n\{2\}$ due to these decays (a single pair is highlighted in red). The chance to find the first particle of the decay in a total of M particle is $1/M$. If it is found, the chance to find the second particle is $1/(M-1)$. Therefore, the total probability to find both particles of a single decay is $1/(M(M-1))$.

In the most extreme case, every particle is correlated to another due to $M/2$ two-particle decays. The probability to find the first particle from any decay is 1. The probability to find the corresponding second particle is $1/(M-1)$. Assuming numerous particles the total probability to find one of the $M/2$ two-particle decays is

$$\delta_{2,n} = \frac{1}{M-1} \approx \frac{1}{M} \,. \tag{3.35}$$

For the four particle cumulant similar arguments can be made. The probability to find four particles correlated through a non-flow sources is

$$\delta_{4,n} = \frac{1}{(M-1)(M-2)(M-3)} \approx \frac{1}{M^3} \,. \tag{3.36}$$

The chance to find two particles which are correlated through anisotropic flow is 1, because all particles are correlated to the common symmetry planes.

By comparing eq. (3.29) to eq. (3.35) and eq. (3.31) to eq. (3.36) a threshold for a stable estimate of the flow coefficients can be derived. For the two and four-particle cumulant the thresholds are

$$\langle v_n^2 \rangle \gg M^{-1} \qquad\qquad \langle v_n^4 \rangle \gg M^{-3} \,. \tag{3.37}$$

The four-particle cumulant shows a much weaker scaling with the number of particles than the two-particle cumulant. Therefore, a smaller bias from non-flow is expected at the same number of particles. It has been demonstrated in simulations, that the flow coefficients measured with more than two-particle cumulants only have negligible contributions from non-flow[123].

3.2.5 Cumulants from Flow Vectors

The computational complexity of the naïve approach of the multi-particle correlations using nested iterations scales with the particle multiplicity M to power of the number of particles m $\mathcal{O}(M^m)$. The solution to this problem is the direct calculation of cumulants from flow vectors including the subtraction of all autocorrelations[124]. This method only scales linearly in computational complexity with the number of particles $\mathcal{O}(M)$.

To derive the needed equations the correlations of the azimuthal angle of particles needs to be transformed into complex products of flow vectors. To illustrate this, the procedure is shown for the two-particle cumulant. The square of a flow vector can be written as

$$\begin{aligned} Q_{n,p}Q_{-n,p} &= \sum_{j,k}^{M} w_i^p w_j^p e^{in(\phi_j-\phi_k)} \\ &= \sum_{\substack{j,k \\ j\neq k}}^{M} w_i^p w_j^p e^{in(\phi_j-\phi_k)} + \sum_{\substack{j,k \\ j=k}}^{M} w_j^p w_k^p e^{in(\phi_j-\phi_k)} \\ &= \sum_{\substack{j,k \\ j\neq k}}^{M} e^{in(\phi_j-\phi_k)} + Q_{0,2p} \end{aligned} \tag{3.38}$$

Inserting into eq. (3.27) gives

$$c_n\{2\} = \langle \frac{Q_{n,1}Q_{-n,1} - Q_{0,2}}{Q_{0,1}Q_{0,1} - Q_{0,2}} \rangle \,. \tag{3.39}$$

All higher order cumulants can be constructed using the same procedure.

The number of terms, determined by the Bell numbers, quickly increases with the number of particles used in the cumulant. For the six particle cumulant already 877 unique terms are needed. The determination of the terms can be performed with a recursive algorithm for all number of particles[121]. The algorithm, shown in eq. (3.40), gives the numerator of the multi-particle correlation function denoted by $N(\langle m \rangle_{n_1,\ldots,n_m})$. The full correlation function is $\langle m \rangle_{n_1,\ldots,n_m} = N(\langle m \rangle_{n_1,\ldots,n_m})/N(\langle m \rangle_{0,\ldots,0})$. The additional parameters $p_1, \ldots, p_m$ of function F correspond to the powers of the weights. The algorithm gives a general solution for all combinations of harmonics $n_1, \ldots, n_m$.

Algorithm $N(\langle m\rangle_{n_1,\ldots,n_m}) = F(\langle m\rangle_{n_1,\ldots,n_m}\{p_1,\ldots,p_m\})$:

```
Initialize p_i ← 1, for all i in 1, ... m
if m = 1 then
    return Q_{n_1,p_1}
else
    C ← Q_{n_m,p_m} × F(⟨m − 1⟩_{n_1,...,n_{m−1}}{p_1, ... , p_{m−1}})
    if p_m ≤ 1 then
        for i ← 1 to m − 1 do
            C ← C − p_i × F(⟨m − 1⟩_{n_1,...,n_i+n_m,...,n_{m−1}}{p_1, ... , p_i +
              1, ... , p_{m−1}})
    return C
```

(3.40)

The closed form of the four-particle correlation function with harmonics $(n, n, -n, -n)$ obtained from the algorithm is

$$\begin{aligned}\langle 4\rangle_{n,n,-n,-n} &= N(\langle 4\rangle_{n,n,-n,-n})\big/N(\langle 4\rangle_{0,0,0,0}) \\ &= \langle Q_{n,1}Q_{n,1}Q_{-n,1}Q_{-n,1} + Q_{2n,2}Q_{-2n,2} \\ &\quad - Q_{n,1}Q_{n,1}Q_{-2n,2} - Q_{-n,1}Q_{-n,1}Q_{2n,2} \\ &\quad + 4Q_{n,1}Q_{-n,3} + 4Q_{-n,1}Q_{n,3} \\ &\quad + 2Q_{0,2}^2 - 4Q_{n,1}Q_{-n,1}Q_{0,2} - 6Q_{0,4}\rangle \\ &\quad \Big/\langle Q_{0,1}^4 - 6Q_{0,1}^2Q_{0,2} + 3Q_{0,2}^2 + 8Q_{0,1}Q_{0,3} - 6Q_{0,4}\rangle\,.\end{aligned} \tag{3.41}$$

Due to the choice of the harmonics indices the total number of terms reduce from 15 to 9. A mixture of flow vectors with different harmonic indices is required to fully subtract all autocorrelations.

First, the correlation functions obtained with the algorithm are averaged over all collisions using eq. (3.14). Next, the cumulants are determined from these averaged multi-particle correlations using eq. (3.22). Finally, The flow coefficients are calculated with these cumulants using eq. (3.34).

3.2.6 Differential Flow

Besides the calculation of the integrated flow coefficients, differential flow coefficients are also of interest to study the behavior in different kinematic regions. Using the regular method, shown in section 3.2.5, in only for a subset of particles greatly reduces the statistical precision, because only the information from the particles in that specific regions are used.

However, the precision of the measurement can be increased by dividing all measured particles into two groups. The first group, the particles of interest (POI), consists of only those particles that are in the kinematic region of interest. The second group, the reference particles (RFP), consists are the particles relative to which the flow coefficients are measured. There may be

overlap between the POI and the RFP. With this split between POI and RFP the differential azimuthal multi-particle correlation function $\langle m' \rangle$ can be written as

$$\langle m' \rangle_{n_1;n_2,\ldots,n_m} = \sum_{l_1}^{M_{POI}} \sum_{\substack{l_2,\ldots,l_m \\ l_1 \neq l_2 \neq \cdots \neq l_m}}^{M_{RFP}} e^{i(n_1\phi_{l_1}+\cdots+n_m\phi_{l_m})} \Bigg/ \sum_{l_1}^{M_{POI}} \sum_{\substack{l_1,\ldots,l_m \\ l_1 \neq \ldots \neq l_m}}^{M_{RFP}} 1 \,. \tag{3.42}$$

It is assumed the first particle of the correlation belongs to the POI and the other particles are part of the RFP.

To simplify the calculations the correlation function is expressed by flow vectors. For this purpose three different flow vectors are defined. The flow vector $P_{n,p}$ includes all the particles classified as POI

$$P_{n,p} = \sum_{k=1}^{M_{POI}} w_k^p e^{in\phi_k} \,. \tag{3.43}$$

The flow vector $R_{n,p}$ includes all the particles classified as RFP

$$R_{n,p} = \sum_{k=1}^{M_{RFP}} w_k^p e^{in\phi_k} \,. \tag{3.44}$$

Autocorrelations are subtracted using the flow vector $W_{n,p}$ of the intersection of POI and RFP

$$W_{n,p} = \sum_{k=1}^{M_{POI\cap RFP}} w_k^p e^{in\phi_k} \,. \tag{3.45}$$

Rewriting the numerator of the correlation function using the flow vectors gives

$$\begin{aligned} N(\langle 2' \rangle_{n;-n}) &= \sum_{j}^{M_{POI}} \sum_{j \neq k}^{M_{RFP}} e^{in(\phi_j - phi_k)} \\ &= \sum_{j}^{M_{POI}} w_j e^{in\phi_j} \sum_{k}^{M_{RFP}} w_k e^{-inphi_k} - \sum_{j=k}^{M_{POI\cap M_{RFP}}} w_j w_k e^{in(\phi_j - phi_k)} \\ &= P_{n,1} R_{-n,1} - W_{0,2} \,. \end{aligned} \tag{3.46}$$

All differential cumulants with an even number of particles are determined by the recursive relation[121]

$$d_n\{2k\} = \langle\langle 2k' \rangle\rangle_{n_1;n_2\ldots n_{2k}} - \sum_{p=1}^{k-1} \binom{n}{k} \binom{n-1}{k} d_n\{2(k-p)\} \langle\langle 2(k-p) \rangle\rangle_{n_1,n_2\ldots n_{2(k-p)}} \,. \tag{3.47}$$

Inserting eq. (3.46) into eq. (3.47) gives the two-particle differential cumulant

$$\begin{aligned} d_n\{2\} &= N(\langle\langle 2' \rangle\rangle_{n;-n}) \big/ N(\langle\langle 2' \rangle\rangle_{0;0}) \\ &= \langle P_{n,1} R_{-n,1} - W_{0,2} \rangle \big/ \langle P_{0,1} R_{0,1} - W_{0,2} \rangle \,. \end{aligned} \tag{3.48}$$

With the same approach also all other differential cumulants can be determined. The four-particle differential cumulant is

$$\begin{aligned} d_n\{4\} &= N(\langle\langle 4'\rangle_{n;n,-n,-n}\rangle)/N(\langle\langle 4'\rangle_{0;0,0,0}\rangle) \\ &= \big[\langle P_{n,1}R_{n,1}R_{-n,1}R_{-n,1} - W_{2n,2}R_{-n,1}R_{-n,1} \\ &\quad - P_{n,1}R_{n,1}R_{-2n,2} - 2R_{n,1}W_{0,2}R_{-n,1} - 2P_{n,1}R_{0,2}R_{-n,1} \\ &\quad + 4W_{n,3}R_{-n,1} + 2R_{0,2}W_{0,2} + 2R_{n,1}W_{-n,3} \\ &\quad + 2P_{n,1}R_{-n,3} + W_{2n,2}R_{-2n,2} - 6W_{0,4}\rangle\big] \\ &\quad \big/\big[\langle P_{0,1}R_{0,1}R_{0,1}R_{0,1} - 3W_{0,2}R_{0,1}R_{0,1} \\ &\quad - 3P_{0,1}R_{0,2}R_{0,1} + 6W_{0,3}R_{0,1} + 3R_{0,2}W_{0,2} \\ &\quad + 2P_{0,1}R_{0,3} - 6W_{0,4}\rangle\big] \,. \end{aligned} \tag{3.49}$$

The differential cumulants can be used in the case of no, partial, and full overlap of the RFP and POI. When there is a full overlap, the differential cumulant is identical to the regular cumulant. The relation of flow to the differential cumulants is given by

$$v_n'\{2k\} = \frac{(-1)^{k-1}}{M^{1/(2k)}} \frac{d_n\{2k\}}{[(-1)^{k-1}c_n\{2k\}]^{1-1/(2k)}} = \frac{d_n\{2k\}}{c_n\{2k\}} v_n\{2k\} \,, \tag{3.50}$$

where M_k is determined by eq. (3.35).

3.2.7 Pseudorapidity Separation

As shown in eq. (3.37) the flow measured with the two-particle cumulant is biased to a greater degree by non-flow than the four-particle cumulant. To reduce these contributions the method of differential cumulants is adapted to two regions separated in pseudorapidity. This pseudorapidity separation between the POI and RFP increases the suppression of non-flow[125,126]. Equation (3.48) reduces to

$$c_n\{2, |\Delta\eta| > X\} = \langle Q_{n,1}^{\eta_1} Q_{-n,1}^{\eta_2}\rangle \big/ \langle Q_{0,1}^{\eta_1} Q_{0,1}^{\eta_2}\rangle \,, \tag{3.51}$$

where Q^{η_i} is the flow vector in a given pseudorapidity window. The flow vector of the intersection $Q^{\eta_1 \cap \eta_2}$ vanishes because of there is no intersection between the POI and RFP. The amount of separation, often referred to a η-gap, is given by X.

In the analysis, a pseudorapidity gap of 1 is used which suppresses non-flow while simultaneously keep enough statistics to calculate the two particle cumulant[125]. A pseudorapidity symmetric selection is chosen. The elliptic flow, with a pseudorapidity gap of 1 can be written as

$$c_2\{2, |\Delta\eta| > 1\} = \frac{\langle Q_2^{\eta<0.5} Q_{-2}^{\eta>0.5}\rangle}{\langle Q_0^{\eta<0.5} Q_0^{\eta>0.5}\rangle} \,. \tag{3.52}$$

3.3 Flow Coefficients Relative to the Spectator Plane

The cumulant method is used primarily with detectors that can reconstruct individual particles, or have a high segmentation. In typical experiments, this limits the acceptance of the detectors to the mid-rapidity region. Detectors with very forward acceptance usually have only limited granularity. Therefore, a different method, known as the scalar product method[123], is used when measuring the flow of the POI relative to the RFP measured by such a forward detector.

3.3.1 Scalar Product Method

The scalar product method correlates the flow vector p_n of the POI with the flow vector r_n of the RFP to determine the flow coefficient

$$v_n\{p_n \cdot r_{-n}\} = \frac{v_{n,obs}}{\mathcal{R}} = \frac{\langle p_n r_{-n}\rangle}{\mathcal{R}(r_n)}\,, \tag{3.53}$$

To suppress non-flow it can be used with two different detectors which have a large pseudorapidity separation. The numerator called the observed flow $v_{n,obs}$. The observed flow needs to be corrected for the resolution of the RFP flow vector $\mathcal{R}(r_n)$. The resolution can be estimated using different methods, for example the three sub-events method[127]

$$\mathcal{R}(r_n) = \sqrt{\frac{\langle r_n s_{-n}\rangle\langle r_n t_{-n}\rangle}{\langle s_n t_{-n}\rangle}}\,, \tag{3.54}$$

which involves combinations of correlations of the reference flow vector with two other flow vectors.

3.3.2 Mixed Harmonics

In the standard scalar product method the RFP flow vector has the same harmonic as the POI flow vector. When the harmonic of the two flow vectors in eq. (3.53) is not the same, for example for p_2 and r_1, the isotropy relation is not fulfilled and the average vanishes. Therefore, to measure the second flow harmonic coefficient relative to a first harmonic symmetry plane a second RFP flow vector needs to be included. With two first harmonic RFP flow vectors (q_{-1} and r_{-1}), and one second harmonic POIflow vector (p_2) the isotropy relation is fulfilled $2 - 1 - 1 = 0$. Hence, the anisotropic flow harmonic coefficient v_{2n} is given by

$$v_{2n}\{p_{2n} \cdot q_{-n} \cdot r_{-n}\} = \frac{v_{2n,obs}}{\mathcal{R}} = \frac{\langle p_{2n} q_{-n} r_{-n}\rangle}{\mathcal{R}(q_n r_{-n})}\,. \tag{3.55}$$

The resolution correction can be deduced from the average over all possible reaction plane orientations

$$\langle p_{2n} q_{-n} r_{-n}\rangle = \int_0^{2\pi} \frac{d\Psi_{RP}}{d2\pi}\, p_{2n} q_{-n} r_{-n} = v_{2n,POI} v_{n,RFP}^2 \tag{3.56}$$

$$\langle q_n r_{-n}\rangle = \int_0^{2\pi} \frac{d\Psi_{RP}}{d2\pi}\, q_n r_{-n} = v_{n,RFP}^2\,, \tag{3.57}$$

where $v_{n,RFP}$ is the flow coefficient of the RFP, and $v_{n,POI}$ is flow coefficient of the POI. Therefore, the correlation averaged over all collisions between the two reference detector can be used as a resolution correction. The complex product of the observed flow $v_{n,obs}$ in eq. (3.55) yields four real and nonzero components To simplify the notation a short notation using the flow vector components is used (e.g. $\langle p_{2n,x} q_{-n,x} r_{-n,x} \rangle = \langle x_{2n} x_{-n} x_{-n} \rangle$). The different components are

$$\begin{aligned} v_{2n,obs}\{p_{2n} \cdot q_{-n} \cdot r_{-n}\} &= \langle p_{2n} q_{-n} r_{-n} \rangle \\ &= \langle x_{2n} x_{-n} x_{-n} \rangle - \langle x_{2n} y_{-n} y_{-n} \rangle + \langle y_{2n} x_{-n} y_{-n} \rangle + \langle y_{2n} y_{-n} x_{-n} \rangle \,. \end{aligned} \tag{3.58}$$

All terms are statistically independent and give an independent estimate of the observed flow coefficients. For the first two terms the resolution correction can be calculated using eq. (3.57). The flow coefficient v_{2n} is given by

$$v_{2n}\{p_{2n} \cdot q_{-n} \cdot r_{-n}\} = \frac{\langle x_{2n} x_{-n} x_{-n} \rangle}{2\langle x_n x_{-n} \rangle} = \frac{\langle x_{2n} y_{-n} y_{-n} \rangle}{-2\langle y_n y_{-n} \rangle} \,. \tag{3.59}$$

Where the relations

$$\langle x_n x_{-n} \rangle = \langle y_n y_{-n} \rangle = \frac{1}{2} v_{n,RFP}^2 \tag{3.60}$$

and

$$\langle x_{2n} x_{-n} x_{-n} \rangle = \langle x_{2n} y_{-n} y_{-n} \rangle = \langle y_{2n} x_{-n} y_{-n} \rangle = \langle y_{2n} y_{-n} x_{-n} \rangle = \frac{1}{4} v_{2n,POI} v_{n,RFP}^2 \tag{3.61}$$

have been used. For the third and fourth terms the correlation between x and y component of the q and r flow vectors cannot be used directly, because there is no signal expected in these correlations. Therefore, the geometric mean of the nonzero correlations $\langle x_n x_{-n} \rangle$ and $\langle y_n y_{-n} \rangle$ is used as a resolution correction instead

$$\mathcal{R}(geo) = \sqrt{4\langle x_n x_{-n} \rangle \langle y_n y_{-n} \rangle} \,. \tag{3.62}$$

The product of the third and fourth terms of eq. (3.58) is divided by the geometric mean of the resolution

$$v_{2n}\{p_{2n} \cdot q_{-n} \cdot r_{-n}, geo\} = \sqrt{\frac{\langle y_{2n} x_{-n} y_{-n} \rangle \langle y_{2n} y_{-n} x_{-n} \rangle}{4\langle x_n x_{-n} \rangle \langle y_n y_{-n} \rangle}} \,. \tag{3.63}$$

This component is called the mixed component.

In the analysis this mixed harmonics method is applied using particles reconstructed as tracks with the ALICE central barrel tracking (q^{Tr}) and two reference flow vectors measured with the ZNA and ZNC (q^{ZNA}, q^{ZNC}). The results obtained with the eq. (3.59) and eq. (3.63) are averaged to increase the statistical precision. Thus, the elliptic flow coefficient relative to the neutron spectators measured with the ZDC can be written as

$$\begin{aligned} v_2\{\Psi_{SP}\} = \frac{1}{3} \Bigg(& \frac{\langle x_2^{Tr} x_{-1}^{ZNA} x_{-1}^{ZNC} \rangle}{2\langle x_1^{ZNA} x_{-1}^{ZNC} \rangle} + \frac{\langle x_2^{Tr} y_{-1}^{ZNA} y_{-1}^{ZNC} \rangle}{-2\langle y_1^{ZNA} y_{-1}^{ZNC} \rangle} \\ & + \sqrt{\frac{\langle x_2^{Tr} x_{-1}^{ZNA} x_{-1}^{ZNC} \rangle \langle x_2^{Tr} y_{-1}^{ZNA} y_{-1}^{ZNC} \rangle}{4\langle x_1^{ZNA} x_{-1}^{ZNC} \rangle \langle y_1^{ZNA} y_{-1}^{ZNC} \rangle}} \Bigg) \,. \end{aligned} \tag{3.64}$$

3.3.3 Relation to Multi-Particle Correlations

It can be shown that the method of scalar product and mixed harmonics is related to the cumulant method from section 3.2. As an example the relation to the mixed harmonics is shown. The 3-particle cumulant is

$$c_n\{3\} = \langle Q_{n_1,1}Q_{n_2,1}Q_{n_3,1} - Q_{n_1+n_2,2}Q_{n_2,1} - Q_{n_2,1}Q_{n_1+n_3,2} - Q_{n_1,1}Q_{n_2+n_3,2} + 2Q_{n_1+n_2+n_3,3}\rangle \Big/ \langle Q_{0,1}Q_{0,1}Q_{0,1} - Q_{0,2}Q_{0,1} - Q_{0,1}Q_{0,2} - Q_{0,1}Q_{0,2} + 2Q_{0,3}\rangle \tag{3.65}$$

To satisfy the isotropy relation the harmonics are chosen to be $2n_1 = -n_2 - n_3$. As a next step, the Flow vector Q is split into 3 parts. The double harmonic flow vector of the POI P_{2n}, and the single harmonic flow vectors of the RFP R_n and S_n. Because they have no intersection with each other, all the terms with autocorrelations are eliminated

$$\begin{aligned} P \neq R \rightarrow \quad & Q_{n_1+n_2,2}Q_{n_2,1} = 0 \\ R \neq S \rightarrow \quad & Q_{n_2+n_3,2}Q_{n_1,1} = 0 \\ P \neq S \rightarrow \quad & Q_{n_1+n_3,2}Q_{n_2,1} = 0 \\ P \neq R \neq S \rightarrow \quad & Q_{n_1+n_2+n_3,3} = 0\,. \end{aligned} \tag{3.66}$$

This reduces eq. (3.65) to the differential three-particle cumulant without intersection

$$d_{2n}\{3\} = \langle P_{2n,1}R_{-n,1}S_{-n,1}\rangle \Big/ \langle P_{0,1}R_{0,1}S_{0,1}\rangle\,. \tag{3.67}$$

The two-particle cumulant is also needed to calculate the differential flow, it reduces to

$$c_n\{2\} = \langle R_{n,1}S_{-n,1}\rangle \Big/ \langle R_{0,1}S_{0,1}\rangle\,. \tag{3.68}$$

Dividing eq. (3.67) by eq. (3.68) yields the same as eq. (3.59).

3.4 Event-shape Engineering

In addition to the classification of collisions based on their centrality it is also of interest to study collisions with specific geometries. One possible way to perform such an event shape selection is to use the flow vector of a subset of the collision and study the observable of interest in another subset[128]. A minimum of two subsets are needed to prevent autocorrelations. These subsets of particles are assigned by their kinematic region. The flow vector Q_n is usually normalized to the square root of the number of particles M that were used to calculate the flow vector

$$q_{n,ese} = Q_n/\sqrt{M}\,. \tag{3.69}$$

For every event the reduced flow magnitude $|q_{n,ese}|$ is calculated. The distribution of the reduced flow vector magnitudes $|q_{n,ese}|$ is then divided into percentiles. The percentiles can be obtained by inverting the cumulative distribution function of $|q_{1,ese}|$. The cumulative distribution function $P(q)$ of a distribution $p(q)$ is given by the integral

$$P(q) = \int_{-\infty}^{q} p(t)dt\,. \tag{3.70}$$

Therefore, the percentile $p_{\%}$ of a given $|q_{1,ese}|$ is given by

$$p_{\%} = P^{-1}(|q_{1,ese}|) \tag{3.71}$$

Besides flow fluctuations also the centrality of the collision can influence the observed flow. To suppress biases due to variations of the flow within a collision centrality, the sample of collisions is divided into 1 % centrality classes before the reduced flow vector magnitude percentiles are calculated. The observable of interest is then studied in classes of the percentiles or ESE-selected samples where for example the largest 10 % is referred as $P(|q_{n,ese}|) > 0.9$. The sample without any selection is called the unbiased sample. To increase statistical precision, the centrality classes can be merged after the percentiles have been calculated. Using this formalism, the elliptic flow can be studied in the percentile classes by looking at the ratios

$$\frac{v_2\{\text{ESE} - \text{selected}\}}{v_2\{\text{unbiased}\}}\,, \tag{3.72}$$

where the ESE-selection is performed using a selection such as $P(|q_{n,ese}|) > 0.9$.

3.5 Non-uniform Acceptance Corrections

Non-uniform acceptance of detectors bias the measurement of flow coefficients; therefore they need to be corrected. The corrections can be applied on the distribution of particles, or on the distribution of the flow vectors. Except for the correction of the reconstruction efficiency these corrections can be determined from quantities averaged over many collisions using the data itself.

3.5.1 Track Reconstruction Efficiency Correction

If the reconstruction efficiency of the particles depends on the transverse momentum of the particles, the integrated flow vectors are biased. The particle weights, introduced in section 3.5, can also be used to re-weight the transverse-momentum composition of particles in the flow vector. The procedure uses the track reconstruction efficiency from a Monte Carlo simulation to re-weight the tracks of different transverse momentum

$$w_\epsilon(p_\mathrm{T}, ...) = N_{generated}(p_\mathrm{T}, ...)/N_{reconstructed}(p_\mathrm{T}, ...), \tag{3.73}$$

where N are the number of generated and measured particles in the corresponding p_T window. The reconstruction efficiency may depend on further particle properties, such as particle identity. This correction requires that the relative track reconstruction efficiency of single particles of data is reproduced by the Monte Carlo simulation.

3.5.2 Azimuthal Non-uniformity

For azimuthal non-uniformity acceptance the corrections can be applied using the re-weighting of particles, or using corrections of the flow vector distribution. Both methods will be introduced in the following sections.

3.5.3 Particle Weights

Non-uniform acceptance of particles in a detector can be corrected using particle weights during the construction of the flow vector eq. (3.3). In general, these weights can be calculated from the inverse efficiency ε of the detector

$$w_{\alpha\times\epsilon}(\phi, \eta, \text{PID}, ...) = 1/\epsilon(\phi, \eta, \text{PID}, ...) \,. \tag{3.74}$$

If the transverse momentum dependent track reconstruction efficiency $\epsilon(p_\text{T}, \text{PID})$ can be factorized with the acceptance of particles $\alpha(\phi, \eta, ...)$

$$\epsilon_{\alpha\times\epsilon}(\phi, p_\text{T}, \eta, \text{PID}, ...) = \alpha(\phi, \eta, ...) \times \epsilon(p_\text{T}, \text{PID}) \,, \tag{3.75}$$

the azimuthal non-uniformity correction can be calculated individually. A separate transverse momentum dependent particle weight can be applied using the procedure explained in section 3.5.1. The relative acceptance α of the detector can be calculated comparing the number of tracks N in a given window of ϕ to the maximum N measured for any ϕ . Because the detector performance may depend on more variables than ϕ, additional dependences are introduced. If the acceptance depends on pseudorapidity η, the pseudorapidity acceptance may be divided into several regions $\eta_1, \eta_2, ..., \eta_n$. In each of the regions, the acceptance needs to be calculated separately according to

$$\alpha(\phi, \eta_i, ...) = N(\phi, \eta_i, ...) \Big/ \max(N(\phi, \eta_i, ...)) \,. \tag{3.76}$$

For tracking detectors, this procedure is also known as *φ-weights*.

The procedure equivalently applies to segmented detectors, where the angle of the center of mass of the channel ϕ_{ch} and average channel amplitudes N_{ch} are used. For segmented detectors the procedure is called *gain equalization*. In the case of no other dependence, the acceptance factor is given by

$$\alpha(\phi_{ch}) = N_{ch}(\phi_{ch}) \Big/ N_{ch,ref}(\phi_{ch,ref}) \,, \tag{3.77}$$

where $N_{ch,ref}(\phi_{ch,ref})$ is the average amplitude of a reference channel used as a normalization. Alternative schemes exist, where instead of a reference channel $N_{ch,ref}(\phi_{ch,ref})$, the maximum amplitude, or an average of all channel amplitudes are used.

3.5.4 Flow Vector Corrections

Detector non-uniformities can also be treated on the level of the flow vectors. The following procedure was introduced in ref.[129]. The advantages compared to re-weighting of the azimuthal particle spectra is that the procedure also works with detectors that have holes in the azimuthal acceptance. The necessary correction factors can be fully determined from the data itself. Monte Carlo simulations are not needed. The corrections can be derived from the effect of a normalized acceptance function $A(\phi)$ on the average of collisions with a fixed

reaction plane of an arbitrary function $f(\phi)$

$$\langle f \rangle_{RP} = \int d\phi A(\phi) f(\phi) \rho(\phi - \Psi_{RP}) \tag{3.78}$$

$$= \int d\phi A(\phi) f(\phi) (1 + 2 \sum_{m=1}^{\infty} \cos(n(\phi - \Psi_{RP}))) \tag{3.79}$$

$$= \overline{f} + 2 \sum_{m=1}^{\infty} v_m \left(\overline{fx}_n \cos(m\Psi_{RP}) + \overline{fy}_n \sin(m\Psi_{RP}) \right) . \tag{3.80}$$

$\overline{f}$ represents the acceptance average

$$\overline{f} = \int \frac{d\phi}{2\pi} A(\phi) f(\phi) . \tag{3.81}$$

The factors $\overline{x}_n$ and $\overline{y}_n$ are the n$^{\text{th}}$ harmonic coefficient of the Fourier series of the acceptance function

$$A(\phi) = 1 + 2 \sum_{n=1}^{\infty} \overline{x}_n \cos(n\phi) + \overline{y}_n \sin(n\phi) . \tag{3.82}$$

An important observation is that the averages over many collisions corresponds to the average over the acceptance

$$\langle f \rangle = \frac{\int d\Psi_{RP} d\phi A(\phi) f(\phi) \rho(\phi - \Psi_{RP})}{\int d\Psi_{RP} d\phi A(\phi) \rho(\phi - \Psi_{RP})} = \overline{f} , \tag{3.83}$$

as long as the reaction plane is uniformly distributed in the data sample. To guarantee this in the experiment the collision centrality is selected with azimuthally uniform detectors.

Equation (3.78) can be written separately for the x and y components of the unit flow vector.

$$\langle x \rangle_{\Psi_{RP}} = \overline{x}_n + v_n a_{2n}^{+} \Big(\cos(n\Psi_{RP}) + \lambda_{2n}^{s+} \sin(n\Psi_{RP}) + \sum_{n \neq m}^{\infty} \left([\lambda_{n-m}^{c+} + \lambda_{n+m}^{c+}] \cos(m\Psi_{RP}) + [\lambda_{n+m}^{s+} - \lambda_{n-m}^{s+}] \sin(m\Psi_{RP}) \right) \Big) \tag{3.84}$$

$$\langle y \rangle_{\Psi_{RP}} = \overline{y}_n + v_n a_{2n}^{-} \Big(\sin(n\Psi_{RP}) + \lambda_{2n}^{s-} \cos(n\Psi_{RP}) + \sum_{n \neq m}^{\infty} \left([\lambda_{n-m}^{c-} - \lambda_{n+m}^{c-}] \sin(m\Psi_{RP}) + [\lambda_{n+m}^{s-} + \lambda_{n-m}^{s-}] \cos(m\Psi_{RP}) \right) \Big) . \tag{3.85}$$

With the newly introduced acceptance coefficient

$$a_{2n}^{\pm} = 1 \pm \overline{x}_{2n} \tag{3.86}$$

and smallness parameters

$$\lambda_{m \mp n}^{x\pm} = \frac{v_m}{v_n} \frac{\overline{x}_{m \mp n}}{a_{2n}^{\pm}}, \quad \lambda_{m \mp n}^{y\pm} = \frac{v_m}{v_n} \frac{\overline{y}_{m \mp n}}{v_n a_{2n}^{\pm}} . \tag{3.87}$$

The identities

$$x_n = \overline{\cos(n\phi)} \quad \text{and} \quad y_n = \overline{\sin(n\phi)}\,, \tag{3.88}$$

and the trigonometric relations

$$2(\cos(n\phi))^2 = 1 + \cos(2n\phi) \quad \text{and} \quad 2\cos(n\phi)\sin(n\phi) = \sin(2n\phi) \tag{3.89}$$

have been used to simplify eq. (3.85) and eq. (3.85).

In general, all terms of eq. (3.85) and eq. (3.85) are required. Therefore, the equations also depend on ratios of the flow coefficients according to eq. (3.87). The magnitude of the terms with $n \neq m$ depends on the smallness parameters. As long as either harmonic n is dominant $v_n \gg v_{m\neq n}$, or the acceptance corrections for harmonics m are small $\overline{y}_{m\mp n}/a^{\pm}_{2n}, \overline{x}_{m\mp n}/a^{\pm}_{2n} \ll 1$, the terms for $n \neq m$ can be neglected. In experiments the dominance of the elliptic flow is observed for all but very central collisions[130,131]. Due to fluctuations of the initial state a different hierarchy is observed in this class of collisions[132,133]. With these observations in the following the terms for $n \neq m$ will be neglected.

The corrections can also be generalized to a generic normalized flow vector q_n with the components x_n and y_n. Using the above-mentioned simplifications

$$\langle x_n \rangle_{\Psi_{RP}} = \overline{x}_n + v_n a^{+}_{2n}\big(\cos(n\Psi_{RP}) + \lambda^{s+}_{2n}\sin(n\Psi_{RP})\big) \tag{3.90}$$

$$\langle y_n \rangle_{\Psi_{RP}} = \overline{y}_n + v_n a^{-}_{2n}\big(\sin(n\Psi_{RP}) + \lambda^{s-}_{2n}\cos(n\Psi_{RP})\big) \tag{3.91}$$

is obtained, where $a^{\pm}_{2n}$ and $\lambda^{x\pm}_{m\mp n}$ are the equivalent quantities which calculated according to the flow vector q_n. Equation (3.8) can be recovered by applying three successive correction steps. The correction factors (the mean, acceptance coefficients, and smallness parameters) are calculated during the first pass over the data. In the second pass they are applied in each collision. The different correction steps are explained in detail below.

Re-centering

A static shift of the detector signals can manifest in a shift of the average flow vector away from the origin. This shift can be removed by subtracting the mean flow vector from the flow vector in each collision

$$\begin{aligned} x'_n &= x_n - \overline{x}_n \\ y'_n &= y_n - \overline{y}_n\,. \end{aligned} \tag{3.92}$$

Diagonalization

The flow vector distribution can appear twisted, if $\sin(n\Psi_{RP})$, or $\cos(n\Psi_{RP})$ terms bias the x_n, or y_n component of the flow vectors. The diagonalization corrections are calculated from the averaged flow vector components with the double harmonic $\overline{x}_{2n}$ and $\overline{y}_{2n}$. The corrected flow vector components in each event are obtained by

$$\begin{aligned} x''_n &= \frac{x'_n - \lambda^{y-}_{2n} y'_n}{1 - \lambda^{y-}_{2n}\lambda^{y+}_{2n}} \\ y''_n &= \frac{y'_n - \lambda^{y+}_{2n} x'_n}{1 - \lambda^{y-}_{2n}\lambda^{y+}_{2n}}\,. \end{aligned} \tag{3.93}$$

Rescaling

A squashed flow vector distribution, which corresponds to different widths in the x and y direction, can be corrected with the rescaling correction. The corrected flow vector components in each event are obtained by

$$\begin{aligned} x_n''' &= \frac{x_n''}{a_{2n}^+} \\ y_n''' &= \frac{y_n''}{a_{2n}^-} \,. \end{aligned} \tag{3.94}$$

3.5.5 Multidimensional Corrections

The distortions of the flow vector caused by the detector non-uniformity can depend on many parameters. These parameters can be the parameters of interesting physics, such as the centrality of the collision. They can also be nuisance parameters, which do not show up in the result and are possibly specific to the experiment, such as the position of the collision in the detector.

In addition to these quantities of the collision, flow can also be studied dependent on the parameters of single particles, such as their momentum, or particle type. To achieve this the differential flow vector is grouping only particle inside a given region of interest together.

However, as the exact origin of the distortion of the flow vectors is often not known, possible correlated effects of all parameters need to be taken into account. This necessitates multi-dimensional corrections of the flow vector.

Figure 3.3 shows the method of the multi-dimensional corrections. The first step is the creation of the flow vectors in each collision. The particles are grouped into the flow vectors according to the "particle-type" parameters. Afterwards, all the collisions are grouped to according to the "collision-type" parameters. The mean value of the flow vector is calculated in all $(p_\mathrm{T}, \eta, \text{centrality}, \text{time})$ regions separately. In the final step, re-centering is performed by subtracting the mean value (arrow 2) from uncorrected flow vector (arrow 1) q_n in each $(p_\mathrm{T}, \eta, \text{centrality}, \text{time})$. The corrected flow vector are obtained (arrow 3) and then passed on to the correlation analysis (arrow 4). The total dimension of the correction is

$$N_\mathrm{dim}(\text{total}) = N_\mathrm{dim}(\text{particles}) \times N_\mathrm{dim}(\text{collision}) \,.$$

3.5.6 Software Implementation

The formalism has been implemented in a software framework known as *FlowVectorCorrections* FlowVectorCorrections. It implements corrections with a multi-dimensional dependence on properties of the collisions. It used in the ALICE experiment for different physics analyses[98,134].

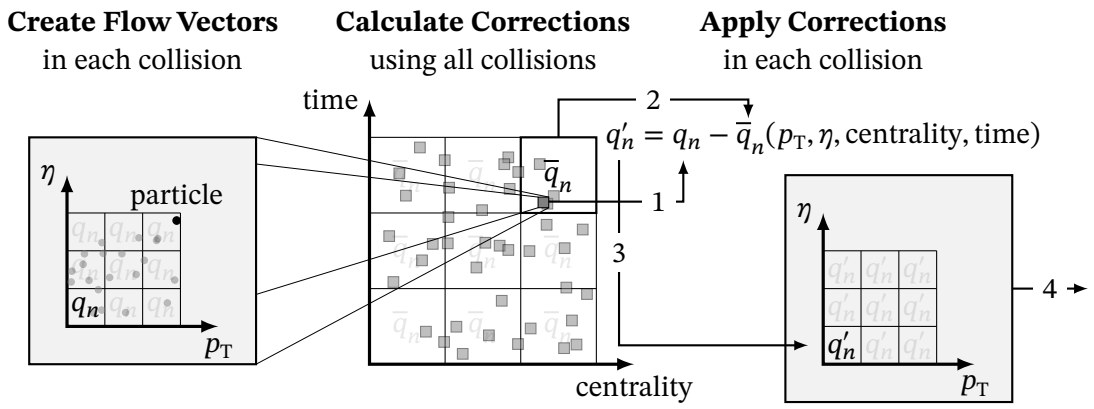

Figure 3.3: Sketch of the multi-dimensional correction procedure. As an example the re-centering correction as a function of p_T, η, centrality, and time is shown.

As part of this work, this software framework was extended and generalized. This new general framework is called *QnTools*[135,1]. The extensions allow to perform the corrections of differential flow vectors, which may depend on a number of particle properties $q_n(p_T, \eta, \text{PID}, ...)$. These differential corrections were not easily performed with the previous framework. An analysis framework is also provided. This allows to perform the physics analysis in terms of flow vectors and event properties, without dependence on the explicit implementation of different experiments. The analysis framework also includes the calculation of several commonly used observables. It takes care of correlated statistical errors using an integrated bootstrapping algorithm. An integration with the high level data analysis framework of ROOT, the RDataFrame, is offered which allows to express the analysis with high level functions, while automatically implementing low level performance optimizations. The *QnTools* framework has also been adopted in the data analysis by different experiments[136–139].

3.5.7 Monte Carlo Study

To study the effects of the corrections a simple Monte Carlo simulation is used. Particles are generated according to eq. (3.5) with given flow coefficient $v_1 = 0.2$ and particle multiplicity $M = 2500$. In this approach no transverse momentum or pseudorapidity dependence is assumed, only the azimuthal distribution of particles is simulated. The particles are measured using two simulated detectors. A tracking detector with perfect acceptance is used for the POI and two segmented detectors with 32 channels each are used to detect the RFP, and calculate the three sub-event resolution. Different acceptance biases are applied to the RFP detector. The flow coefficients are calculated using the scalar product method shown in eq. (3.53). The resolution correction is applied using the three sub-event method shown in eq. (3.54). Flow fluctuations and non-flow are not included in the simulation.

Figure 3.4 shows the impact of the different correction steps on a flow vector distribution generated with a simple Monte Carlo simulation. The distribution has the shape of an ellipse, because fluctuations of the flow magnitude are not included in the model. This model also allows simulating how well the corrections correct the bias on flow observables.

Figure 3.5 shows the impact on directed flow $v_1\{q_{POI} \cdot q_{RFP}\}$ calculated with two different flow vectors. The tracking detector measuring the POI has an azimuthally uniform acceptance. The acceptance of the segmented detector measuring the RFP is subject to the non-uniform bias. The colored lines correspond to different biases, which maximize the impact of different correction steps. In all cases, the input flow coefficient from the Monte Carlo simulations is reconstructed, if all necessary corrections are applied. The re-centering correction has the leading contribution, when all biases are convoluted.

In a real experiment, the detector azimuthal anisotropy may depend on many properties, such as time, centrality, position of the primary vertex. There may also be a correlated effect between these variables. To take into account the correlations the corrections need to be performed in small regions of this multi-dimensional parameter space. The impact of the corrections on real data is shown in section 4.5.

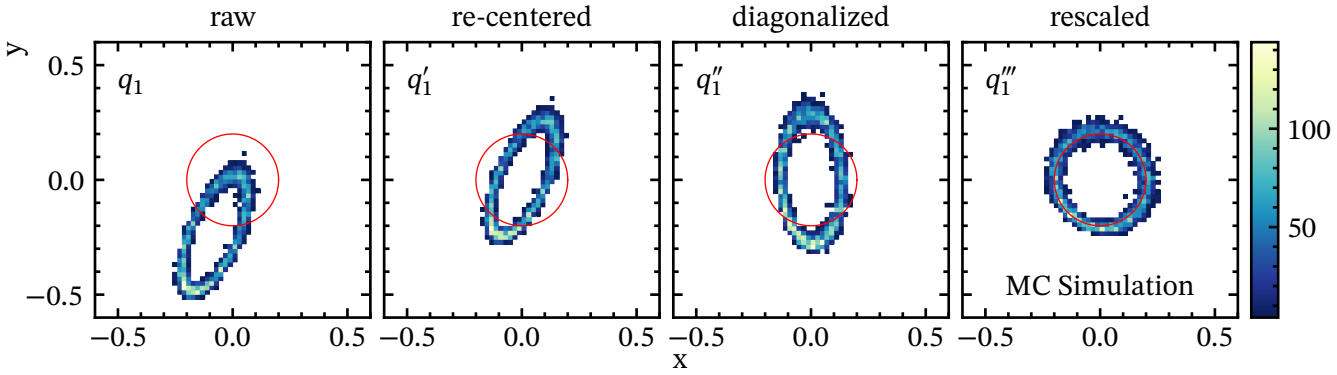

Figure 3.4: Two-dimensional distributions of a flow vector from a detector with strongly non-uniform acceptance after different corrections are applied. The two-dimensional shows the distribution obtained from a simple Monte Carlo simulation. The red circle shows the expected flow vector without statistical fluctuations due to limited number of particles for a flow coefficient $v_1 = 0.2$.

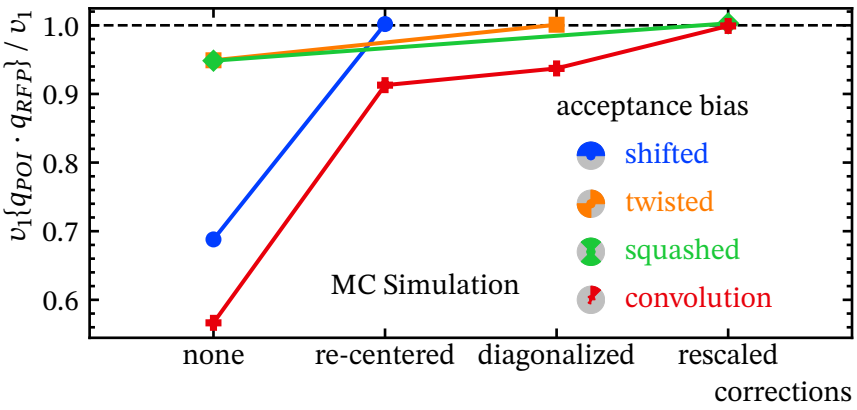

Figure 3.5: Ratio of reconstructed flow $v_1\{q \cdot q_{bias}\}$ over expected flow of $v_1 = 0.2$, where one flow vector in the scalar product method has been biased by a non-uniform acceptance of the detector. The x-axis corresponds to the different corrections which are applied. The colored pie charts show the detector non-uniformity corresponding to the lines of the same color.

4 Data Analysis

In this chapter, the data analysis is explained. First, the selection of data samples and MC simulation is introduced. Second, the event and track selections are described. Then, the necessary corrections to reduce biases in the measurements are shown. The selection of collisions using the event-shape engineering technique is explained. The calculations of the initial state using the T$_\mathrm{R}$ENTo simulation are shown. A fit of the EPM is performed to flow coefficients measured with the multi-particle cumulant method to extract the initial eccentricities. The performance of the ZDC in all heavy-ion data samples is presented and the impact on the analysis is explained. The analysis of the systematic uncertainties of the measurements is explained and the different contributions to the systematic uncertainties are summarized.

4.1 Data Samples

For this study two different data samples are used. The larger sample contains data of 14×10^6 symmetric collisions of lead (^{208}Pb) ions at $\sqrt{s_{\mathrm{NN}}} = 2.76\,\mathrm{TeV}$. It was recorded during the first heavy-ion data-taking period of the LHC at the end of 2010. The second smaller sample contains data of 13×10^5 symmetric collisions of xenon (^{129}Xe) ions at $\sqrt{s_{\mathrm{NN}}} = 5.44\,\mathrm{TeV}$. It was recorded during a short break in the pp data-taking period of the LHC in 2017. Using this unique data set allows to compare the features observed in collisions of intermediate-mass ions with those of the heavy lead ions. An extensive evaluation of the neutron ZDC performance during the heavy-ion data-taking and the reasons for limiting the analysis to the two aforementioned periods is discussed in section 4.7.

Table 4.1: Heavy-ion data samples recorded in LHC run 1 and run 2. The periods selected for the physics analysis are shown in bold. The events column lists the number of minimum bias triggered collisions available for physics analysis. The number of events of the data samples from 2011 and 2018 show the sum of minimum bias, central and semi-central triggered events.

LHC Run	Year	System	$\sqrt{s_{\mathrm{NN}}}$ (TeV)	Events / 10^6	β^* (m)	crossing angle α (μrad)
1	**2010**	**Pb-Pb**	**2.76**	**14.2**	**3.5**	**0**
	2011	Pb-Pb	2.76	49†	1.0	60
2	2015	Pb-Pb	5.02	78.4	0.8	60
	2017	**Xe-Xe**	**5.44**	**1.3**	**10.0**	**60**
	2018	Pb-Pb	5.02	260†	0.5	60

†The events are split into minimum bias, central, and semi-central triggers.

4.2 Monte Carlo Simulation Samples

Besides the analysis of the experimental data, also data from Monte Carlo simulations are utilized. In particular, the track reconstruction efficiency which depends on the transverse-momentum of the particle is extracted from the Monte Carlo simulations as shown in section 3.5.1. To achieve this, complete simulations of the event generation and propagation through the material are performed by the ALICE collaboration. For this analysis, HIJING event generators are used for both collision systems. HIJING is a Monte Carlo event generator built to reproduce the particle production in high energy heavy-ion collisions[140]. It does not include any interactions in the medium besides energy-loss of jets and therefore does not reproduce the collective behavior of the particles (such as elliptic flow). After the particle generation, the interaction with the detector is simulated using GEANT[141].

Table 4.2: Monte Carlo simulations used to calculate the track reconstruction efficiency.

System	$\sqrt{s_{\mathrm{NN}}}$ (TeV)	Generator	Events / 10^5
Pb-Pb	2.76	Hijing	6.0
Xe-Xe	5.44	Hijing	7.6

4.3 Event Selection

In the following section the event selection of the data analysis in both Pb-Pb and Xe-Xe data is explained. This selection ensures the quality of the reconstruction and the selection of hadronic interaction events, through the rejection of background events and is part of the standard data preparation for physics analyses in ALICE[98].

Besides the hadronic interaction of interest, the colliding ions can also interact via the electromagnetic interaction. The events from electromagnetic interactions have a much larger cross section than hadronic interactions at LHC collision energies. However, much fewer particles are produced in an electromagnetic interaction event, such as electromagnetic dissociation, which causes one nucleus to emit a single neutron. Because the multiplicity of produced particles is low, these events only contribute to the very peripheral centrality classes. In this analysis they can be removed by excluding peripheral events with a centrality larger than 90%. During the Xe-Xe data-taking the trigger was tuned to reject the larger than usual contribution from electromagnetic interactions due to the decreased magnetic field, see section 2.3.1.

Other important sources of background events are being induced by the LHC itself. They are referred to as machine induced background. A possible source is the interaction of the beams with material inside the beam pipe. These events can be removed using the correlation of sum and difference of the signal times of the V0 detectors. In these correlations the nominal beam 1 and beam 2 interaction can be distinguished from interactions of either one of the beams with residual material within the path of the beam.

Another source is the parasitic collisions between a main bunch and a satellite bunch from another RF bucket. Due to the spacing between the main and satellite bunches, the A-side

and C-side going neutron spectators originating from a main-satellite or satellite-satellite bunch collisions will arrive at different times at the ZNA and ZNC, respectively. By using the correlation between sum and difference of the signal times of the ZDC detectors the events not belonging to main-main type interactions can be rejected. The bunch spacing also gives the approximate location along the beam axis where these parasitic collisions take place. This yields a displaced vertex in multiples of 2.5 ns $c/2 \approx 37.5$ cm, which is well outside the fiducial range of $v_z = 10$ cm.

In addition to the nominal triggered collision, further collisions between pairs of ions can occur inside the same bunch crossing. These are referred to as in-bunch pileup events. All detectors are affected equally by these events, and they can only be distinguished by reconstruction of the multiple primary vertices. During the Pb-Pb and Xe-Xe data-taking the average number of hadronic interactions per bunch crossing was very low. For Pb-Pb it was on the order of $10^{-5} - 10^{-4}$. Therefore, the chance for in-bunch pileup events is negligible.

Collisions which happen in different bunch crossings can also overlap with the nominal triggered event. This out-of-bunch pileup is dependent on the readout time of the specific detector. The TPC, due to its long readout time, integrates as many as 4000 bunch crossings. During this time the particles from the out-of-bunch pileup will cause additional tracks which are shifted in z towards the readout planes. The high occupancy of the TPC, due to these additional tracks, causes degraded performance of the track reconstruction and particle identification. The faster detectors like the SPD, which integrates over 12 bunch crossings, and the V0, which integrates just over a single bunch crossing, are able to distinguish the out-of-bunch pileup events from the nominal event. The easiest approach to deal with the out-of-bunch pileup events is the removal by rejecting the events based on the correlation of signals from a fast and a slow detector.

There are more sophisticated methods available and in development, which take into account the modification of the tracking and particle identification inside the TPC due to the presence of pile-up events[104]. By restoring the performance of the detector it would be feasible to only reject the individual tracks from the pile-up event. Many out-of-bunch pileup events are expected to occur during data-taking with a high interaction rate. By rejecting the whole events during the event selection a large fraction of the statistics is potentially lost. These improved methods are therefore especially important for data-taking of Pb-Pb collisions in the LHC run 2 and later heavy-ion collisions in run 3 and beyond.

For this analysis, it was observed that there is a small, but non-negligible contribution of tracks from out-of-bunch pile-up to the multiplicity of tracks measured with the TPC in the data of Pb-Pb collisions from 2010. The removal of these events is crucial, because they bias the event weighting of four particle correlation $C_2\{4\}$ in peripheral collisions, which is proportional to the number of permutations of tracks in the TPC. In the case of $C_2\{4\}$ it is equivalent to $N(N-1)(N-2)(N-3)$, which can give these high multiplicity outliers a much larger weight than the other events in the same centrality class. These events are visible as outliers in the correlation of the TPC-out track multiplicity with the sum of the signal in both V0 detectors. TPC-out are those tracks, which reach the outer radius of the TPC active volume. Events are removed if the number of tracks in the TPC is greater than the selection parametrized by a polynomial function. In addition, these pile-up events are also visible in the correlation of the

Table 4.3: Number of events in Pb-Pb and Xe-Xe collision data samples after the event selection criteria are applied.

	Selection criterion	Value	Events / 10^6
Pb-Pb	$\|V_z\|$	10 cm	14.2
	centrality	5 – 70 %	10.5
	signal in both neutron ZDC		10.5
	pile-up rejection		10.5
Xe-Xe	$\|V_z\|$	10 cm	1.3
	centrality	5 – 70 %	0.9
	signal in both neutron ZDC		0.9

number of clusters in the SPD layers correlated with the TPC-only track multiplicity. Events with number of TPC tracks deviating more than three standard deviations from the mean of the distribution are rejected. A combination of selections based on these correlations rejects these pileup events.

Figure 4.1 shows the correlations used for rejection in the upper and center panels between the TPC tracks and the signals measured in the V0 and ITS, respectively. The left side show the correlations before the rejection. the right side shows the correlations after the rejection of events. Only the tails of the distributions are affected by the rejection. In the bottom panels, the weighted $C_2\{4\}$ distribution as a function of centrality before and after rejection of the high multiplicity outlier events is shown. Before the rejection, additional events with very small $C_2\{4\}$ are observed for peripheral events. The rejection removes these events. The rejection of out-of-bunch pileup events based on the correlations is not needed for the Xe-Xe data.

All events within the centrality range 5 % to 70 % are analyzed. In peripheral collisions, fewer particles are created. This means less particles are available for calculating $C_2\{4\}$. This quickly increases the statistical fluctuation of the measurement and limits the upper range of the measurement of $v_2\{4\}$ to 70 %. In addition, for very central events, $c_2\{4\}$ changes sign and $v_2\{4\}$ cannot be calculated. On the lower edge, and to lesser extend also on the upper edge, the centrality range is also limited by the resolution of the ZDC (see section 4.5.2). When events are shifted along the longitudinal direction to either side with respect to the interaction point $V_z = 0$, the geometrical acceptance changes for particles on one side compared to the other side. These shifted events may have a non-uniform acceptance in the ITS and TPC in the longitudinal direction for charged particle within the pseudorapidity range of $|\eta| < 0.8$. To ensure all events have a uniform acceptance, only events with a vertex position along the longitudinal direction V_z within ±10 cm around the nominal interaction point are selected for the analysis. Therefore, only events with vertices that have a minimum vertex contributor of one are used, to ensure the quality of the vertex reconstruction. A signal is required in the ZNA and ZNC detector, to allow the calculation of the observables. Table 4.3 summarizes the event selections applied in the data analysis and shows the number of events after applying the selections.

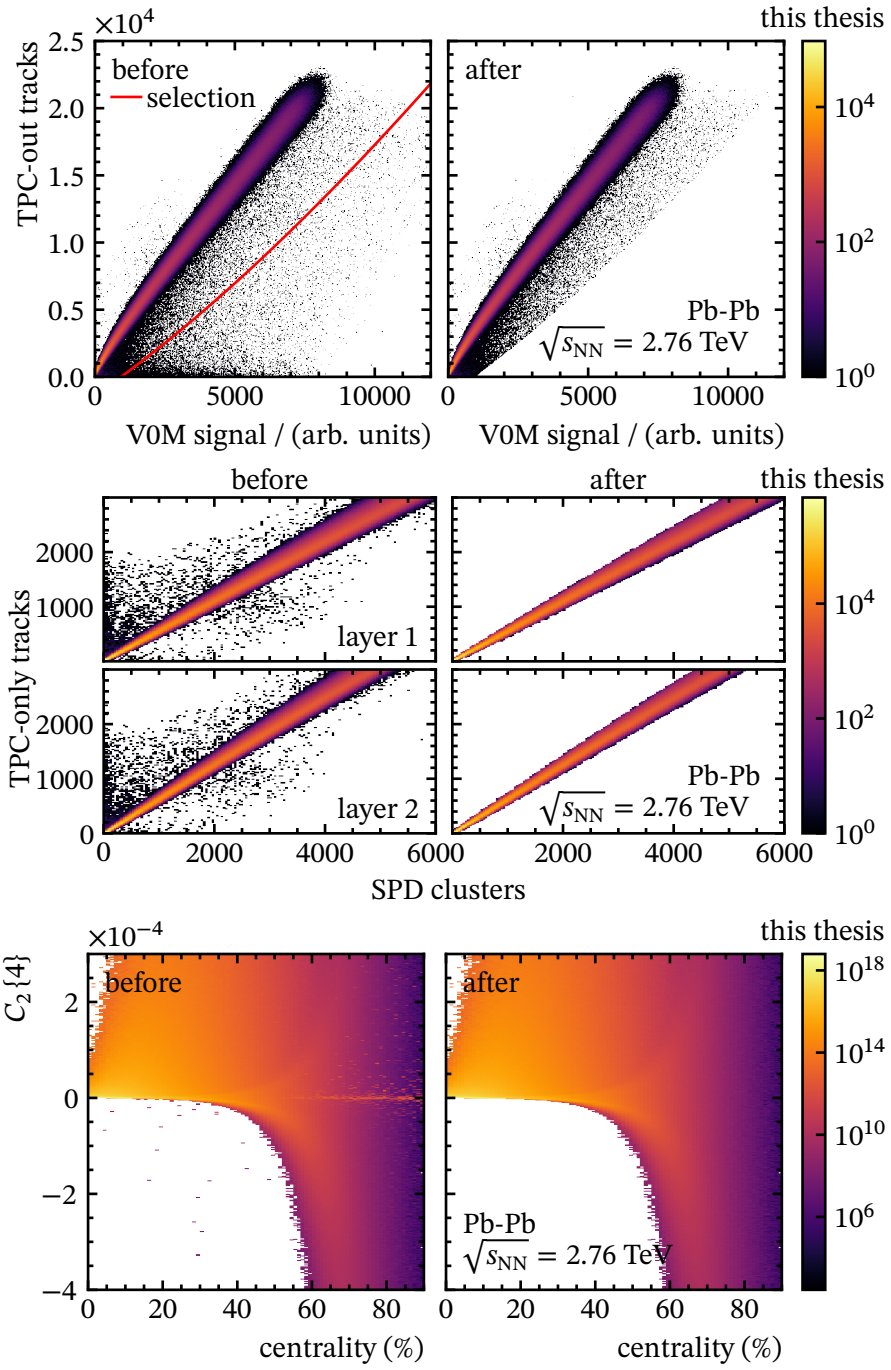

Figure 4.1: Upper panels: Correlation of TPC-out tracks with V0 signal amplitudes before and after the pile-up rejection. The selection based on a polynomial function is indicated by the red line. Center panels: Correlation of TPC-only tracks with number of clusters in the SPD before and after the pile-up rejection. Lower panels: Distribution of $C_2\{4\}$ as a function of V0M centrality before and after rejection of the pile-up events.

4.4 Track Selection

This section describes the track selection criteria that are applied in the data analysis. The track selection is part of the standard data preparation for physics analyses in ALICE[98]. The particles are reconstructed using the main tracking detectors ITS and TPC as described in section 2.4.2. Table 4.4 summarizes the track selection criteria described in this section.

The measurement is performed in a wide range of transverse momentum of $0.2\,\mathrm{GeV}/c < p_{\mathrm{T}} < 30\,\mathrm{GeV}/c$. This range is given by the detector setup. At a magnetic field of the ALICE solenoid of $B = 0.5\,\mathrm{T}$ a sharp cut-off of the ALICE tracking for pions at around $200\,\mathrm{MeV}/c$ is observed. To ensure the track reconstruction efficiency does not change with pseudorapidity, the longitudinal acceptance of the tracks is limited to range $(-0.8, 0.8)$ in pseudorapidity. In this range, their trajectory is entirely inside the TPC active volume. Tracks outside this range exit through the read-out chambers and therefore generate fewer clusters. This gives a worse reconstruction efficiency.

Since a large fraction of the SPD modules was inactive during the data-taking period in 2010, a large variation in the azimuthal acceptance of the ITS-TPC global tracks is observed. To restore the uniform acceptance of the tracks for the data analysis, the ITS-TPC global tracks with a hit in the SPD are complemented by those without a hit in the SPD. For the complementary tracks the ITS-TPC parametrization constrained to the primary vertex is used. The constraint to the primary vertex improves the transverse momentum resolution. This hybrid selection makes a compromise between a uniform azimuthal acceptance and improved track reconstruction efficiency on one hand, and a worsened transverse momentum resolution on the other hand. For the study of systematic uncertainties, different selections of the track parametrization will be used. To study the influence of particles from secondary vertices, tracks with strict distance-of-closest approach requirements are used. Hereafter, this setting of track selections is referred to as “tight-DCA” setting. The influence of the non-uniformity of the ITS, and the hybrid selection is studied by using the TPC-only tracks constrained to the primary vertex. Details on the systematic uncertainties studies are found in section 4.10. The track selections are summarized in table 4.4. In the following the parameters of the hybrid selection of tracks is explained in detail. The difference in the track selection of the 2010 Pb-Pb and the 2017 Xe-Xe data are explained at the end of section 4.4.

For all tracks which have a hit in the SPD and were refitted in the ITS during third iteration of the track reconstruction the ITS-TPC parametrization will be used. Tracks with wrongly assigned ITS clusters have a low transverse-momentum resolution at high transverse-momentum. They are removed by rejecting tracks with an unusually large quality of fit parameter. Therefore, the χ^2 per ITS cluster is required to be smaller than 36.

Tracks with hits in the ITS have significantly better transverse momentum resolution. A hit in the SPD and a ITS refit in third iteration of the reconstruction algorithm is requested only for the first category of hybrid tracks. For the second category without the hit in the SPD an ITS refit is not requested. Instead, the ITS-TPC track is constrained to the primary vertex.

To ensure the good quality of the track parameters a refit of the track in third iteration of the reconstruction in the TPC and a maximum χ^2 of the momentum fit per cluster in the TPC of four are required. Short tracks are removed by considering only tracks with a minimum of 70 of a total of 159 TPC clusters. Multiple reconstructions of the same track and fake tracks are rejected by checking how many clusters of a certain track are shared with other tracks in its vicinity. This is quantified by the ratio of all clusters shared with other tracks relative to the total amount of clusters used in the track fit. Only tracks below the threshold of 0.4 are accepted for the analysis. The fraction can be larger than one, because not all the assigned clusters of the tracks are necessarily used for the fitting of the track. To reduce the number of secondary particles originating from interaction with the material, a selection based on the distance-of-closest approach to the primary vertex, d_0, is used. Only tracks which have a d_0 closer than 2.4 cm in the transverse plane and 3.2 cm in the longitudinal plane are selected. In addition, the tracks must satisfy the ellipse equation

$$\left(d_0^{xy}/2.4\,\mathrm{cm}\right)^2 + \left(d_0^{z}/3.2\,\mathrm{cm}\right)^2 < 1.$$

The tracks which do not satisfy this relation are rejected. As explained in section 2.4.2, tracks originating from a secondary weak decay vertex are flagged during the reconstruction. They are rejected from the analysis using this flag.

The scattering of particles with the detector material between ITS and TPC as well as wrongly assigned hits in the ITS can significantly bias the transverse momentum of high transverse momentum tracks. To exclude these tracks the squared distance $\chi^2_{\mathrm{ITS-TPC}}$ between the track parameters of the TPC-only track constrained to the primary vertex and the ITS-TPC track is evaluated

$$\chi^2_{\mathrm{ITS-TPC}} = (\mathbf{X}_{\mathrm{TPC}} - \mathbf{X}_{\mathrm{ITS-TPC}})\,(\Sigma_{\mathrm{TPC}} + \Sigma_{\mathrm{ITS-TPC}})^{-1}\,(\mathbf{X}_{\mathrm{TPC}} - \mathbf{X}_{\mathrm{ITS-TPC}})\,. \tag{4.1}$$

$\mathbf{X} = (y, z, \sin(\theta), \tan(\lambda), 1/p_{\mathrm{T}})$ is the vector of track parameters[142] and Σ is the covariance matrix of $\mathbf{X}$ of the corresponding track type. The tracks with the fake momentum are rejected by selecting tracks with low $\chi^2_{\mathrm{ITS-TPC}} < 36$. The constraint to the primary vertex is only valid for primary particles. Therefore, the $\chi^2_{ITS-TPC}$ can also be large for tracks from secondary vertices, and they can be rejected as well.

The track selection parameters that were applied to the Xe-Xe data differ from those of the Pb-Pb data analysis in the following cases. An additional selection is applied inside the TPC to improve the track selection using information from sub-threshold clusters. The selection which is based on the fraction of crossed rows over findable clusters in the TPC, is required to be larger than 0.8. The number of crossed rows takes into account all pad rows a track passes, even as long as the surrounding pad rows gave a signal. Thereby, sub-threshold clusters are taken into account. The number of findable clusters is equal to the total number of pads crossed the track, where only the areas with functional read-out are considered. This fraction can be larger than unity, if a fraction of the trajectory passes over the sector boundaries of the TPC. Furthermore, an ITS-refit is required for all hybrid tracks.

Table 4.4: Overview of the track selection criteria for the Pb-Pb 2010 and Xe-Xe 2017 running periods. The different values columns correspond to the different track types. The slash between two values inside a column indicates that there are two possible values relating to whether a hit in the SPD was found (a hit was found / no hit was found). By default, the same selections are applied in the Pb-Pb and Xe-Xe collision systems. Deviations in the selections between the two data sets are marked explicitly in the column of the system. A – shows the selection criterion was not used by the track selection.

		Values		
Track selection criteria	System	TPC-only	Hybrid	Tight-DCA
ITS				
Required hits in layer		–	SPD: any / –*	SPD: any / SDD: 1*
Max. χ^2 per cluster		–	36	36
Refit	Pb-Pb	no	yes / no*	yes
	Xe-Xe	no	yes	yes
TPC				
Min. crossed rows / findable clusters	Xe-Xe	0.8	0.8	0.8
Max. χ^2 per cluster		4	4	4
Min. number of clusters		70	70	70
Max. fraction of shared clusters		–	0.4	–
Refit		no	yes	yes
Distance to closest approach				
Max. distance to vertex (xy) / cm		2.4	2.4	$7\sigma_{d_0^{xy}}$ †
Max. distance to vertex (z) / cm		3.2	3.2	2
2D ellipse constraint		yes	yes	no
Kink tracks		no	no	no
Max. squared distance $\chi^2_{\mathrm{ITS-TPC}}$		–	36	36
Pseudorapidity		$(-0.8, 0.8)$	$(-0.8, 0.8)$	$(-0.8, 0.8)$
Transverse momentum range / GeV/c		$(0.2, 30)$	$(0.2, 30)$	$(0.2, 30)$

*Only used for tracks without hit in SPD.

†Transverse distance to closest approach resolution parametrized by $\sigma_{d_0^{xy}} \approx \left(26 + 50\,\mathrm{GeV}/c \cdot {p_\mathrm{T}}^{-1.01}\right) \times 10^4$

4.5 Azimuthal Acceptance Correction

The correction of non-uniform azimuthal acceptance plays a crucial role in the analysis of anisotropic flow. The bias caused by a non-uniform azimuthal acceptance is indistinguishable from the real flow signal. As introduced in section 3.5 there are correction procedures, based solely on the measured data, which allow to recover the real signals. In this section, the corrections of the azimuthal non-uniform acceptance of the tracks measured with the ITS and TPC, and energy measured with the ZNA and ZNC are shown.

4.5.1 Reweighting of Azimuthal Distribution of Tracks

The uniformity of the flow vector of the particle tracks is restored by using φ-weights (introduced in section 3.5.3). These weights are calculated from the azimuthal track multiplicity distribution. To take into account variations of the azimuthal uniformity along the longitudinal direction, the particle weight defined in eq. (3.76) is calculated separately for regions of η of the tracks and the V_z of the collisions. For each of the η-V_z regions, the weight for tracks in a given φ-bin is calculated by dividing the maximum track multiplicity found within this region by the track multiplicity within the given φ-bin.

During the analysis, each track, which makes up the flow vector, is assigned a weight $w_\alpha(\varphi, V_z, \eta)$. The binning of the track multiplicity histogram used for the calculation of this weight is summarized in table 4.5. The binning along the V_z direction is optimized such that an equal number of events are in each bin. In the other dimensions, the bins are equally-spaced. Variations of the azimuthal uniformity between different runs are treated by performing the procedure individually for each run. For the hybrid selection of tracks, the correction is very small as shown in fig. 4.3 (p. 81). The top two panels show slices of the track distribution in η and V_z as a function of the azimuthal angle of the tracks φ without applying φ-weights. The bottom panels show the same distributions after applying φ-weights. Only a small differences in the azimuthal structure before and after the corrections is observed. The longitudinal structure of the collisions is preserved by the correction. Figure A.1 in appendix A.1 shows the track distribution for Xe-Xe collisions.

Figure 4.2 shows the flow vector components of the tracks as a function of centrality, and the components of the three-dimensional vertex positions (V_x, V_y, and V_z) before any corrections are applied. The figure only shows one data run in the Pb-Pb sample. As a function of centrality the width of the flow vector distribution increases strongly with centrality. The resolution is reduced, because the number of particles strongly decreases in more peripheral collisions. The width of the distribution is independent of the vertex position as indicated by the dashed red line. The mean, indicated by the red line, is in agreement with zero.

To see the impact of the recentering, the scale has to be increased as the deformations of the tracking are small. Figure 4.4 shows the impact of the correction on the components of the average flow vector $\langle q_2 \rangle$ as a function of the centrality on the left and the centrality-average on the right. The bottom panels show the impact on the hybrid selection of tracks. The centrality dependence and the total correction is small. The top panels show the impact for the tight-DCA selection of tracks. This selection of tracks has a much larger non-uniformity

than the hybrid selection. Before the corrections are applied, the offset of $\langle y_2 \rangle$ is one order of magnitude larger than for the hybrid selection.

Table 4.5: Binning of the four-dimensional multiplicity histograms for extraction of the φ-weights. The vertex position is expressed in number of σ of the width of the vertex distribution in the quoted direction.

Variable	Range	Number of bins
Vertex z position in $n\sigma_{V_z}$	(-1.56, 1.42)	10
Pseudorapidity η	(-0.8, 0.8)	6
Azimuthal angle φ	$(0, 2\pi)$	40

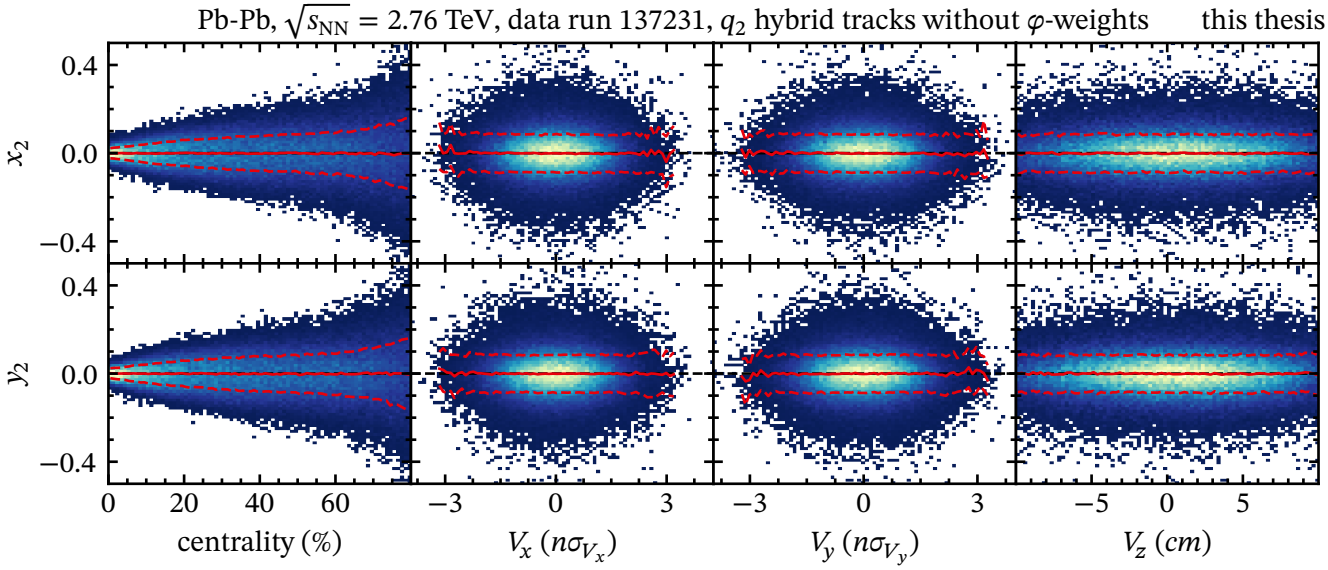

Figure 4.2: Distributions of flow vector components x_2 and y_2 of hybrid tracks as a function of centrality and vertex positions v_x, v_y, v_z for one data run of Pb-Pb collisions at $\sqrt{s_{\mathrm{NN}}} = 2.76$ TeV. The mean and one standard deviation are shown by the red lines.

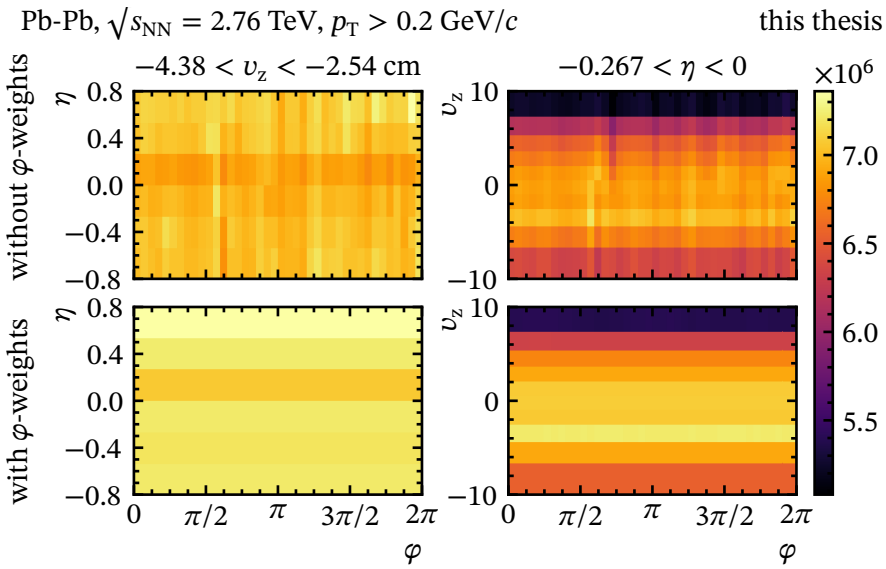

Figure 4.3: Azimuthal track distribution of the hybrid tracks inside a η-V_z window of the Pb-Pb data sample. The top panels show the distribution before the correction. On the bottom panels, the distribution is shown after the φ-weights are applied.

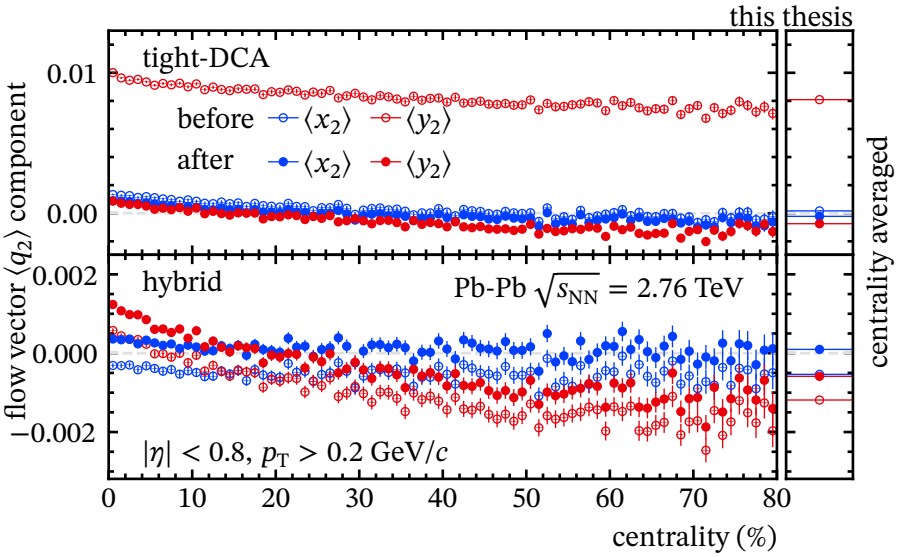

Figure 4.4: Centrality dependence of the x and y components of the flow vector q_2 for two different selections of tracks. The open (closed) points show the flow vector components before (after) applying the φ-weights. Red (blue) point indicate the x (y) component of the flow vector q_2. Right panels show the centrality-averaged flow vector.

4.5.2 Correction of ZDC Flow Vectors

The flow vectors measured with the ZNA and ZNC also show effects of non-uniform azimuthal acceptance. These originate from a combination of an imperfect detector calibration and a distortion of the distribution of impinging neutrons. Figure 4.7 (p. 85) shows the distribution of flow vectors q_1 constructed from the ZNA and ZNC signals for one data run in the Pb-Pb sample. As discussed in section 3.1, the average of a flow vector over many collisions is expected to be zero for a detector with a uniform azimuthal acceptance. However, the x and y components of the observed flow vector averaged over many events $\langle q_1 \rangle$ is nonzero. Dependences on the centrality and the three-dimensional primary vertex position (V_x, V_y and V_z). The red line shows these nonzero averages of the distributions. A correction of the flow vector is necessary. Along the centrality, V_x and V_y directions the dependences are strong. The dependence on the V_z position is weaker. The width of the distribution is indicated by the dashed line for a $\pm 1\sigma$ interval. The broadening of the distribution indicates a worsened resolution. The distribution becomes broader for central and peripheral collisions. For different primary vertex positions the width stays constant.

Figure 4.5 shows the mean position of the x and y components of the ZNA and ZNC flow vectors as a function of the data run. The x and y components of the flow vectors have been rescaled to cm and therefore correspond to the mean position of the energy deposition on the ZDC (centroid position). Large variations can be seen between different data runs. A jump in the y-components is observed when the polarity of the solenoid magnet of ALICE was switched.

To correct for the non-zero mean, recentering is applied. The default correction scheme recenters the flow vectors simultaneously in four dimensions (centrality, V_x, V_y and V_z). This four-dimensional correction is chosen to treat correlations between the independent variables. Furthermore, to treat possible variations in time and changes in the experimental setup during the different data runs the correction is calculated separately for each data run.

Table 4.6 shows the binning of the four-dimensional correction histograms used for the recentering correction. The binning along the V_x ,V_y, and V_z directions is optimized such that an equal number of events are in each bin. Along the centrality dimension, the bins are equally-spaced.

Figure 4.8 (p. 86) shows the average flow vector components before and after the recentering is applied as a function of centrality, and the primary vertex directions. After the recentering is applied the averaged flow vectors are compatible with zero.

As introduced in section 3.3, the $\langle x_1^{ZNA} x_1^{ZNC} \rangle$ and $\langle y_1^{ZNA} y_1^{ZNC} \rangle$ correlations are critical for the calculation of $v_2\{\Psi_{SP}\}$. In the following, the labels for the detectors are omitted ($\langle x_1 x_1 \rangle = \langle x_1^{ZNA} x_1^{ZNC} \rangle$). For the ZNA-ZNC correlations the $\langle x_1 y_1 \rangle$ and $\langle y_1 x_1 \rangle$ correlations are expected to vanish as the deflection of the spectators happens along the spectator plane. The $\langle x_1 x_1 \rangle$ and $\langle y_1 y_1 \rangle$ correlations carry the information about the spectator deflection and the spectator plane. A negative correlation is expected for $\langle x_1 x_1 \rangle$ and $\langle y_1 y_1 \rangle$ due to the deflection of the spectator neutrons in opposite directions. In regions where the magnitude of the signal correlations $\langle x_1 x_1 \rangle$ and $\langle y_1 y_1 \rangle$ are much larger than the $\langle x_1 y_1 \rangle$ and $\langle y_1 x_1 \rangle$ correlations, the

resolution needed for the calculation of $v_2\{\Psi_{SP}\}$ is well-defined. When non-zero contributions of $\langle x_1 y_1 \rangle$ and $\langle y_1 x_1 \rangle$ are in the same order as $\langle x_1 x_1 \rangle$ and $\langle y_1 y_1 \rangle$, or the $\langle x_1 x_1 \rangle$ or $\langle y_1 y_1 \rangle$ signals are zero, a reliable extraction of the resolution is not possible.

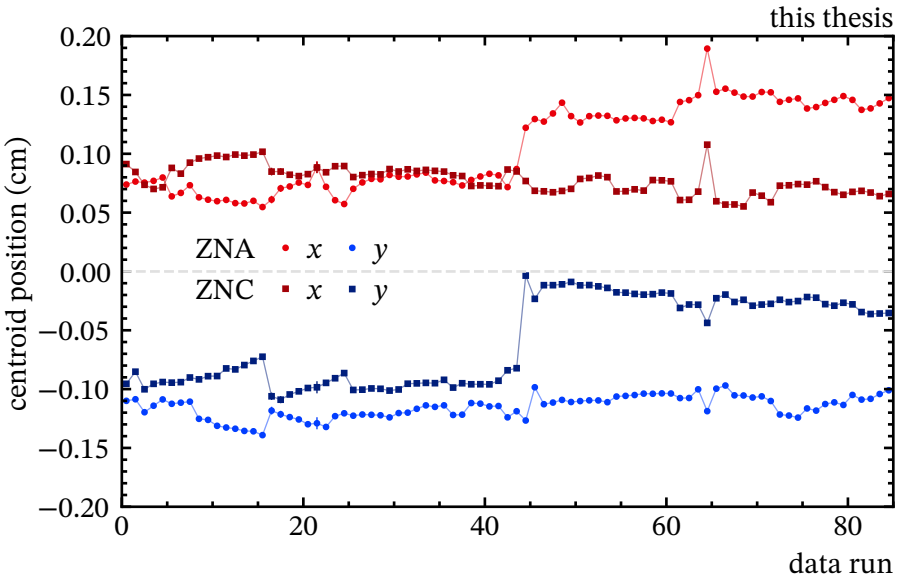

Figure 4.5: Centroid position on the ZNA and ZNA for different data runs in the Pb-Pb data sample. The centroid position is described in the text.

Table 4.6: Binning of the four-dimensional recentering correction histograms of the default correction scheme.

Variable	Range	Number of bins
Vertex x position in $n\sigma_{V_x}$	(-3, 3)	3
Vertex y position in $n\sigma_{V_y}$	(-3, 3)	3
Vertex z position in $n\sigma_{V_y}$	(-3, 3)	3
Centrality	(0,80)	80

Figure 4.6 shows these correlations in Pb-Pb on the left and Xe-Xe collisions on the right. The lines in the upper panels show the four different correlations before the correction is applied. The data points show the correlations after the corrections are applied. The bottom panels show the correlations after recentering with a rescaled y-axis.

Before the correction, the centrality-dependence between the $\langle x_1 x_1 \rangle$ and $\langle y_1 y_1 \rangle$ components are very different. For some centrality regions a positive correlation of $\langle x_1 x_1 \rangle$ and $\langle y_1 y_1 \rangle$ is observed, which is not expected. Also the $\langle x_1 y_1 \rangle$ and $\langle y_1 x_1 \rangle$ correlations are non-zero. Without the corrections a well-defined resolution cannot be calculated.

After recentering, the $\langle x_1 y_1 \rangle$ and $\langle y_1 x_1 \rangle$ correlations are approximately zero. In centralities of 5 % to 40 % a small deviation from zero is observed. The $\langle x_1 x_1 \rangle$ and $\langle y_1 y_1 \rangle$ correlations show the expected negative sign for the centrality range 5 % to 80 %. They reach a minimum for the centrality range 20 % to 40 %, where the number of spectator neutrons is also largest. In

Pb-Pb a significant difference is observed between the $\langle x_1 x_1 \rangle$ and the $\langle y_1 y_1 \rangle$ correlations for centralities smaller than 55 %. In Xe-Xe the magnitude of the correlations is reduced and the difference between $\langle x_1 x_1 \rangle$ and $\langle y_1 y_1 \rangle$ is not observed within the statistical precision of the data. The signal correlations become very small for centralities below 5 %, which makes the extraction of the resolution unfeasible.

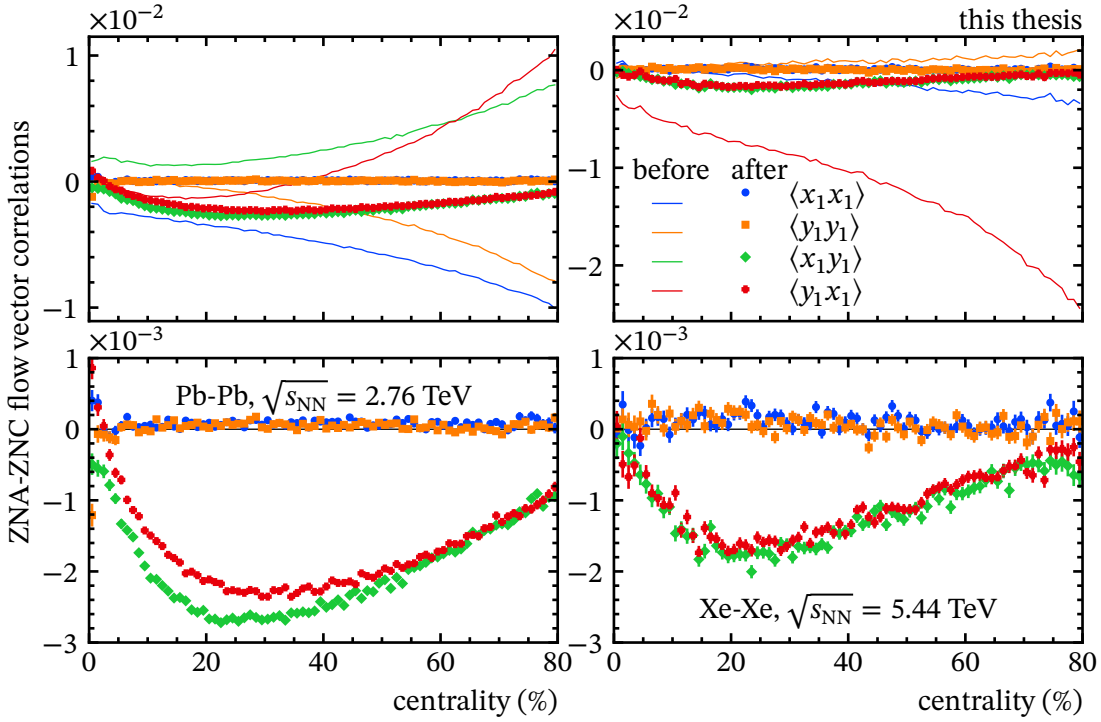

Figure 4.6: Correlations between ZNA an ZNC flow vector components. The upper panels show the correlations before (lines) and after (markers) the recentering correction is applied. The lower panels show the data after recentering with a rescaled y-axis. The left panels show the correlations in Pb-Pb collisions at $\sqrt{s_{\mathrm{NN}}} = 2.76$ TeV. The right panels show the correlations in Xe-Xe collisions at $\sqrt{s_{\mathrm{NN}}} = 5.44$ TeV.

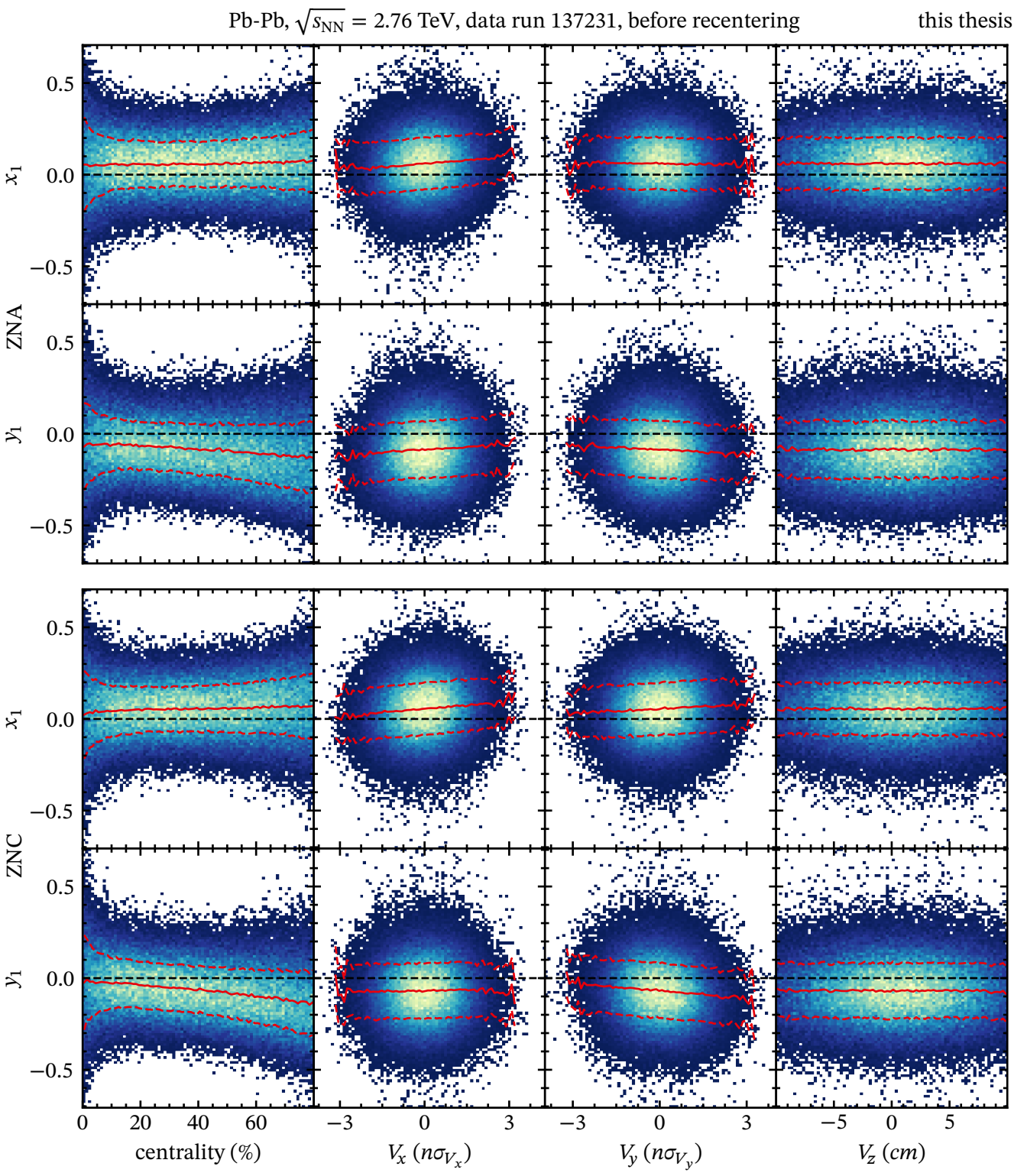

Figure 4.7: Distributions of flow vector components x_1 and y_1 of ZNA and ZNC as a function of centrality and vertex positions v_x, v_y, v_z. The data shown was collected in one data run of Pb-Pb collisions at $\sqrt{s_{\mathrm{NN}}} = 2.76$ TeV. The mean and standard deviation are shown by the red lines.

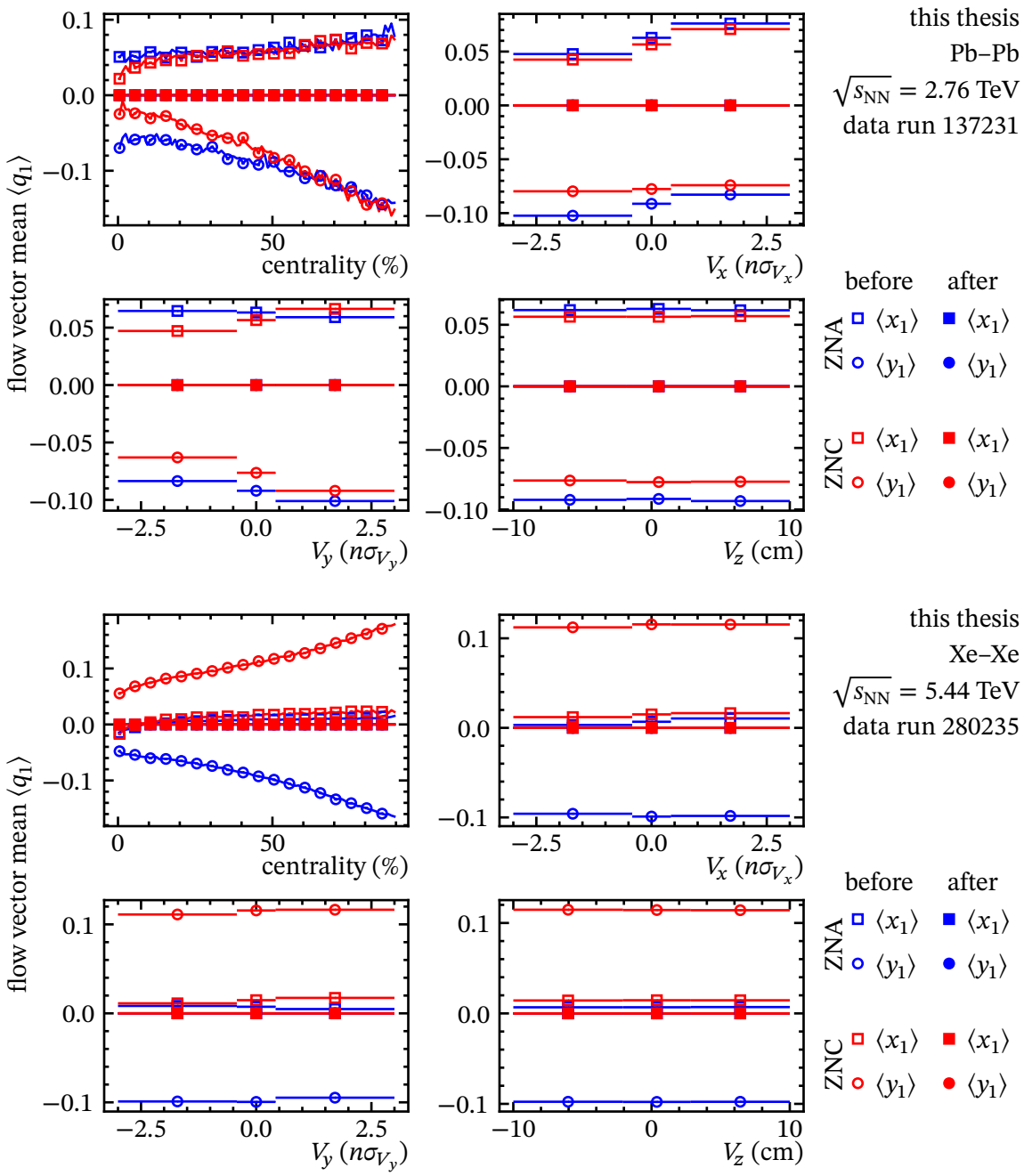

Figure 4.8: Mean flow vector components $\langle x_1 \rangle$ and $\langle y_1 \rangle$ of ZNA and ZNC as a function of centrality and vertex positions v_x, v_y, and v_z before (open markers) and after (closed markers) the correction procedure is applied. The upper panel shows one data run of Pb-Pb collisions at $\sqrt{s_{NN}} = 2.76$ TeV. The lower panel shows one data run of Xe-Xe collisions at $\sqrt{s_{NN}} = 5.44$ TeV.

4.6 Track Reconstruction Efficiency Correction

The track reconstruction efficiency gives the probability to reconstruct a track from the detector signals caused by physical particles. In ALICE this efficiency depends on the transverse momentum of the measured particle, which results in an alteration of the measured transverse momentum distribution. The anisotropic flow also depends on the transverse momentum of the measured particles. Therefore, if no correction is performed, the track reconstruction efficiency will bias the measured integrated flow. In contrast to the measurement of the invariant yield of particles, the magnitude of the efficiency does not influence the measurement of flow, as it cancels due to the normalization of flow. This cancellation of the magnitude can be seen, for example, in eq. (3.48). The reconstruction efficiency factorizes with the non-uniform acceptance correction. Therefore, the total weight assigned to the particles can be decomposed into

$$w_{total}(\varphi, \eta, V_z, p_\mathrm{T}) = w_\alpha(\varphi, \eta, V_z) \times w_\epsilon(p_\mathrm{T}) \tag{4.2}$$

It is therefore sufficient to calculate the reconstruction efficiency only as a function of the transverse momentum.

The correction for the track reconstruction efficiency is implemented using particle weights. Because the track reconstruction efficiency within the chosen acceptance, shown in section 4.4, does not depend on η and V_z, its correction can be factorized with the non-uniform acceptance correction. The track reconstruction efficiency itself is calculated using Monte Carlo simulations. The Monte Carlo simulation data samples are referenced in table 4.2. In the simulations the information of the particle generation is stored together with the simulated detector signals. This allows to associate a reconstructed track from the detector signals with a physical particle from the particle generation. By tagging all tracks which belong to particles from a primary interaction the probability to reconstruct it as a track can be calculated using eq. (3.73). Using only primary tracks the equation can be written as

$$\epsilon(p_\mathrm{T}) = \frac{N_{rec}^{primary}(p_\mathrm{T})}{N_{gen}^{primary}(p_{\mathrm{T},gen})} \tag{4.3}$$

where $N_{rec}^{primary}(p_\mathrm{T})$ is the number of reconstructed tracks originating from a primary interaction within a given p_T bin. $N_{gen}^{primary}(p_{\mathrm{T},gen})$ is the total number of generated primary particles in the same bin using the p_T of the generated particle. $N_{rec}^{primary}(p_\mathrm{T})$ and $N_{gen}^{primary}(p_{\mathrm{T},gen})$ are each filled into histograms as a function of p_T. The ratio given by eq. (4.3) is calculated in each p_T-bin. The resulting histogram is interpolated using a cubic spline to obtain a smooth efficiency[143]. The cubic spline is evaluated at the transverse momentum of the particle to obtain the efficiency. The inverse efficiency is then applied as a correction during the construction of the flow vector.

$$w_\epsilon(p_\mathrm{T}) = 1/\epsilon(p_\mathrm{T}). \tag{4.4}$$

Figure 4.9 shows these track reconstruction efficiency histograms as a function of the transverse momentum of the reconstructed particles for different track selections. The default track selection is shown in blue data points. The cubic spline interpolation is shown by the blue line. A sharp drop-off of the reconstruction efficiency is observed at 0.2 GeV/c. For higher p_T it increases to $\approx$ 80 % for the default hybrid track selection. For Pb-Pb the efficiency for the hybrid selection is larger than in Xe-Xe, because the track selection criteria

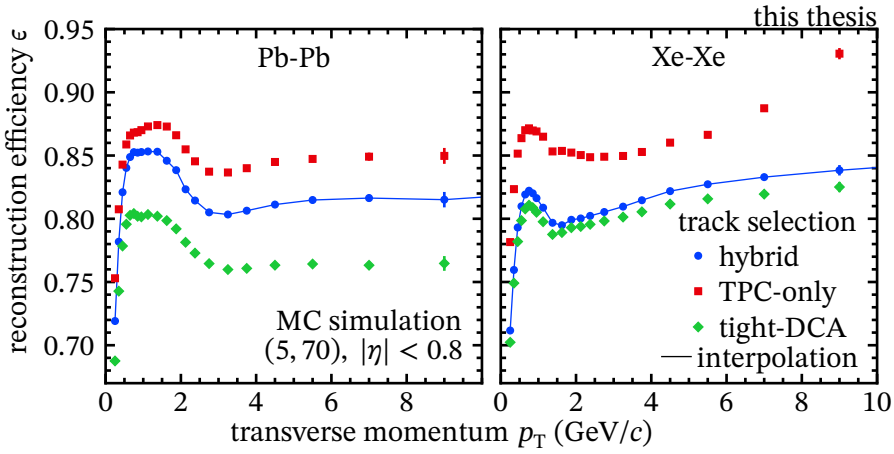

Figure 4.9: Transverse momentum dependence of the track reconstruction efficiency averaged in the 5 % to 70 % centrality range for the three different selection of tracks. The blue line indicates the cubic spline interpolation used in the analysis.

in Xe-Xe are stricter (compare to table 4.4). The stricter selection (tight-DCA) has a less efficient track reconstruction and the looser track selection (TPC-only) has a more efficient track reconstruction. As explained in section 4.4, the hybrid selection offers the optimum compromise.

Figure 4.10 indicates the centrality dependence of the track reconstruction efficiency as a function of transverse momentum. The track reconstruction efficiency in the indicated centrality ranges are divided by the centrality-averaged track reconstruction efficiency. The p_T-dependent shape of the track reconstruction efficiency with centrality are up to approximately 2 %. The average reconstruction efficiency changes by up to 2 % between the lowest value in central collisions to the highest value in peripheral collisions, where the track density is much lower. However, since the absolute scale of the efficiency is not relevant for the measurement of flow, the centrality-averaged track reconstruction efficiency is used. The impact of the p_T-dependent shape on the results is investigated.

Figure 4.11 shows the secondary contamination in the data samples calculated in the MC simulation by

$$\text{secondary contamination} = \frac{N_{rec}(p_T, cent)}{N_{gen}^{primary}(p_{T,gen}, cent)} - 1\,, \tag{4.5}$$

where the numerator counts all reconstructed particles, without the constraint of it being a primary particle. The contamination is largest for central collisions and becomes small for peripheral collisions on the order of 1 % to 2 % for Pb-Pb and Xe-Xe collisions. At high transverse momentum the secondary contamination in Pb-Pb is slightly higher due to the less strict track selection criteria. In central Xe-Xe collisions the secondary contamination is slightly higher at low transverse momentum due to the lower magnetic field[144]. For this study no correction of the secondary contamination is applied. The comparison of the secondary contamination to the other track selection is shown in fig. A.4.

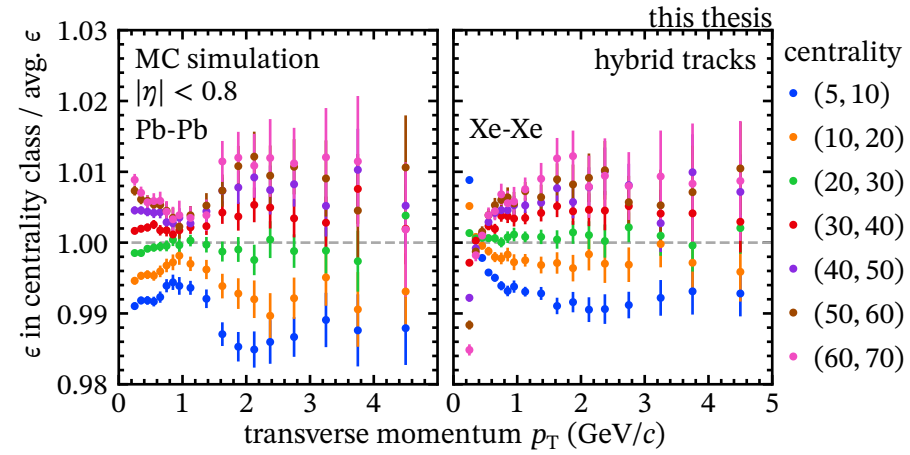

Figure 4.10: Ratios of the track reconstruction efficiency in a given centrality class to the centrality-averaged track reconstruction efficiency (blue data points in fig. 4.9) as a function of transverse momentum.

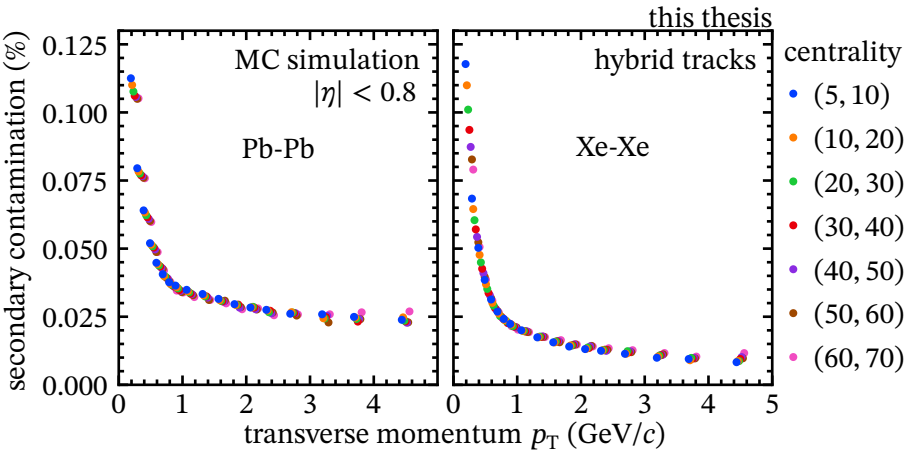

Figure 4.11: Secondary contamination of the reconstructed tracks in the 5 % to 70 % centrality range. The data points of the different centrality classes are slightly shifted along the p_T direction for better visualization of the differences.

4.7 Performance of the Zero Degree Calorimeters in Different Data Samples

For this analysis, the performance of the ZDC to estimate the flow and the event plane resolution is crucial. In this section, an extensive study of the ZDC in correlation analysis in all heavy-ion collision data sets is presented.

Table 4.1 lists all analyzed data sets and the corresponding LHC beam parameters. In the following, the period are called by the year in which they were recorded. The 2010 data sample was recorded with one of the largest β^* and correspondingly one of the lowest focussing of the beam and collision rate. A lower collision rate typically accumulates fewer collisions in the same time interval. The collision rate was increased by stronger focussing of the beam in the later periods. The 2017 sample is special, because of a unique short term possibility to have Xe-Xe collision in the LHC. The beam settings for this period correspond to the proton-proton collision beam settings. A validation of a new beam setting would have been too time-consuming. Therefore, only change was the adaptation of the crossing angle to 60 µrad to allow neutron spectators to reach the ZDC[145].

Higher collision rates and therefore higher accumulated statistics are needed for differential studies. As a part of this work, a preliminary study of $v_2\{\Psi_{SP}\}$ was performed in the 2018 data to extend the presented data analysis to more differential observables. Large deviations from the presented data analysis in 2010 and 2017 data is observed. In addition, previous studies have also revealed differences in the ZDC performance in the 2015 data relative to the 2010 data[146]. In the following, the performance of the ZDC in the 2010 and 2017 data samples are compared to the other heavy-ion data samples.

Figure 4.12 shows the signal components of the ZNA-ZNC and Tracks-ZNA-ZNC correlations used for constructing $v_2\{\Psi_{SP}\}$ as a function of the centrality after a recentering correction is applied. The two data periods used for the physics results obtained in this work are shown in black (2010) and gray (2017). These reference data are compared to the other periods. For 2015 and 2018 only data from one data run is shown. In the top panels, which show the ZDC-only correlations, strong differences are observed between the group of 2011, 2015, 2018 periods and the 2010 period. The difference increases for more peripheral collisions. At larger values, a zero-crossing of the 2011, 2015, 2018 periods is observed. Such a change of sign is not expected from the physical expectation of the spectator deflection. The period of 2017 is expected to be different due to the difference of the collision systems. The projection of the zdc correlation on mid-rapidity flow vector component $x_2x_1x_1$, shown in the bottom panels, does not have this unexpected sign change. However, for the 2015 and 2018 data samples there are still some differences observed compared to the 2010 and 2017 periods. They show an earlier drop-off and the correlations do not reach the same magnitude. The projection of the ZDC correlations on mid-rapidity seems to be affected to a lesser extent than the ZDC-only correlations.

Figure 4.13 shows the $\langle x_2x_1x_1\rangle$ component of $v_2\{\Psi_{SP}\}$ for the different periods as function of centrality. For 2015 and 2018, only data from one data run is shown. A strong bias is observed for the 2011, 2015 and 2018 periods. This bias increases for more peripheral collisions. The figure only shows the data within the axis ranges. Such large differences of elliptic flow is not

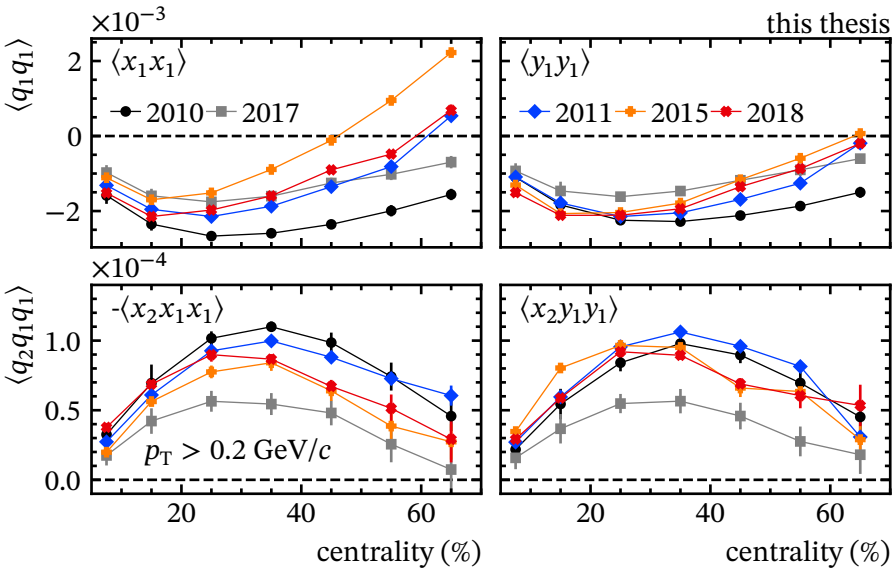

Figure 4.12: Centrality dependence of $\langle x_1 x_1 \rangle$ and $\langle y_1 y_1 \rangle$ in the upper panels. Centrality dependence of $\langle x_2 x_1 x_1 \rangle$ and $\langle x_2 y_1 y_1 \rangle$ in the lower panels. The colored markers indicate the different data samples.

expected to originate from an increase in energy. Studies of the anisotropic flow in ALICE have shown that there is only a slight variation of the flow between $\sqrt{s_{\mathrm{NN}}} = 2.76\,\mathrm{TeV}$ and $\sqrt{s_{\mathrm{NN}}} = 5.02\,\mathrm{TeV}$ Pb-Pb collisions[68]. This is further evidenced by the fact that the 2011 period, within uncertainties, also shows the same behavior as the 2011 and 2015 periods. Only the 2010 and 2017 periods show the expected maximum at mid-central collisions and a decrease for peripheral collisions.

The results imply a correlated effect on the spectator measurement with the ZDC. The effects observed in the data are not sufficiently resolved by only applying a recentering correction procedure on the ZDC flow vectors. In addition to the mean of the flow vectors the shape of the distribution may also be modified through an unknown effect. To test this, the flow vector distribution in all data samples are investigated.

Figure 4.15 (p. 93) shows the distribution of x_1 and y_1 for ZNA and ZNC for the five data samples. Similar to the correlation between the ZNA and ZNC also for the single detector measurements a clear difference is observed between the 2010 and 2017 samples and the 2011, 2015 and 2018 data samples. The 2010 and 2017 samples have the lowest spread in mid-central collisions, when the expected directed flow is the largest. In central and peripheral the width becomes larger as the number of spectators hitting the ZDC shrinks. The other periods have the smallest standard deviation in central collisions, when only few spectators are expected to impinge on the ZDC. In peripheral collisions, the distribution in these period becomes increasingly non-gaussian and in the 2018 data even indications for a double peak structure are visible. The reason for the difference of width between peripheral and central collisions is not yet clear. In both cases the number of spectators hitting the ZDC is small since in peripheral collisions most of the spectators are bound in large nuclear fragments.

Figure 4.16 (p. 94) shows the relative signal of a given channel with respect to the total signal of the ZNC. The red line indicates the mean of the distribution. The bright yellow

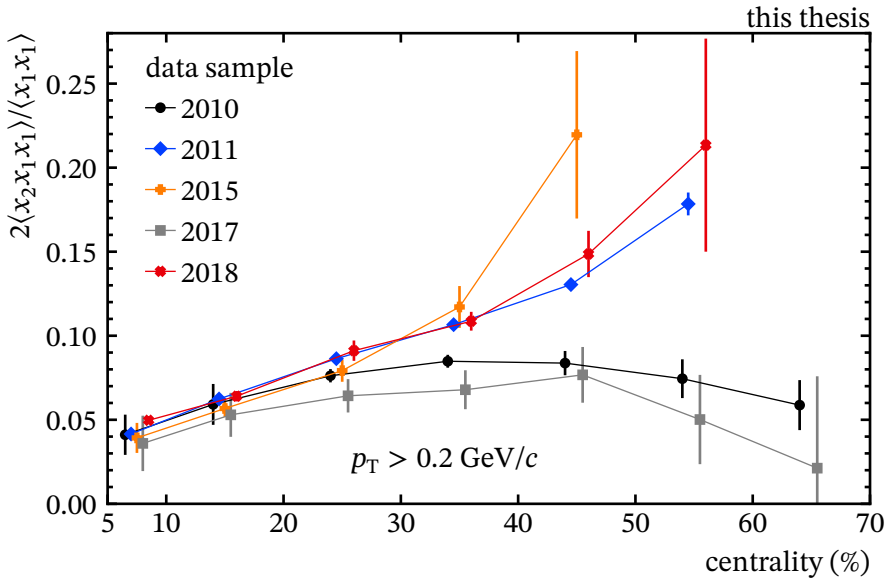

Figure 4.13: Centrality dependence of $2\langle x_2x_1x_1\rangle/\langle x_1x_1\rangle$ for different data samples. The data samples are indicated by colored markers.

indicates the most probable value. For a distribution of neutrons centered around (0,0) a relative signal of 25 % is expected for all channels. The inset shows the projection in peripheral collisions (60 % to 70 %). Only for the 2010 and 2017 data samples the distribution is Gaussian in peripheral collisions. For the other data samples the distribution has a heavy tail towards high relative signals. This indicates that a large fraction of the total signal measured by the ZDC in these events is measured in one of the channels. The neutron energy deposition is contained in one quadrant of the calorimeter. The ZNA exhibits the same behavior (fig. A.14).

A sensitivity of the ZDC event plane reconstruction on the beam parameters of the LHC has been calculated before in studies using a dedicated Monte Carlo simulation[147]. The bias observed in this work cannot be corrected with the MC-based weights derived in this previous study. Figure 4.14 shows $\langle x_2x_1x_1\rangle/\langle x_1x_1\rangle$ with flow vector weights $p = \alpha = 0.395$ divided by $\langle x_2x_1x_1\rangle/\langle x_1x_1\rangle$ without flow vector weights $p = 1$. Only a small difference in the order of 1 % is observed, which is much smaller than the observed bias (compare to fig. 4.13).

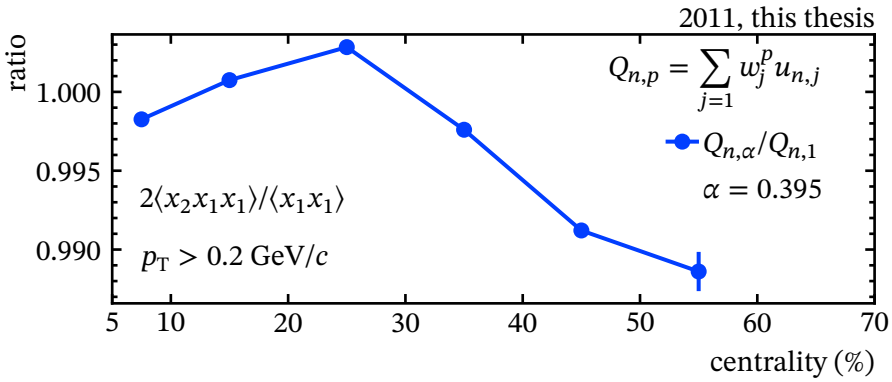

Figure 4.14: Influence of flow vector weights presented in[147] on $\langle x_2x_1x_1\rangle/\langle x_1x_1\rangle$ as a function of centrality in the 2011 Pb-Pb collision data sample at $\sqrt{s_{NN}} = 2.76$ TeV.

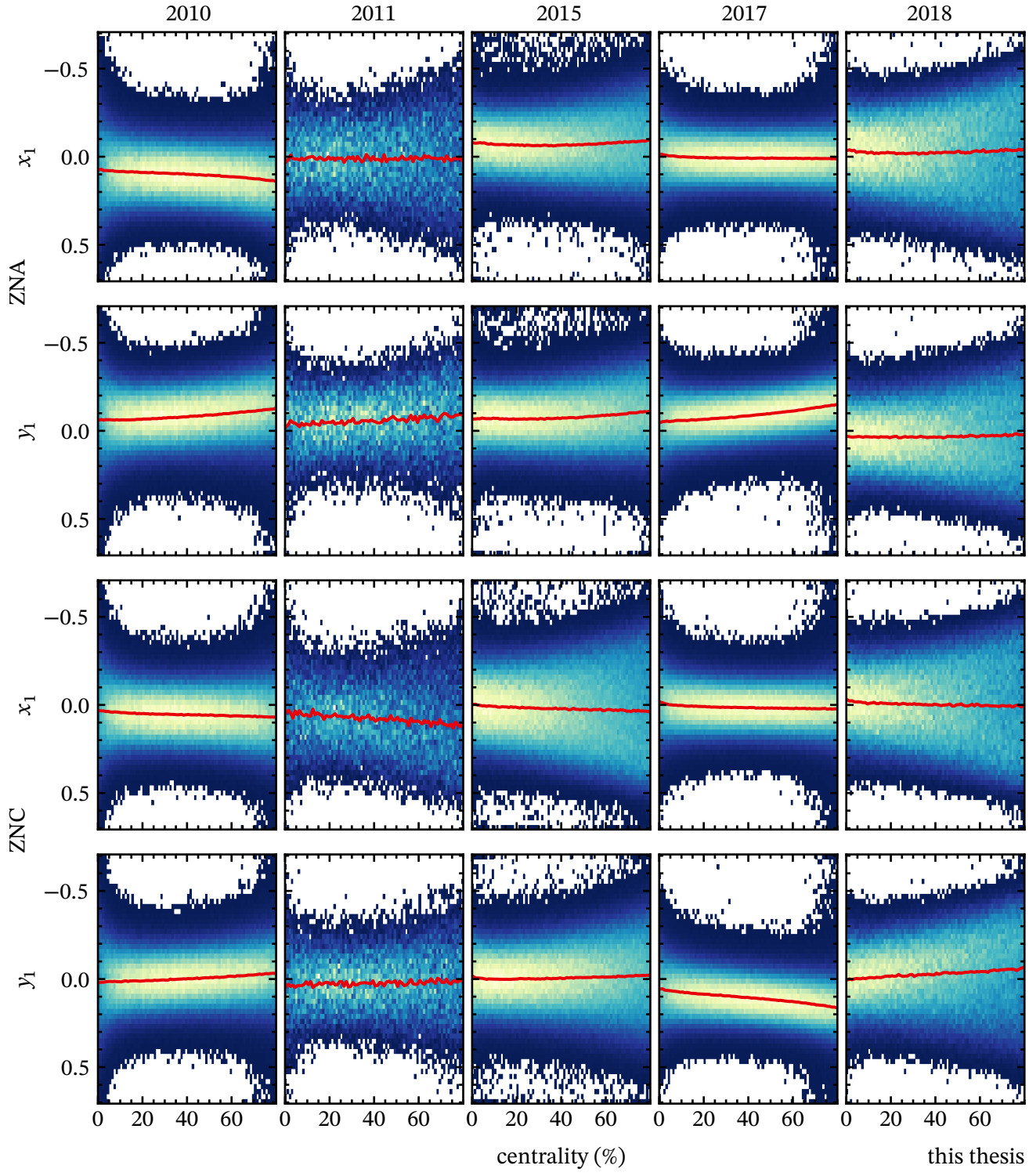

Figure 4.15: Centrality dependence of x_1 and y_1 for ZNA and ZNC in the different data samples. Only one data run per data sample is shown. The red line shows the means $\langle x_1 \rangle$ and $\langle y_1 \rangle$. The flow vectors are not recentered.

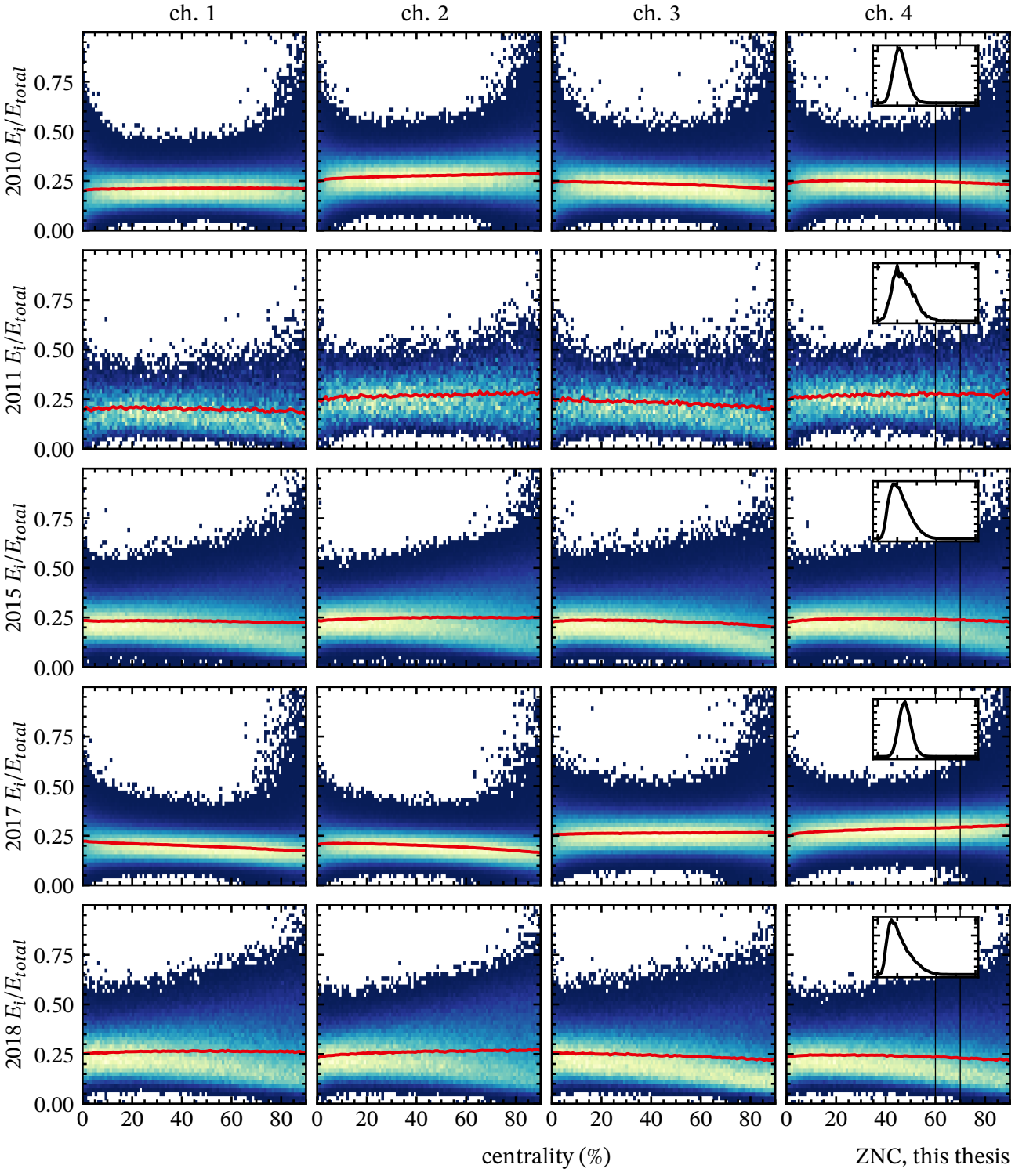

Figure 4.16: Centrality dependence of the relative signal E_i/E_{total} for the ZNA in different data samples. Only one data run per data sample is shown. The red line shows the means signal. The insets show the projection of the 60 % to 70 % centrality range for the fourth channel.

4.8 Classification of Events using Event-Shape Engineering

Using the method introduced in section 3.4 the collisions are classified based on the $|q_{1,ese}^{ZNA}|$ and $|q_{1,ese}^{ZNC}|$.

Numerically, the cumulative distribution function introduced in eq. (3.70) is approximated by summing the binned distribution of $|q_{1,ese}|$ in the following way

$$P(x) = \sum_{i=1}^{x} p(i) \Big/ \sum_{i=1} f(i)\,, \tag{4.6}$$

where the sum in the numerator goes from the first bin to the bin x and the sum in the denominator sums over the whole histogram. The continuous cumulative distribution function is approximated by interpolating the resulting histogram with a cubic spline[143].

Figure 4.17 shows the distributions of $|q_{1,ese}|$ for ZNA on the left and ZNC on the right side. The centrality dependence, quantified by the mean of the data (dashed line), is very similar for both detectors. No large differences are observed. As shown, the measured distribution of $|q_{1,ese}|$ changes with the centrality. In order to prevent a bias from the wide centrality bins the percentiles of the $|q_{1,ese}|$ distribution are calculated in 1 % bins. The red lines indicate the 25 % to 26 % centrality range. In each of these slices the cumulative distribution function is calculated according to the method mentioned above.

Figure 4.18 shows the histogram obtained for $|q_{1,ese}|$ measured in the ZNA in the 25 % to 26 % slice in blue. The distribution is normalized to one. In red the numerically obtained cumulative distribution function is shown. The large number of events results in very small statistical uncertainties of $P(q_{1,ese})$. The interpolation is on top of the histogram. Due to the high number of bins no difference is visible. To select the events with the 20 % largest $|q_{1,ese}|$ in the sample, only the collisions where $P(|q_{1,ese}|) > 0.8$ are accepted. In the figure, this is indicated by the dashed black line. By inverting $P(|q_{1,ese}|)$ the threshold value of $|q_{1,ese}|$ can be determined, as shown by the vertical black line. All events right of the threshold are selected.

Figure 4.19 shows the distributions of $|q_{1,ese}|$ for different centrality classes for the ZNA. The distributions are fitted with a Bessel-Gaussian model of flow fluctuations. To a good approximation, the $|q_{1,ese}|$ distributions are described by the model. The bottom panels show the ratios between data and model. The different centrality classes are offset by a constant factor for better visualization. However, the distribution of $|q_{1,ese}|$ has not been unfolded for the detector resolution and are not equivalent to the event-by-event flow presented in fig. 1.21.

After the collisions are classified based on the $|q_{1,ese}|$ from ZNA and ZNC, the observables $v_2\{2, |\Delta\eta| > 1\}$ and $v_2\{4\}$ are calculated separately in these classes. The ratio of the ESE-selected classes over the unbiased is calculated according to eq. (3.72).

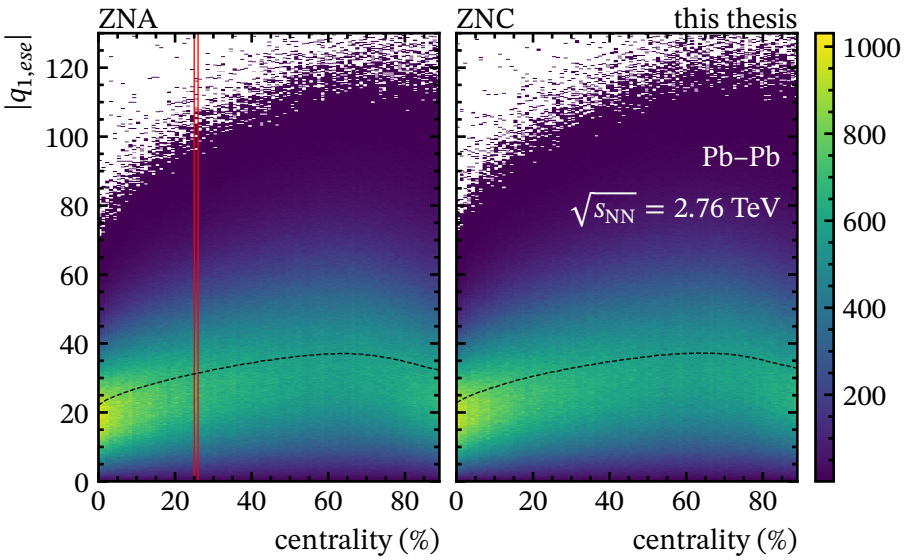

Figure 4.17: Distribution of $q_{1,ese}$ as a function of centrality. The black dashed line indicates the mean of the distribution in each centrality bin. Red lines indicate the 25 % to 26 % centrality bin.

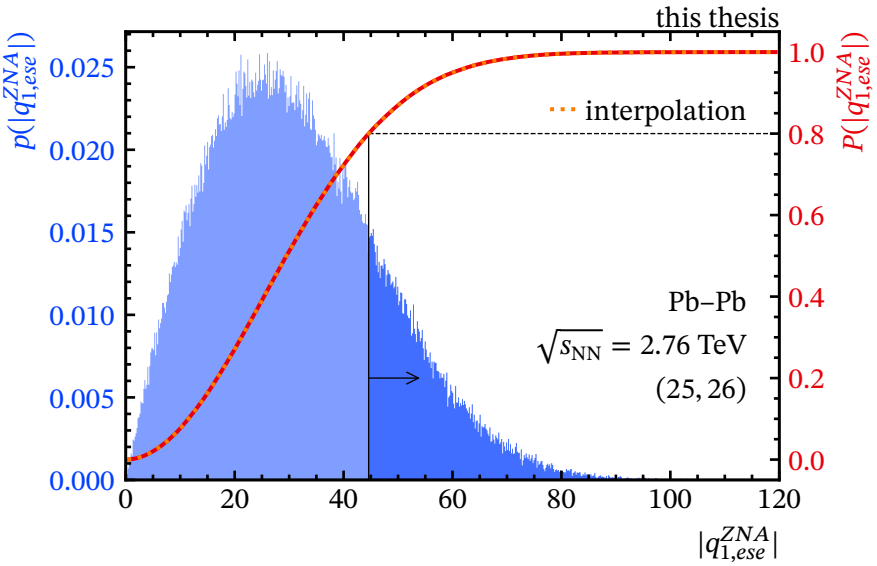

Figure 4.18: Illustration of $|q_{1,ese}|$ percentile selection for the 25 % to 26 % centrality Pb-Pb collisions at $\sqrt{s_{NN}} = 2.76$ TeV. The blue histogram shows the distribution of $|q_{1,ese}|$. The red and orange lines shows the cumulative distribution function. The thin black line illustrates a selection of $P(q_{1,ese}) > 0.8$.

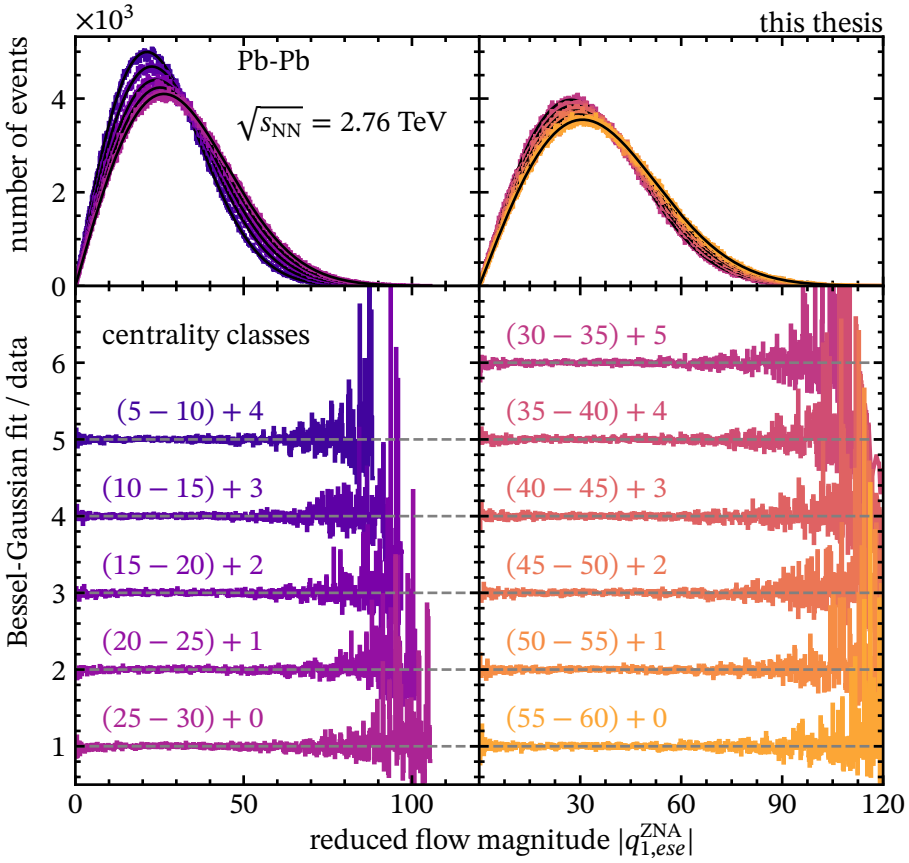

Figure 4.19: Distribution of $|q_{1,ese}|$ sliced in 5 % centrality intervals. Top panel shows the distributions in colored lines. A Bessel-Gaussian fit to the distribution is shown in black lines. The bottom panels show the ratio between the Bessel-Gaussian fit and the data. The ratios are offset by a constant for better visualization.

4.9 Initial State Models

4.9.1 TRENTo model Calculations

The T$_R$ENTo model is used for the investigation of the multiplicity scaling of flow and to compare the flow ratios to the ratios of the initial eccentricities. For this purpose, optimized model parameters from ref.[56] will be used to calculate the initial state properties. Table 4.7 shows these parameters.

Table 4.7: T$_R$ENTo model parameters from ref.[56].

Parameters	Reduced thickness p	Fluctuations k	Nucleon width w	Min. distance d
Values	0.007	1.187	0.956	1.27

In T$_R$ENTo, the integrated reduced thickness function, or pseudo-multiplicity, is used to classify collisions in centrality. The entropy of the initial state given by Equation (1.11) is used

as a proxy for the multiplicity of particles, because the average charged particle multiplicity $\langle N_{ch} \rangle$ after the hyrodynamic evolution is to a good approximation proportional to the total initial entropy[44,66]

$$\langle N_{ch} \rangle \propto \int dxdyT_R \,. \tag{4.7}$$

The scaling with the pseudo-multiplicity is used to divide the collisions into the centrality classes according to the quantiles of the pseudo-multiplicity distribution.

The pseudo-multiplicity is scaled with a factor and compared to the distribution in data to check if the multiplicity distribution in data is correctly described. Figure 4.20 shows the comparison between the V0M multiplicity measured in the forward V0 scintillators and the $\mathrm{T_R}$ENTo pseudo-multiplicity scaled to approximately fit the data. $\mathrm{T_R}$ENTo reproduces the overall shape of the distribution, but gives slightly fewer number of events for the bulk of the distribution. The high multiplicity tail is overpredicted by $\mathrm{T_R}$ENTo. An exact fit is not expected as the scaling with the pseudo-multiplicity in $\mathrm{T_R}$ENTo holds for mid-rapidity. Also, improvements in the fit procedure would result in a better fit. This fit and the scaling factor are not used in the further analysis.

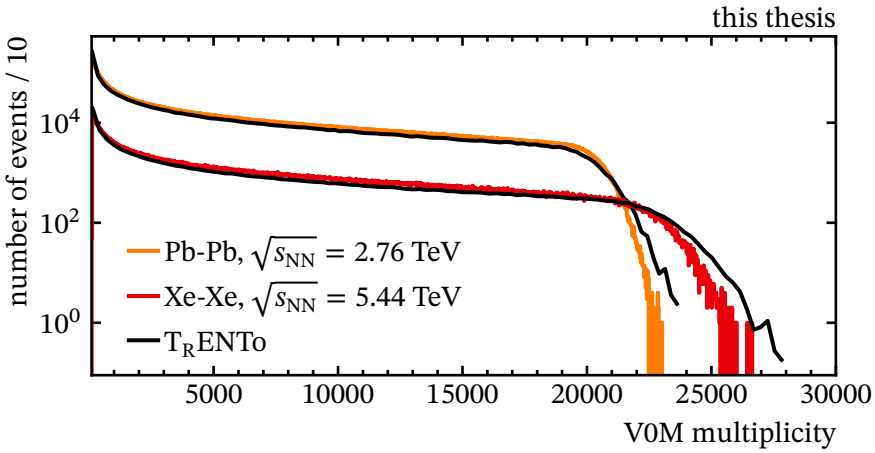

Figure 4.20: Multiplicity of $\mathrm{T_R}$ENTo (black curves) scaled to the V0M multiplicity, which is used to estimate the centrality in Xe-Xe (red curve) and Pb-Pb (orange curve) collisions.

The initial eccentricity of a single collision in $\mathrm{T_R}$ENTo is calculated using eq. (1.4). $\mathrm{T_R}$ENTo discretizes the reduced thickness function $T_R(x, y)$ in the transverse plane xy. The eccentricities can be rewritten by using the weighted variances along the x and y direction

$$\begin{aligned}
\sigma_x^2 &= \frac{1}{\sum_i T_R(x_i)} \sum_i T_R(x_i)(x_i - \overline{x})^2 \\
\sigma_y^2 &= \frac{1}{\sum_i T_R(y_i)} \sum_i T_R(y_i)(y_i - \overline{y})^2 \\
\sigma_{xy}^2 &= \frac{1}{\sum_{i,j} T_R(x_i, y_j)} \sum_{i,j} T_R(x_i, y_j)(x_i - \overline{x})(y_j - \overline{y}) \,,
\end{aligned} \tag{4.8}$$

where $T_R(x_i)$ is integrated over the y direction, and vice versa. Therefore, the eccentricities in a single collision are

$$\begin{aligned} \varepsilon_{RP} &= \frac{\sigma_x^2 - \sigma_y^2}{\sigma_x^2 + \sigma_y^2} \\ \varepsilon_2 &= \frac{\sqrt{(\sigma_x^2 - \sigma_y^2)^2 - 4\sigma_{xy}^2}}{\sigma_x^2 + \sigma_y^2} \end{aligned} \tag{4.9}$$

where x' and y' describe the positions in the center-of-mass frame. The average eccentricities in T$_\mathrm{R}$ENTo are calculated in these centrality classes using

$$\begin{aligned} \varepsilon_2\{\Psi_{RP}\} &= \langle \varepsilon_{RP} \rangle \\ \varepsilon_2\{2\} &= \sqrt{\langle \varepsilon_2^2 \rangle} \\ \varepsilon_2\{4\} &= \sqrt[4]{-\langle \varepsilon_2^4 \rangle + 2\langle \varepsilon_2 \rangle^2}\,, \end{aligned} \tag{4.10}$$

where the cumulants correspond to the estimates of v_2 introduced in section 3.2.2.

Figure 4.21 shows the average eccentricities for Pb-Pb and Xe-Xe collisions. For peripheral collisions a splitting between $\varepsilon_2\{4\}$ and $\varepsilon_2\{\Psi_{RP}\}$ is observed. For Xe-Xe a strong increase of the ratios $\varepsilon_2\{2\}/\varepsilon_2\{4\}$ and $\varepsilon_2\{\Psi_{RP}\}/\varepsilon_2\{4\}$ is seen in central collisions. These ratios can be compared to the ratios obtained from the measurement.

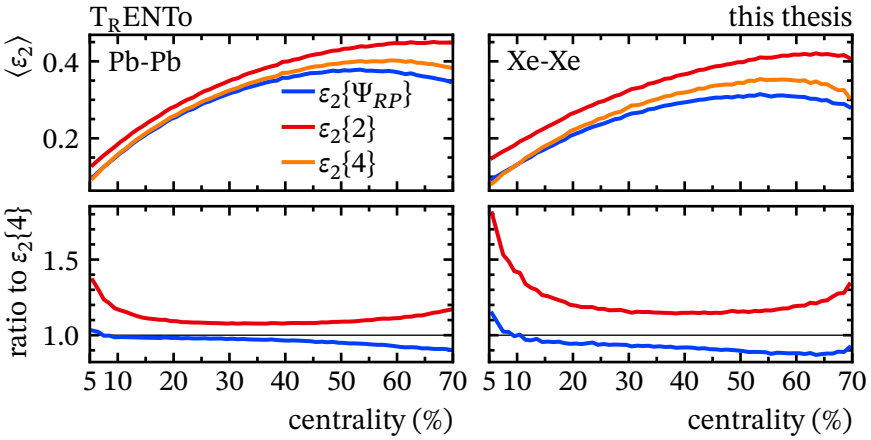

Figure 4.21: Average eccentricities as a function of the centrality in T$_\mathrm{R}$ENTo for Pb-Pb and Xe-Xe collisions. Lower panels show the ratio to $\varepsilon_2\{4\}$.

For the multiplicity scaling of elliptic flow, the transverse area S of the collision is needed. The average transverse area[67] S of a class of collisions can be calculated using eq. (4.8) as follows

$$S = 4\pi\sigma_x\sigma_y\,. \tag{4.11}$$

Figure 4.22 shows the centrality-dependence of the transverse area S for Pb-Pb and Xe-Xe collisions. A larger average transverse area is observed for Pb-Pb collisions at the same centrality as is expected from the larger number of colliding nucleons.

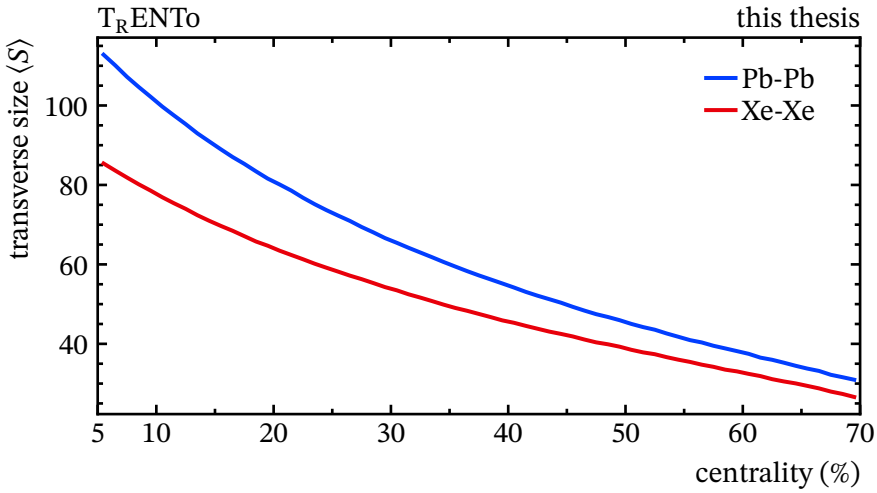

Figure 4.22: The average transverse area $\langle S \rangle$ as a function of the centrality in T$_R$ENTo for Pb-Pb and Xe-Xe collisions.

4.9.2 Extraction of Elliptic Power Model Parameters

The elliptic power model parameters can be extracted from a fit to the flow cumulants. For the extraction at least four cumulants are necessary. In this analysis $c_2\{2\}$, $c_2\{4\}$, $c_2\{6\}$ and $c_2\{8\}$ are being used for the estimation. The cumulants, measured by ALICE[68] in Pb-Pb collisions at $\sqrt{s_{\mathrm{NN}}} = 2.76\,\mathrm{TeV}$, are shown in fig. 4.23. The measured cumulants are combined into 5 % bins between 5 % to 70 % centrality.

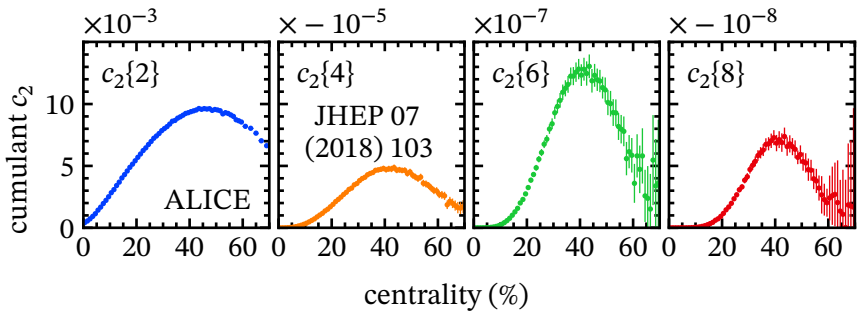

Figure 4.23: Centrality dependence of the multi-particle cumulants in Pb-Pb collisions at $\sqrt{s_{\mathrm{NN}}} = 2.76\,\mathrm{TeV}$ from ref.[68]. The cumulants are used for the elliptic power model fits. Only the statistical uncertainty is shown.

The curve fitting is performed by using the method of least squares to minimize the χ^2/ndf of the EPM[148]. In each centrality interval a separate minimization is performed. Figure 4.24 shows the resulting χ^2/ndf distribution in different slices of the three parameters. The minimum χ^2/ndf gives the optimal parameters of the model. The best fit parameters are shown by the red point in the upper plots and the dashed red line in the lower plot. Figure 4.25 shows the values of the three parameters of the EPM model as a function of centrality. The open red squares correspond to the parameters extracted in Pb-Pb collisions at $\sqrt{s_{\mathrm{NN}}} = 5.02\,\mathrm{TeV}$ collisions in ref.[68]. The fit is consistent with the parameters extracted at higher energies. A

similar result is shown in fig. 1.21, where the difference between the measurements of ATLAS and the EPM prediction extracted from fits to ALICE data at higher energies are in good agreement. As both results are consistent, the parameters extracted as a part of this work at $\sqrt{s_{\mathrm{NN}}} = 2.76\,\mathrm{TeV}$ will be used.

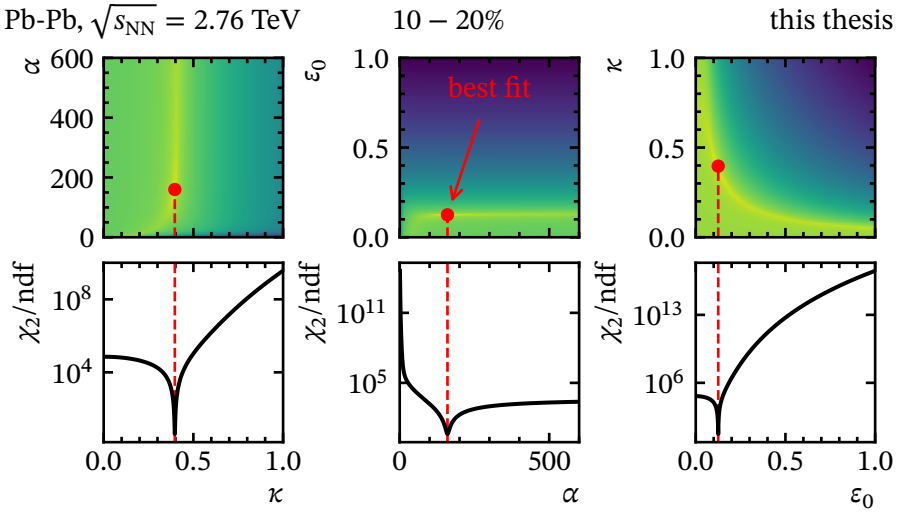

Figure 4.24: Goodness of fit χ^2/ndf of the EPM fit to the cumulants in centrality range 10 % to 20 %. In the upper panels low values are indicated by brighter regions. The best fit parameters are shown by the red points.

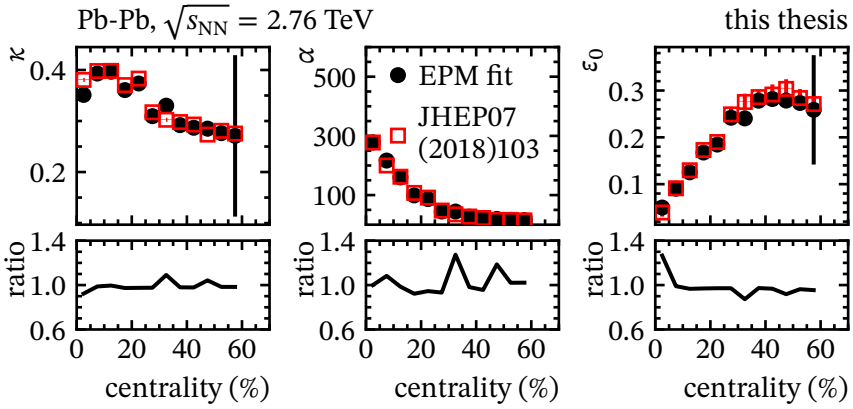

Figure 4.25: Fit parameters κ, α, ε_0 extracted from the elliptic power model fits. Results obtained from the fit to Pb-Pb collisions at $\sqrt{s_{\mathrm{NN}}} = 2.76\,\mathrm{TeV}$ (black points) are compared to fits to Pb-Pb collisions at $\sqrt{s_{\mathrm{NN}}} = 5.02\,\mathrm{TeV}$ (red open squares) from ref.[68].

4.10 Studies of Systematic Uncertainties

Systematic uncertainties are uncertainties related to an incomplete knowledge of the measurement or a theoretical model. These uncertainties need to be estimated using dedicated studies and careful considerations of the analysis procedure.

In the following section, the method to evaluate the systematic uncertainties is introduced. It can be summarized as follows. First, possible sources of systematic uncertainties in the analysis procedure are identified. Second, their impact on the resulting measurement is evaluated by altering the default analysis. Then, the statistical significance of these different variations is evaluated using the Barlow test. Finally, all the statistically significant and independent systematic uncertainties are combined in quadrature. After the different steps in the evaluation of the uncertainties have been introduced, the whole procedure is explained using the example of $v_2\{\Psi_{SP}\}$. The section ends with a summary of the total systematic uncertainties of the measurements.

4.10.1 Sources of Systematic Uncertainties

The sources of systematic uncertainties can be broadly categorized according to the different steps of the analysis procedure.

1. Event selection
2. Track selection
3. Correction of the tracking detector non-uniform acceptance and efficiency
4. Correction of the ZDC non-uniform acceptance
5. Calculation of observables

For some sources the evaluation of the systematic uncertainty relates to a change of the numerical value of the selection criteria (e.g. the track selection criteria). For others the impact on the measurement is evaluated by changing the whole procedure. An overview showing all included variations is given in table 4.8. The details of the variations of the analysis procedure are explained in section 4.10.2.

Table 4.8: Overview of all variations performed for the different sources of systematic uncertainties.

Analysis Variation	Default setting	Varied setting
Event selection		
Centrality estimator	V0M	CL1
Primary vertex position $\lvert V_z \rvert$	< 10 cm	< 8 cm
Solenoid magnet polarity	both	separate
Track selection		
Filter bit selection	hybrid	tight-DCA
Min. clusters TPC	70	90
Max. χ^2 per TPC cluster	4	3
Charge	both	separate
Tracking detectors non-uniformities		
Non-uniform acceptance	φ-weights	no weights
Reconstruction efficiency	all particles	π, K, p, μ, e only
ZDC non-uniform acceptance correction		
q_n re-centering	4d procedure	iterative procedure
Gain equalization	not applied	applied
$\langle xy \rangle \langle yx \rangle$ bias	not applied	applied
Calculation of $v_2\{\Psi_{SP}\}$		
averaging of components	average	separate
Calculation of Multiplicity scaling		
T$_\mathrm{R}$ENTo model parameters	Nature Phys.[56]	Phys. Rev. C[149]

4.10.2 Variations of the Analysis Procedures

In this section the changes of the analysis procedure related to the estimation of the systematic uncertainty are explained.

4.10.2.1 Iterative Recentering of ZDC Flow Vectors

An alternative correction scheme is used to evaluate the sensitivity of the elliptic flow coefficient on the correction procedure. The impact of the coarse binning of the default recentering scheme along the vertex position dimensions is investigated by using an iterative recentering procedure. In this iterative recentering procedure, the dependence along the components of the vertex position is treated with a finer binning of the correction histograms. In this iterative approach, with each iteration the binning switches between a fine-grained one-dimensional correction and a coarse grained four-dimensional correction. Table 4.9 summarizes the iterations and the corresponding binning of the correction histograms. The iterative procedure is divided into eight steps. The recentered flow vector of one iteration step is the input flow vector into the next iterative recentering step. In the first step, a coarse four-dimensional correction is used to recenter the flow vector and take into account the correlations between the

variables. Afterward, the recentered flow vector of the first step is recentered again using four successive recentering corrections with respect to each of the variables. The next iterations repeat this cycle of $1 \times 4d \rightarrow 4 \times 1d$ corrections as indicated by the "iteration" row in the table, where the four-dimensional correction is step a and the one-dimensional corrections are step b.

Figure 4.26 shows the mean flow vector of ZNA $\langle q_1 \rangle$ after each of the four iterations. The improvement in each iteration is largest for the V_z component, because it is the first of the one-dimensional iterations.

Table 4.9: Binning of the iterative recentering correction histograms. The "Iteration" column shows in which iteration binning is used. The "Dimensions" column indicates whether 4×1-dim histograms or the 4-dim histogram is used.

		Binning		
Variable	Range	Coarse	Finer	Finest
Vertex z position in $n\sigma_{V_y}$	$(-3, 3)$	5	25	50
Vertex x position in $n\sigma_{V_x}$	$(-3, 3)$	5	25	50
Vertex y position in $n\sigma_{V_y}$	$(-3, 3)$	5	25	50
Centrality	$(0, 80)$	5	40	80
	Iteration	$1a, 2a, 3a, 4a$	$1b, 2b$	$3b, 4b$
	Dimensions	1×4-dim	4×1-dim	4×1-dim

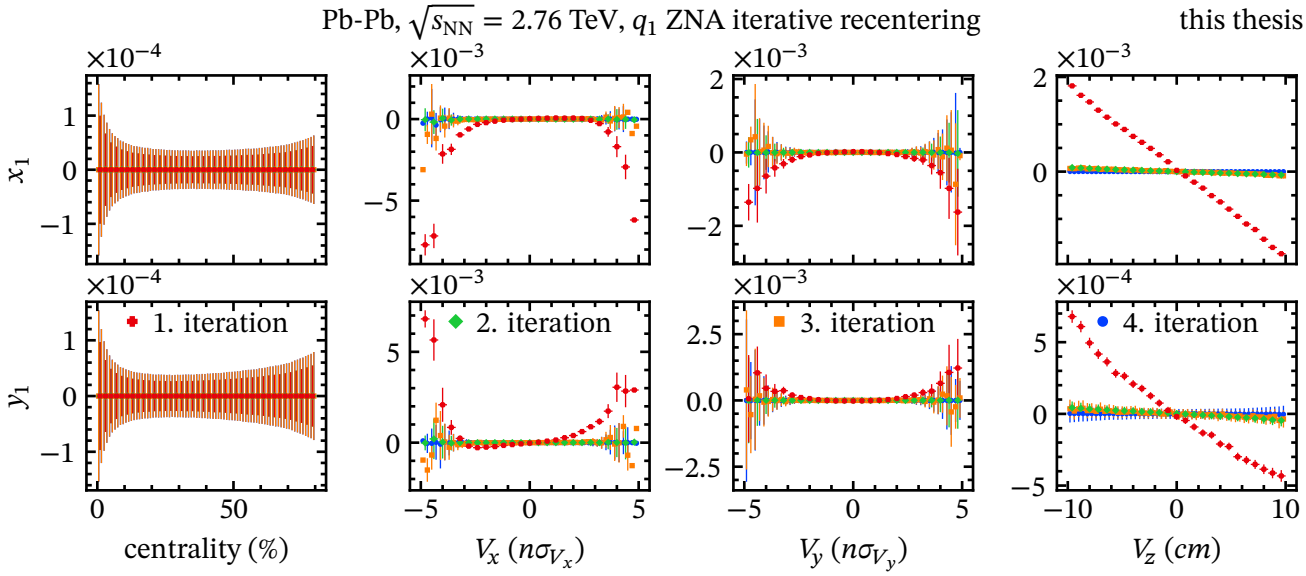

Figure 4.26: Mean of x_1 and y_1 of ZNA as a function of centrality and vertex positions v_x, v_y, v_z for Pb-Pb collisions at $\sqrt{s_{\mathrm{NN}}} = 2.76$ TeV. The mean flow vector components are presented after the correction is applied in the binning of the correction histogram. The different colored markers correspond to the iterations.

4.10.2.2 Gain Equalization of ZDC Flow Vectors

Gain equalization, introduced in section 3.5.3, is applied as an additional correction before the default recentering correction.

For this the average signal in the four channels in each of the ZDC is calculated in each of the data runs, separately. The average signals of the channels are then equalized using eq. (3.77).

The average signals of the four ZNA and ZNC channels are shown in fig. 4.27 for one data run in Xe-Xe and Pb-Pb collisions, respectively. Prior to recentering all channels have a different average signal $\langle E_i \rangle$. After recentering the average signals are equalized.

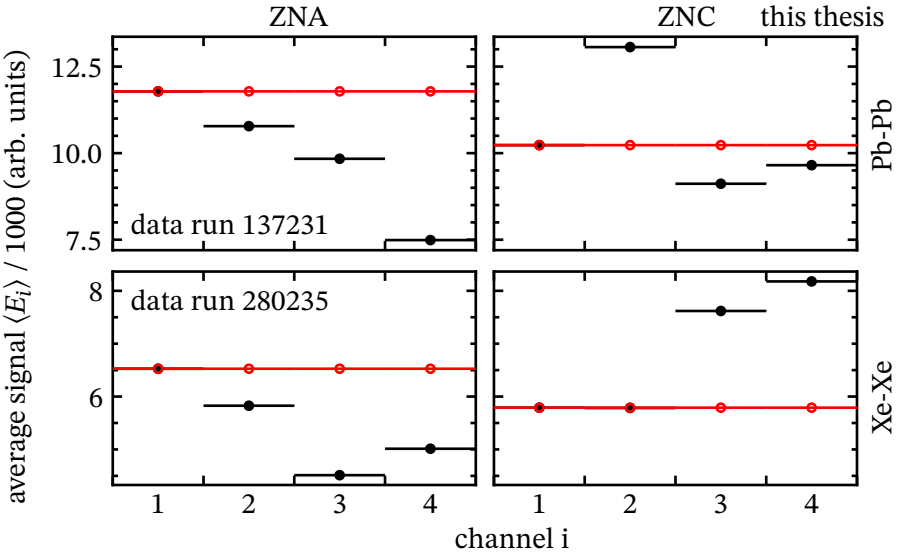

Figure 4.27: Average signals of the four ZNA and ZNC channels without (black data points) and with (red data points) gain equalization applied for one data run in the Xe-Xe and Pb-Pb data samples.

4.10.2.3 Non-zero Correlation Terms of ZDC

As observed in fig. 4.6, even after the recentering correction is applied, a non-zero signal is present for the $\langle x_1 y_1 \rangle$ and $\langle y_1 x_1 \rangle$ correlations. Such a correlation between different spatial components of the deflection of the spectators on opposite sides of the collision is not expected. It could indicate an unknown and uncorrected contribution from an imperfect correction procedure. Figure 4.28 shows a zoom into the $\langle x_1 y_1 \rangle$ $\langle y_1 x_1 \rangle$ correlations in the upper right panel. The correlations do not show the expected zero signal. These nonzero signals could originate from correlated deformations of both ZNA and ZNC which cannot be treated with the recentering correction procedure used in this analysis, as it only corrects for single detector anisotropies. To estimate the impact of such a non-zero component on the final observable the so-called ZDC-scale uncertainty is introduced. The scale uncertainty is

given by

$$\text{ZDC scale uncertainty} = \sqrt{\left|\frac{\langle x_1 y_1\rangle\langle y_1 x_1\rangle}{\langle x_1 x_1\rangle\langle y_1 y_1\rangle}\right|}\,. \tag{4.12}$$

Figure A.5 shows the scale uncertainty for the Xe-Xe collision data sample. Within the statistical precision of the data the ZDC-scale uncertainty is independent of the centrality. Therefore, a centrality-average uncertainty is applied for the ZDC-scale uncertainty.

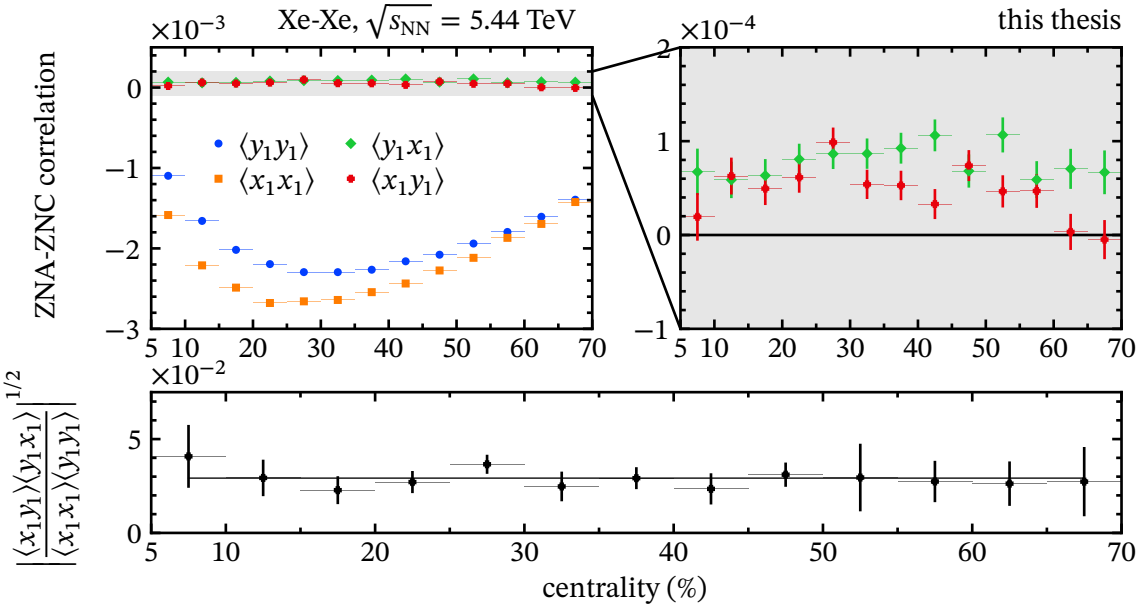

Figure 4.28: ZNA-ZNC correlations and ZDC-scale uncertainty for the Pb-Pb collisions data sample. Upper left plot shows the centrality dependence of the correlation (also shown in fig. 4.6). The gray area corresponds to the area covered by the upper right panel. The black line at zero shows the expectation for the $\langle x_1 y_1\rangle$ and $\langle y_1 x_1\rangle$ correlations. The lower panel shows the derived scale uncertainty. The black line in the lower panel corresponds to a fit of a constant to the data to guide the eye.

4.10.2.4 Track Reconstruction Efficiency

To evaluate the systematic uncertainty related to the extraction of the track reconstruction efficiency an alternative definition of the efficiency is used. This alternative definition only includes the following particles in the calculation of the efficiency: all charged π, e, μ, charged K, p and their corresponding antiparticles.

Figure 4.29 shows the comparison between the track reconstruction efficiency calculated using the default selection of tracks that includes all primary particles versus the alternative definition. For low transverse momenta, the difference is negligible. For higher transverse momentum, the difference grows to approximately 5 %. The secondary contamination is identical for both approaches.

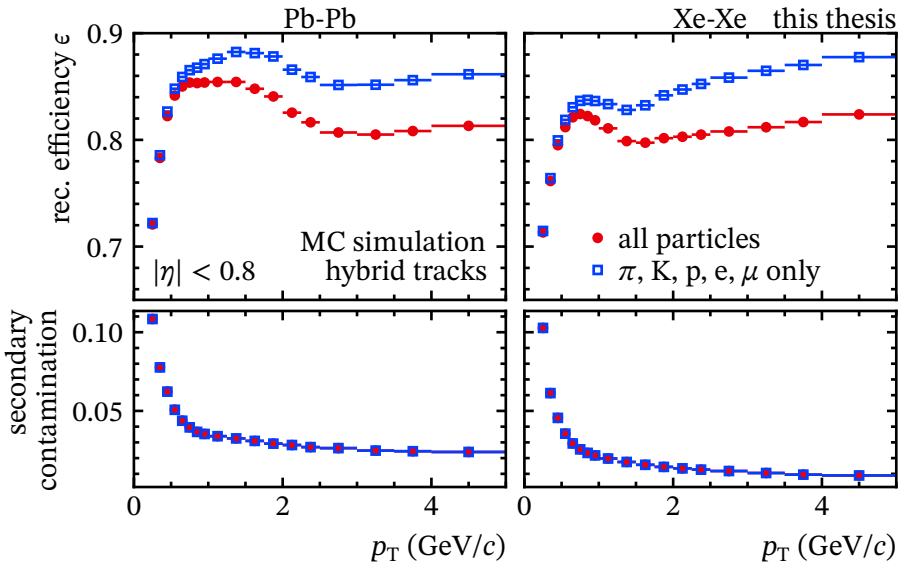

Figure 4.29: The transverse momentum dependence of the track reconstruction efficiency for the 5–70% centrality range shown for the default selection of tracks compared to the efficiency obtained only with charged π, e, μ, charged K, p and their corresponding antiparticles.

4.10.2.5 TRENTo model parameters

To estimate the systematic uncertainty related to the T$_\mathrm{R}$ENTo model the model parameters are varied. Besides the default parameters (called Nat. Phys.) shown in section 4.9.1 the model parameters from ref.[149] (called JETSCAPE) are used. The parameters have been extracted using Bayesian inference from Pb-Pb collisions at $\sqrt{s_{\mathrm{NN}}} = 2.76$ TeV and Au-Au collisions at $\sqrt{s_{\mathrm{NN}}} = 200$ GeV.

Table 4.10: T$_\mathrm{R}$ENTo model parameters JETSCAPE from ref.[149].

Parameters	Reduced thickness p	Fluctuations k	Nucleon width w	Min. distance d
Values	0.048	0.873	1.05	1.429

Figure 4.30 shows the impact of the different T$_\mathrm{R}$ENTo parameters on the reaction plane eccentricity ε_{RP} and the transverse area S. For both ε_{RP} and S, the difference between the Nat. Phys. and the JETSCAPE result increases as the collisions become more peripheral. In Pb-Pb and Xe-Xe the same trend can be observed. JETSCAPE predicts a lower eccentricity and simultaneously a higher transverse size. The impact of this on the multiplicity scaling is studied and a systematic uncertainty is assigned to the multiplicity scaling.

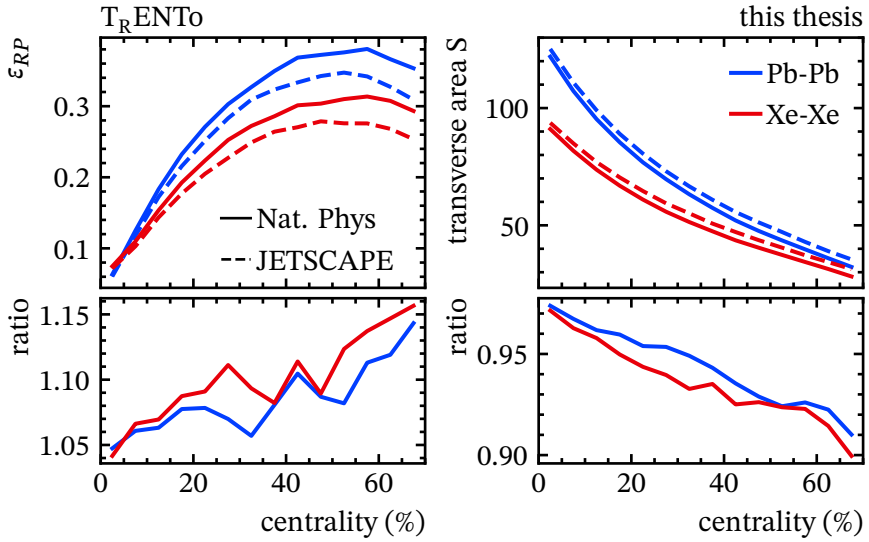

Figure 4.30: Comparison of reaction plane eccentricity and transverse area S from T$_R$ENTo using the Nat. Phys. settings from ref.[56] and JETSCAPE settings from ref.[149] for Xe-Xe and Pb-Pb collisions.

4.10.3 Evaluation and Combination of Systematic Uncertainties

The sensitivity of the measurement to these variations of the analysis procedure is evaluated by comparing the results obtained with the default analysis to the result obtained using a varied selection.

4.10.3.1 Barlow Test

For a given test only one of the variables is varied. The Barlow σ estimates the significance of the varied selection by

$$\sigma_{Barlow} = \frac{|x_{var} - x_{std}|}{\sqrt{|\sigma^2_{var} \mp \sigma^2_{var}|}} , \tag{4.13}$$

where x_{std} is the result obtained with the default selection, x_{var} is the result obtained with the varied selection, $\sigma_{stat,var}$, and $\sigma_{stat,std}$ are the statistical uncertainties of the measurement. If the default and the varied measurement are statistically uncorrelated, the plus sign has to be used in the denominator. The variation of the change of the analysis procedure is statistically significant, if

$$\sigma_{Barlow} > 1 \tag{4.14}$$

is fulfilled. In this case the variation has failed the Barlow test. The choice of larger than one is a common choice in the ALICE Collaboration.

If the variation failed the Barlow test the variation is considered as a source of systematic uncertainty. The relative variation is given by the ratio

$$\sigma_{sys} = \frac{|x_{var} - x_{std}|}{x_{std}} . \tag{4.15}$$

It is equivalent to a percentage error on the mean of the default measurement x_{def}.

The Barlow test is performed for every centrality bin separately. If more than 32% of the bins fail the criterion the variation is applied as a systematic uncertainty for all bins. The Barlow test is performed for all variations.

4.10.3.2 Combination of Systematic Uncertainties

If a variation fails the Barlow test, the impact on the measurement is evaluated. For p_{T}-integrated measurements the systematic uncertainty is calculated as a function of the centrality. A larger binning of 10 % is used for Pb-Pb collisions to reduce the impact of statistical fluctuations. For Xe-Xe collisions, the uncertainty is averaged over the whole centrality range 5 % to 70 % due to much larger statistical fluctuations.

For the transverse-momentum differential measurements the systematic uncertainties are divided into uncertainties that only depend on the centrality of the collision, or correlated systematic uncertainties and those that depend on p_{T} also called uncorrelated systematic uncertainties. The correlated systematic uncertainties are evaluated using the same method as for the p_{T}-integrated measurements. For the p_{T}-differential flow measurements these two contributions are added in quadrature.

Under the assumption that the individual components of variation are uncorrelated, all contributions to the systematic uncertainty are summed in quadrature. The total systematic uncertainty σ_{tot} therefore is

$$\sigma_{sys,tot} = \sqrt{\sum_i \sigma_{sys,i}^2}\,, \tag{4.16}$$

where $\sigma_{sys,i}$ is the relative variation of the selection i.

For the analysis of Pb-Pb collisions, the total systematic uncertainties are interpolated using a cubic spline to obtain the uncertainties in 5 %-bins.

For the ESE-selected elliptic flow ratios, the systematic uncertainties are calculated for each selection using each detector separately. Afterward, the high and low $|q_{1,ese}|$-selection are averaged for a given detector.

4.10.4 Example of the Evaluation of Systematic Uncertainties

In the following, the systematic uncertainty evaluation is explained using the example of the measurement of $v_2\{\Psi_{SP}\}$ in Pb-Pb collisions.

Event Selection

Figure 4.31 shows the comparison between the default analysis and the analysis performed with the variation of the event selection criteria. Each variation is shown separately in the form of three figures. The top panel shows the observable. The default analysis is shown in red lines, and the variation is shown as black points. The center panel shows the ratio between the variation and the default as black data points. The red band shows the statistical uncertainties of the ratio. The black arrow on the right border indicates centrality average of

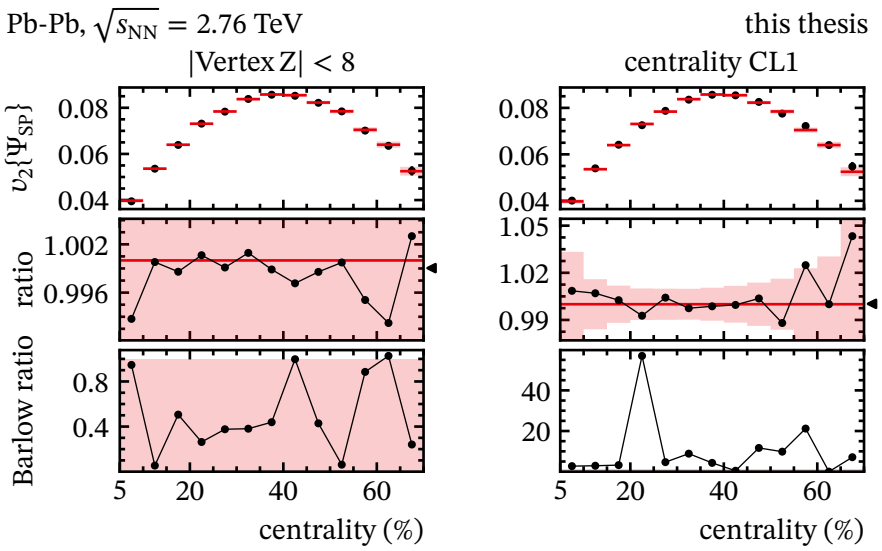

Figure 4.31: Comparison of the varied selection with the default analysis for $v_2\{\Psi_{SP}\}$ measured in Pb-Pb collisions at $\sqrt{s_{NN}} = 2.76$ TeV related to the event selection. The figure is explained in the text.

the ratio. On the bottom panel the Barlow criterion is shown. The red band highlight the 1σ region in which the Barlow criterion is passed.

The variation of the position of the primary vertex along the z-direction the interval is chosen smaller -8 cm to 8 cm than the standard selection -10 cm to 10 cm in ALICE. The position of the vertex might have an influence on the signals observed in the ZDC. If there is a correlated effect on both signals, this may not be rectified by flow vector non-uniformity corrections. It could also slightly affect the tracking performance of the tracking detectors. The variation observed for the vertex position is not statistically significant.

To estimate the influence of the choice of centrality estimator an alternative estimator (CL1), which is based on the number of SPD clusters, is used. The variation is shown on the right panel. This variation can be sensitive to possible biases from using the same centrality estimator for flow vector corrections and for the calculation of the observables. The variation is statistically significant and has the largest contribution in peripheral collisions.

Magnet Polarity

For the solenoid magnet polarity variation, the data samples taken with only positive (negative) magnet polarity are compared to the default. Figure 4.32 show that both variation fluctuate around the default selection. By construction, they show the opposite behavior. A systematic uncertainty is assigned equal to the average deviation between the two polarity settings. As there is no centrality-dependent trend visible and due to the large fluctuations the centrality-averaged ratios are used to estimate the deviations from the default analysis.

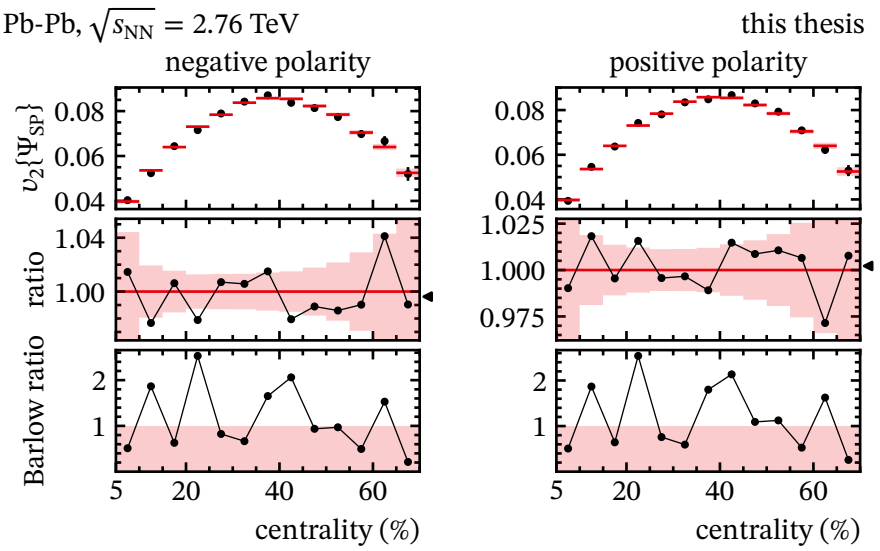

Figure 4.32: Comparison of the varied selection with the default analysis for $v_2\{\Psi_{SP}\}$ measured in Pb-Pb collisions at $\sqrt{s_{NN}} = 2.76$ TeV related to the solenoid magnet polarity. The figure is explained in the text.

Track Selection

In the analyzed data sample, most of the tracking details are encoded in the track selection. To estimate the influence of the tracking performance and contribution from particles from secondary decays to the analysis the default selection (hybrid tracks) is compared to a selection with a stricter distance to primary vertex constraint (tight-DCA tracks). The difference between the two track selections is shown in table 4.4. The default analysis is also compared to one based on the TPC-only tracks. Because of the known large contamination from secondary decays there is no systematic uncertainty associated to the difference of the hybrid tracks and TPC-only tracks. The impact on the analysis is shown in fig. 4.33. A systematic uncertainty is assigned to the difference between the tight-DCA and the default track selection.

An additional improvement of the tracking accuracy is possible by requiring more TPC clusters or a lower χ^2 per cluster in the TPC. Additionally, stricter selections lead to a worse track reconstruction efficiency. The comparisons of the default analysis with varied selections are shown in fig. 4.34. The selection on higher number of clusters may bias the selection of tracks towards higher transverse momenta. Both additional track selection criteria have a statistically significant but small impact on the analysis. A systematic uncertainty is assigned to take these effects into account.

The influence of the charge of the particles is studied comparing the results calculated only with positively or negatively charged particles. The variation is compared to the default selection including both charges. The particle charge variations are shown in fig. 4.35. The variations with charge of the particles are not statistically significant and do not fail the Barlow test. Therefore, no systematic uncertainty is assigned.

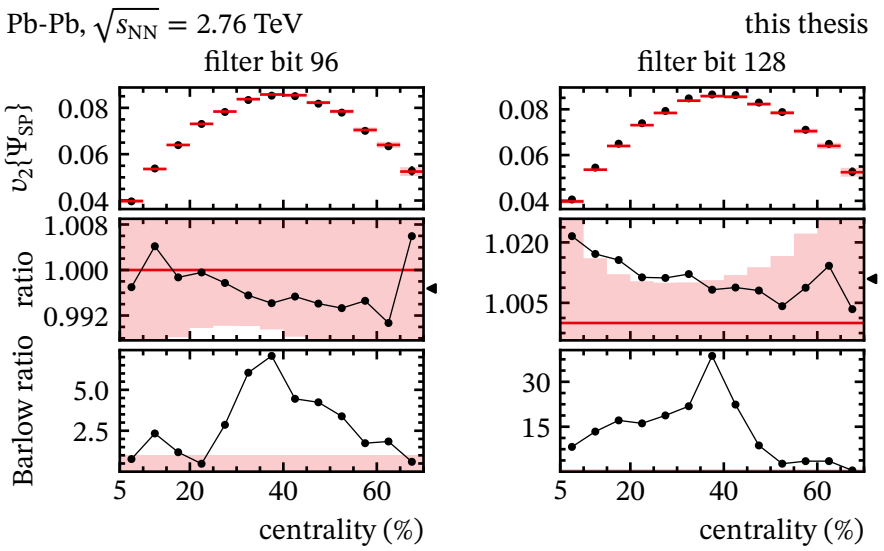

Figure 4.33: Comparison of the varied selection with the default analysis for $v_2\{\Psi_{SP}\}$ measured in Pb-Pb collisions at $\sqrt{s_{NN}} = 2.76$ TeV related to the track selection. The figure is explained in the text.

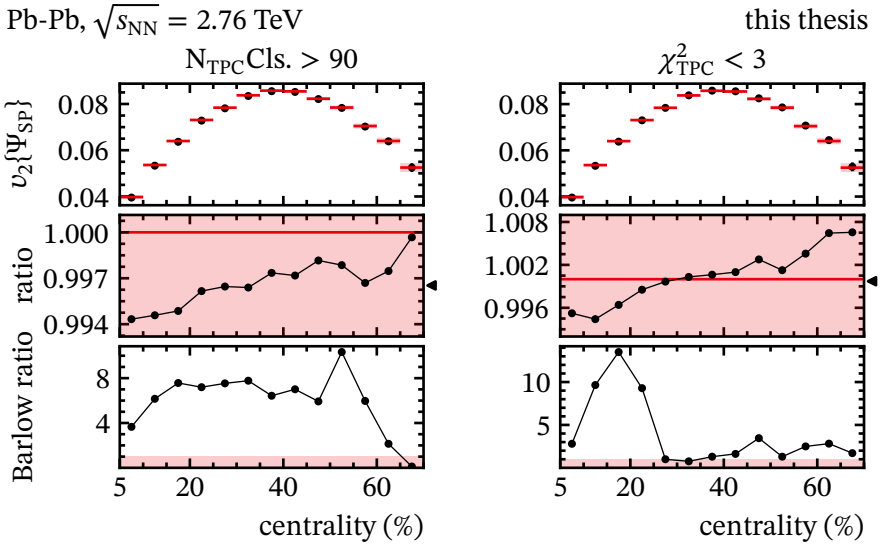

Figure 4.34: Comparison of the varied selection with the default analysis for $v_2\{\Psi_{SP}\}$ measured in Pb-Pb collisions at $\sqrt{s_{NN}} = 2.76$ TeV related to the track selection. The figure is explained in the text.

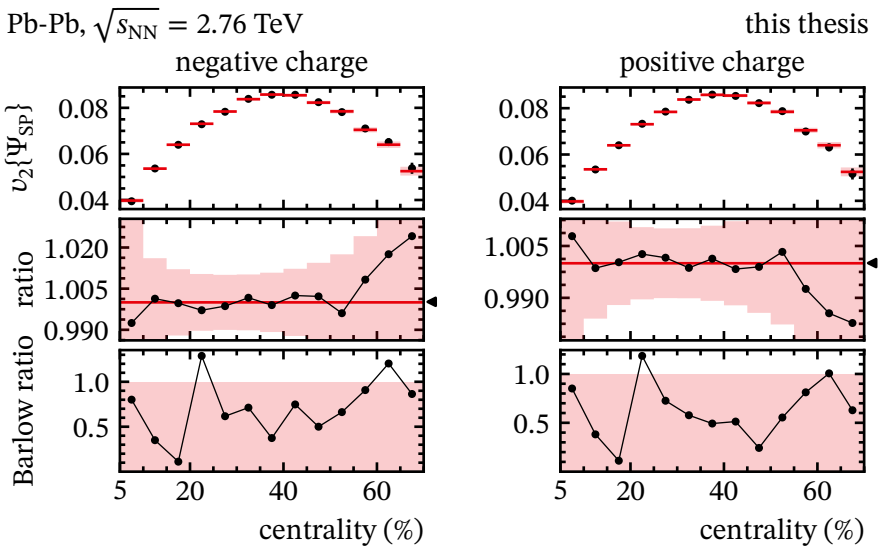

Figure 4.35: Comparison of the varied selection with the default analysis for $v_2\{\Psi_{SP}\}$ measured in Pb-Pb collisions at $\sqrt{s_{\mathrm{NN}}} = 2.76$ TeV related to the charges of the reconstructed particles. The figure is explained in the text.

Correction Procedure

In addition, the impact of the non-uniform acceptance weights (φ-weights) correction and the track reconstruction efficiency is shown in fig. 4.36. No systematic uncertainty is assigned to the φ-weights correction procedure. Even without applying φ-weights the changes pass the Barlow test. The systematic uncertainty associated to the track reconstruction efficiency is evaluated by only selecting pions, kaons, protons, electrons and muons in the MC simulation by relying on generated particle properties. With this special selection a small statistical significant difference is observed and therefore a systematic uncertainty is assigned to the track reconstruction efficiency.

Variations related to the ZDC flow vector correction scheme are shown in fig. 4.37. The left panels show the difference when the iterative flow vector recentering correction procedure is applied. The center panels show the impact of the gain equalization of the ZDC signals. The right panels indicate the size of leftover ZDC scale uncertainty. All three variations fail the Barlow test. Systematic uncertainties associated with the ZDC flow vector correction procedure are assigned to take these effects into account.

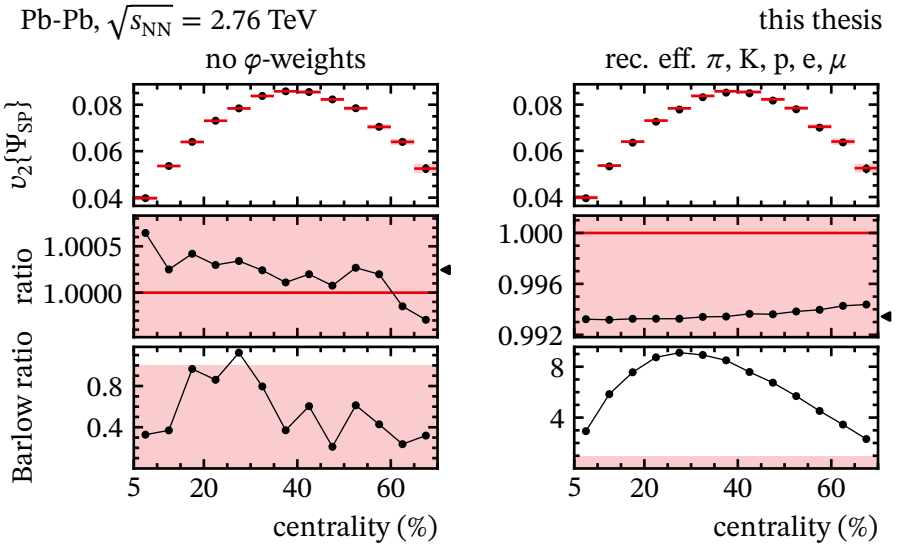

Figure 4.36: Comparison of the varied selection with the default analysis for $v_2\{\Psi_{SP}\}$ measured in Pb-Pb collisions at $\sqrt{s_{NN}} = 2.76$ TeV related to the corrections of the tracks. The figure is explained in the text.

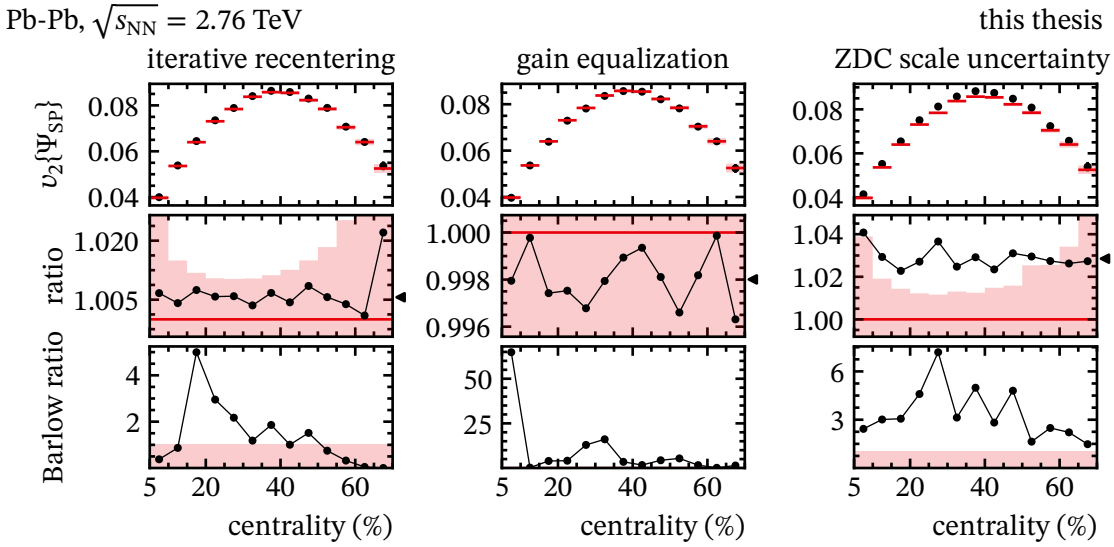

Figure 4.37: Comparison of the varied selections with the default analysis for $v_2\{\Psi_{SP}\}$ measured in Pb-Pb collisions at $\sqrt{s_{NN}} = 2.76$ TeV related to the flow vector corrections. The figure is explained in the text.

4.10.4.1 Calculation of the Observable

Figure 4.38 shows the variations related to the three different components in the average of the $v_2\{\Psi_{SP}\}$ (eq. (3.64)). The left, right, and center panels show the differences between the individual components of $v_2\{\Psi_{SP}\}$ and the average of $v_2\{\Psi_{SP}\}$ (see eq. (3.64)). The deviations of the variation of the $(\langle y_2 x_1 y_1\rangle\langle y_2 y_1 x_1\rangle)^{1/2}$ component is statistically significant. Therefore, a systematic uncertainty is assigned.

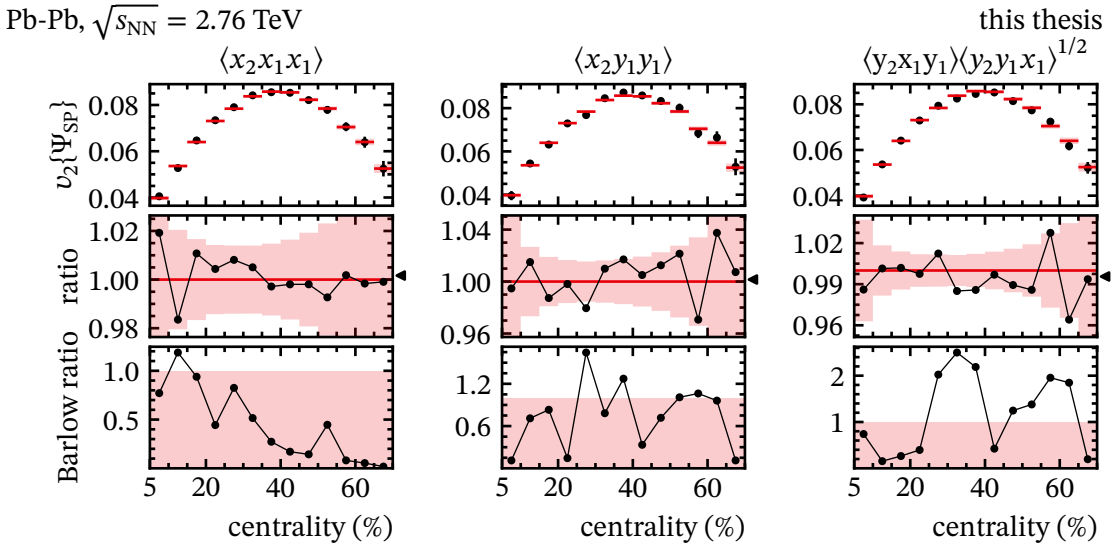

Figure 4.38: Comparison of the varied selections with the default analysis for $v_2\{\Psi_{SP}\}$ measured in Pb-Pb collisions at $\sqrt{s_{NN}} = 2.76$ TeV related to the different components in the $v_2\{\Psi_{SP}\}$ average. The figure is explained in the text.

4.10.4.2 Combination of Systematic Uncertainties

This results in the total systematic uncertainty as follows. As seen in this example, the Barlow ratios can have large fluctuations when they are calculated in 5 % centrality bins. This can affect the stability of the systematic uncertainty. Large jumps in the size of the systematic uncertainties are not expected. Figure 4.39,Figure 4.40, and Figure 4.41 shows a compilation of the total systematic uncertainties for $v_2\{\Psi_{SP}\}$ evaluated using three different centrality intervals: 5 % bins, 10 % bins, and the average over the whole 5 % to 70 % centrality range. The averaged result does not capture any dependence on centrality. The 5 % binning seems to suffer from large jumps in the contributions of the systematic uncertainties from different sources. The 10 % binning offers a compromise because it still captures the trend of the systematic uncertainties with centrality but is less effected by fluctuations. To obtain the systematic uncertainties in 5 % bins, they are evaluated by interpolating with a cubic spline.

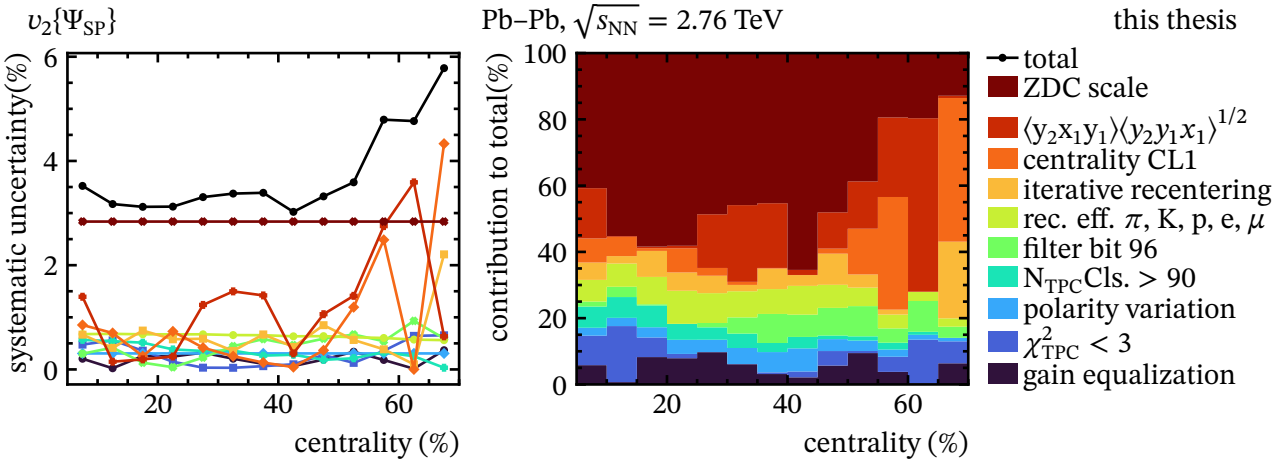

Figure 4.39: Systematic uncertainties in 5 % centrality bins.

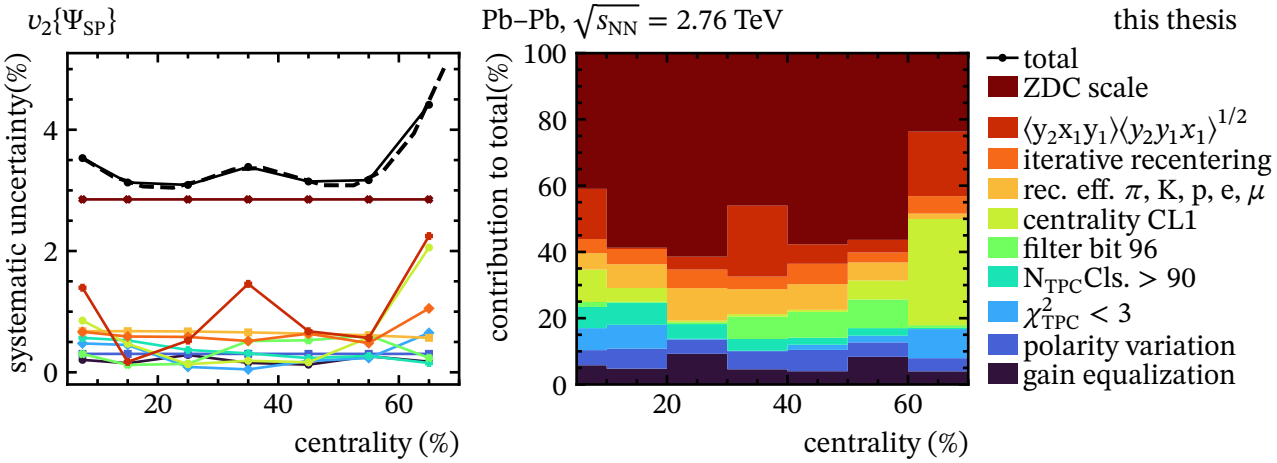

Figure 4.40: Systematic uncertainties in 10 % centrality bins.

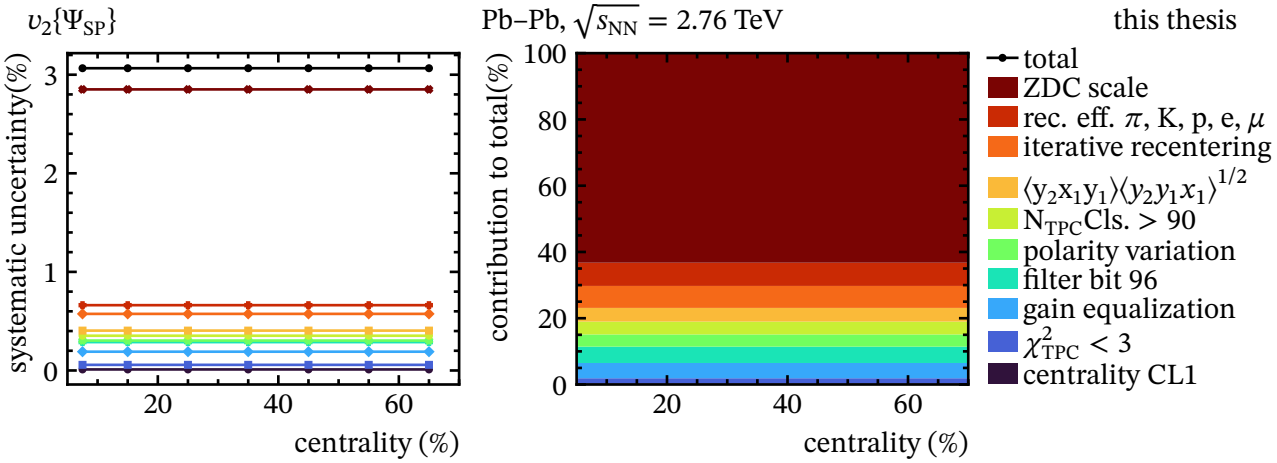

Figure 4.41: Systematic uncertainties averaged over 5 % to 70 % centrality.

4.10.5 Summary of Systematic Uncertainties

In the following tables the systematic uncertainties of the final measurements are summarized. Table 4.11 gives the total systematic uncertainties as a function of centrality in Pb-Pb collisions. Table 4.11 gives the total systematic uncertainties averaged over all centralities in Xe-Xe collisions. Table 4.13 gives the systematic uncertainty of the ratios of elliptic flow measured in ESE-selected over unbiased collisions performed for the Pb-Pb data sample. Table 4.14 gives the correlated systematic uncertainty of the p_{T}-differential measurements performed in Pb-Pb collisions. The uncorrelated p_{T}-differential systematic uncertainties are shown in appendix A.2.

Table 4.11: Overview of the systematic uncertainties as a function of centrality in Pb-Pb collisions.

	Systematic Uncertainty (%)				
Centrality (%)	$v_2\{\Psi_{\mathrm{SP}}\}$	$v_2\{2, \lvert\Delta\eta\rvert > 1\}$	$v_2\{4\}$	$\frac{v_2\{\Psi_{\mathrm{SP}}\}}{v_2\{4\}}$	$\frac{v_2\{2,\lvert\Delta\eta\rvert>1\}}{v_2\{4\}}$
$5-10$	3.5	0.9	1.9	3.8	1.8
$10-15$	3.2	0.9	1.2	3.2	1.2
$15-20$	3.1	0.9	0.9	3.0	0.8
$20-25$	3.0	0.9	0.8	3.0	0.7
$25-30$	3.2	1.0	0.8	3.1	0.5
$30-35$	3.3	1.1	0.9	3.2	0.5
$35-40$	3.4	1.1	0.9	3.3	0.5
$40-45$	3.2	1.2	1.0	3.1	0.6
$45-50$	3.1	1.2	1.2	3.0	0.7
$50-55$	3.1	1.2	1.5	3.0	0.9
$55-60$	3.3	1.3	2.0	3.1	1.4
$60-65$	3.9	1.4	2.8	3.6	2.5
$65-70$	5.0	1.6	4.0	4.4	4.4

Table 4.12: Overview of the systematic uncertainties as a function of centrality in Xe-Xe collisions.

	Systematic Uncertainty (%)				
Centrality (%)	$v_2\{\Psi_{\mathrm{SP}}\}$	$v_2\{2, \lvert\Delta\eta\rvert > 1\}$	$v_2\{4\}$	$\frac{v_2\{\Psi_{\mathrm{SP}}\}}{v_2\{4\}}$	$\frac{v_2\{2,\lvert\Delta\eta\rvert>1\}}{v_2\{4\}}$
$5-70$	9.2	2.3	2.4	8.8	0.3

Table 4.13: Overview of the systematic uncertainties for the ESE-selected ratios of elliptic flow as a function of centrality in Pb-Pb collisions. ZNA and ZNC stand for the detector used for the selection of $|q_{1,ese}|$

	Systematic Uncertainty (%)				
	$\frac{v_2\{2,\|\Delta\eta\|>1,\text{ selected}\}}{v_2\{2,\|\Delta\eta\|>1,\text{ unbiased}\}}$			$\frac{v_2\{4,\text{ selected}\}}{v_2\{4,\text{ unbiased}\}}$	
Centrality (%)	ZNA	ZNC	Centrality (%)	ZNA	ZNC
$5-10$	0.2	0.5	$5-10$	0.5	0.5
$10-15$	0.2	0.3	$10-20$	0.3	0.3
$15-20$	0.2	0.2			
$20-25$	0.2	0.2	$20-30$	0.2	0.2
$25-30$	0.2	0.2			
$30-35$	0.2	0.2	$30-40$	0.2	0.2
$35-40$	0.2	0.2			
$40-45$	0.2	0.2	$40-50$	0.2	0.2
$45-50$	0.3	0.2			
$50-55$	0.4	0.3	$50-60$	0.2	0.2
$55-60$	0.7	0.4			
$60-65$	1.0	0.6	$60-70$	0.2	0.2
$65-70$	1.4	1.0			

Table 4.14: Overview of the bin-to-bin correlated systematic uncertainties for the p_{T}-differential measurements in Pb-Pb collisions.

Centrality (%)	$v_2\{\Psi_{\mathrm{SP}}\}$	$\frac{v_2\{\Psi_{\mathrm{SP}}\}}{v_2\{4\}}$
$5-10$	3.4	3.7
$10-20$	3.0	3.1
$20-30$	3.0	3.0
$30-40$	3.3	3.3
$40-50$	3.0	3.0
$50-60$	3.0	3.0
$60-70$	4.3	4.0

5 Results

In this section, the results on the elliptic flow measured in Pb-Pb and Xe-Xe collisions at $\sqrt{s_{\mathrm{NN}}} = 2.76\,\mathrm{TeV}$ and $\sqrt{s_{\mathrm{NN}}} = 5.44\,\mathrm{TeV}$ are presented. Ratios of elliptic flow are compared to ratios of initial eccentricities predicted by the $\mathrm{T_R ENTo}$ and elliptic power models. The correlation between the elliptic flow in mid-rapidity and the magnitude of directed flow of spectators using event shape engineering is presented.

The results on the elliptic flow, flow fluctuations, and the multiplicity scaling of elliptic flow have been internally reviewed by the ALICE Collaboration and are approved for publication. The publication[2] is currently in preparation.

5.1 Elliptic Flow

The basic observable reconstructed in the analysis is the elliptic flow. The measurement of elliptic flow is performed using three different flow estimators $v_2\{\Psi_{SP}\}$, $v_2\{4\}$, and $v_2\{2, |\Delta\eta| > 1\}$ (introduced in chapter 3). From the measurements of the elliptic flow coefficients using the three different methods, observables sensitive to the flow fluctuations are constructed. The measurement of $v_2\{4\}$ and $v_2\{2, |\Delta\eta| > 1\}$ has been re-performed to study the systematic uncertainties consistently with the novel $v_2\{\Psi_{SP}\}$ measurement. The re-analysis is in agreement with the previously obtained results[67,68].

The p_{T}-integrated flow is determined in both collision systems as a function of the collision centrality for particles within $|\eta| < 0.8$ and $p_{\mathrm{T}} > 0.2\,\mathrm{GeV}/c$. The p_{T}-differential flow is been measured in Pb-Pb collisions in several centrality classes for particles within $|\eta| < 0.8$.

5.1.1 Centrality Dependence

The p_{T}-integrated flow has been determined in the range of 5 % to 70 % centrality. For Pb collisions, the measurement is performed in 5 %-wide bins. In Xe collisions, the measurement is performed in the centrality percent intervals (5, 10), (10, 20), (20, 30), (30, 40), (50, 60), (60, 70). The results obtained in Pb collisions are more differential due to the larger number of recorded collisions. Figure 5.1 shows the results for Pb-Pb collisions in the left panel and Xe-Xe collisions in the right panel.

In central collisions, an excess of $v_2\{2, |\Delta\eta| > 1\}$ measured in Xe-Xe collisions compared to Pb-Pb collisions is observed. This observation is in agreement with a previous measurement of $v_2\{2, |\Delta\eta| > 2\}$ in Pb-Pb collisions at $\sqrt{s_{\mathrm{NN}}} = 5.02\,\mathrm{TeV}$ and Xe-Xe collisions shown in fig. 1.23. This excess in central Xe-Xe collision is explained by two effects. First, it has been demonstrated in simulations that the size of the fluctuations depends inversely on the number of sources or nucleons in the initial state in spherical symmetric systems[35]. Therefore, larger fluctuations are expected in central Xe-Xe collisions since the mean value of the number of participants is lower than in central Pb-Pb collisions. The larger fluctuations increase the initial eccentricity $\varepsilon_n\{2\}$ that propagates to the measured $v_2\{2, |\Delta\eta| > 1\}$. Second, the shape

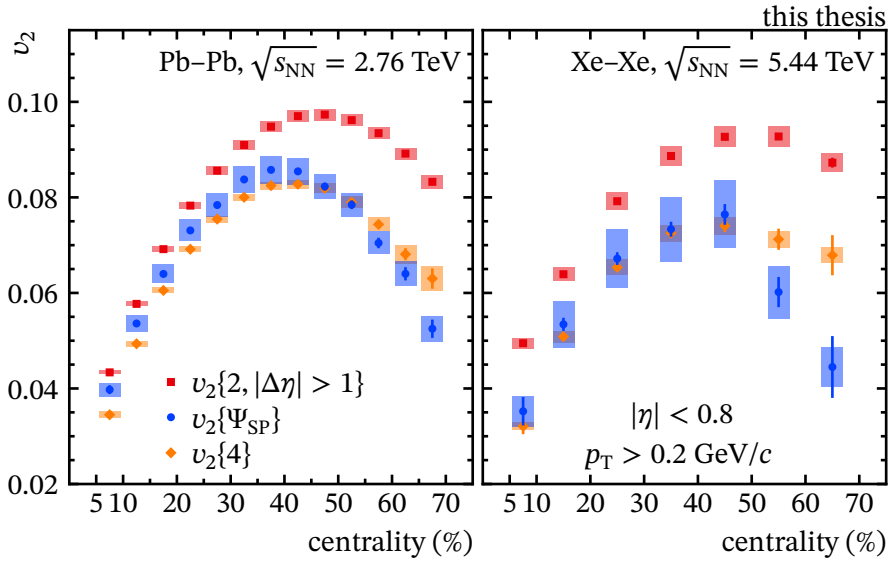

Figure 5.1: Centrality dependence of elliptic flow. Results from Pb-Pb collisions at $\sqrt{s_{NN}}$ = 2.76 TeV are shown on the left and Xe-Xe collisions at $\sqrt{s_{NN}}$ = 5.44 TeV are shown on the right. The colored markers show the three flow estimators. The vertical lines indicate the statistical uncertainties. The boxes show the systematic uncertainties.

of the colliding nuclei influences the initial eccentricities[67]. Since Xe in contrast to Pb is deformed[116], a larger initial eccentricity is expected in central collisions. The impact of the deformation is expected to reduce for more peripheral collisions, when the shape of the initial state is dominated by the geometric component of the initial state[35].

For very central collisions an excess of $v_2\{4\}$ in Xe-Xe is observed in previous measurements from ALICE[67,68]). For $v_2\{4\}$ and $v_2\{\Psi_{SP}\}$, this excess is not observed within the centrality range. Within the statistical uncertainties, also no enhancement of $v_2\{\Psi_{SP}\}$ is observed in central Xe-Xe collisions.

5.1.2 Transverse Momentum Dependence

Figure 5.2 shows the transverse momentum dependence of elliptic flow in six centrality classes (5, 10), (10, 20), (20, 30), (30, 40), (50, 60) percent in the p_T range $0.2 < p_T < 6$ GeV.

The ordering of the different elliptic flow estimators has the same qualitative behavior as the integrated flow measurement. The low transverse-momentum particles dominate the integrated flow measurement. A separate study of the high transverse-momentum behavior is not possible due to the limited statistical precision of the measurement.

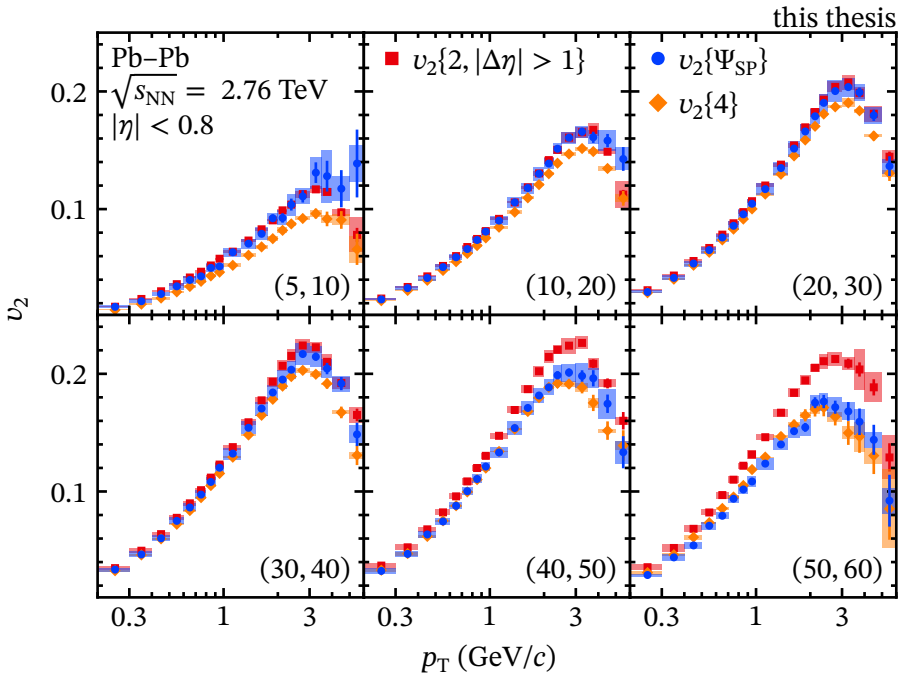

Figure 5.2: Transverse momentum dependence of elliptic flow for different centrality classes in Pb-Pb collisions at $\sqrt{s_{\mathrm{NN}}} = 2.76\,\mathrm{TeV}$. The differently colored markers show the three flow estimators. The vertical lines indicate the statistical uncertainties. The boxes show the systematic uncertainties. The bin-to-bin correlated systematic uncertainty is included in the systematic uncertainties. The centrality classes are shown in the lower right of each panel.

5.2 Elliptic Flow Ratios

The ratios of the elliptic flow estimators are sensitive to the shape of the flow fluctuations. The re-analysis of the elliptic flow measured with multi-particle cumulants allows the cancellation of systematic uncertainties of the measurement of the ratio, which increases the precision of the measurement. The measured ratios are compared to calculations of initial state models by exploiting the approximate linear scaling of the initial eccentricities and the flow coefficients (see eq. (1.39)).

5.2.1 Centrality Dependence

Figure 5.3 shows the ratio between $v_2\{\Psi_{SP}\}$ and $v_2\{4\}$ as well as $v_2\{2, |\Delta\eta| > 1\}$ and $v_2\{4\}$ as a function of the centrality for Pb-Pb (left) and Xe-Xe (right) collisions. The integrated flow ratios have been determined in the range of 5 % to 70 % centrality. For Pb collisions, the measurement is performed in 5 %-wide bins. In Xe collisions, the measurement is performed in the centrality percent intervals (5, 10), (10, 20), (20, 30), (30, 40), (50, 60), (60, 70). $v_2\{2, |\Delta\eta| > 1\}/v_2\{4\}$ has a minimum for semi-central collisions at 20 % to 30 % centrality for both collision systems. For central and peripheral collisions, the ratio increases. In central Xe-Xe collisions, the ratio is approximately 25 % larger than in central Pb-Pb collisions.

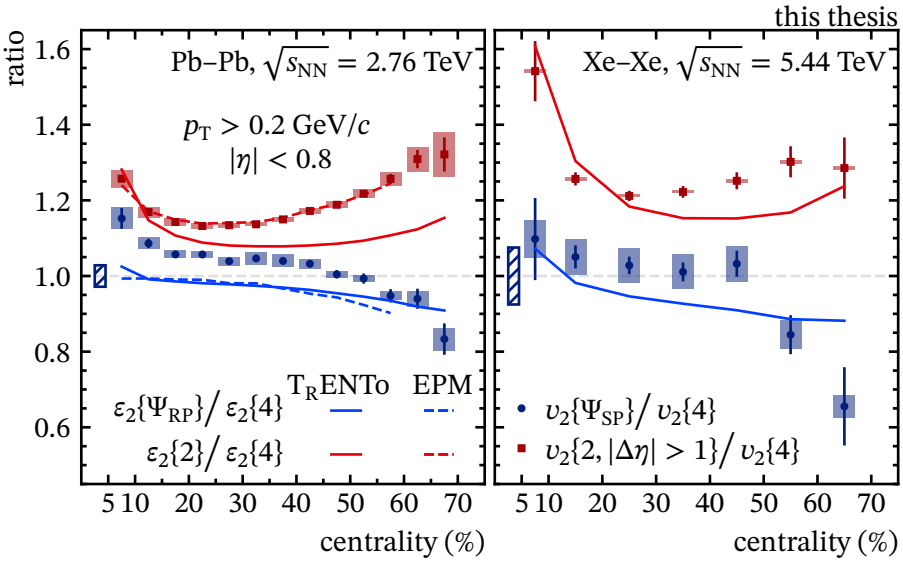

Figure 5.3: Centrality dependence of the ratios $v_2\{\Psi_{SP}\}/v_2\{4\}$ and $v_2\{2, |\Delta\eta| > 1\}/v_2\{4\}$. Results from Pb-Pb collisions at $\sqrt{s_{\mathrm{NN}}} = 2.76$ TeV are shown on the left and Xe-Xe collisions at $\sqrt{s_{\mathrm{NN}}} = 5.44$ TeV are shown on the right. $v_2\{2, |\Delta\eta| > 1\}/v_2\{4\}$ is shown by red squares. $v_2\{\Psi_{SP}\}/v_2\{4\}$ is shown by blue circles. The statistical uncertainties are indicated by the vertical lines and the uncorrelated systematic uncertainties are shown by error boxes. The hatched box shows the bin-to-bin correlated ZDC-scale uncertainty assigned to $v_2\{\Psi_{SP}\}/v_2\{4\}$. The full line shows the prediction of the eccentricity ratios $\varepsilon_2\{\Psi_{RP}\}/\varepsilon_2\{4\}$ $\varepsilon_2/\varepsilon_2\{4\}$ from the TRENTo initial conditions model with parameters from ref.[56]. The dashed lines show the EPM fit.

The ratio of $v_2\{\Psi_{SP}\}/v_2\{4\}$ is compatible with unity within the uncertainties for ranges of 20 % to 50 % centrality. For Pb-Pb collisions, a significant increase of the ratio of 15 % is observed in the most central collisions (5 % to 10 %). The statistical precision of the Xe-Xe measurements is not enough to observe the increase. For peripheral (larger than 50 % centrality) collisions, a decrease of the ratio to below unity is observed. The TRENTo calculations of the ratio of the initial state quantities $\varepsilon_2/\varepsilon_2\{4\}$ show an agreement with the ratio $v_2\{2, |\Delta\eta| > 1\}/v_2\{4\}$ measured in data for the most central measurements. For more peripheral collisions, the deviation from data increases. This could indicate that the linear scaling between the initial eccentricities and the flow coefficients eq. (1.39) only holds approximately. A non-linear scaling could lead to a difference of $\varepsilon_2/\varepsilon_2\{4\}$ and $v_2\{2, |\Delta\eta| > 1\}/v_2\{4\}$. Such a non-linear scaling can either manifest as a non-linear dependence of v_n on ε_n, or as a dependence on other properties of the initial state for example radial density modulations or other harmonics $m \neq n$. However, a study performed in ref.[70] does not find a non-linear scaling with a significant centrality dependence.

The measurement of $v_2\{\Psi_{SP}\}/v_2\{4\}$ is compared to the ratio $\varepsilon_2\{\Psi_{RP}\}/\varepsilon_2\{4\}$ obtained from TRENTo. $\varepsilon_2\{\Psi_{RP}\}/\varepsilon_2\{4\}$ shows an increase above unity for very central collisions (compare to fig. 4.21). In the Pb-Pb data, a much larger increase is observed than predicted by the TRENTo model in the most central bins. In peripheral collisions, the TRENTo model qualitatively reproduces the decrease of $v_2\{\Psi_{SP}\}/v_2\{4\}$ in peripheral collisions for both collision systems.

The EPM fit is performed to the measured multi-particle cumulants from previous measurements of ALICE[68] (see section 4.9.2). Therefore, an excellent agreement of $\varepsilon_2/\varepsilon_2\{4\}$ with $v_2\{2, |\Delta\eta| > 1\}/v_2\{4\}$ is expected by construction. Due to the limited statistical precision of the multi-particle cumulants, the EPM fit cannot be performed in the Xe-Xe-collision data sample. The prediction of the $\varepsilon_2\{\Psi_{RP}\}/\varepsilon_2\{4\}$ ratio is in agreement with the T$_\mathrm{R}$ENTo model for all but the most central point. The ratio $\varepsilon_2\{\Psi_{RP}\}/\varepsilon_2\{4\}$ is always below unity for the EPM prediction. For peripheral collisions, the decreasing trend of the data is reproduced.

For Bessel-Gaussian fluctuations a ratio of unity is expected for $\varepsilon_2\{\Psi_{RP}\}/\varepsilon_2\{4\}$. The deviation below unity of $\varepsilon_2\{\Psi_{RP}\}/\varepsilon_2\{4\}$ in peripheral collisions is therefore an indication for increasingly non Bessel-Gaussian fluctuations. This observation qualitatively agrees with previous studies using multi-particle cumulants[68] (shown in fig. 1.20). Both T$_\mathrm{R}$ENTo and EPM models predict this non Bessel-Gaussian behavior of the fluctuations.

The tension between the measurement of $v_2\{\Psi_{SP}\}/v_2\{4\}$ and the ratio of $\varepsilon_2\{\Psi_{RP}\}/\varepsilon_2\{4\}$ from the models, especially in central collisions, show that the spectator dynamics are not described within the model. These tensions are significant, because the magnitude of the flow fluctuations relative to the spectators is up to half the magnitude of the flow fluctuations of the participants estimated by $v_2\{2, |\Delta\eta| > 1\}/v_2\{4\}$. However, the differences to the model could have multiple sources. The first possible source is the deviation of the measured spectator plane Ψ_SP from the reaction plane Ψ_RP. A decrease in the number of spectator neutrons in central collisions could increase the observed fluctuations, which increases the ratio $v_2\{\Psi_{SP}\}/v_2\{\Psi_{SP}\}$. The presence of spectator fluctuations is in agreement with the measurement of a non-zero symmetric component of directed flow[76] (compare to fig. 1.25). The second possible source is a missing contribution to the eccentricity fluctuations in the overlap region from the dynamics of the spectators. The third possible source is a non-linear response of the fluid dynamics, which could modify the observed flow coefficients. The contributions of these sources cannot be distinguished from each other without a model of the initial state that includes the spectator dynamics.

5.2.2 Transverse Momentum Dependence

Figure 5.4 shows the transverse momentum dependence in of $v_2\{\Psi_{SP}\}/v_2\{4\}$ for six centrality classes in Pb-Pb collisions at $\sqrt{s_\mathrm{NN}} = 2.76\,\mathrm{TeV}$. Overlaid on the ratio is a linear fit to the data in the range $0.2\,\mathrm{GeV}/c$ to $3\,\mathrm{GeV}/c$. The constant offset parameter of the fit is consistent with the ratio obtained for the integrated ratio. The slope parameter of the fit is indicated in the figure.

A non-zero slope is observed for events in the 20 % to 30 % centrality range. The statistical precision of the data cannot constraint the p_T-dependence of $v_2\{\Psi_{SP}\}/v_2\{4\}$ in first and last centrality interval. The results are consistent with previous observations of a very small p_T-dependence[72] in the 10 % to 50 % centrality range of $[(v_2\{EP\}^2 - v_2\{4\}^2)/(v_2\{EP\}^2 + v_2\{4\}^2)]^{1/2}$ (shown in fig. 1.22).

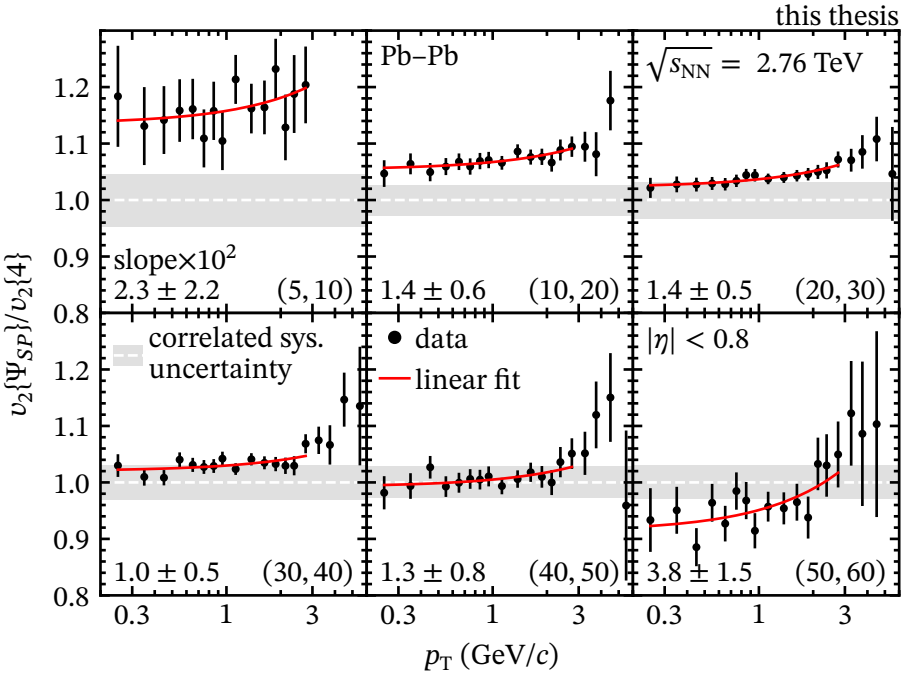

Figure 5.4: Transverse momentum dependence of the ratios $v_2\{\Psi_{SP}\}/v_2\{4\}$ for different centrality classes in Pb-Pb collisions at $\sqrt{s_{\mathrm{NN}}} = 2.76\,\mathrm{TeV}$. The results are shown in a semi-log plot. The data (black points) are compared to a linear fit (red). The slope parameter of the linear fit is given in the lower left of each panel. The centrality class is given in the lower right corner of each panel. The bin-by-bin correlated systematic uncertainty is given by the gray band around unity. The statistical uncertainties are indicated by the vertical lines.

5.3 Multiplicity Scaling of Elliptic Flow

In ideal hydrodynamics, a system exhibits scale invariance and therefore only depends on its equation of state. This universality of the hydrodynamic evolution is broken by the hadronic freeze-out of the matter since the relevant scale, the critical energy density does not depend on the initial geometry of the collision. An additional breaking of the scaling is observed for systems that behave according to viscous hydrodynamics. The shear viscosity over entropy density η_s/s leads to an additional suppression in smaller collisions systems which "shifts" the data points down relative to a system of ideal hydrodynamics. Additional entropy generation through viscous effects generate larger $\mathrm{d}N_{ch}/\mathrm{d}\eta$ which "shifts" the data point to the left relative to a system of ideal hydrodynamics[66]. Since a small significant η_s/s have been observed in experimental data[56,66,149], a splitting is expected in the data.

Figure 5.5 shows the multiplicity scaling of elliptic flow comparing data from Pb-Pb and Xe-Xe collisions. The y-axis shows the value of elliptic flow v_2 rescaled by the initial state eccentricity ε_2. The x-axis shows the charged-particle multiplicity density $\mathrm{d}N_{ch}/\mathrm{d}\eta$, which is rescaled by the transverse size of the system S. The initial state quantities have been extracted from the T$_{\mathrm{R}}$ENTo model using the parameters from ref.[56]. The $\mathrm{d}N_{ch}/\mathrm{d}\eta$ for the corresponding centrality classes is taken from measurements of ALICE[113,151].

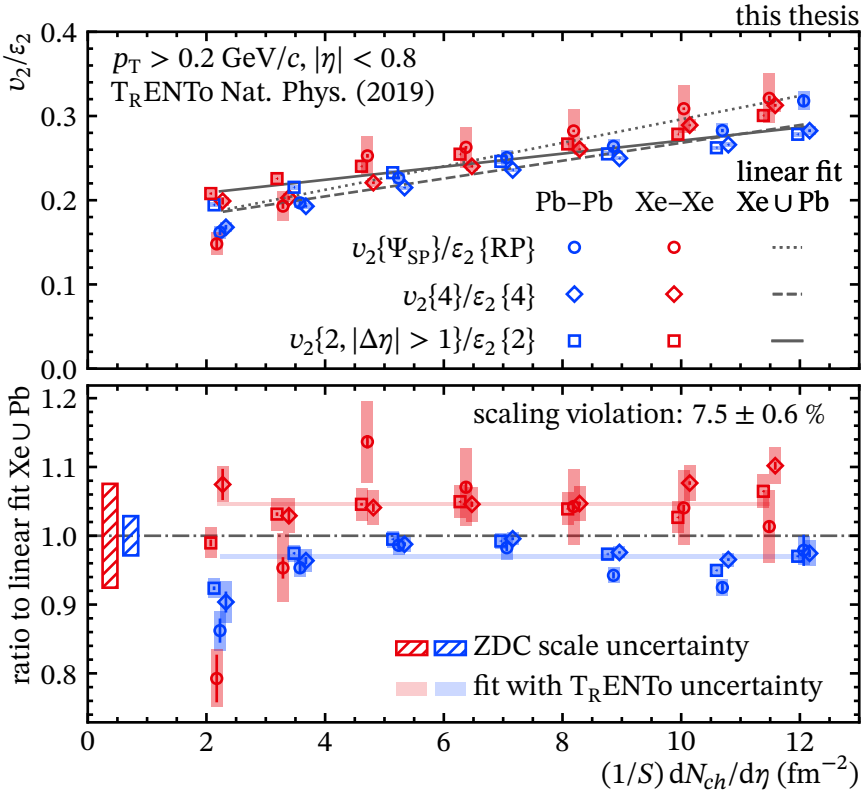

Figure 5.5: Multiplicity scaling of elliptic flow. The upper panel shows v_2/ε_2 as a function $1/S\,dN_{ch}/d\eta$. The bottom panel shows the ratio of the data to the linear fit (gray lines). The T$_R$ENTo model parameters are obtained from ref.[56]. The charged-particle multiplicity density is measured by ALICE[113,150]. The color of the points indicates the collision system. The marker shape indicates the flow estimator. The statistical (systematic) uncertainties are indicated by the lines (boxes). The hatched box shows the ZDC-scale uncertainty of $v_2\{\Psi_{SP}\}/\varepsilon_2\{\Psi_{RP}\}$.

In the top panel, the measurement of both systems cluster around a slight linear increase with charged-particle multiplicity. A slight splitting is observed between the Pb and Xe collisions systems. All flow estimators show a similar trend with multiplicity. The difference between the two collision systems is isolated by a simultaneous linear fit to the Pb-Pb and Xe-Xe measurements. Each flow estimator is fit separately. The linear fits are shown in the figure as gray lines.

The bottom panel shows the ratios of the data to the corresponding linear fit. The hatched box indicates the ZDC-scale uncertainty which only applies to the $v_2\{\Psi_{SP}\}$ measurement. For perfect scaling, a ratio of one would be expected for all data points. The flow estimators cluster into two groups, one for each collision system. A larger rescaled elliptic flow is observed in Xe-Xe collisions at the same rescaled $dN_{ch}/d\eta$. The scaling violation is evaluated by performing a fit of a constant to the ratios for each collision system separately. The width of the band corresponds to the uncertainty related to the T$_R$ENTo parameters. The difference between the measurements rescaled with T$_R$ENTo using one set of parameters versus T$_R$ENTo using a

second set of parameters is used as the model uncertainty. The parameters from refs[56,149] are used to evaluate the uncertainty bands.

A scaling violation of $7.5 \pm 0.6\,\%$ is observed. The scaling violation does not show a strong dependence on the multiplicity. The clustering of the data points according to the collision system indicates a similar sensitivity of the flow estimators to the scaling violation. No significant deviation of the $v_2\{\Psi_{SP}\}$ measurements is observed. Under the assumptions of a similar scaling of $v_2\{\Psi_{SP}\}$ this seems to indicate that the ZDC-scale uncertainty gives a conservative estimate of the systematic uncertainty[†].

[†]The ZDC-scale uncertainty is explained in section 4.10.

5.4 Event Shape Engineering using Neutron Spectators

Event-shape engineering allows selecting different initial state anisotropies using the reduced flow vector magnitude $|q_{n,ese}|$. With the selection of collisions with large (small) $|q_{1,ese}|$ of the spectator neutrons, the correlation of the magnitude of the spectator deflection with the elliptic flow measured at mid-rapidity can be studied.

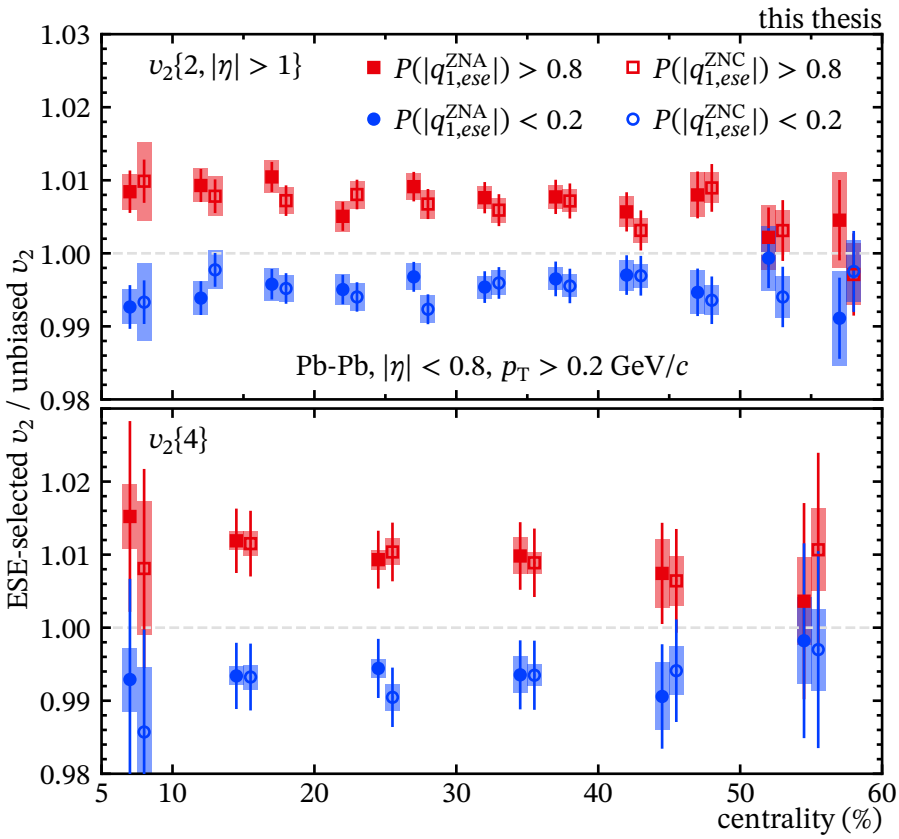

Figure 5.6: Centrality dependence of ESE-selected elliptic flow to unbiased elliptic flow measured in Pb-Pb collisions at $\sqrt{s_{\mathrm{NN}}} = 2.76$ TeV. The data points are shifted by 1 % in centrality for better visualization. The Statistical (systematic) uncertainties are indicated by the lines (boxes).

Figure 5.6 shows the ratio of the elliptic flow measured solely in the ESE-selected collisions relative to the unbiased measurement for $v_2\{2, |\Delta\eta| > 1\}$ and $v_2\{4\}$ in the top and bottom panel, respectively. The selection selects 20 % of the collisions which exhibit the smallest (largest) reduced flow vector measured with the neutron spectators in ZNA, or ZNC. For $v_2\{2, |\Delta\eta| > 1\}$ the results are reported in 5 % centrality bins. The $v_2\{4\}$ measurement uses 10 % centrality bins except for the most central bin, which has a 5 % bin width.

Both measurements are sensitive to the selection of the events. A significant difference of ≈ 2 % between the two selections is observed. A slight decreasing trend of the difference with centrality is observed. Within the current statistical precision, both detectors show the same selectivity which is expected for symmetric Pb-Pb collisions.

The elliptic flow measured at mid-rapidity is sensitive to the fluctuations of the spectator deflection in the centrality interval 5 % to 50 %. No contributions from autocorrelations are expected due to the large pseudorapidity separation between the measurement of elliptic flow at $\eta \approx 0$ and the selection using ESE at $|\eta| > 8.8$. A much smaller selectivity is observed compared to ESE-selections based on $q_{2,ese}^{\mathrm{TPC}}$ or $q_{2,ese}^{\mathrm{V0C}}$ reported in previous measurements by ALICE[78]. Measurements of the directed flow[76] indicate a momentum transfer between the participant region and the spectators during the passing of the two nuclei in the order of 16 MeV/c. The measurements of elliptic flow in ESE-selected classes using based on the spectator deflection presented here indicate a sensitivity to fluctuations of this small momentum transfer. For better understanding of this effect, initial state models which include the spectator dynamics are required.

6 Conclusion and Outlook

In this thesis, novel studies of elliptic flow and flow fluctuations in heavy-ion collisions measured with ALICE at the LHC are presented. These measurements contribute to the understanding of the initial state of relativistic heavy-ion collisions by highlighting the importance of the spectator dynamics.

Above temperatures of 150 MeV, strongly-interacting matter undergoes a transition to a QGP: a phase of deconfined quarks and gluons. The extreme energy densities necessary (1-3 times the energy density of nuclear matter)[25] for this transition can only be reached in the laboratory through relativistic collisions of heavy ions. However, the QGP cannot be observed directly. Therefore, to learn about the properties of the QGP models simulating the complete evolution of the heavy-ion collision are compared to observations from experimental data. These model-to-data comparisons are performed using observables averaged over many collisions. A complete understanding of the initial state of the collision, which describes the energy deposition immediately after the nuclei collide, is crucial. It directly influences the precision with which the properties of the QGP can be extracted from these comparisons[56].

State-of-the-art initial state models describe the energy density of the overlap region in the transverse direction. The spatial fluctuations of the nuclear matter distribution in the colliding nuclei are modeled to achieve this. In the initial state, these fluctuations are imprinted on the initial energy density in the participant region of the collision. These initial state models do not take the dynamics of the spectator nucleons into account.

After thermalization, the QGP transforms this spatial anisotropy into a momentum anisotropy of the produced particles[71], called anisotropic flow. This process is sensitive to the transport properties such as viscosity. In an ideal-fluid description, the transformation of spatial anisotropies to momentum anisotropies is linear[46]. By introducing viscous corrections in the fluid dynamic description, as observed in heavy-ion collisions, a non-linear response of the fluid is expected. Violations of such a linear response are sensitive to the shear viscosity of the QGP[66]. This effect can be probed by investigating the *multiplicity scaling of elliptic flow*. In this work, such a violation of linear scaling is quantified by comparing Pb-Pb and Xe-Xe collisions which are rescaled using the T_RENTo initial state model. These studies set new constraints on the fluid dynamic description of the QGP. The observed scaling violation does not strongly depend on the flow estimator used for extracting the elliptic flow coefficient.

The fluctuations of the initial state eccentricities are translated in the QGP to fluctuations of anisotropic flow. In the picture of many sources (nucleons) of the fluctuations, the shape is assumed to be Gaussian. Deviations from such Gaussian fluctuations give access to the properties of the initial state[70]. The measurement of the *elliptic flow fluctuations using the spectator neutrons* gives new insights into the underlying shape of these fluctuations. Tensions between the measurement and predictions of initial state models are observed. The magnitude of the elliptic flow fluctuations using the spectators is up to 50 % as large as the magnitude of

fluctuations measured exclusively with particles originating from the overlap region (multi-particle cumulants method), which shows the importance of including the spectator dynamics in the initial state. The elliptic flow fluctuations relative to the spectator deflection show a strong enhancement in central collisions, which could indicate large fluctuations of the spectator deflection. In peripheral collisions, the measurements support previous observations of increasingly non-Gaussian shape of the fluctuations due to the lower number of sources. Modifications of the initial state from the dynamics of the spectators are also a possible source of the observed difference. The spectator dynamics need to be included in the models of the initial state to disentangle these different sources.

The fluctuations of the spectator deflection demonstrate the influence of the spectators on the dynamics in the QGP, which is created after the spectators have decoupled from the overlap region. This is shown by the correlation between the spectator deflection and the elliptic flow measured with multi-particle cumulants at mid-rapidity using the *event-shape engineering* technique. A significant modification of the elliptic flow observed in mid-rapidity in collisions with small (large) spectator deflection is observed.

The results on the elliptic flow, flow fluctuations, and the multiplicity scaling of elliptic flow have been internally reviewed by the ALICE Collaboration and are approved for publication. The publication[2] is currently in preparation.

The measurements presented in this work cannot be explained by state-of-the-art initial state models. To increase the precision of the understanding of the QGP, improved models of the initial state need to take the dynamics of the spectators into account. Such models, which include the dynamics of the spectators, could also provide an improved understanding of the strong magnetic field of up to 1×10^{15} T induced by the passing of the spectator protons. This strong magnetic field influences particle production by breaking the symmetry relative to the reaction plane of the collision[152,153].

More differential studies of the flow fluctuations using spectators, such as the measurements with respect to particle species, or the measurement at higher transverse momentum, could further improve the understanding of the initial state. Such measurements require larger data samples with more collisions to improve statistical precision and an improved understanding of the systematic uncertainties. Several technical challenges have to be addressed to be able to perform these measurements. A performance study presented in this thesis demonstrates a strong dependence of the ZDC performance on the beam parameters. Especially in the future LHC Run 3 and Run 4, much higher luminosities are expected in nucleus-nucleus collisions, which may affect the ZDC performance in correlation studies. Therefore, a better understanding of the interplay of the beam parameters and the spectator measurement will be mandatory. The LHC experiments ATLAS[154] and CMS[155] that also have zero-degree calorimeters may also profit from a better understanding of these effects.

A Supplementary Figures

A.1 Track and Flow Vector Distributions in Xe-Xe Collisions

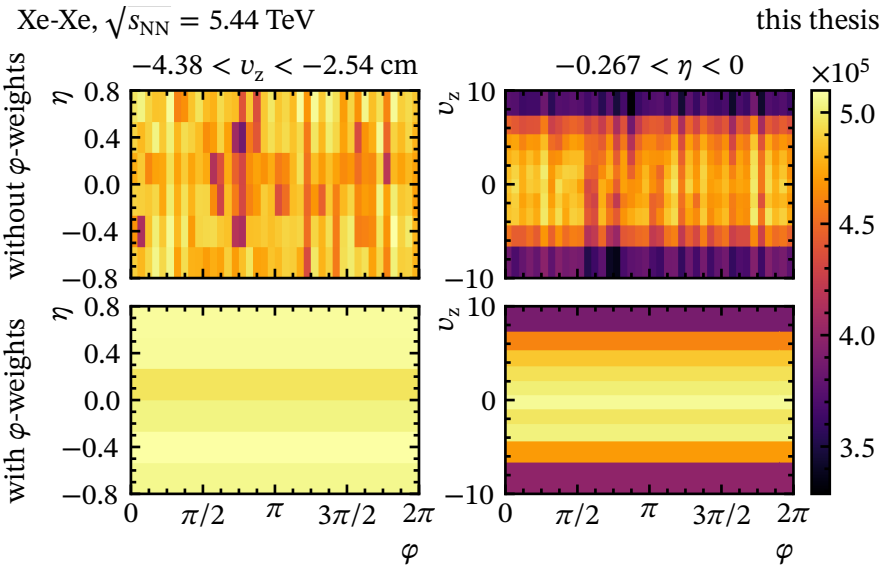

Figure A.1: Azimuthal track distribution of the hybrid tracks inside a η-V_z window of the Xe-Xe data sample. The top (bottom) panels show the distribution before (after) φ-weights are applied.

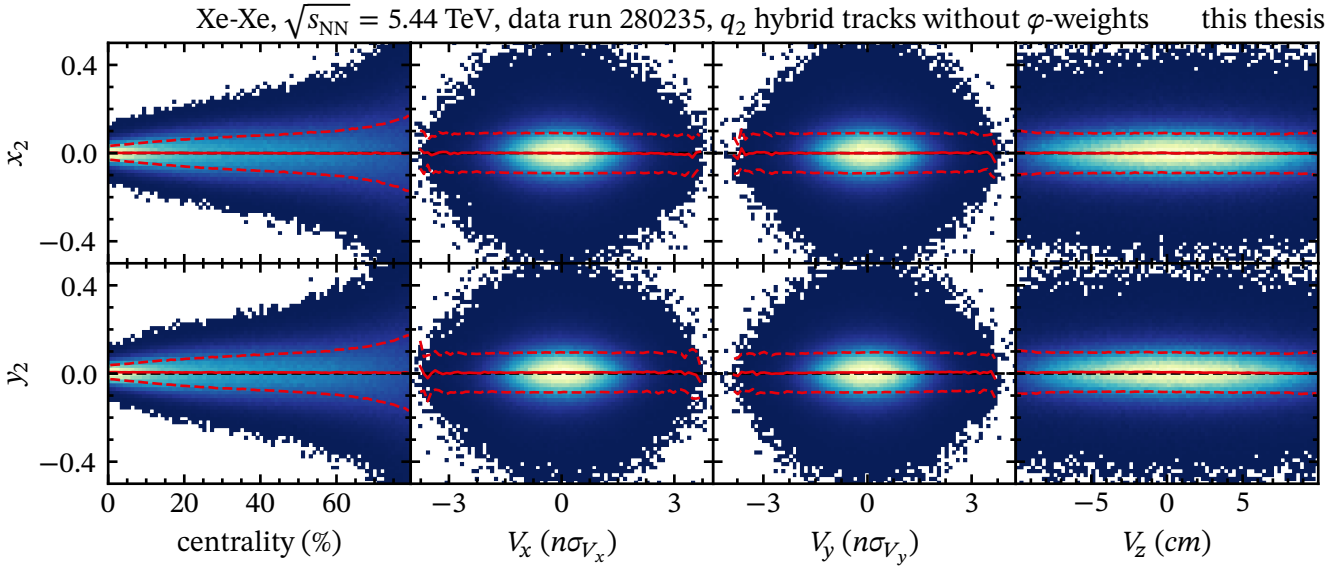

Figure A.2: Distributions of flow vector components x_2 and y_2 of hybrid tracks as a function of centrality and vertex positions V_x, V_y, V_z for one data run of the Xe-Xe data sample. The mean and one standard deviation are shown by the red lines.

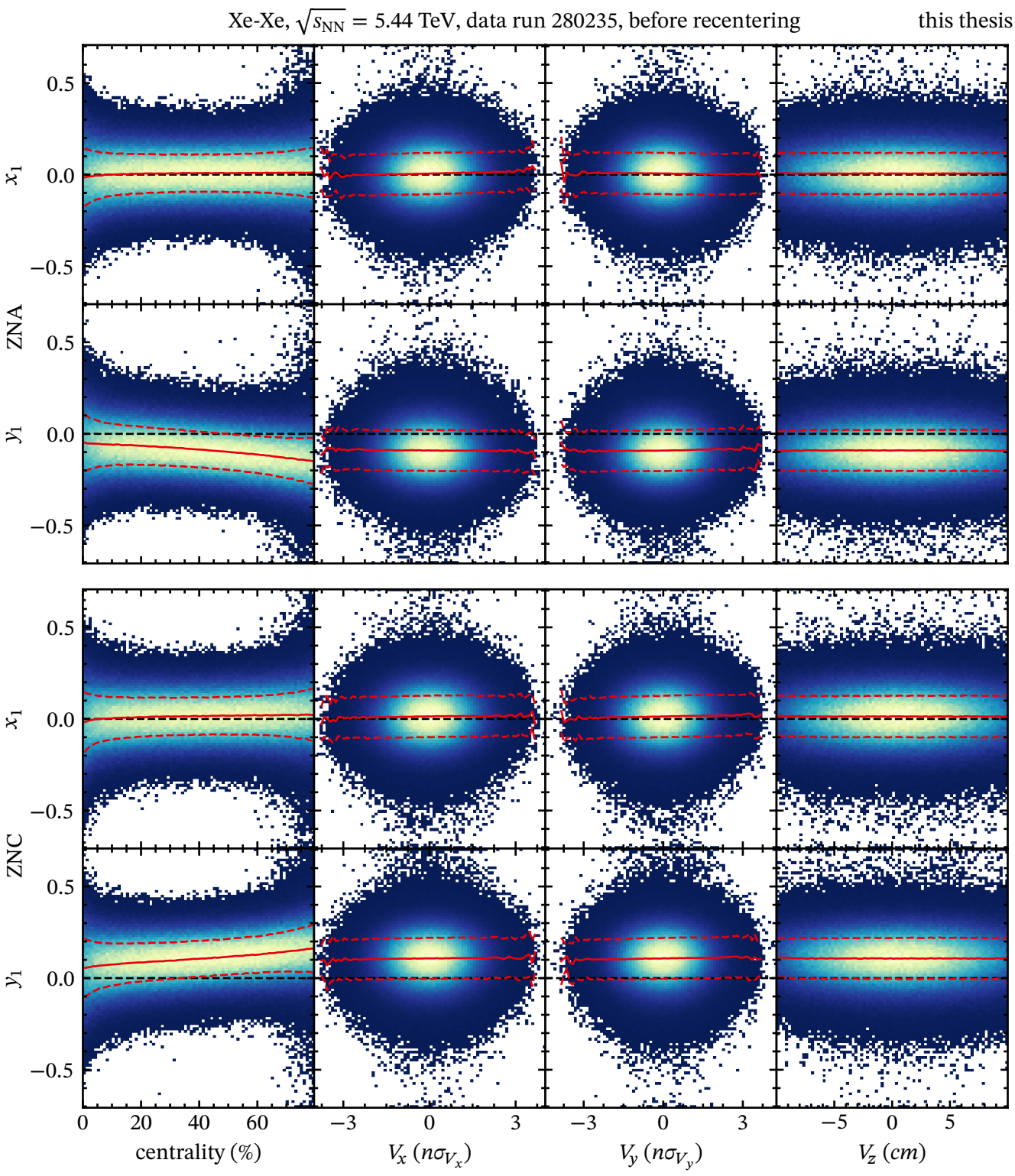

Figure A.3: Distributions of flow vector components x_1 and y_1 of ZNA and ZNC as a function of centrality and vertex positions v_x, v_y, v_z. The upper panel shows one data run of Xe-Xe collisions at $\sqrt{s_{\mathrm{NN}}} = 5.44$ TeV. The mean and standard deviation are shown by the red lines.

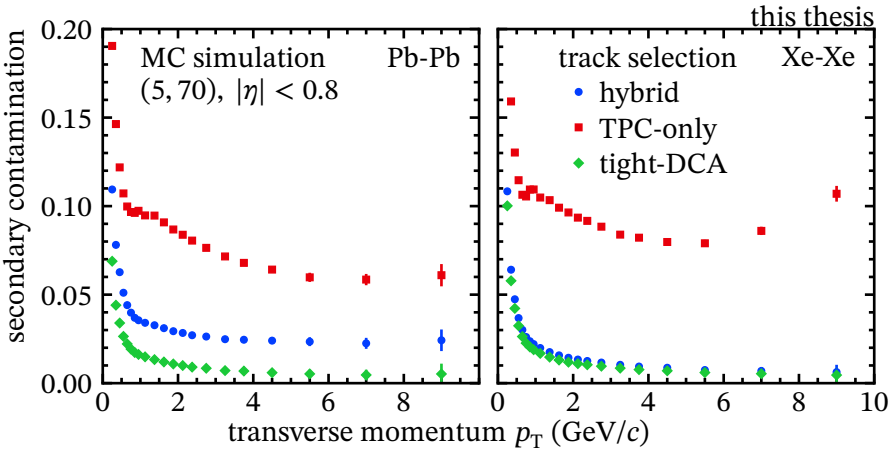

Figure A.4: Comparison of the secondary contamination for different track selections as a function of the transverse momentum in Pb-Pb and Xe-Xe collisions. The secondary contamination is calculated in a HIJING MC simulation.

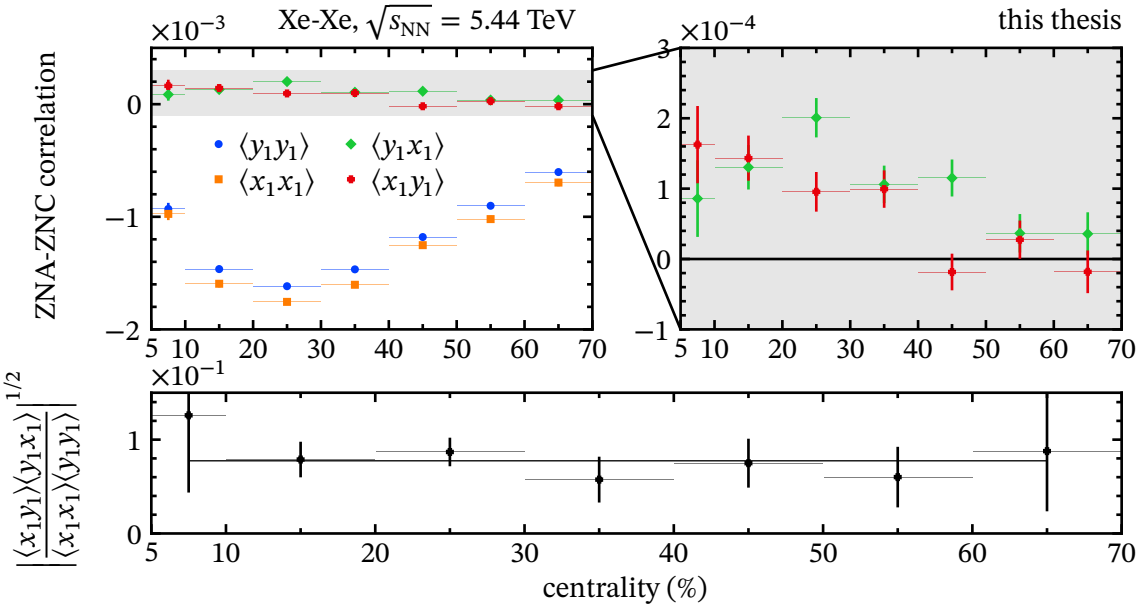

Figure A.5: ZNA-ZNC correlations and ZDC scale uncertainty for the Xe-Xe collisions data sample. Upper left plot shows the centrality dependence of the correlation (also shown in fig. 4.6). The gray area corresponds to the area covered by the upper right panel. The black line at 0 shows the expectation for the $\langle x_1 y_1 \rangle$ and $\langle y_1 x_1 \rangle$ correlations. The lower panel shows the derived scale uncertainty.

A.2 Systematic Uncertainties

A.2.1 Centrality Dependence

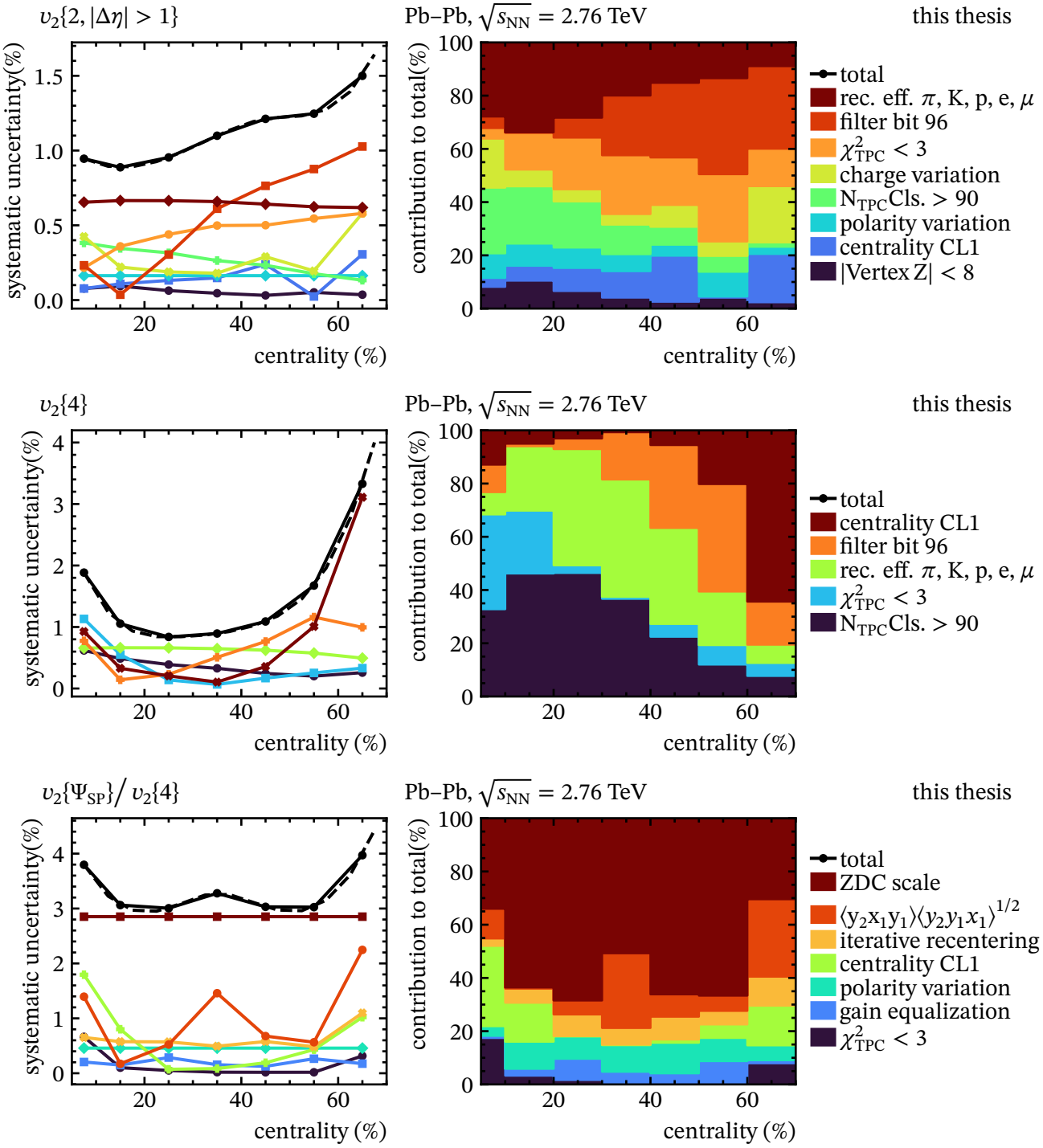

Figure A.6: Centrality dependence of the systematic uncertainties of $v_2\{2, |\Delta\eta| > 1\}$, $v_2\{4\}$ and $v_2\{\Psi_{SP}\}/v_2\{4\}$ in Pb-Pb collisions.

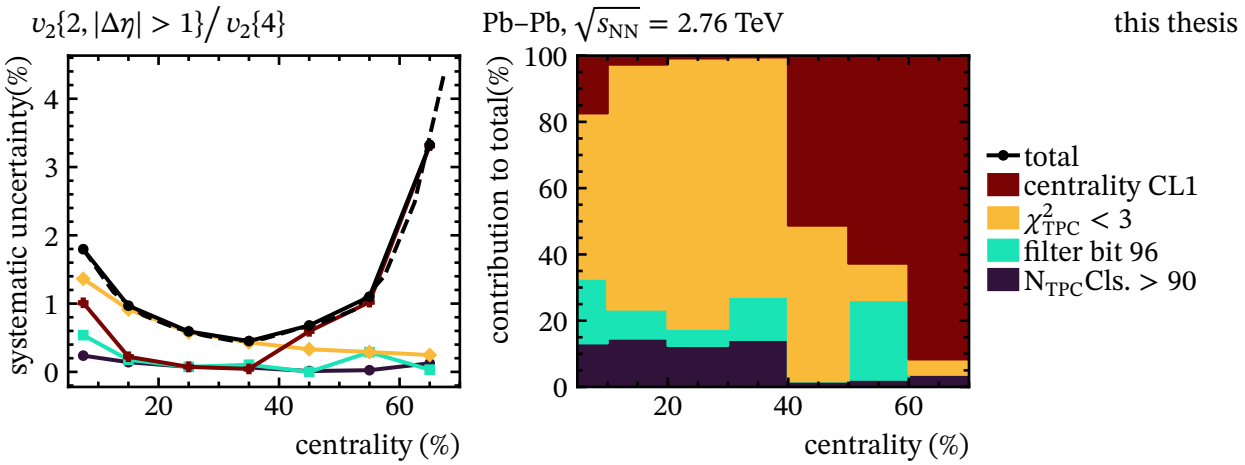

Figure A.7: Centrality momentum dependence of the systematic uncertainties of $v_2\{2, |\Delta\eta| > 1\}/v_2\{4\}$ in Pb-Pb collisions.

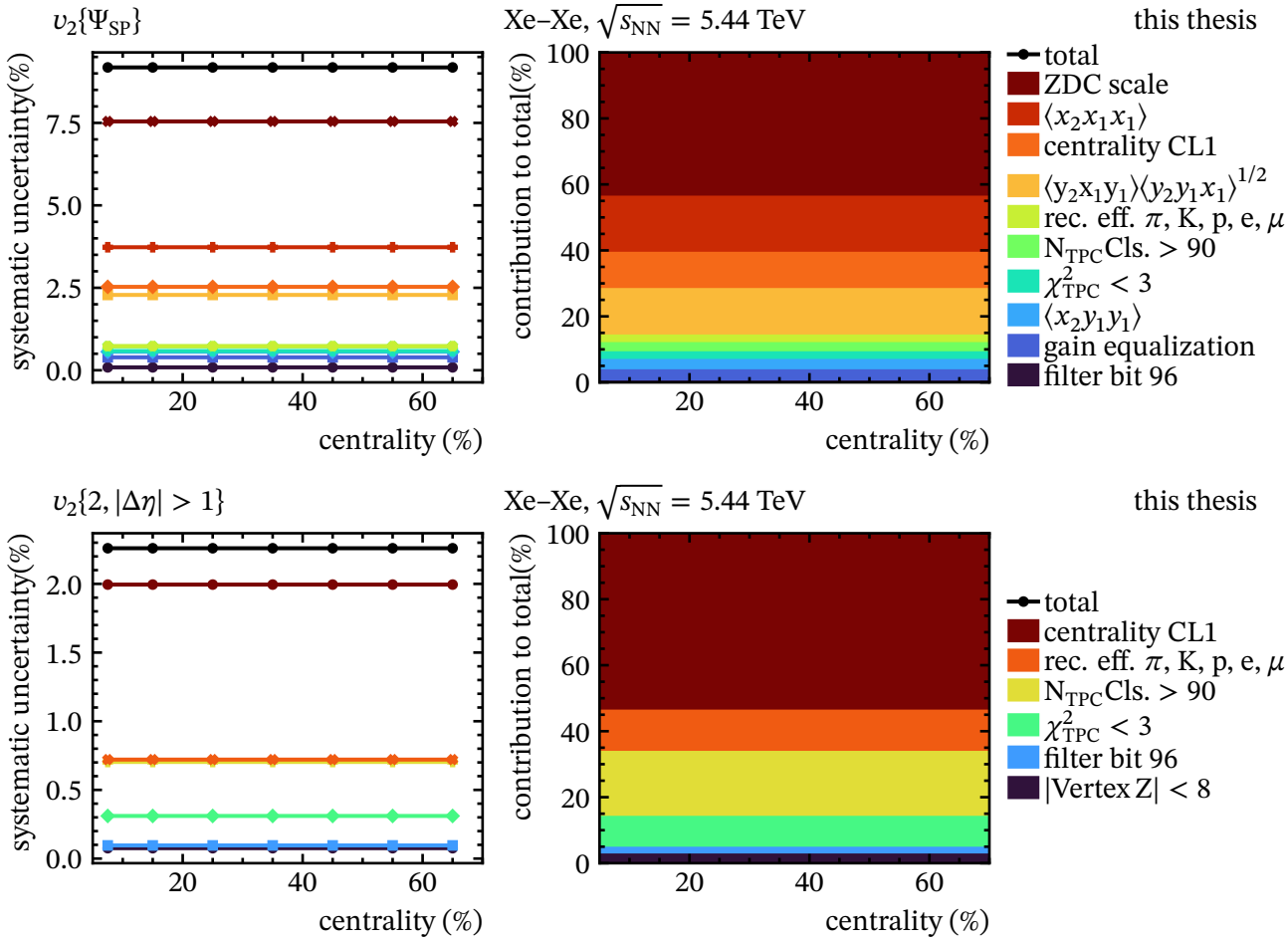

Figure A.8: Centrality dependence of the systematic uncertainties of $v_2\{\Psi_{SP}\}$ and $v_2\{2, |\Delta\eta| > 1\}$ in Xe-Xe collisions.

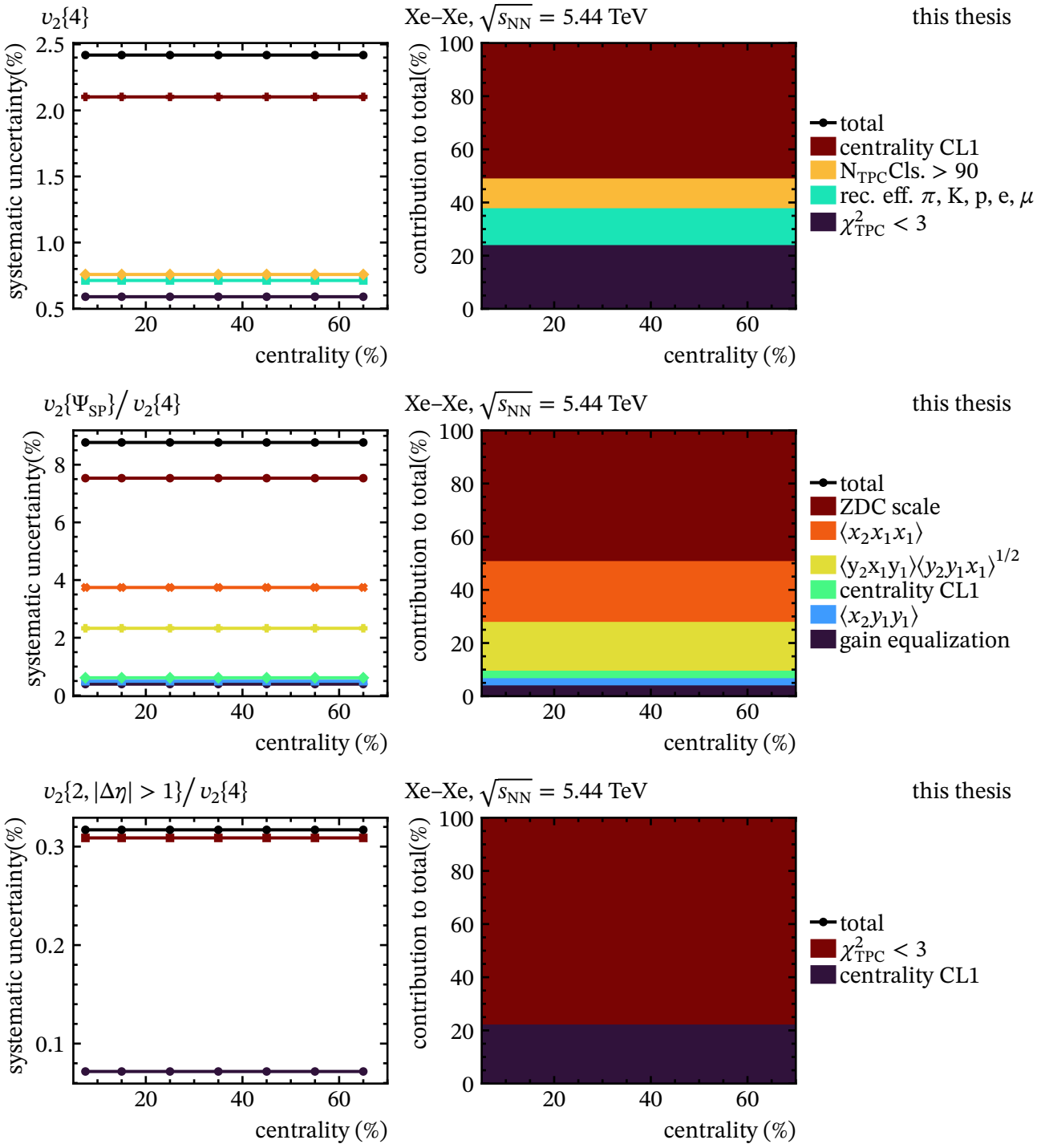

Figure A.9: Centrality dependence of the systematic uncertainties of $v_2\{4\}$, $v_2\{\Psi_{SP}\}/v_2\{4\}$, and $v_2\{2, |\Delta\eta| > 1\}/v_2\{4\}$ in Xe-Xe collisions.

A.2.2 Transverse Momentum Dependence of Elliptic Flow and Elliptic Flow Ratios

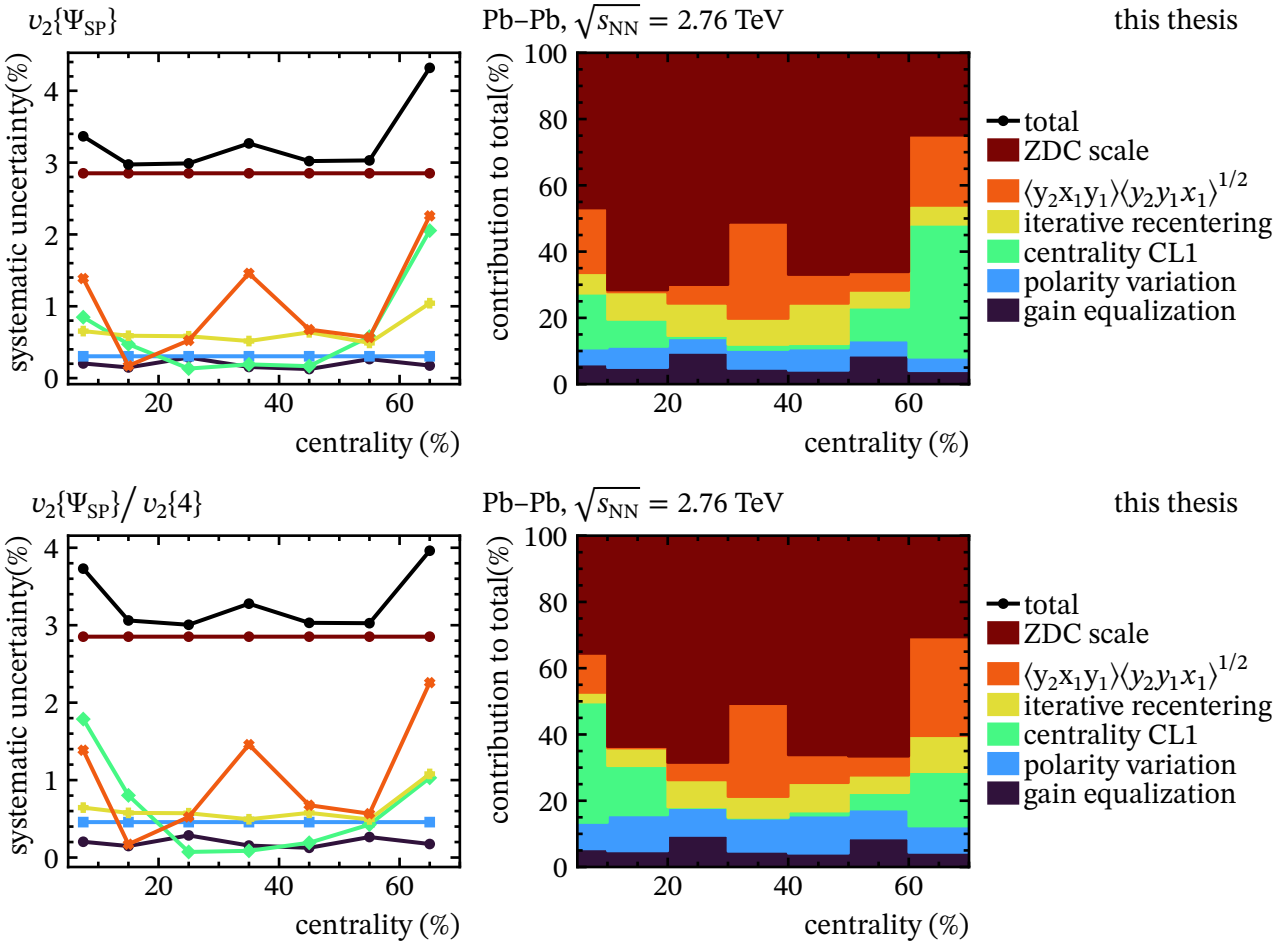

Figure A.10: Centrality dependence of the correlated systematic uncertainties of $v_2\{\Psi_{SP}\}$ and $v_2\{\Psi_{SP}\}/v_2\{4\}$ in Pb-Pb collisions.

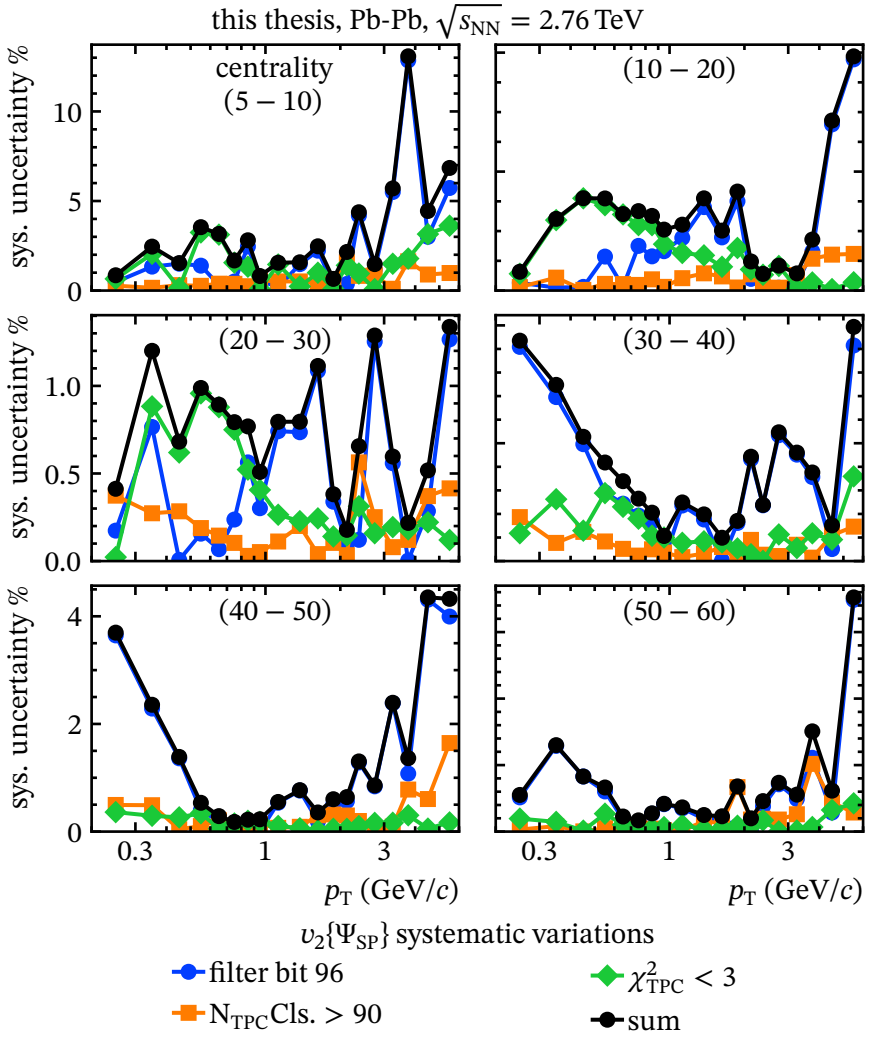

Figure A.11: Transverse momentum dependence of the uncorrelated systematic uncertainties of $v_2\{\Psi_{SP}\}$ in Pb-Pb collisions.

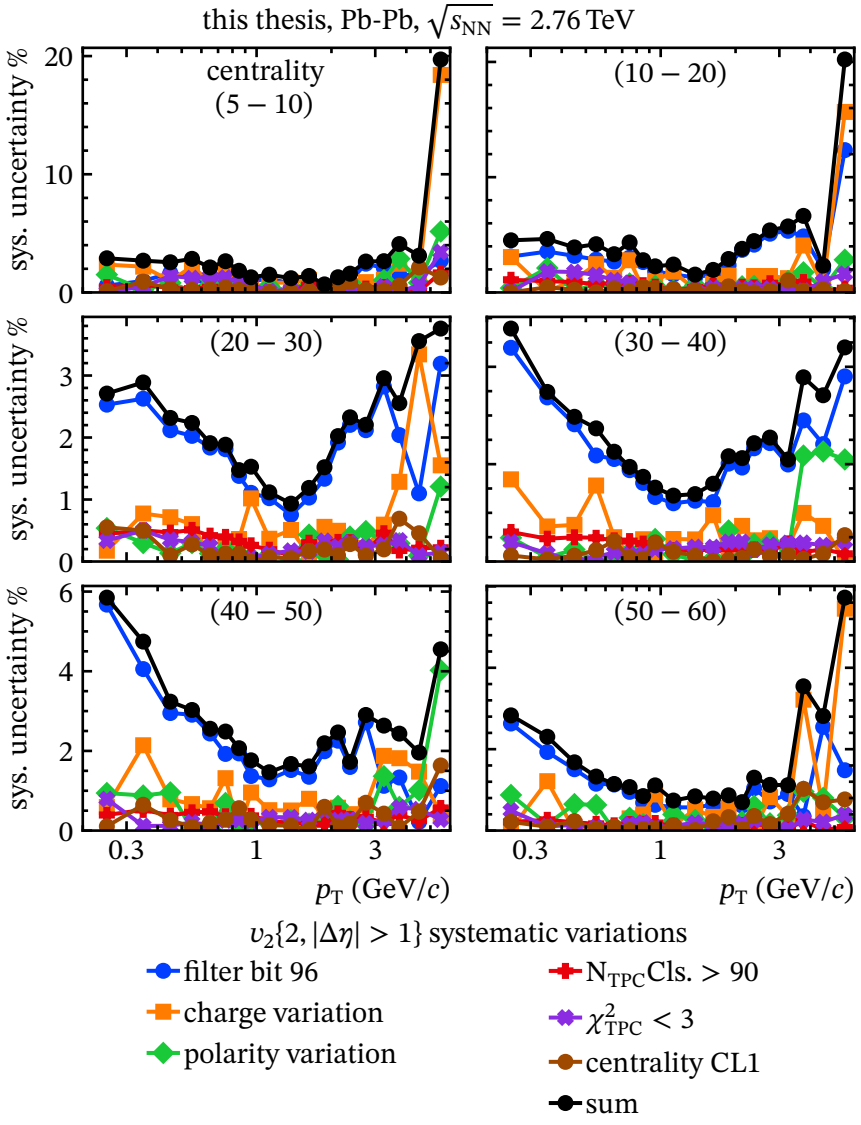

Figure A.12: Transverse momentum dependence of the uncorrelated systematic uncertainties of $v_2\{2, |\Delta\eta| > 1\}$ in Pb-Pb collisions.

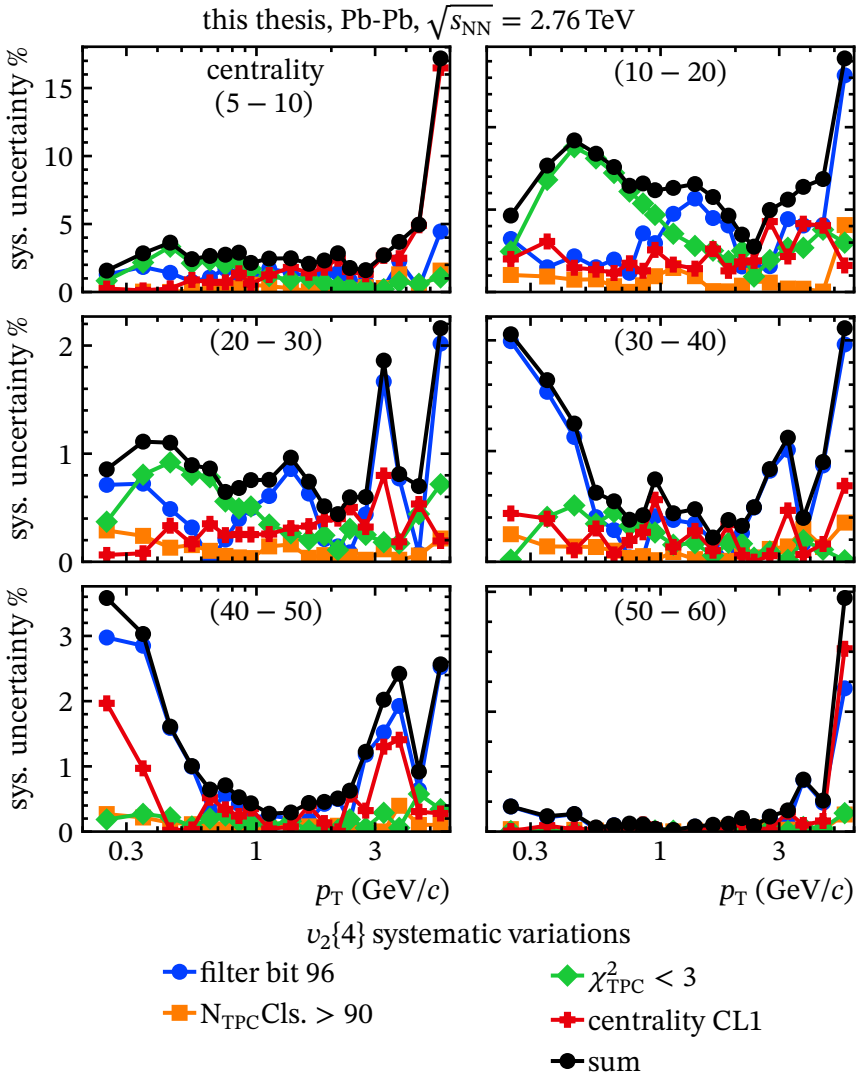

Figure A.13: Transverse momentum dependence of the uncorrelated systematic uncertainties of $v_2\{4\}$ in Pb-Pb collisions.

A.3 Performance of Zero Degree Calorimeters in Different Data Samples

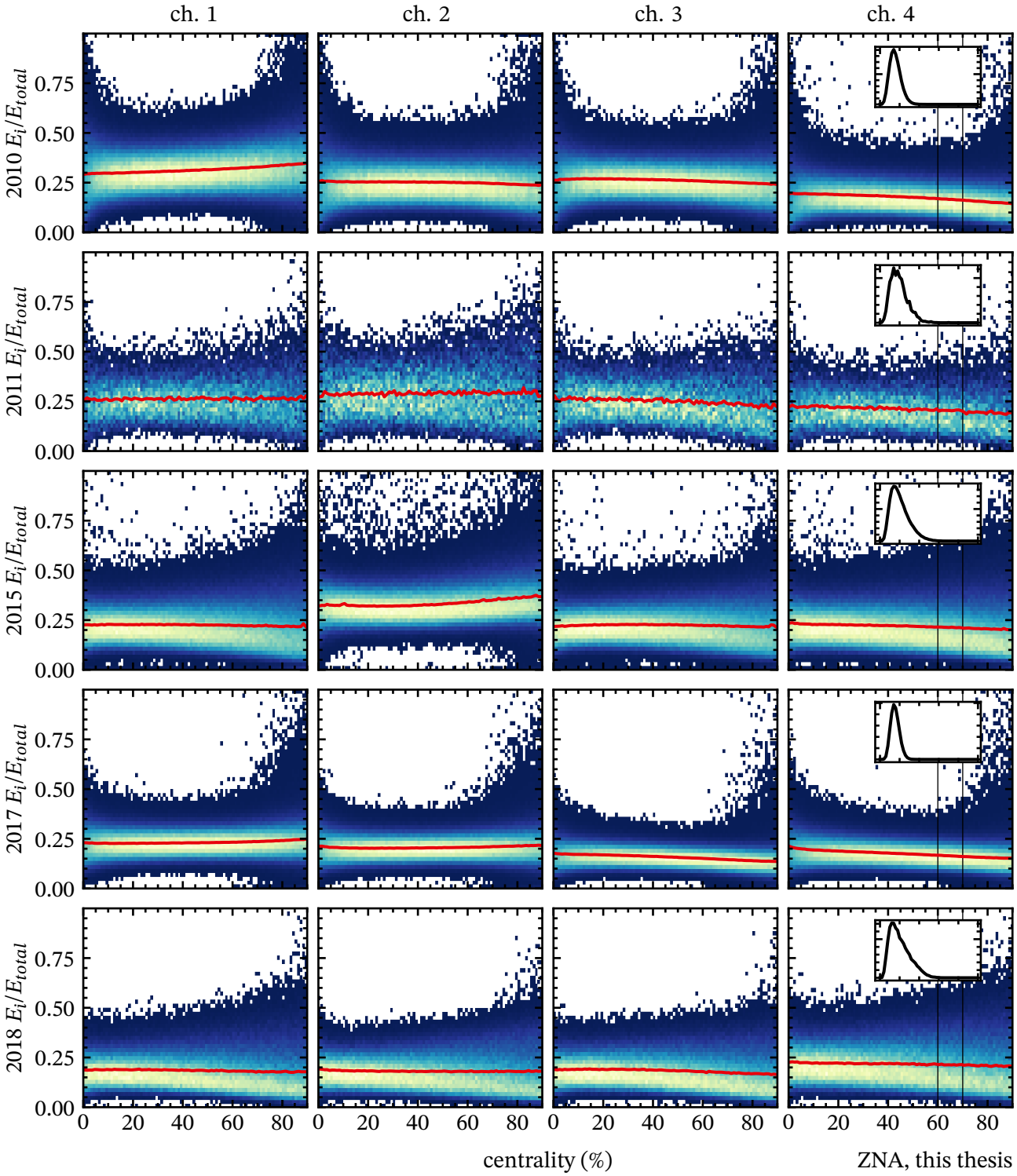

Figure A.14: Centrality dependence of the relative signal E_i/E_{total} for the ZNA in different data samples. See section 4.7 for the description of the figure.

List of Publications

This thesis is based on a publication currently in preparation. The physics analysis, on which the publication is based, has been reviewed internally in the ALICE collaboration and has been approved for publication. The target format of the publication is a letter. Results on the development of the flow vector software framework have been presented as a poster on the quark matter conference in 2019.

1. L. Kreis, V. Gonzalez, and I. Selyuzhenkov, “An object-oriented software framework for anisotropic flow analysis”, Poster, Quark Matter, (Wuhan, 2019).
2. ALICE Collaboration, “Elliptic flow fluctuations probed with spectator neutrons in Pb–Pb and Xe–Xe collisions”, in preparation.

Bibliography

3. Particle Data Group, “Review of particle physics”, Prog. Theor. Exp. Phys. 2020, 083C01 (2020).
4. P. W. Higgs, “Broken symmetries and the masses of gauge bosons”, Phys. Rev. Lett. 13, 508 (1964).
5. F. Englert and R. Brout, “Broken symmetry and the mass of gauge vector mesons”, Phys. Rev. Lett. 13, 321 (1964).
6. S. Weinberg, “A model of leptons”, Phys. Rev. Lett. 19, 1264 (1967).
7. ATLAS Collaboration, “Observation of a new particle in the search for the standard model higgs boson with the ATLAS detector at the LHC”, Phys. Lett. B 716, 1 (2012).
8. CMS Collaboration, “Observation of a new boson at a mass of 125 GeV with the CMS experiment at the LHC”, Phys. Lett. B 716, 30 (2012).
9. S. Kluth, “Tests of quantum chromo dynamics at e^+ e^- colliders”, Rept. Prog. Phys. 69, 1771 (2006).
10. M. Gell-Mann, “Symmetries of baryons and mesons”, Phys. Rev. 125, 1067 (1962).
11. K. G. Wilson, “Confinement of quarks”, Phys. Rev. D 10, 2445 (1974).
12. D. J. Gross and F. Wilczek, “Ultraviolet behavior of non-abelian gauge theories”, Phys. Rev. Lett. 30, 1343 (1973).
13. H. D. Politzer, “Reliable perturbative results for strong interactions?”, Phys. Rev. Lett. 30, 1346 (1973).
14. Y. Nambu and G. Jona-Lasinio, “Dynamical model of elementary particles based on an analogy with superconductivity. 1.”, Phys. Rev. 122, 345 (1961).
15. Y.-B. Yang et al., “Proton mass decomposition from the QCD energy momentum tensor”, Phys. Rev. Lett. 121, 212001 (2018).
16. R. Hagedorn, “Statistical thermodynamics of strong interactions at high-energies”, Nuovo Cim. Suppl. 3, 147 (1965).
17. N. Cabibbo and G. Parisi, “Exponential hadronic spectrum and quark liberation”, Phys. Lett. B 59, 67 (1975).
18. R. D. Pisarski and F. Wilczek, “Remarks on the chiral phase transition in chromodynamics”, Phys. Rev. D 29, 338 (1984).
19. D. Boyanovsky, H. J. de Vega, and D. J. Schwarz, “Phase transitions in the early and the present universe”, Ann. Rev. Nucl. Part. Sci. 56, 441 (2006).
20. G. Jaeger, “The Ehrenfest classification of phase transitions: introduction and evolution”, Arch. Hist. Exact Sci., 51 (1998).
21. D. Banuti, “Crossing the widom-line – supercritical pseudo-boiling”, J. Supercrit. Fluids. 98, 12 (2015).
22. W. Florkowski, “The realistic QCD equation of state in relativistic heavy-ion collisions and the early universe”, Nucl. Phys. A 853, 173 (2011).

23. HotQCD Collaboration, “The chiral and deconfinement aspects of the QCD transition”, Phys. Rev. D 85, 054503 (2012).

24. J. M. Lattimer, “The nuclear equation of state and neutron star masses”, Annu. Rev. Nucl. Part. Sci 62, 485 (2012).

25. HotQCD Collaboration, “Equation of state in (2 + 1)-flavor QCD”, Phys. Rev. D 90, 094503 (2014).

26. J. L. Nagle and W. A. Zajc, “Small system collectivity in relativistic hadronic and nuclear collisions”, Ann. Rev. Nucl. Part. Sci. 68, 211 (2018).

27. ALICE Collaboration, “Measurement of transverse energy at midrapidity in Pb-Pb collisions at $\sqrt{s_{\mathrm{NN}}} = 2.76$ TeV”, Phys. Rev. C 94, 034903 (2016).

28. L. D. McLerran and R. Venugopalan, “Gluon distribution functions for very large nuclei at small transverse momentum”, Phys. Rev. D 49, 3352 (1994).

29. W. Busza, K. Rajagopal, and W. van der Schee, “Heavy ion collisions: the big picture, and the big questions”, Ann. Rev. Nucl. Part. Sci. 68, 339 (2018).

30. A. Andronic et al., “Decoding the phase structure of QCD via particle production at high energy”, Nature 561, 321 (2018).

31. H.-W. Lin and H. B. Meyer, *Lattice QCD for nuclear physics*, (Springer, 2015).

32. B. Schenke, P. Tribedy, and R. Venugopalan, “Fluctuating glasma initial conditions and flow in heavy ion collisions”, Phys. Rev. Lett. 108, 252301 (2012).

33. D. Teaney and L. Yan, “Triangularity and dipole asymmetry in heavy ion collisions”, Phys. Rev. C 83, 064904 (2011).

34. M. Miller and R. Snellings, “Eccentricity fluctuations and its possible effect on elliptic flow measurements”, arXiv: nucl-ex/0312008 (2003).

35. A. Bzdak, P. Bozek, and L. McLerran, “Fluctuation induced equality of multi-particle eccentricities for four or more particles”, Nucl. Phys. A 927, 15 (2014).

36. W. van der Schee, P. Romatschke, and S. Pratt, “Fully dynamical simulation of central nuclear collisions”, Phys. Rev. Lett. 111, 222302 (2013).

37. J. Berges et al., “Turbulent thermalization process in high-energy heavy-ion collisions”, Nucl. Phys. A 931, 348 (2014).

38. A. Kurkela and E. Lu, “Approach to equilibrium in weakly coupled non-abelian plasmas”, Phys. Rev. Lett. 113, 182301 (2014).

39. R. J. Glauber, “Cross-sections in deuterium at high-energies”, Phys. Rev. 100, 242 (1955).

40. K. J. Eskola et al., “EPPS16: nuclear parton distributions with LHC data”, Eur. Phys. J. C 77, 163 (2017).

41. J. J. Ethier and E. R. Nocera, “Parton distributions in nucleons and nuclei”, Ann. Rev. Nucl. Part. Sci. 70, 43 (2020).

42. C. Loizides, J. Kamin, and D. d’Enterria, “Improved monte carlo glauber predictions at present and future nuclear colliders”, Phys. Rev. C 97, 054910 (2018), Erratum: Phys.Rev.C 99, 019901 (2019).

43. R. D. Woods and D. S. Saxon, “Diffuse surface optical model for nucleon-nuclei scattering”, Phys. Rev. 95, 577 (1954).
44. J. S. Moreland, J. E. Bernhard, and S. A. Bass, “Alternative ansatz to wounded nucleon and binary collision scaling in high-energy nuclear collisions”, Phys. Rev. C 92, 011901 (2015).
45. T. Lappi and R. Venugopalan, “Universality of the saturation scale and the initial eccentricity in heavy ion collisions”, Phys. Rev. C 74, 054905 (2006).
46. U. Heinz and R. Snellings, “Collective flow and viscosity in relativistic heavy-ion collisions”, Ann. Rev. Nucl. Part. Sci. 63, 123 (2013).
47. S. A. Voloshin et al., “Elliptic flow in the gaussian model of eccentricity fluctuations”, Phys. Lett. B 659, 537 (2008).
48. L. Yan, J.-Y. Ollitrault, and A. M. Poskanzer, “Eccentricity distributions in nucleus-nucleus collisions”, Phys. Rev. C 90, 024903 (2014).
49. L. D. Landau and E. M. Lifshitz, *Fluid mechanics*, 2nd ed., (Pergamon, 1959).
50. W. Israel and J. M. Stewart, “Transient relativistic thermodynamics and kinetic theory”, Ann. Phys. (N. Y.) 118, 341 (1979).
51. N. Christiansen et al., “Transport coefficients in Yang-Mills theory and QCD”, Phys. Rev. Lett. 115, 112002 (2015).
52. N. Astrakhantsev, V. Braguta, and A. Kotov, “Temperature dependence of shear viscosity of $SU(3)$–gluodynamics within lattice simulation”, J. High Energy Phys. 04, 101 (2017).
53. G. Policastro, D. T. Son, and A. O. Starinets, “The shear viscosity of strongly coupled N=4 supersymmetric yang-mills plasma”, Phys. Rev. Lett. 87, 081601 (2001).
54. J. D. Bjorken, “Highly relativistic nucleus-nucleus collisions: the central rapidity region”, Phys. Rev. D 27, 140 (1983).
55. B. B. Back et al., “Significance of the fragmentation region in ultrarelativistic heavy-ion collisions”, Phys. Rev. Lett. 91, 052303 (2003).
56. J. E. Bernhard, J. S. Moreland, and S. A. Bass, “Bayesian estimation of the specific shear and bulk viscosity of quark–gluon plasma”, Nat. Phys. 15, 1113 (2019).
57. D. Devetak et al., “Global fluid fits to identified particle transverse momentum spectra from heavy-ion collisions at the Large Hadron Collider”, J. High Energy Phys. 06, 044 (2020).
58. F. Becattini, “An introduction to the statistical hadronization model”, in International School on Quark-Gluon Plasma and Heavy Ion Collisions: past, present, future (2009).
59. M. Juric et al., “A new determination of the binding-energy values of the light hypernuclei ($A \leq 15$)”, Nucl. Phys. B 52, 1 (1973).
60. B. Schenke, S. Jeon, and C. Gale, “Anisotropic flow in $\sqrt{s} = 2.76$ TeV Pb+Pb collisions at the LHC”, Phys. Lett. B 702, 59 (2011).
61. E. Schnedermann, J. Sollfrank, and U. W. Heinz, “Thermal phenomenology of hadrons from 200-A/GeV S+S collisions”, Phys. Rev. C 48, 2462 (1993).

62. ALICE Collaboration, “Pion, kaon, and proton production in central Pb–Pb collisions at $\sqrt{s_{\mathrm{NN}}} = 2.76$ TeV”, Phys. Rev. Lett. 109, 252301 (2012).
63. STAR Collaboration, “Identified particle distributions in pp and Au+Au collisions at $\sqrt{s_{\mathrm{NN}}} = 200$ GeV”, Phys. Rev. Lett. 92, 112301 (2004).
64. ALICE Collaboration, “Anisotropic flow of charged particles in Pb-Pb collisions at $\sqrt{s_{\mathrm{NN}}} = 5.02$ TeV”, Phys. Rev. Lett. 116, 132302 (2016).
65. S. A. Voloshin (STAR Collaboration), “Energy and system size dependence of elliptic flow: using rapidity gaps to suppress non-flow contribution”, AIP Conf. Proc. 870, 691 (2006).
66. H. Song and U. W. Heinz, “Multiplicity scaling in ideal and viscous hydrodynamics”, Phys. Rev. C 78, 024902 (2008).
67. ALICE Collaboration, “Anisotropic flow in Xe-Xe collisions at $\sqrt{s_{\mathrm{NN}}} = 5.44$ TeV”, Phys. Lett. B 784, 82 (2018).
68. ALICE Collaboration, “Energy dependence and fluctuations of anisotropic flow in Pb-Pb collisions at $\sqrt{s_{\mathrm{NN}}} = 5.02$ and 2.76 TeV”, J. High Energy Phys. 07, 103 (2018).
69. B. H. Alver et al., “Triangular flow in hydrodynamics and transport theory”, Phys. Rev. C 82, 034913 (2010).
70. L. Yan, J.-Y. Ollitrault, and A. M. Poskanzer, “Azimuthal anisotropy distributions in high-energy collisions”, Phys. Lett. B 742, 290 (2015).
71. S. A. Voloshin, A. M. Poskanzer, and R. Snellings, “Collective phenomena in non-central nuclear collisions”, in *Relativistic heavy ion physics* (Springer, 2010), pp. 293–333.
72. ALICE Collaboration, “Anisotropic flow of charged hadrons, pions and (anti-)protons measured at high transverse momentum in Pb-Pb collisions at $\sqrt{s_{\mathrm{NN}}} = 2.76$ TeV”, Phys. Lett. B 719, 18 (2013).
73. A. Bzdak and V. Skokov, “Multi-particle eccentricities in collisions dominated by fluctuations”, Nucl. Phys. A 943, 1 (2015).
74. ALICE Collaboration, “Pseudorapidity dependence of the anisotropic flow of charged particles in Pb-Pb collisions at $\sqrt{s_{\mathrm{NN}}} = 2.76$ TeV”, Phys. Lett. B 762, 376 (2016).
75. E. Molnar et al., “Influence of temperature-dependent shear viscosity on elliptic flow at backward and forward rapidities in ultrarelativistic heavy-ion collisions”, Phys. Rev. C 90, 044904 (2014).
76. ALICE Collaboration, “Directed flow of charged particles at midrapidity relative to the spectator plane in Pb-Pb collisions at $\sqrt{s_{NN}}$=2.76 TeV”, Phys. Rev. Lett. 111, 232302 (2013).
77. ALICE Collaboration, “Harmonic decomposition of two-particle angular correlations in Pb-Pb collisions at $\sqrt{s_{NN}} = 2.76$ TeV”, Phys. Lett. B 708, 249 (2012).
78. ALICE Collaboration, “Event shape engineering for inclusive spectra and elliptic flow in Pb-Pb collisions at $\sqrt{s_{\mathrm{NN}}} = 2.76$ TeV”, Phys. Rev. C 93, 034916 (2016).
79. O. S. Brüning et al., *LHC design report vol.1: the LHC main ring*, CERN Yellow Reports: Monographs, (CERN, 2004).

80. M. Benedikt et al., *LHC design report. vol.3: the LHC injector chain*, (Dec. 2004).
81. O. S. Brüning et al., *LHC design report. vol.2: the LHC infrastructure and general services*, CERN Yellow Reports: Monographs, (CERN, Geneva, 2004).
82. L. Evans and P. Bryant, "LHC machine", J. Inst. 3, S08001 (2008).
83. E. Mobs, "The CERN accelerator complex - 2019", General Graphic (2019).
84. J. Jowett, "Colliding heavy ions in the LHC", in Proc. 9th international particle accelerator conference (2018).
85. ALICE Collaboration, *ALICE website*, (2021) `https://alice.cern/` (2021-06-17).
86. ATLAS Collaboration, *ATLAS website*, (2021) `https://atlas.cern/about` (2021-06-17).
87. CMS Collaboration, *CMS website*, (2021) `https://cms.cern/detector` (2021-06-17).
88. LHCb Collaboration, *LHCb website*, (2021) `https://lhcb-public.web.cern.ch/` (2021-06-17).
89. FASER Collaboration, "Technical proposal for FASER: ForwArd Search ExpeRiment at the LHC", CERN-LHCC-2018-036 (2018).
90. LHCf Collaboration,
91. MoEDAL Collaboration, "Technical design report of the MoEDAL experiment", CERN-LHCC-2009-006 (2009).
92. TOTEM Collaboration, "TOTEM: technical design report. total cross section, elastic scattering and diffraction dissociation at the large hadron collider at CERN", CERN-LHCC-2004-002 (2004).
93. H. Wiedemann, *Particle accelerator physics*, 4th ed., (Springer, 2015).
94. ALICE Collaboration, "Measurement of the cross section for electromagnetic dissociation with neutron emission in Pb-Pb collisions at $\sqrt{s_{\mathrm{NN}}} = 2.76$ TeV", Phys. Rev. Lett. 109, 252302 (2012).
95. A. J. Baltz, M. J. Rhoades-Brown, and J. Weneser, "Heavy ion partial beam lifetimes due to coulomb induced processes", Phys. Rev. E 54, 4233 (1996).
96. J. Jowett et al., "The 2018 heavy-ion run of the LHC", in 10th International Particle Accelerator Conference (2019).
97. ALICE Collaboration, "The ALICE experiment at the CERN LHC", J. Instrum. 3, S08002 (2008).
98. ALICE Collaboration, "Performance of the ALICE experiment at the CERN LHC", Int. J. Mod. Phys. A 29, 1430044 (2014).
99. ALICE Collaboration, "ALICE technical design report of the zero degree calorimeter (ZDC)", CERN-LHCC-99-05 (1999).
100. J. M. Jowett, M. Schaumann, and R. Versteegen, "Heavy-ion operation of HL-LHC", Adv. Ser. Direct. High Energy Phys. 24, 359 (2015).
101. ALICE Collaboration, "ALICE technical design report of the inner tracking system (its)", CERN-LHCC-99-12 (1999).

102. ALICE Collaboration, “ALICE: technical design report of the time projection chamber”, CERN-LHCC-2000-001 (2000).

103. H. Bethe, “Zur Theorie des Durchgangs schneller Korpuskularstrahlen durch Materie”, Ann. Phys. (Berl.) 397, 325 (1930).

104. ALICE Collaboration, “Upgrade of the ALICE time projection chamber”, CERN-LHCC-2013-020 (2014).

105. ALICE TPC Collaboration, “The upgrade of the ALICE TPC with GEMs and continuous readout”, J. Instrum. 16, P03022 (2021).

106. ALICE Collaboration, “ALICE technical design report on forward detectors: FMD, T0 and V0”, CERN-LHCC-2004-025 (2004).

107. P. Gorodetzky et al., “Quartz fiber calorimetry”, Nucl. Instrum. Methods Phys. Res. A 361, 161 (1995).

108. P. A. Cherenkov, “Visible emission of clean liquids by action of γ radiation”, Doklady Akademii Nauk SSSR. 2 (1934).

109. G. Anzivino et al., “Quartz fibre calorimetry — monte carlo simulation”, Nucl. Instrum. Methods Phys. Res. A 357, 380 (1995).

110. G. Dellacasa et al., “The neutron zero degree calorimeter for the ALICE experiment”, Nucl. Instrum. Meth. A 564, 235 (2006).

111. J. M. Jowett, M. Schaumann, and R. Versteegen, “Heavy ion operation from run 2 to HL-LHC”, in RLIUP: review of LHC and injector upgrade plans (2014), pp. 167–184.

112. ALICE Collaboration, “Performance of the ALICE VZERO system”, J. Instrum. 8, P10016 (2013).

113. ALICE Collaboration, “Centrality and pseudorapidity dependence of the charged-particle multiplicity density in Xe–Xe collisions at $\sqrt{s_{\mathrm{NN}}} = 5.44$ TeV”, Phys. Lett. B 790, 35 (2019).

114. R. Frühwirth, “Application of Kalman filtering to track and vertex fitting”, Nucl. Instrum. Methods Phys. Res. A 262, 444 (1987).

115. ALICE Collaboration, “Centrality determination in heavy ion collisions”, ALICE-PUBLIC-2018-011 (2018).

116. ALICE Collaboration, “Centrality determination using the Glauber model in Xe-Xe collisions at $\sqrt{s_{\mathrm{NN}}} = 5.44$ TeV”, ALICE-PUBLIC-2018-003 (2018).

117. C. A. Charalambides, *Enumerative combinatorics*, (CRC Press, 2002).

118. J. F. Kenney and E. S. Keeping, “Mathematics of statistics, pt. 2, 2nd ed.”, in (Princeton, 1951) Chap. Cumulants and the Cumulant-Generating Function, pp. 77–80.

119. E. T. Bell, “Exponential polynomials”, Ann. Math. 35, 258 (1934).

120. N. Borghini, P. M. Dinh, and J.-Y. Ollitrault, “A new method for measuring azimuthal distributions in nucleus-nucleus collisions”, Phys. Rev. C 63, 054906 (2001).

121. A. Bilandzic et al., “Generic framework for anisotropic flow analyses with multi-particle azimuthal correlations”, Phys. Rev. C 89, 064904 (2014).

122. N. J. A. Sloane, *A handbook of integer sequences*, (Academic Press, 1973).

123. STAR Collaboration, "Elliptic flow from two and four particle correlations in Au+Au collisions at $\sqrt{s_{\mathrm{NN}}} = 130$ GeV", Phys. Rev. C 66, 034904 (2002).

124. A. Bilandzic, R. Snellings, and S. Voloshin, "Flow analysis with cumulants: direct calculations", Phys. Rev. C 83, 044913 (2011).

125. ALICE Collaboration, "Multi-particle azimuthal correlations in p–Pb and Pb–Pb collisions at the CERN large hadron collider", Phys. Rev. C 90, 054901 (2014).

126. Y. Zhou et al., "Investigation of possible hadronic flow in $\sqrt{s_{\mathrm{NN}}} = 5.02$ TeV p-Pb collisions", Phys. Rev. C 91, 064908 (2015).

127. A. M. Poskanzer and S. A. Voloshin, "Methods for analyzing anisotropic flow in relativistic nuclear collisions", Phys. Rev. C 58, 1671 (1998).

128. J. Schukraft, A. Timmins, and S. A. Voloshin, "Ultra-relativistic nuclear collisions: event shape engineering", Phys. Lett. B 719, 394 (2013).

129. I. Selyuzhenkov and S. Voloshin, "Effects of nonuniform acceptance in anisotropic flow measurements", Phys. Rev. C 77, 034904 (2008).

130. ATLAS Collaboration, "Measurement of the azimuthal anisotropy for charged particle production in $\sqrt{s_{\mathrm{NN}}} = 2.76$ TeV lead-lead collisions with the ATLAS detector", Phys. Rev. C 86, 014907 (2012).

131. ALICE Collaboration, "Higher harmonic anisotropic flow measurements of charged particles in Pb-Pb collisions at $\sqrt{s_{\mathrm{NN}}} = 2.76$ TeV", Phys. Rev. Lett. 107, 032301 (2011).

132. Z. Qiu and U. W. Heinz, "Event-by-event shape and flow fluctuations of relativistic heavy-ion collision fireballs", Phys. Rev. C 84, 024911 (2011).

133. M. Luzum and J.-Y. Ollitrault, "Extracting the shear viscosity of the quark-gluon plasma from flow in ultra-central heavy-ion collisions", Nucl. Phys. A 904-905, 377c (2013).

134. J. Onderwaater (ALICE Collaboration), "Charge dependence of identified two-hadron correlation relative to the reaction plane in Pb-Pb collisions measured with ALICE", J. Phys. Conf. Ser 612, 012044 (2015).

135. L. Kreis et al., *QnTools*, `https://github.com/HeavyIonAnalysis/QnTools` (2021-06-17).

136. V. Klochkov and I. Selyuzhenkov (NA61/SHINE Collaboration), "NA61/SHINE measurements of anisotropic flow relative to the spectator plane in Pb+Pb collisions at 30A GeV/c", Nucl. Phys. A 982, 439 (2019).

137. V. Klochkov and I. Selyuzhenkov (CBM Collaboration), "CBM performance for anisotropic flow measurements", KnE Energ. Phys. 3, 416 (2018).

138. O. Golosov et al. (NA49 Collaboration), "Effects of the detector non-uniformity in pion directed flow measurement relative to the spectator plane by the NA49 experiment at the CERN SPS", EPJ Web Conf. 204, 06011 (2019).

139. M. Mamaev, O. Golosov, and I. Selyuzhenkov (HADES Collaboration), "Directed flow of protons with the event plane and scalar product methods in the HADES experiment at SIS18", J. Phys. Conf. Ser. 1690, 012122 (2020).

140. M. Gyulassy and X.-N. Wang, "HIJING 1.0: a monte carlo program for parton and particle production in high-energy hadronic and nuclear collisions", Comput. Phys. Commun. 83, 307 (1994).

141. R. Brun et al., *GEANT: detector description and simulation tool*, CERN Program Library, (CERN, 1993).

142. Y. Belikov et al., "TPC tracking and particle identification in high density environment", in Proceedings, 13th International Conference on Computing in High-Enery and Nuclear Physics (CHEP), Vol. C0303241 (2003), TULT011.

143. J. D. Burden R. L.; Faires and A. C. Reynolds, *Numerical analysis*, 6th ed., (Brooks/Cole, 1997).

144. J. M. Gronefeld, *Transverse momentum distributions and nuclear modification factors in heavy-ion collisions with ALICE at the large hadron collider*, dissertation, (Technische Universität Darmstadt, 2018).

145. M. Schaumann et al., "First xenon-xenon collisions in the LHC", in 9th International Particle Accelerator Conference (2018).

146. ALICE Collaboration, "Probing the effects of strong electromagnetic fields with charge-dependent directed flow in Pb-Pb collisions at the LHC", Phys. Rev. Lett. 125, 022301 (2020).

147. R. Gemme, *Study of the ALICE ZDC detector performance*, dissertation, (Turin University, 2006).

148. M. Winkler and F. James, *Minuit2*, `https://root.cern.ch/doc/v624/Minuit2Page.html` (2021-07-15).

149. JETSCAPE Collaboration, "Multisystem bayesian constraints on the transport coefficients of QCD matter", Phys. Rev. C 103, 054904 (2021).

150. ALICE Collaboration, "Charged-particle multiplicity density at mid-rapidity in central Pb-Pb collisions at $\sqrt{s_{\mathrm{NN}}} = 2.76$ TeV", Phys. Rev. Lett. 105, 252301 (2010).

151. ALICE Collaboration, "Centrality dependence of the charged-particle multiplicity density at midrapidity in Pb-Pb collisions at $\sqrt{s_{\mathrm{NN}}} = 2.76$ TeV", Phys. Rev. Lett. 106, 032301 (2011).

152. V. Skokov, A. Y. Illarionov, and V. Toneev, "Estimate of the magnetic field strength in heavy-ion collisions", Int. J. Mod. Phys. A 24, 5925 (2009).

153. K. Tuchin, "Particle production in strong electromagnetic fields in relativistic heavy-ion collisions", Adv. High Energy Phys. 2013, 490495 (2013).

154. M. A. L. Leite (ATLAS Collaboration), "Performance of the ATLAS zero degree calorimeter", in 2013 IEEE nuclear science symposium and medical imaging conference (2013).

155. O. Surányi et al., "Performance of the CMS zero degree calorimeters in pPb collisions at the LHC", J. Instrum. 16, P05008 (2021).